

# VU Research Portal

## A GridPix TPC readout for the ILD experiment at the future International Linear Collider

Ligtenberg, Cornelis

2021

### **document version**

Publisher's PDF, also known as Version of record

[Link to publication in VU Research Portal](#)

### **citation for published version (APA)**

Ligtenberg, C. (2021). *A GridPix TPC readout for the ILD experiment at the future International Linear Collider*. s.n.

### **General rights**

Copyright and moral rights for the publications made accessible in the public portal are retained by the authors and/or other copyright owners and it is a condition of accessing publications that users recognise and abide by the legal requirements associated with these rights.

- Users may download and print one copy of any publication from the public portal for the purpose of private study or research.
- You may not further distribute the material or use it for any profit-making activity or commercial gain
- You may freely distribute the URL identifying the publication in the public portal ?

### **Take down policy**

If you believe that this document breaches copyright please contact us providing details, and we will remove access to the work immediately and investigate your claim.

### **E-mail address:**

[vuresearchportal.ub@vu.nl](mailto:vuresearchportal.ub@vu.nl)

VRIJE UNIVERSITEIT

**A GridPix TPC readout for the ILD experiment at  
the future International Linear Collider**

ACADEMISCH PROEFSCHRIFT

ter verkrijging van de graad Doctor of Philosophy aan  
de Vrije Universiteit Amsterdam,  
op gezag van de rector magnificus  
prof.dr. V. Subramaniam,  
in het openbaar te verdedigen  
ten overstaan van de promotiecommissie  
van de Faculteit der Bètawetenschappen  
op dinsdag 28 september 2021 om 13.45 uur  
in de aula van de universiteit,  
De Boelelaan 1105

door

Cornelis Ligtenberg

geboren te Amstelveen

promotoren:            prof.dr. H.G. Raven  
                              prof.dr. S.C.M. Bentvelsen

copromotoren:        dr.ir. P.M. Kluit

promotiecommissie:  prof.dr. M.H.M. Merk  
                              prof.dr. N. de Groot  
                              prof.dr.ing. B. van Eijk  
                              prof.dr. H.L. Bethlem  
                              dr. H.L. Snoek  
                              dr. J.M. Sonneveld



Dit werk maakt deel uit van het onderzoekprogramma van de Stichting voor Fundamenteel Onderzoek der Materie (FOM), die deel uitmaakt van de Nederlandse Organisatie voor Wetenschappelijk Onderzoek (NWO).

---

# Contents

---

<b>Introduction</b>	<b>1</b>
<b>1 The Standard Model of particle physics</b>	<b>5</b>
1.1 Description of the Standard Model . . . . .	5
1.1.1 Forces and their carriers . . . . .	6
1.1.2 Fermions . . . . .	8
1.1.3 The Higgs mechanism . . . . .	8
1.2 Beyond the Standard Model . . . . .	9
1.2.1 Reasons for physics beyond the Standard Model . . . . .	9
1.2.2 Beyond the Standard Model and the Higgs boson . . . . .	10
1.3 Higgs production at an electron positron collider . . . . .	11
1.3.1 Higgs boson production . . . . .	11
1.3.2 Higgs boson decay . . . . .	13
1.3.3 Higgs boson physics goals . . . . .	13
1.3.4 Higgs physics at the ILC . . . . .	14
<b>2 ILC and ILD</b>	<b>17</b>
2.1 The international linear collider . . . . .	18
2.1.1 Layout of the ILC accelerator . . . . .	18
2.1.2 Beam conditions . . . . .	20
2.1.3 Luminosity and event rate . . . . .	20
2.2 The international large detector . . . . .	21
2.2.1 Detector requirements . . . . .	22
2.2.2 Overview of the detector . . . . .	23
2.2.3 Tracking detectors . . . . .	25
2.2.4 Calorimeter system . . . . .	28
2.2.5 Forward calorimeters . . . . .	30
2.2.6 Outer detector . . . . .	30
2.2.7 Data acquisition . . . . .	30

<b>3</b>	<b>Gaseous detector physics and the TPC</b>	<b>33</b>
3.1	Energy loss of charged particles . . . . .	33
3.1.1	Cross section and mean free path . . . . .	34
3.1.2	Mean energy loss of charged particles . . . . .	35
3.1.3	Fluctuations on the energy loss . . . . .	36
3.1.4	Multiple scattering . . . . .	37
3.2	Charge transport in gas . . . . .	38
3.2.1	Drift velocity . . . . .	38
3.2.2	Diffusion . . . . .	40
3.3	The amplification of charge . . . . .	40
3.3.1	Fluctuations on the amplification of charge . . . . .	41
3.3.2	Ion backflow . . . . .	41
3.4	Micropattern gaseous detectors . . . . .	42
3.4.1	The gas electron multiplier (GEM) . . . . .	42
3.4.2	The micro-mesh gaseous structure (Micromegas) . . . . .	43
3.4.3	The GridPix . . . . .	44
3.5	The choice of a gas mixture . . . . .	44
3.5.1	Factors that determine the gas choice . . . . .	44
3.5.2	Motivation for the use of T2K gas mixture . . . . .	47
3.6	A TPC as a tracker in a collider experiment . . . . .	48
3.6.1	The ILD TPC at the ILC . . . . .	48
3.6.2	A TPC for a detector at the compact linear collider . . . . .	48
3.6.3	A TPC for a detector at the future circular collider . . . . .	49
3.6.4	A TPC for a detector at the circular electron positron collider . . . . .	50
<b>4</b>	<b>The GridPix</b>	<b>51</b>
4.1	The GridPix . . . . .	52
4.1.1	The protection layer . . . . .	53
4.1.2	Production . . . . .	53
4.1.3	Other applications of GridpPix detectors . . . . .	54
4.2	The Timepix3 . . . . .	55
4.2.1	Threshold equalisation . . . . .	57
4.2.2	ToT-charge calibration . . . . .	58
4.3	Properties of a GridPix detector . . . . .	58
4.3.1	Gas gain of the GridPix . . . . .	58
4.3.2	Efficiency of a GridPix detector using source measurements . . . . .	59
4.3.3	Ion backflow . . . . .	62
4.3.4	Resistivity and charging up of the protection layer . . . . .	62

---

<b>5</b>	<b>Performance of a GridPix detector</b>	<b>67</b>
5.1	Description of the GridPix device . . . . .	67
5.2	Test beam measurement . . . . .	68
5.3	Track reconstruction and event selection . . . . .	70
5.3.1	Track fitting . . . . .	70
5.3.2	Selections . . . . .	71
5.4	Test beam results . . . . .	72
5.4.1	Time over threshold and approximate gain . . . . .	72
5.4.2	Number of hits on track . . . . .	73
5.4.3	Time walk correction . . . . .	73
5.4.4	Hit resolution in the pixel plane . . . . .	75
5.4.5	Hit resolution in the drift direction . . . . .	76
5.4.6	Deformations . . . . .	76
5.4.7	Energy loss measurement and particle identification . . . . .	77
5.5	Conclusions . . . . .	81
<b>6</b>	<b>Performance of the GridPix detector quad</b>	<b>83</b>
6.1	Quad detector design and construction . . . . .	83
6.1.1	The quad module design and assembly . . . . .	84
6.1.2	The quad detector . . . . .	84
6.2	Test beam measurement . . . . .	84
6.3	Track reconstruction and event selection . . . . .	87
6.3.1	Track reconstruction procedure . . . . .	87
6.3.2	Selections . . . . .	89
6.4	Results . . . . .	89
6.4.1	Number of hits . . . . .	90
6.4.2	Hit time corrections . . . . .	91
6.4.3	Time walk correction . . . . .	91
6.4.4	Hit resolution in the pixel plane . . . . .	92
6.4.5	Hit resolution in the drift direction . . . . .	93
6.4.6	Deformations in the pixel plane . . . . .	93
6.4.7	Deformations in the drift direction . . . . .	94
6.4.8	Quad detector resolution . . . . .	94
6.5	Conclusions and outlook . . . . .	97
<b>7</b>	<b>Pixel TPC simulation</b>	<b>101</b>
7.1	Virtual geometry of the TPC . . . . .	102
7.2	Simulation of the TPC . . . . .	103
7.2.1	Simulation of the pad readout . . . . .	103
7.2.2	Simulation of the pixel readout . . . . .	105

7.2.3	Comparison of the hit resolution for the pad and pixel readout	107
7.3	Track reconstruction	108
7.3.1	Track parameters	109
7.3.2	The extended Kalman filter	110
7.3.3	The extended Kalman filter for track fitting	111
7.3.4	Track fitting for a TPC	111
7.3.5	Track finding and fitting procedure	112
<b>8</b>	<b>Pixel TPC performance and design</b>	<b>117</b>
8.1	The simulated TPC with a pixel readout	117
8.1.1	End plate layout	118
8.1.2	Energy loss in the TPC gas	118
8.1.3	Number of pixel hits	119
8.2	Tracking performance	121
8.2.1	Momentum resolution	121
8.2.2	z-resolution and time resolution	126
8.2.3	Two-track separation performance	128
8.2.4	Energy loss measurement	128
8.3	Performance of the ILD	130
8.3.1	Tracking performance of the ILD	130
8.4	The Higgs boson decay to tau leptons	133
8.4.1	Cross section and number of events	133
8.4.2	Object definitions	134
8.4.3	Efficiency	134
8.4.4	Recoil mass	134
8.4.5	Tau reconstruction	136
8.4.6	Comparison of the pixel and pad tracking performance	136
8.5	The TPC system with GridPix readout	137
8.5.1	Power consumption	137
8.5.2	Cooling	138
8.5.3	Occupancy, necessary link speeds, and data volume	138
8.5.4	Influence of ions in the drift volume	139
8.5.5	Costing	140
	<b>Conclusions and outlook</b>	<b>141</b>
<b>A</b>	<b>A negative-ion TPC prototype with GridPix readout</b>	<b>147</b>
A.1	Introduction	148
A.2	Quad detector	149
A.2.1	Gridpix	149
A.2.2	Quad module	149

---

A.2.3	Experimental setup . . . . .	150
A.3	Analysis . . . . .	152
A.4	Performance . . . . .	154
A.4.1	Number of hits . . . . .	154
A.4.2	Drift velocity measurements . . . . .	156
A.4.3	Diffusion measurements . . . . .	157
A.4.4	Reconstruction of drift distance . . . . .	159
A.5	Conclusions and outlook . . . . .	161
A.6	Acknowledgements . . . . .	162
<b>B</b>	<b>Cost estimate of a TPC with GridPix readout</b>	<b>163</b>
	<b>Acronyms</b>	<b>165</b>
	<b>Bibliography</b>	<b>166</b>
	<b>Summary</b>	<b>183</b>
	<b>Samenvatting</b>	<b>189</b>





---

# Introduction

---

Fundamental particles are constituents of the universe. There are only a few different kind of particles, and all particles of one type are identical. Their behaviour is governed by a set of laws, and particle physics is the study of these fundamental laws of nature. Our current best theory of physics at the most fundamental level is the Standard Model of particle physics (see e.g. [1]), covering all established fundamental particles and describing three of the four known fundamental forces using symmetries. The recent discovery [2, 3] of the long-expected Higgs boson [4, 5] by the ATLAS and CMS experiments at the Large Hadron Collider (LHC) completes the particle content of the Standard Model.

Still, the Standard Model is not a complete description of nature, since it does not include the gravitational force [6], nor does it describe dark matter [7], and does not explain the abundance of matter over anti-matter, see e.g. [8]. Additional particles, an extra force, or other new physics is needed to supplement the current theories. As the only fundamental scalar particle, the Higgs boson can receive quantum corrections from undiscovered particles and it is considered to be a probe for new physics. In Chapter 1, the Standard Model, motivations for new physics, and the role of the Higgs boson herein will be discussed.

Many research efforts are concentrated around the experiments at the LHC, which will be upgraded in different stages over the course of the next decade(s) [9]. Nevertheless, the precision of some measurements will be limited. There is consensus that a new electron positron collider will be an important next step [10], because it can produce large numbers of Higgs bosons in a clean environment. The proposed future electron positron colliders are either circular or linear machines.

In a circular collider two counter circulating beams are bent by a series of magnets and can repeatedly cross at multiple interaction points. However, the bending along a radius  $R$  does cause the particles to lose energy  $\Delta E$  through synchrotron radiation proportional to the energy of the particle  $E$  to the fourth power:  $\Delta E \propto E^4/R$ . If the cost of a circular collider is proportional to some linear combination of the energy lost per turn  $\Delta E$  and the radius  $R$ , the cost-optimised radius is proportional to the

energy squared:  $R \propto E^2$ . This makes the cost of a circular electron positron collider scale proportional to the squared energy of the colliding particles, i.e.  $\text{cost} \propto E^2$  [11].

In the linear layout the beams are accelerated on a straight trajectory, and collide in one central interaction point. The achievable energy is primarily limited by the accelerating gradient and the length of the accelerator. The cost is roughly proportional to the energy of the accelerated particles:  $\text{cost} \propto E$  [11]. Therefore, a linear collider is ultimately the most scalable technology to collide electron and positrons at extremely high energies of the order of a TeV.

The International Linear Collider [12] is one of the proposed linear colliders, which will initially operate at a lower centre-of-mass energy of 250 GeV. However, uniquely to linear colliders, it can be upgraded to reach higher centre-of-mass energies. The International Linear Collider is described in Chapter 2 along with the International Large Detector [13], a possible experiment at this collider. The experiment will study the high energy particles produced in the collisions and their decay products. This will be accomplished through a series of subdetectors, among which is a gaseous Time Projection Chamber (TPC) [14] as the main tracking detector.

The tracking detectors measure the trajectory of charged particles. The use of gaseous detectors in high energy particle physics has a long history, e.g. [15–17]. The TPC is an established type of tracking detector at electron positron collider experiments [18, 19], because of their low material budget, cost-efficiency, and particle identification capabilities. The physics of gaseous detectors and the TPC is discussed in Chapter 3.

The performance of a TPC is to a large extent determined by the technologies used for the signal amplification and readout. Micropattern structures [20, 21] are used in TPCs to provide signal amplification before the signal is read out by a pad readout plane. However, these more customary pad readouts have a granularity much lower than the amplification structures. The most precise measurement can be made with a readout granularity that matches the micropattern amplifications structures. This is achieved with the GridPix readout [22, 23], which was pioneered at Nikhef and integrates a micropattern amplification structure on a highly segmented silicon chip to achieve sensitivity to single ionisation electrons. The added benefit is that the digitisation of the signal is processed on the chip. The topic of Chapter 4 is the GridPix based on the novel Timepix3 [24] chip and its characterisation, to which the author contributed.

The Timepix3 based GridPix was used to build a small-size detector, which was tested using high energy electrons at the test beam facility in Bonn. For the experiment described in Chapter 5, the author participated in data taking, and performed the data analysis. The chapter is based on the results published in [25].

Given that the detector performed well, a quad module with four GridPix chips was designed and built for the construction of larger detectors. This module was

---

also tested at the test beam facility in Bonn. The author contributed to the data acquisition, the experiment, and analysed the data. The Chapter 6 is based on the publication [26]. The same module was applied in a negative ion TPC, the description of which can be found in a publication under review, attached as appendix A.

A GridPix readout can enhance the performance of the detectors at future colliders, including the International Large Detector at the International Linear Collider. The author has made a simulation of a pixel TPC within the existing software framework, by modifying the geometry, physics simulation, track finding, and track reconstruction. This is described in Chapter 7. The simulated tracking performance is investigated by the author, and is discussed in Chapter 8. The detector performance for events in which a produced Higgs boson decays to a pair of tau leptons is briefly explored. Finally, some topics connected to the implementation of a GridPix readout in the International Large Detector are described.



## The Standard Model of particle physics

---

Our current best understanding of the behaviour of the fundamental particles and their interactions is captured in the Standard Model of particle physics (SM). The current model was formulated in the 1970s [27–30] after a series of experimental (e.g. [31–34]) and theoretical (e.g. [4, 5, 35–38]) developments over the course of the last century. Since then, the model was consolidated by a large number of observations and discoveries [39–43]. With the discovery of the Higgs boson in 2012 [2, 3], all SM particles have been observed. Accessible descriptions of the SM are found in textbooks [1, 44] and reviews [45].

Despite its successes, the SM cannot be the ultimate theory of particle physics for a number of reasons, several of which are related to the Higgs boson as will be discussed below. The study of the Higgs boson produced in electron positron collisions will provide unique ways to search for new physics beyond the SM.

### 1.1 Description of the Standard Model

The SM contains two categories of particles, characterised by their spin. The fermions that make up most of the matter have half integer spin<sup>1</sup>. The Dirac equation [46] captures the dynamics of the fermions. Bosons are characterised by integer spin. The weak force, the electromagnetic force and the strong force are mediated by vector bosons with spin 1. Each of the fundamental forces is described by a relativistic

---

<sup>1</sup>In this thesis natural units are used,  $\hbar = c = 1$

quantum field theory (QFT). The Higgs boson is a spin-0 scalar particle, and provides a mechanism that gives mass to the other particles. An overview of the particles of the SM is shown in Figure 1.1.

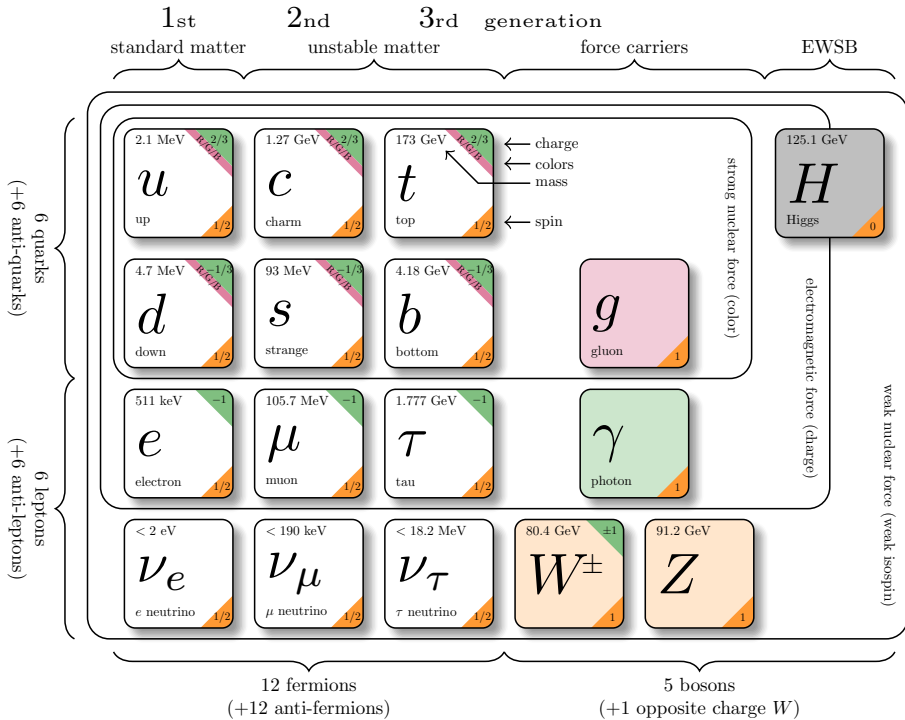


Figure 1.1: Particle content of the Standard Model with the mass, electromagnetic charge and spin indicated. Graphics adapted from [47], and values taken from [45].

### 1.1.1 Forces and their carriers

The fundamental forces are described by a non-abelian gauge theory, called Yang-Mills theory [35]. The interactions between particles correspond to the exchange of a gauge boson. The gravitational force is not described by the SM, but by the theory of general relativity [6]. Due to its small strength on the scales relevant for particle physics, gravity can be neglected when considering the other fundamental forces.

The electromagnetic force and the weak force are jointly described by electroweak theory (the Glashow-Salam-Weinberg model [27–29]), which has the  $SU(2)_L \otimes U(1)_Y$

symmetry associated to it. The electromagnetic force is mediated by the massless photon  $\gamma$  and has unlimited range, but the weak force is mediated by the massive  $W^\pm$  and  $Z$  gauge bosons, and therefore its range is limited.

The weak interaction has a chiral structure, which is introduced by defining left- and right-handed chiral projection operators using the  $\gamma_5$  matrix related to the covariant formulation of the Dirac equation. The fermions' left-handed chirality eigenstates are organised in doublets while the fermions' right-handed eigenstates are organised in singlets. In the limit that the energy is much larger than the mass of a particle, the chirality states are equal to the helicity states, defined as the projection of its spin on the direction of its momentum. The gauge transformation  $SU(2)_L$  effectively acts only on the particle doublets, so that the charged weak current mediated by the  $W$  bosons couples only to left-handed particles. The neutral current interactions mediated by the  $Z$  boson and photon  $\gamma$  are the result of the mixing of the neutral fields of the  $U(1)_Y$  and  $SU(2)_L$  gauge symmetries. Consequently, the photon  $\gamma$  and the  $Z$  boson couple to both the left and right handed part of particles, albeit the  $Z$  boson does not do so equally.

The strong force is described by quantum chromodynamics (QCD), and has 8 gluons as its gauge bosons. The gluons are massless and thus the strong force is not limited in range. The associated group is the  $SU(3)_C$  symmetry group. The three components of the charge are named after the three colours: red, green and blue. The gluons have color charge themselves, giving rise to self-interactions.

Determination of the observable decay rates  $\Gamma$  and interaction cross sections  $\sigma$  requires the calculation of the quantum-mechanical transition probability, for which Feynman diagrams are often utilised. A Feynman diagram that has been drawn with a set of Feynman rules derived from the theory, represents a contribution to the quantum-mechanical transition probability (the matrix element) [48]. The transition probability between two states is the sum of all possible diagrams.

In general there are an infinite number of diagrams for every transition. In this infinite sum divergences occur which are problematic. These can be solved by absorbing the infinite sum of contributions in the propagators and vertices of the Feynman diagrams. This is called re-normalisation [30, 49, 50] and makes it possible to perform reliable calculations and precise predictions. As a consequence, the masses of particles receive corrections and the interactions depend on the energy scale.

Calculations are usually performed using perturbation theory. At low energies, both the size of the squared coupling constant for the electromagnetic force,  $g^2 = \alpha \approx 1/137$ , and weak interactions,  $g_2 = \alpha_W \approx 1/30$ , is small enough that diagrams with increasing number of vertices can safely be neglected. The strong force has the largest coupling constant of all the gauge interactions, and it depends strongly on the energy scale. At an energy of 1 GeV, the squared coupling constant  $g_S^2 = \alpha_S = \mathcal{O}(1)$  is too large to use perturbation theory. Fortunately, at typical collider experiment



energies ( $q \approx m_Z$ ) the coupling constant is  $\mathcal{O}(0.1)$ , which is small enough to apply perturbation theory. This is known as asymptotic freedom [51, 52].

### 1.1.2 Fermions

The fermions are divided into 6 quarks and 6 leptons, and corresponding antiparticles with the same properties but opposite charges. Both the quarks and leptons are divided into three generations. The particles in the three generations differ by their mass. Every generation has an up-type quark with electromagnetic charge  $2/3e$  and a down-type quark with electromagnetic charge  $-1/3e$ . The strong force causes quarks to always occur as bound colourless states, called hadrons. Mesons are bound states consisting of a quark and an anti-quark, and (anti)baryons are bound states consisting of three (anti)quarks. Additionally, every generation has a charged lepton with electromagnetic charge  $-1e$  and an associated, much lighter, neutral neutrino.

For both quarks and leptons, the mass eigenstates are not equal to the weak eigenstates. They are transformed by the Cabibbo–Kobayashi–Maskawa (CKM) matrix [53, 54] for the quarks and the Pontecorvo–Maki–Nakagawa–Sakata (PMNS) matrix [55, 56] for the leptons. A free phase in both matrices is chosen such that the up-type quarks and the charged leptons have the same mass and weak eigenstates, and the down-type quarks and the neutrinos mix. The largest elements of the CKM matrix are found on the diagonal [57], which suppresses the interaction between the different generations of quarks. The CKM matrix has one complex phase allowing for CP-violation, which is the violation of the combined charge conjugation (interchange of particle and antiparticle) and parity (inversion of spatial coordinates) symmetries.

### 1.1.3 The Higgs mechanism

The Higgs mechanism of electroweak symmetry breaking (EWSB) generates the observed masses of the  $W$  and  $Z$  bosons, while preserving the  $SU(2)_L \otimes U(1)_Y$  symmetry at high energies [4, 5, 58–61]. It is introduced by adding a complex scalar isospin doublet  $\phi$  to the Lagrangian together with an accompanying symmetry breaking potential  $V(\phi)$ . The potential gives the neutral part a non-zero vacuum expectation value  $v$ , around which the scalar fields are expanded. After symmetry breaking, there are three massless Goldstone bosons [38]. These degrees of freedom are absorbed by a gauge transformation, and reappear as the longitudinal polarisation states of the  $W$  and  $Z$  bosons. In the end, the  $W$  and  $Z$  bosons have acquired mass terms, and the last remaining degree of freedom from the scalar isospin doublet becomes the Higgs boson  $H$ . The masses of the fermions are also generated in EWSB through the postulated Yukawa interaction [62] between the fermions and the Higgs field.

The mass of a particle is proportional to the Yukawa coupling between the particle and the Higgs boson. Therefore, the Higgs coupling to the gauge bosons  $g_{HVV}$  and

fermions  $g_{Hff}$  can be expressed as

$$g_{HVV} = g_V m_V \quad \text{and} \quad g_{Hff} = \sqrt{2} \frac{m_f}{v}, \quad (1.1)$$

where  $m_V$  is the gauge boson mass, and  $m_f$  is the fermion mass. Although the Higgs boson does not couple directly to the massless photon and gluon, there is a sizeable interaction through a loop of virtual top quarks or  $W$  bosons.

## 1.2 Beyond the Standard Model

The SM is not the ultimate theory, because it does not include the gravitational force as described by the theory of general relativity [6]. Predictions of the theory of general relativity and quantum field theory will break down near the Planck scale at an energy of  $10^{19}$  GeV, because quantum gravity effects become important [63, 64]. However, up to that energy the SM is potentially self-consistent [65]. A priori, there is no guarantee that new physics will be discovered at any future particle collider [66]. Nevertheless, the SM description is seen as unsatisfactory and searches for physics beyond the SM at energies below a few TeV are considered a high priority, e.g. by [10]. In addition to the text books [67] and other materials [68], a good review of these topics in the context of future facilities is given in [66].

### 1.2.1 Reasons for physics beyond the Standard Model

There are many reasons why the SM should be embedded in a more complete theory already at lower energy scales. These reasons range from concrete unexplained phenomena, to theoretical arguments containing more paradigmatic elements. Here the most important reasons, and arguments related to (Higgs) physics at future colliders will be given, omitting for example neutrino physics.

Besides the absence of the gravitational force, cosmology provides more indications that the SM is not complete. The evolution of the universe and many aspects of cosmology are well described by the  $\Lambda$  Cold Dark Matter ( $\Lambda$ CDM) model, which is also referred to as the standard cosmological model (see e.g. [69]). Evidence for the theory are measurements of the cosmological microwave background dating from the early universe, and the observed large-scale structure of the universe. In the  $\Lambda$ CDM model the energy content of the universe is 4.9% standard matter, 26.4% cold dark matter and about 68.5% is accounted for by the cosmological constant  $\Lambda$  [7].

The SM has issues with each of these three energy types. The SM covers the standard matter particles, but it cannot explain the abundance of matter over anti-matter, see e.g. [8]. The SM does not provide a suitable particle for the dark matter. A deeper problem is that the cosmological constant represents a contribution from

vacuum energy, but is many orders of magnitude smaller than the vacuum energy derived from QFT or the vacuum energy of the Higgs boson, see e.g. [70].

Despite these shortcomings, within particle physics almost all measurements agree with the SM to an extraordinary precision, e.g. [71]. However, there are deviations with, at present, a too low significance to claim new discoveries. Some of the most tantalising examples are the anomalous magnetic dipole moment of the muon  $g - 2$  [72], and a pattern of smaller deviations in the decays of  $B$  mesons [73, 74].

A well-known argument is that the large number of free parameters hints at an underlying organising principle to be discovered. The SM is the collection of theoretical ideas and has a total of 25 free parameters that have to be measured: 12 Yukawa couplings, 3 gauge coupling constants, 2 parameters of the Higgs potential, and 8 parameters of the PMNS and CKM matrices. Moreover, there are clear patterns in the parameters. The fermion masses have a clear hierarchy, the largest entries of the CKM matrix are found on the diagonal [57], the gauge interactions are of similar magnitude and their running hints at an approximate convergence at an energy scale of about  $10^{15}$  GeV [75–78]. Indeed, patterns in the parameters of a model have historically been an indication of an underlying theory (e.g. [36, 37, 79]).

### 1.2.2 Beyond the Standard Model and the Higgs boson

So the SM is not complete and new physics is required. Owing to its unique set of properties, the study of the Higgs boson represents a promising possibility to look for new physics. A simple reason is that out of the 25 parameters of the SM, 14 are directly related to the Higgs boson. A more involved argument is based on the so-called hierarchy problem, which is related to the fact that the Higgs boson is the only fundamental scalar in the SM.

The hierarchy problem arises when new physics is introduced at a higher energy scale [80–83]. Like the other particles, the Higgs boson propagator receives quantum corrections from higher order diagrams. The Higgs boson is a scalar, hence the corrections are proportional to the squared energy scale of new physics. If the energy scale of new physics is high, the smaller observed Higgs mass requires a high degree of fine tuning in the theory to cancel the corrections. In order to avoid excessive fine tuning, new physics theories should eliminate the large corrections and must be observable at an energy scale below a few TeV.

There are three main categories of new physics scenarios that alleviate the hierarchy problem and that can be probed at current and future colliders. First, the problem can be solved by introducing a new symmetry (super symmetry [84–87]) between fermions and bosons to cancel the divergences [88, 89]. Alternatively, the Higgs boson is not a fundamental scalar but a composite particle held together by a new force [90]. Thirdly, extra dimensions can be involved to explain the discrepancy

in energy scales [91, 92]. In all of these scenarios, the Higgs boson couplings are modified.

The magnitude and character of possible modifications to the Higgs couplings will provide information about the new physics scenarios. A method to parametrise the effect of a higher energy new physics contribution on the SM interactions is an effective field theory, which extends the SM Lagrangian with a set of higher dimension operators, see e.g. [93, 94]. The magnitude of the modification can be linked to an energy scale of new physics. The modifications are roughly proportional to  $m_H^2/M^2$ , where  $M$  is the energy scale of new physics, e.g. the mass of a new particle. Hence, deviations of the order of percents will hint to new physics at the TeV scale.

Another reason to investigate the Higgs boson, is the unknown origin of EWSB. The SM Higgs potential is arbitrarily chosen. Measurements of the Higgs boson self-interactions can probe the Higgs potential. Specifically, the Higgs boson trilinear gauge coupling can be measured.

Additionally, a modified Higgs potential would help accommodate Baryogenesis. Baryogenesis is the hypothetical process that introduced the asymmetry between the amount of matter and anti-matter in the universe and relies on the three Sacharov conditions to be full filled [95]. Two of these conditions can be satisfied if the electroweak phase transition in the early universe was first-order. The dynamics of the phase transition is determined by the Higgs potential. A Higgs potential with a modified trilinear gauge coupling could have led to a first-order phase transition [96], instead of the continuous phase transition predicted by the SM [97].

## 1.3 Higgs production at an electron positron collider

The study of the Higgs boson in great detail is a major objective of all recently proposed high energy electron positron colliders [12, 98–100]. A high energy electron positron collider will be a highly important instrument for the progression of the study of particle physics. An overview of physics at future (linear) collider is for example given in reference [101]. The physics programme of these colliders also includes among others the measurements of electroweak precision observables, top studies, and (indirect) new physics searches, but the discussion here will be restricted to Higgs physics.

### 1.3.1 Higgs boson production

The cross section of the most important SM Higgs processes at an electron positron collider as a function of centre-of-mass energy  $\sqrt{s}$  are given in Figure 1.2.

Higgs strahlung  $HZ$  production, is the production of a Higgs boson in association with a  $Z$  boson. The tree level diagram is shown in Figure 1.4a. The cross section

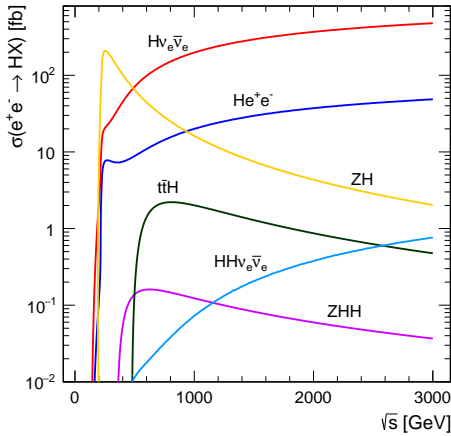


Figure 1.2: Cross section for the main Higgs production modes at an electron positron collider with unpolarised beams as a function of centre-of-mass energy  $\sqrt{s}$ . Figure taken from [102].

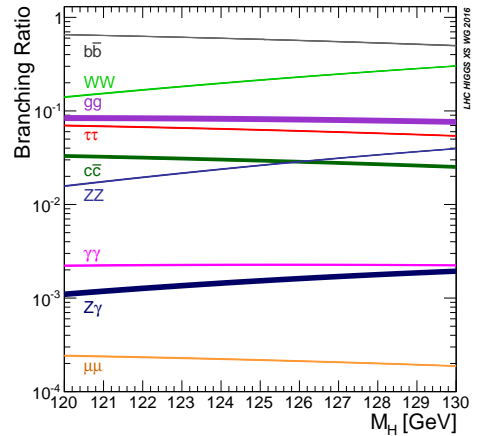
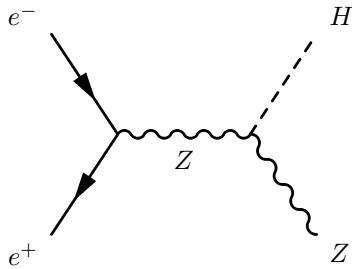
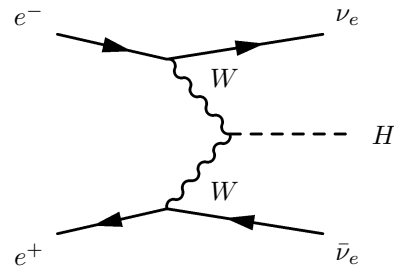


Figure 1.3: The branching ratios for the main decay modes of the Higgs boson as a function of the assumed Higgs boson mass  $M_H$ . Figure taken from [103].



(a)  $ZH$  production (Higgstrahlung)



(b)  $W$  boson fusion

Figure 1.4: Leading order Feynman diagrams of the dominant Higgs boson production modes at an electron positron collider. Note that the anti-particles are redundantly annotated by both labels and reversed arrows.

peaks at an energy of 250 GeV and decreases proportionally to  $1/s$  towards higher energies. The Higgs production through this channel can independently be identified through the decay products of the recoiling  $Z$  boson, allowing the determination of the total Higgs width.

At higher energies the dominant Higgs production modes are the vector boson fusion processes, proportional to  $\ln(s/m_H^2)$ . Herein, a Higgs is produced in the interaction of two  $W$  bosons ( $H\nu_e\bar{\nu}_e$ ) or the rarer interaction of two  $Z$  bosons ( $He^+e^-$ ). The former is shown as a Feynman diagram in Figure 1.4b. At an energy of about 800 GeV the production of a Higgs boson in association with two top quarks  $t\bar{t}H$  is maximal. The cross section is relatively small, but the production process is important for the measurement of the top quark Yukawa coupling.

The simultaneous production of two Higgs bosons is important because it contains the Higgs three point vertex. Analogous to the  $HZ$  production and vector boson fusion, two Higgs bosons are produced in the  $HHZ$  and  $HH\nu_e\bar{\nu}_e$  production process.

### 1.3.2 Higgs boson decay

The Higgs boson branching ratios as a function of the Higgs boson mass are shown in Figure 1.3. The relative branching ratios to fermions can be explained by the Higgs boson coupling to fermions being proportional to fermion mass, see Equation (1.1). Although the largest coupling is actually to top quarks, the decay is forbidden, because the top quark mass is larger than the Higgs boson mass. The Higgs boson primarily decays to bottom quarks. The second largest decay mode is into two  $W$  bosons, where at least one of them is virtual. The Higgs boson decay to gluons  $gg$ , photons  $\gamma\gamma$ , and  $Z\gamma$  is mediated by virtual particle loops of primarily top quarks, bottom quarks and if possible  $W$  bosons.

### 1.3.3 Higgs boson physics goals

There are a number of important measurements of the Higgs boson that will be made at future electron positron colliders starting at a centre-of-mass energy around 250 GeV. The physics reach can be extended with higher centre-of-mass energy stages of 500 GeV and beyond.

At a collision energy of 250 GeV, the Higgs mass will be measured. A precisely known Higgs mass is important to determine the branching ratio of Higgs to two  $W$  bosons or two  $Z$  bosons, because these depend on the Higgs mass, see Figure 1.3. The Higgs boson mass is equal to the recoil mass of the  $Z$  boson in the  $HZ$  production channel, which allows for a precise measurement when the  $Z$  boson decays to muons or electrons.

None of the detectors at the proposed colliders will be sufficiently sensitive to determine the expected Higgs width of  $(4.07 \pm 0.02)$  MeV [104] directly. The total

Higgs width will primarily be inferred from the Higgs branching ratio to  $Z$  bosons, and the Higgs production cross section  $\sigma(HZ)$ , which can accurately be detected even in the case of invisible Higgs decays through reconstruction of the recoil mass. The total Higgs width  $\Gamma_h$  is given by

$$\Gamma_h = \frac{\Gamma_{ZZ}}{BR_{ZZ}} = \frac{\Gamma_{WW}}{BR_{WW}}, \quad (1.2)$$

where  $\Gamma_{ZZ}$  ( $\Gamma_{WW}$ ) is the partial decay width to  $Z$  bosons ( $W$  bosons), and  $BR_{ZZ}$  ( $BR_{WW}$ ) is the branching ratio to  $Z$  bosons ( $W$  bosons). The partial decay width is proportional to the cross section, i.e.  $\Gamma_{ZZ} \propto \sigma(HZ)$  and  $\Gamma_{WW} \propto \sigma(H\nu_e\bar{\nu}_e)$ .

The quantum numbers of the Higgs boson can be determined. If the Higgs boson is a CP-eigenstate, it has been measured to have spin 0 and even parity +1 with high probability. However, it is possible that there is CP-violation associated to the Higgs boson and it is a mixture of CP-even and CP-odd components. With a future electron positron collider, Higgs bosons decaying to pairs of tau's can be used to measure a possible CP-odd component. The decay to pairs of tau leptons is specifically suited, because the tau leptons couple directly to both components, and some of the tau decays give access to the spin properties through angular distributions of the decay products. The measurement of the Higgs boson decaying to tau leptons will be discussed in Section 8.4.

An important measurement at a higher energy is the measurement of the top Yukawa coupling. Despite being near the threshold of the process, the measurement can be accurately performed at 500 GeV. At 500 GeV also di-Higgs boson production becomes available, and the Higgs potential can be probed [105]. At higher energies the precision for this measurement will be even better.

### 1.3.4 Higgs physics at the ILC

The prospects for Higgs physics at an electron positron collider will be illustrated using the International Linear Collider (ILC), which is the proposed collider described in the next chapter. The physics case for the ILC is made in references [106, 107]. Important in this assessment is the additional experimental value a collider can offer in addition to the constructed and operational Large Hadron Collider (LHC), and its approved High Luminosity Upgrade (HL-LHC).

At the ILC at a centre-of-mass energy of 250 GeV, the absolute cross section of  $ZH$  production can be measured to 1.0% precision. The total Higgs width will have a precision of 2.5%, and the branching ratio of the Higgs boson to invisible particles can be constrained to below 0.3%. The Higgs boson mass will be known with a precision of 13 MeV.

In Figure 1.5 the expected precision of the Higgs couplings is shown for the HL-

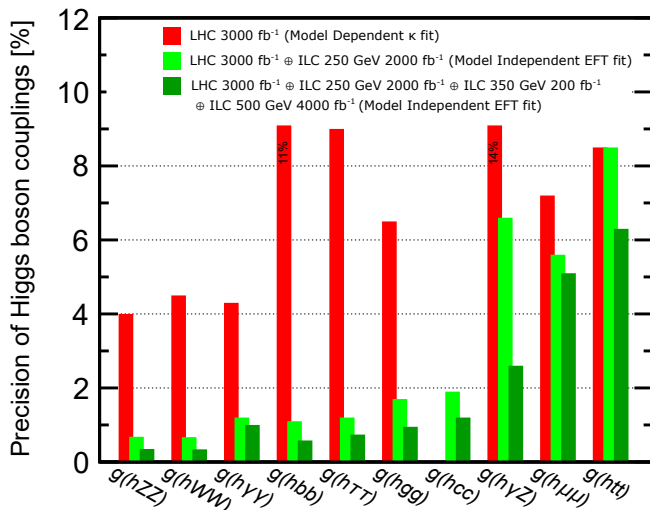


Figure 1.5: Expected uncertainties for the ILC from model independent effective field theory fits (EFT) [107], compared to the projection of model dependent uncertainties for the ATLAS experiment at the LHC [108]. Figure adapted from [107].

LHC (ATLAS experiment), and the ILC at a centre-of-mass energy of 250 GeV and 500 GeV. The ILC expectations are given within the effective field theory framework, while the quoted HL-LHC predictions are in the  $\kappa$  framework [109], which is a more model dependent parametrisation in which the Higgs couplings are scaled. Already at an energy of 250 GeV the ILC offers an improvement in all channels, except the coupling to top quarks which only becomes available in the 500 GeV energy stage. The largest improvements are made in the channels limited by the backgrounds at the HL-LHC, exemplified by the measurement of the Higgs boson coupling to charm quarks. The least improvement is seen in statistically limited measurements, such as the coupling of Higgs to muons. The Higgs decay to two photons is also statistically limited, but a combination of ILC and HL-LHC data allows for a much more precise determination of this coupling than the HL-LHC alone. The coupling to the  $W$  and  $Z$  bosons can be improved over the expected HL-LHC results using input from the cross section measurement.

The Higgs boson self coupling can only be measured at a centre-of-mass energy of 500 GeV and above. With the full ILC data set up to an energy of 500 GeV, the expected precision on the Higgs self coupling is expected to be 27 %.





# The international linear collider and the international large detector

---

High energy particle collisions are important to investigate the outstanding problems introduced in the previous chapter and advance the field of particle physics.

Currently the LHC is operational at CERN and collides high energy protons at a centre-of-mass energy of 13 TeV [110, 111]. Because a proton is a stable particle and has a large mass-to-charge ratio, it is possible to achieve such energies. However, protons are composite objects and the initial state is thus not known exactly, which can be an obstacle in interpreting the results. In addition, the quarks and gluons in the proton interact strongly, and as a result QCD processes result in major sources of background.

In contrast, an accelerator colliding electrons and positrons has complementary properties. Because of the small mass-to-charge ratio of the electrons it is more difficult to reach high energies. However electrons are fundamental particles with a well-defined initial state that do not interact strongly. Backgrounds are much lower at an electron positron collider. Hence, an electron positron collider is eminently suitable for precision measurements of the properties of the Higgs boson.

The ILC is a linear electron positron collider operating at the energy frontier. At the ILC two detectors are foreseen in a push-pull configuration, one of which is the International Large Detector (ILD).

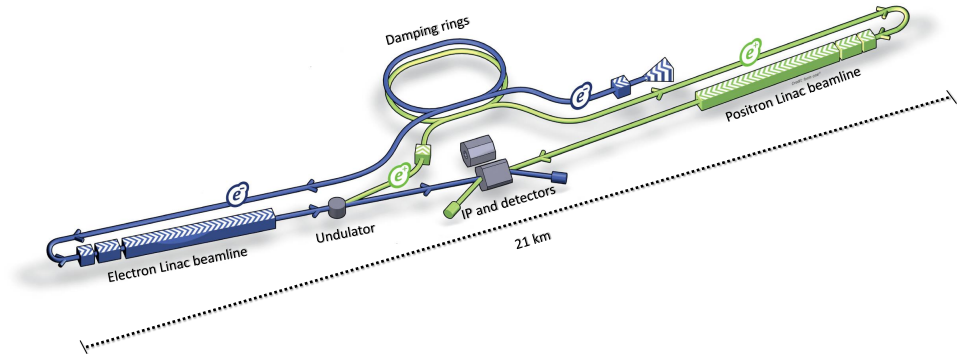


Figure 2.1: Layout of the ILC in the 250 GeV configuration, adapted from [12].

## 2.1 The international linear collider

The ILC is a proposed linear electron positron collider using 1.3 GHz Superconducting Radio-Frequency (SCRF) accelerating technology [12, 112, 113]. As a linear collider, the accelerator is upgradable to higher energies by extending the length of the two main linacs. The mature ILC project was recently updated with a more phased approach, featuring a cost-optimised first 250 GeV stage [114]. In subsequent stages, the centre-of-mass energy can be upgraded from 250 GeV to maximally 1 TeV. A candidate site for the construction is located in the Kitakami mountains in the Tohoku area, about 400 km north of Tokyo, Japan.

The electrons and positrons in the beams are organised in bunches to facilitate acceleration using SCRF technology. The ILC will feature polarised beams. At a centre-of-mass energy of 250 GeV the polarisation can be used to boost the Higgs production. At higher energies it is beneficial for signal separation in e.g. the  $W$  fusion Higgs production ( $H\nu_e\bar{\nu}_e$ ), and can be used in the search for new physics.

### 2.1.1 Layout of the ILC accelerator

The layout of the main ILC accelerator is shown in Figure 2.1. The electrons and positrons are accelerated and brought into collision by a chain of accelerator structures. The ILC will have beam Interaction Point (IP) shared between two detectors in a push-pull configuration.

The electron source provides polarised electrons liberated from a strain gallium arsenide photo-cathode by illumination with a titanium-sapphire laser. The electrons are expected to have at least 85% polarisation after production, and have no less than 80% polarisation at the IP. The polarisation is defined as the asymmetry ( $n_+ -$

$n_-)/(n_+ + n_-)$  in the number of electrons with positive spin  $n_+$  (right chirality) and negative spin  $n_-$  (left chirality). A subsequent linear accelerator gives the polarised electrons an energy of 5 GeV before injection into the damping ring.

Polarised positrons are produced using high energy photons from an undulator. The undulator consists of a periodic alternating series of dipole magnets such that the electrons traverse a magnetic field and radiate an intense beam of photons. The electron beam from the main linac is directed to a 147 m long superconducting undulator. In the helical undulator a beam of circularly polarised photons is produced with a maximum energy of 30 MeV, depending on the electron beam energy. The photons hit a rotating titanium alloy target producing a beam of electron-positron pairs. The positrons are separated and accelerated in a linac to an energy of 5 GeV, and injected in the damping ring. At the IP the positrons will have a polarisation of at least 30%.

The electron and positron damping rings have a circumference of 3.2 km and share a common tunnel. In the damping rings the injected beams with large emittance are damped to beams with low emittance. Emittance measures the spread in the position-momentum phase space of a beam. A highly focused, monochromatic beam has lower emittance and produces a higher luminosity. The beams are damped by 113 m of superferric wigglers in each ring, causing the electrons and positrons to emit radiation in a way that reduces their emittance. The two Rings To Main Linac (RTMLs) provide beam transport from the two damping rings to the main linac beamlines while preserving the polarisation and low emittance of the beam as much as possible. The electron and the positron main beamlines both consist of a two-stage bunch compressor system and a main linac. The bunch compressor system compresses the bunches from a few millimeters to a few hundreds of micrometers in length and accelerates the beam from 5 GeV to 15 GeV.

The main linac then accelerates the beam to the required energy at the IP. The main linac uses nine-cell niobium SCRF cavities operated at a temperature of 2 K. Cavities with specifications close to the ILC requirements were mass produced and are successfully used at the European X-ray Free Electron Laser [115]. Considering the performance of those cavities, an average accelerating gradient of 35 MV/m seems feasible. The 12.65 m long cryomodules contain either nine cavities or eight cavities and a quadrupole as part of the necessary beam optics. The main linac tunnels are designed to follow the curvature of the earth to facilitate helium transport for cooling.

The final part in the beamlines is the 2.25 km long beam delivery system, which focuses the beams to the required sizes and brings them into collision. A beam crossing angle of 14 mrad allows both beams to be extracted to the high pressure water beam dumps after passing through the interaction region.

## 2.1.2 Beam conditions

The ILC will deliver  $\sim 1$  ms bunch trains, containing 1312 bunches each, at a repetition rate of 5 Hz. The detailed design parameters of the initial stage and possible upgrades are shown in Table 2.1. To maximise the luminosity, the beams are focused to nanometer size at the IP. The beam particles have a spread in energy, causing a variation in the centre-of-mass energy of collision. Despite this spread, 73% of the collisions are expected in the top 1% of the energy.

The main source of background consists of beamstrahlung photons in the forward regions. These photons can convert either to electron positron pairs or to hadrons, which can enter the detector as background. Other sources of background are muons produced upstream from the detector and neutrons produced in the beam dumps.

Table 2.1: Table with ILC run parameters, adapted from [114, 116].

Quantity	Initial	$\mathcal{L}$ Upgrade	Energy upgrades	
Centre-of-mass energy	250 GeV	250 GeV	500 GeV	1000 GeV
Luminosity ( $\times 10^{34} \text{cm}^{-2} \text{s}^{-1}$ )	1.35	2.7	1.8/3.6	4.9
Polarisation for $e^- (e^+)$	80 % (30 %)	80 % (30 %)	80 % (30 %)	80 % (20 %)
Repetition frequency	5 Hz	5 Hz	5 Hz	4 Hz
Bunches per pulse	1312	2625	1312/2625	2450
Bunch population	$2 \times 10^{10}$	$2 \times 10^{10}$	$2 \times 10^{10}$	$1.74 \times 10^{10}$
Linac bunch interval	554 ns	366 ns	554/366 ns	366 ns
Beam current in pulse	5.8 mA	5.8 mA	5.8 mA	7.6 mA
Beam pulse duration	727 $\mu\text{s}$	961 $\mu\text{s}$	727/961 $\mu\text{s}$	897 $\mu\text{s}$
Average beam power	5.3 MW	10.5 MW	10.5/21 MW	27.2 MW
Norm. hor. emitt. at IP	5 $\mu\text{m}$	5 $\mu\text{m}$	10 $\mu\text{m}$	10 $\mu\text{m}$
Norm. vert. emitt. at IP	35 nm	35 nm	35 nm	30 nm
RMS hor. beam size at IP	516 nm	516 nm	474 nm	335 nm
RMS vert. beam size at IP	7.7 nm	7.7 nm	5.9 nm	2.7 nm
Luminosity in top 1%	73 %	73 %	58.3 %	44.5 %
Energy loss from beamstrahlung	2.6 %	2.6 %	4.5 %	10.5 %
Site AC power	129 MW	$\sim 161$ MW	163/204 MW	300 MW
Site length	20.5 km	20.5 km	31 km	40 km

## 2.1.3 Luminosity and event rate

The number of events  $N$  expected for a given final state at the ILC is given by

$$N = \mathcal{L}\sigma, \quad (2.1)$$

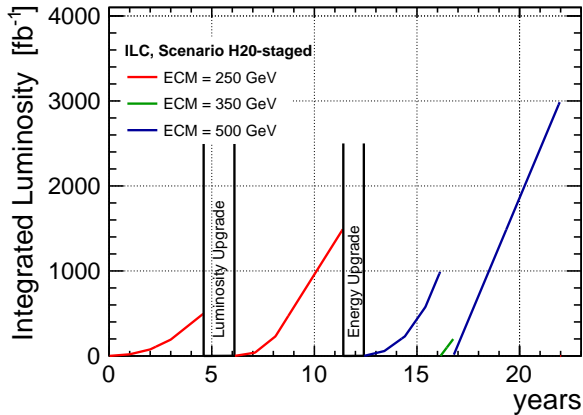


Figure 2.2: The nominal, 22 year long, planned running scenario for the ILC, taken from [114].

where  $\sigma$  the interaction cross section for this final state,  $\mathcal{L}$  is the integrated luminosity given by  $\mathcal{L} = \int L dt$ , and  $L$  is the instantaneous luminosity. In an analysis, often a set of final states is selected that can be attributed to a specific process under study with high probability.

Initially the ILC has a design instantaneous luminosity of  $1.35 \times 10^{34} \text{ cm}^{-2}\text{s}^{-1}$ . The nominal run scenario with integrated luminosities at the different energy stages is shown in Figure 2.2. After an initial running period of about 5 years, the current scenario calls for a luminosity upgrade, followed by an upgrade to a centre-of-mass energy of 500 GeV. The ILC run plan remains flexible and has the capability to operate at energies down to 90 GeV, depending on future physics results. This lower energy operation allows for both  $Z$  pole running and a threshold scan of the  $W$  boson pair production around 160 GeV.

The beam polarisation is set to acquire four independent data sets with different mixtures of physics processes. The most important Higgs production process, Higgs strahlung, has the largest cross section for an asymmetrically configured polarisation. Hence the polarisation will be set to  $(P(e^+), P(e^-)) = (+, -)$  and  $(-, +)$  each for 45% of the time, and to the same sign configurations  $(+, +)$  and  $(-, -)$  both for 5% of the time.

## 2.2 The international large detector

The ILD is a multi-purpose detector proposed as one of the two experiments at the ILC [13, 117, 118]. A rendered view is shown in Figure 2.3. Although it should

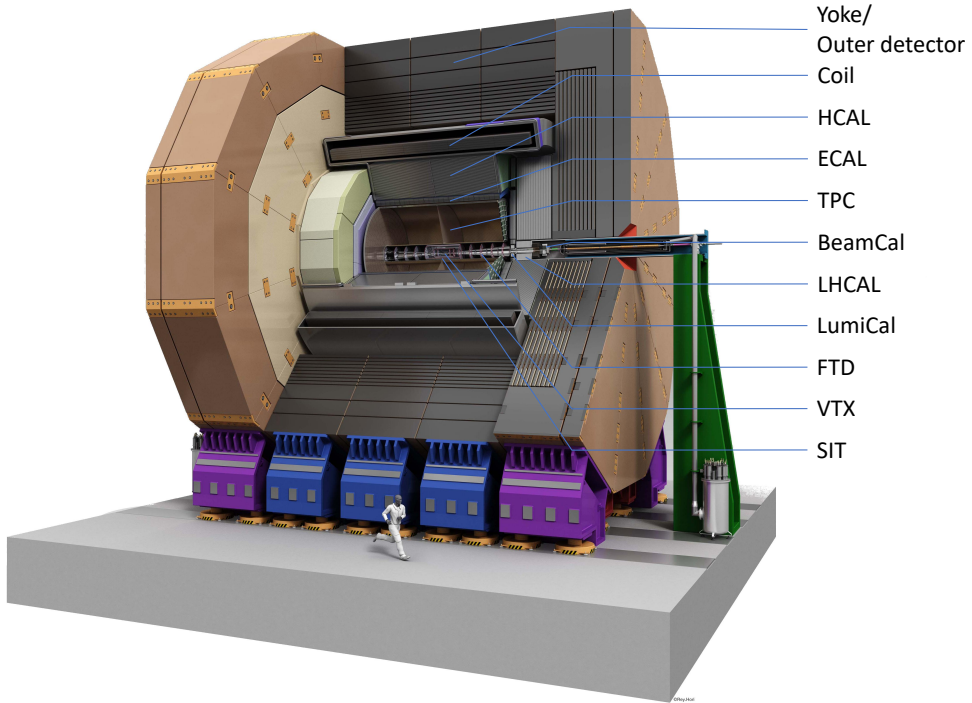


Figure 2.3: Rendered cut open view of the ILD, adapted from [13].

provide excellent performance for the full ILC physics program between 90 GeV and 1 TeV, most of the recent optimisation work has focused on the performance at the initial 250 GeV stage. The ILC physics programme is driven by the need to obtain the best possible precision and as a result it places stringent requirements on the ILD.

### 2.2.1 Detector requirements

The ILD has been designed to optimise physics performance while respecting operational constraints. The operational environment is relatively benign compared to that at a hadron collider. The magnetic field needs to be at least 3 T to confine electron pairs from beamstrahlung to within the beam pipe. Even so, the first vertex layer cannot be closer than 15 mm to the beamline. Secondly, the push-pull scheme must be taken into account in the integration and the machine-detector interface. Fortunately, the bunch structure does not give strong constraints: the long idle period between bunches facilitates the use of triggerless readout schemes and allows for power pulsing in the front end electronics to save power, which limits the necessary cooling power

and thus minimises the amount of associated material.

There are also important physics performance considerations. At 250 GeV, Higgs strahlung is the dominant Higgs production mode. Independent from its decay mode, the production of a Higgs boson can be inferred through the detection of the associated  $Z$  boson, allowing unambiguous cross section measurements. The  $Z$  boson is selected by its momentum, which puts stringent requirements on the tracker. The tracker has to be highly efficient and have excellent resolution. In order to make sure that the Higgs recoil mass measurement in the channel  $e^+e^- \rightarrow H, Z \rightarrow \mu^+\mu^-$  is dominated by the beam energy spread, the asymptotic momentum resolution goal is set to  $\sigma_{1/P_T} = 2 \times 10^{-5} \text{ GeV}^{-1}$ .

The Higgs boson decays need to be differentiated by quark and lepton flavour, requiring great flavour tagging. This requires a high precision and low material vertex detector, as well as a calorimeter with sufficient granularity to identify leptons in jets.

The calorimeter performance requirements are predominantly set by the need to identify top quarks,  $W$  bosons and  $Z$  bosons. This requires good spatial separation and a jet energy resolution  $\sigma_E/E$  of better than 4%, which can be achieved by particle flow calorimetry. In particle flow, information from the trackers and the calorimeters is combined to acquire the best possible jet energy resolution. The performance is optimal when the calorimeter clusters are well separated and can efficiently be matched to tracks. Therefore the calorimeters are highly granular and placed inside the coil, close to the tracker.

Furthermore, hermeticity is required to effectively deduce the presence of particles invisible to the detector such as neutrinos. Thus the tracker needs to be able to reconstruct particles even at small angles with respect to the beam pipe.

### 2.2.2 Overview of the detector

The ILD detector follows a conventional particle detector design with subdetectors organised as a series of shells around the IP. Particles are detected through their interactions with the sensitive material of the subdetectors. A large solenoid creates an axial magnetic field parallel to the beam, which enables momentum measurements of charged particles in the inner tracking detector shells. The shells on the outside of the trackers are the calorimeters that measure the energy of particles by absorbing their energy. In the barrel part, there are two calorimeters: the Electromagnetic Calorimeter (ECAL) and Hadronic Calorimeter (HCAL). The outermost shell is the return yoke of the magnet, which also serves as the outer detector. A quadrant view of the ILD detector is shown in Figure 2.4.

Two versions of the detector are described: a large version, prioritising performance, and a newer, smaller version focusing more on cost-effectiveness<sup>1</sup>. The small

---

<sup>1</sup>This results in the remarkable name "The Small International Large Detector"



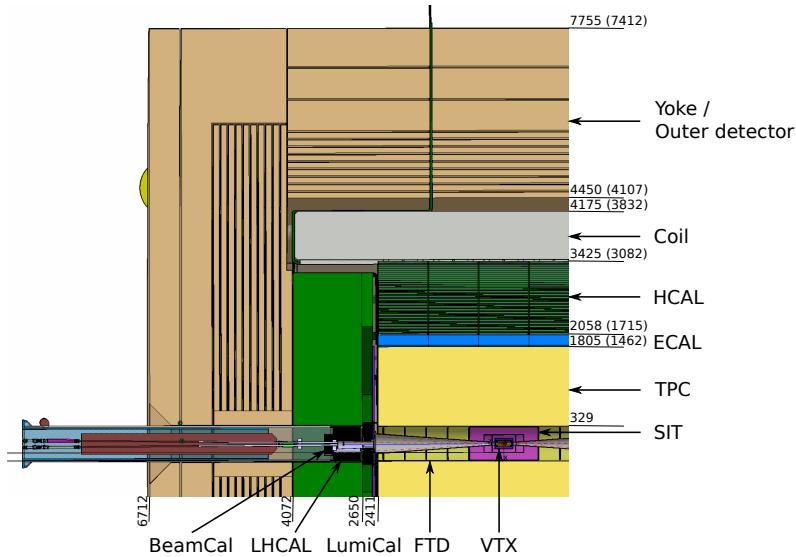


Figure 2.4: Quadrant view of the ILD with some of the inner radii of sub-detectors indicated in mm for the large version (small version). Adapted from [118].

version has an ECAL inner radius of 146 cm, compared to a ECAL inner radius of 181 cm for the large version. The surrounding detectors are adjusted accordingly. The main cost-savers are the smaller calorimeters. For the momentum resolution of high momentum tracks  $(\delta p_T/p_T)_{\text{res.}} \propto 1/(BL^2)$  holds, see Equation (8.1). So in order to acquire a comparable momentum resolution for high momentum tracks, the reduced lever arm is compensated by increasing the magnetic field from 3.5 T to 4 T.

For some technologies multiple mature options and developing alternatives are given. A choice is to be taken when the ILD develops into a detector proposal.

### Particle flow

The ILD design is optimised for particle flow. Particle flow is a method to determine the energy of particles produced in collisions [119, 120]. In traditional calorimetry the energy of a jet is determined by a measurement in the calorimeter alone. However, the energy resolution of the calorimeter can be improved by using momentum information from the more precise tracker. The jet energy is the sum of the particles in the jet, which requires the four vectors of all visible particles in the event to be individually reconstructed. The charged particles are primarily reconstructed in the tracker, while neutral hadrons and photons are reconstructed in the calorimeters. Frequently, the calorimeter clusters of charged and neutral particles overlap, which can make it more difficult to find the neutral particle and precisely measure its energy. This confusion

in the association of clusters is what limits the calorimeter resolution at large jet energies.

The particle flow approach to calorimetry has consequences for the detector design. The standalone calorimeter performance is no longer the guiding principle, but the joint performance of all subdetectors has to be optimised. To limit confusion, calorimeter clusters have to be separable, so the calorimeter should be highly granular. Good particle identification is required to identify the particle type. All particles have to be detected, therefore the detectors need to be highly efficient and tracking fake rates have to be low, as this might wrongfully subtract energy from clusters. Furthermore, to improve the matching of calorimeter clusters and tracker information the amount of material between those detectors has to be minimised.

ILD applies the Pandora particle flow algorithm [121]. This C++ algorithm is optimised using simulated events, and is flexible enough to be applied to different detector designs.

### 2.2.3 Tracking detectors

The main goal of the tracking detectors is to measure the trajectory and momentum of charged particles. A charged particle leaves a trail of detectable interactions called hits in the tracker that can be reconstructed as a track. From the curvature of the track in the magnetic field, the momentum is determined. If an interaction produces multiple tracks, the point of interaction, called the vertex, can be reconstructed. In order not to disturb measurements in the tracker and in the more outward detectors, the amount of material has to be minimised.

The ILD tracker consists of a number of silicon trackers and a Time Projection Chamber (TPC). The most central detectors are silicon trackers, which have an excellent position resolution important for the reconstruction of the vertex and to determine the direction of the particles. Silicon trackers require a relatively large amount of material per measurement point, so only a few measurement points are taken. Around the central silicon trackers a large TPC is foreseen. As a gaseous detector, the amount of material per measurement point is relatively small. Therefore the TPC takes a large number of measurement points to aid pattern recognition, over a large radial distance for a precise determination of the momentum. In addition, the gaseous TPC can identify particles by the characteristic energy loss  $dE/dx$ .

The tracker requirements are mainly set by lepton momentum measurements from  $Z$  boson decays in the Higgs recoil measurements. For a centre-of-mass energy of 500 GeV, the Higgs decay to two muons is seen as a benchmark for high momentum tracks. The flavour tagging requirements of jets with  $c$  and  $b$  quarks drives the vertex detection requirements. The primary benchmark process is the Higgs branching ratio measurements to these types of jets. The minimal required resolution is 3  $\mu\text{m}$  in both

$r$  and  $\phi$  directions.

### Technology options for the silicon tracking detectors

The silicon detectors use a semiconductor as the sensitive material. In the semi-conducting silicon a high energy charged particle produces electron-hole pairs, which are separated and collected using an electric field. The semiconductor properties are tuned through doping the material with impurities.

For a silicon detector, the position of a hit is determined from the known position of the sensitive material. In order to improve the spatial precision of a measurement point, the devices are compartmentalised in strips or pixels each acting as separate sensitive volume. The silicon trackers are organised in layers to acquire multiple hits per track. In some cases the sensitivity of the volumes can be tuned to detect multiple hits per layer, which is used to improve the position measurement.

The silicon detector has four subsystems; the vertex detector (VTX) located in the centre of the detector, the Silicon Inner Tracker (SIT) located between the vertex detector and the TPC, the Forward Tracking Disks (FTD) located in the forward direction around the beam pipe, and the Silicon outer layers (SET) on the outside of the barrel part of the TPC. There are three technology options under consideration for the VTX, as well as for the other silicon detectors.

- Complementary Metal Oxide Semiconductor (CMOS) pixels are a well established technology which can be produced industrially. In CMOS sensors the analog signal are digitised per pixel. One advantage of the CMOS type sensors is the low material budget. Current developments focus on keeping the power consumption low while maintaining readout speed, and on reducing the material budget of the layers even further.
- A fine pixel Charge-Coupled Device (CCD) is another option under investigation. The main difference compared to CMOS technology is that the signal charge is transferred between pixels before being digitised usually per column. Fine pixel CCDs can be built with small pixel sizes ( $\sim 5 \mu\text{m}$  pitch), offering high precision and low occupancy. CCDs with fine pixels have not yet found full size applications in major particle physics experiments and radiation hardness currently is a point of attention.
- Another option are Depleted Field Effect Transistor (DEPFET) sensors, which work with a field effect transistor per pixel which controls the flow of current by an electric field. The advantages are low noise, low power operation with fast readout speeds.

**Vertex detector**

The VTX is the detector closest to the IP and is optimised for vertex detection. It consists of 3 double layers located between 16 mm and 58 mm. Based on the power consumption of the CMOS pixels option, the vertex detector can be cooled by an air or nitrogen gas flow. To reach the vertex detection requirements the amount of material per layer cannot exceed 0.15%  $X_0$ , where  $X_0$  is the radiation length of the material used.

**Silicon inner tracker**

The SIT provides a measurement point to aid the reconstruction of charged particles and to improve the momentum resolution for low transverse momentum charged particles. The SIT consist of two layers. In a previous baseline design both layers were made of two single-sided strip layers, but thanks to recent progress in CMOS sensors, it is now also possible to instrument the SIT with pixels instead.

**Silicon outer tracker**

The SET provides a precise space point near the outer edge of the TPC to improve the momentum resolution. By calculating the offset between the SIT and SET tracks and the TPC tracks in the drift direction, timing information is obtained. The same strip sensor as for the SIT can also be used for the SET, but implementing the SET as a first layer of the calorimeter is also under investigation. Sensors with precise timing of  $\mathcal{O}(10\text{ ps})$  would allow Time of Flight (ToF) measurements, which can be utilised for particle identification. The particle type can be identified by comparing the momentum and speed measurements.

**Forward tracker**

The FTD consist of seven disks between the beam pipe and the inner field cage of the TPC. They provide tracking in the forward direction for tracks at an angle with respect to the beamline between  $4.8^\circ$  and  $35^\circ$ . The first two disks are highly granular pixel detectors, for which the same technology considerations as for the VTX apply. The other five disks might be implemented using strips or, given the recent progress in this area, (elongated) CMOS pixels. Possibly the FTD sensors will be able to also provide precise timing information for ToF measurements.

**Time projection chamber**

The design foresees a gaseous TPC as the main tracking detector. The TPC allows continuous, three-dimensional tracking with a minimal material budget at relatively

low cost. The TPC provides a stand alone momentum resolution  $\sigma_{1/P_T}$  of at least  $10^{-4} \text{ GeV}^{-1}$ . Electron identification and other particle identification applications require the TPC to be able to measure the energy loss  $dE/dx$  to better than 5%.

The TPC consists of a cylindrical field cage, capped on both sides by readout end plates. Some of the geometrical parameters of the large version are summarised in Table 2.2. The electric field runs from the anode readout end plates to a thin-membrane cathode spanned between two rings in the centre of the TPC. Field shaping on the inner and outer cylinder is provided by field shaping metal strips. The TPC end plates are cooled by two-phase  $\text{CO}_2$  cooling. The inner and outer cylinders have a material budget of 1% and 3% of a radiation length  $X_0$  respectively and will consist of composite materials. The end caps, including the readout electronics, have a maximal material budget of 25%  $X_0$  and can be realised as an aluminium structure in which the 240 readout modules can be placed. The small version of the ILD detector has a reduced TPC outer radius of 1427 mm and 152 modules, but has otherwise largely the same geometry.

The workings and the readout of the TPC will be described in the next chapter.

Table 2.2: Geometric parameters of the ILD TPC with a possible pad based readout implementation.

TPC parameter	Version:	large	small
Half length		2350 mm	
Inner radius		329 mm	
Outer radius		1770 mm	1427 mm
Maximum drift length		2225 mm	
Inner service area and wall		43.1 mm	
Outer service area and wall		73.1 mm	
Number of modules		240	152

### 2.2.4 Calorimeter system

The primary purpose of the calorimeter system is to determine the energy and direction of neutral particles. The calorimeter measures the energy of all strongly and electromagnetically interacting particles by absorbing their energy. High energy particles create a cascade of particles in the calorimeters, referred to as showers.

The ECAL is designed for photons and electrons, which lose their energy through electromagnetic interactions. The longitudinal spread of the shower can be modelled using the radiation length of the material  $X_0$ . The HCAL is designed for particles that, in addition to the electromagnetic interaction, also lose energy through the strong interaction. No analytical description exist, but the size in the direction of the

shower is characterised by the strong interaction length  $\lambda_I$ . In order to separate the particles interacting only electromagnetically from strongly interacting particles, the ECAL is situated in front of the HCAL, and should have a large  $\lambda_I/X_0$  ratio.

The calorimeters are optimised for particle flow, which sets requirements on the granularity. To achieve the necessary granularity, a sampling calorimeter is foreseen for both systems with alternating layers of absorber and sensitive material. To minimise material between the calorimeters and trackers, both are placed inside the coil. The readout of the calorimeters is the most critical part to cool and for this water cooling lines are foreseen.

### Electromagnetic calorimeter

The main goal of ECAL is to precisely measure the energy of photons, even in the presence of nearby particles. The ECAL requirements are set by the benchmark processes  $e^+e^- \rightarrow Z\gamma$ , and the Higgs branching ratio measurement to high energy photons.

The ECAL has to be made compact, because it is positioned inside the coil. Tungsten (W) is a good option as absorber material for the ECAL, because of its density and its large interaction length to radiation length ratio  $\lambda_I/X_0$ . The ILD design has 30 layers of tungsten, interleaved with sensitive layers read out by silicon pin diodes with a  $5\text{ mm} \times 5\text{ mm}$  size. The construction has an octagonal shape, in which the layers are arranged in a way that avoids uninstrumented regions in the radial direction. The baseline design has a total radiation length of  $24X_0$ .

### Hadronic calorimeter

The HCAL will measure the energy of the neutral hadrons and must be able to separate them from other clusters. Jets consist for only about 10% of neutral hadronic particles, but their contribution to the energy resolution as measured by the HCAL is dominant for jet energies up to 100 GeV. For higher energy jets, the resolution is limited by confusion in the association of energy deposits to different clusters by the particle flow algorithm.

The HCAL is a sampling calorimeter with steel absorber plates, and scintillator tiles or gaseous devices as detection layers. The scintillator tiles with a suggested size of  $30\text{ mm} \times 30\text{ mm} \times 3\text{ mm}$  are read out by Silicon Photo Multipliers (SiPMs). Alternatively, gaseous detectors would allow even thinner sensors with a very fine segmentation.

HCAL energy resolution requirements are set by the identification of  $W$ ,  $Z$ , and  $H$  boson jets. The resolution has to be sufficient to separate  $W$  and  $Z$  boson jets. For Higgs bosons it is important to accurately measure and reconstruct jets of all quark flavours.

### 2.2.5 Forward calorimeters

In addition to the ECAL and HCAL in the barrel region, there are three calorimeters in the forward region. The LumiCal will measure the luminosity using the well-known Bhabha scattering process of electron-positron pairs with a precision better than  $10^{-3}$  at 500 GeV. The BeamCal will provide fast beam monitoring and the LHCAL extends the hadronic calorimeter coverage in the forward region down to 41 mrad with respect to the beamline. The three forward calorimeters use technologies similar to the ECAL.

### 2.2.6 Outer detector

The outer detector serves both as muon detector and tail catcher for jets not fully contained in the calorimeters. Muons are identified as tracks in the muon detector. The requirements on the outer detector are not very stringent. There is no trigger, and the occupancy is expected to be low because of the clean environment at the ILC. However, matching the track segments in the outer detector with the signal in the calorimeters does require a position resolution in the azimuthal direction of better than 1 cm.

The outer detector is implemented as an instrumented iron return yoke. It has a minimal thickness of approximately 275 cm to return the magnetic flux. Mechanical constraints require the thickness of the layers to be at least 10 cm. The barrel part consists of 1 sensitive layer in front of the return yoke, 10 sensitive layers spaced 14 cm apart on the yoke, and 3 sensitive layers separated by 60 cm outside the yoke. The forward part consists of 10 layers spaced 14 cm apart, and 2 sensitive layers spaced by 60 cm.

The sensitive parts are scintillating bars with wavelength shifting fibres read out by SiPMs at each end. The transverse resolution is set by the bar width. The longitudinal position is determined from the time difference of the SiPM signals. An alternative readout uses a resistive plate chamber. This is a gaseous detector made of a gas chamber between two parallel plates consisting of high resistive material and readout strips on the outside. Traversing charged particles can ionise electrons in the gas, causing an avalanche between the two plates that is detected by the strips.

### 2.2.7 Data acquisition

The data acquisition benefits from the ILC bunch train structure with 200 ms long idle periods, and the relatively low rate,  $\mathcal{O}(0.1 \text{ hadronic event/bunch crossing})$ , of relevant physics events. Therefore the readout of the ILD can proceed without a trigger. Depending on the subdetector, data is first digitised, zero-suppressed and time stamped by application-specific integrated circuits (ASICs) and field-programmable gate arrays (FPGAs). The data is then gathered per bunch train and sent to an offline-computer

---

farm for calibration and reconstruction. The raw data rate is of  $\mathcal{O}(100\text{ MB})/\text{train}$ , and the storage required is  $\mathcal{O}(10\text{ PB})/\text{year}$ .





# Gaseous detector physics and the time projection chamber

---

In this chapter the physics and working principles of gaseous tracking detectors are discussed. In these detectors, charged particles are detected through their interactions with a gaseous detection medium to which a small amount of energy is transferred. The characteristics of the interactions depend on the incident particle and the gas.

We will focus on the working principles of the TPC [14, 122, 123]. A TPC is a gaseous detector that reconstructs trajectories of charged particles in three dimensions. The principle of a time projection chamber is shown in Figure 3.1. An energetic charged particle ionises the gas in the drift region. As part of the ionisation process, electrons are freed from molecules or atoms leaving behind charged ions. The liberated ionisation electrons in the drift region are transported to a readout plane by an electric field. At the readout plane, the charge is usually amplified before being detected by electronic components. The position in the plane is detected directly, and the distance along the drift direction is calculated from the measured drift time.

We will look into the mechanism for the creation of free charges and the fluctuations hereupon. The transport of charge is discussed, as well as the amplification and detection of charge. Finally some considerations for the operation of a TPC are discussed. These topics are discussed in more detail in e.g. [45, 125].

### 3.1 Energy loss of charged particles

Charged particles lose energy mostly through electromagnetic interactions with the electrons of the gas. For hadrons the additional strong force contribution is negligible

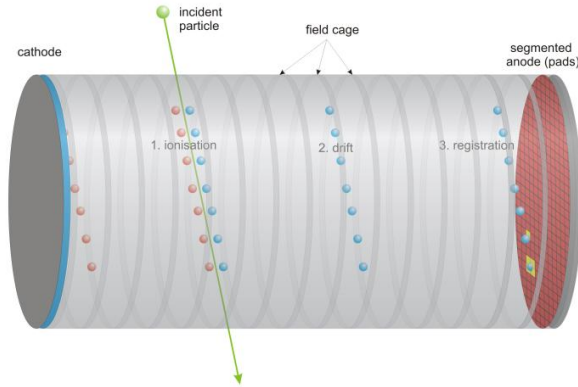


Figure 3.1: Schematic overview of a TPC, image taken from [124].

because of its short range. If the energy of the charged particle is high enough, the electromagnetic interactions can cause excitation which brings the atoms (and molecules) of the gas in an excited state, or ionisation which liberates electrons from the atoms (and molecules). Electrons freed directly from an atom (or molecule) are called primary ionisation.

Most ionisation however is from secondary ionisation. Secondary ionisation is caused by a primary ionisation electron or when an excited state of one atom species causes ionisation in a second species of atoms in a gas mixture. The latter is known as the Penning effect [126].

Occasionally a primary ionisation electron has sufficient energy to make an identifiable track of ionisation by itself, at which point it is referred to as a delta electron. These delta electrons often have a large angle with respect to the primary track.

### 3.1.1 Cross section and mean free path

The probability of an interaction between a charged particle and the gas is quantified by the cross section  $\sigma$ . For moving particles, the mean distance without interaction, i.e. the mean free path  $\lambda$ , is given by

$$\lambda = \frac{1}{n_e \sigma}, \quad (3.1)$$

where  $n_e$  is the electron density of the medium. Interactions are purely random, and hence the number of interactions follows a Poisson distribution.

### 3.1.2 Mean energy loss of charged particles

The Bethe-Bloch equation [127, 128] describes the mean energy loss of a relativistic charged particle at intermediate energies of  $0.1 < \beta\gamma < 1000$ , where  $\beta$  is the particle speed expressed as a fraction of the speed of light  $c$ , and  $\gamma$  the relativistic Lorentz factor. Traveling in a medium with atomic number  $Z$ , atomic mass number  $A$ , and mean excitation energy  $I$ , the mean energy loss [45] is

$$\left\langle -\frac{dE}{dx} \right\rangle = (4\pi N_A r_e^2 m_e c^2) z^2 \frac{Z}{A} \frac{1}{\beta^2} \left[ \frac{1}{2} \ln \frac{2m_e c^2 \beta^2 \gamma^2 W_{\max}}{I^2} - \beta^2 \right], \quad (3.2)$$

where  $N_A$  is Avogadro's number,  $r_e$  is the classical electron radius,  $m_e$  is the electron mass,  $z$  is the charge number of the incident particle. The maximum energy transfer per collision is

$$W_{\max} = \frac{2m_e c^2 \beta^2 \gamma^2}{1 + 2\gamma m_e/M + (m_e/M)^2}, \quad (3.3)$$

where  $M$  is the mass of the incident particle.

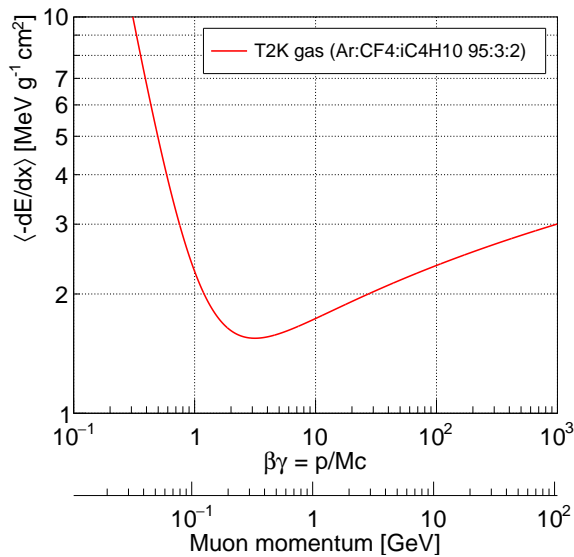


Figure 3.2: Energy loss in T2K gas mixture as calculated with the Bethe-Bloch equation as a function of the Lorentz factor  $\beta\gamma$ . The equivalent momentum for a muon is shown on the extra bottom axis.

In Figure 3.2 the Bethe-Bloch curve is shown for the T2K gas mixture, described in Section 3.5, and which is a good choice for the ILD TPC. At lower energy there is a  $1/\beta^2$  dependence. A particle with a  $\beta\gamma$  corresponding to the minimum of the curve

is called a Minimum Ionising Particle (MIP). Moving towards higher energy there is a logarithmic rise. At higher energies, an effect due to the polarisability of the material depending mostly on the density can play a role [129]. For gases which have a low density, this effect can be neglected at intermediate energies. At even higher energies, not shown in the curve and outside the applicability of the Bethe-Bloch equation, there are radiative effects which grow proportional with the energy.

Electrons and positrons have to be treated separately from heavier particles. Electrons and positrons are deflected more by the collisions, and bremsstrahlung dominates above a relatively low energy threshold (of about 100 MeV) and grows proportional with the energy. As they lose energy, positrons have an increasing chance to annihilate with one of the electrons in the detection medium and produce two photons.

Although the Bethe-Bloch equation is accurate to within a few percent and conceptually useful, it cannot be directly applied to the ionisation of a single charged particle, because of the large fluctuations on the energy loss.

### 3.1.3 Fluctuations on the energy loss

Per interaction there are large fluctuations on the energy loss, which in turn causes the mean over a limited number of interactions to have large variations. For thick samples these fluctuations are described by a Landau distribution [130], but any gaseous detector applications are well outside this regime. In thin layers the mean energy loss of charged particles is influenced by a few interactions with large energy deposits (see e.g. [131]). Therefore the mean, and the most probable energy loss depend on the sample thickness.

To match the ionisation of a particle to the Bethe-Bloch curve, the fluctuations caused by these large deposits are reduced by taking the truncated mean of the energy loss. This is the mean from a fixed fraction (typically between 50%-90%) of the samples with the lowest energy. An application will be discussed in Section 5.4.7.

On the other hand, to calculate the distribution of ionisation for a charged particle with a given momentum, the Photo-Absorption Ionisation model (PAI model) gives a useful description.

#### The Photo-Absorption Ionisation model

The PAI model is a method to calculate the ionisation of a charged particle, which incorporates information of the atomic structure from the photo-absorption spectrum [132]. The model uses random discrete scatters in which each scatter causes the ionisation of one or more electrons. The number of ionisation electrons form the cluster size distribution, which includes all secondary ionisation electrons because they are often very close to the primary encounter.

At low energy, the cluster size distribution is determined by the atomic structure of the gas. At high energy, the binding energy can be neglected and the distribution follows the Rutherford scattering equations of free electrons. The probability to create an ionisation cluster is proportional to  $1/E^2$ , where  $E$  is the energy transferred in the collision (see e.g. [133] for an experimental demonstration).

In order to illustrate the PAI model a few simulated distributions are shown in Figure 3.3. Tracks of 2.5 GeV electrons with a length of 27.5 mm were simulated for the T2K gas mixture using HEED. HEED is a well know gas simulation program with a PAI based model [134]. In Figure 3.3a, the cluster size distribution is shown following the  $1/E^2$  dependence. At lower energy the atomic structure is visible in the second peak around a cluster size of 12, because of electrons from the L shell. Figure 3.3b displays the number of clusters on a track of 27.5 mm, which is fitted with a Gaussian distribution to highlight that the Poisson distributed number of clusters closely approaches a Gaussian distribution for this track length. The last Figure 3.3c shows the total ionisation using the PAI model. The distribution of the total number of electron-ion pairs is dominated by a few high energy deposits and has a long tail.

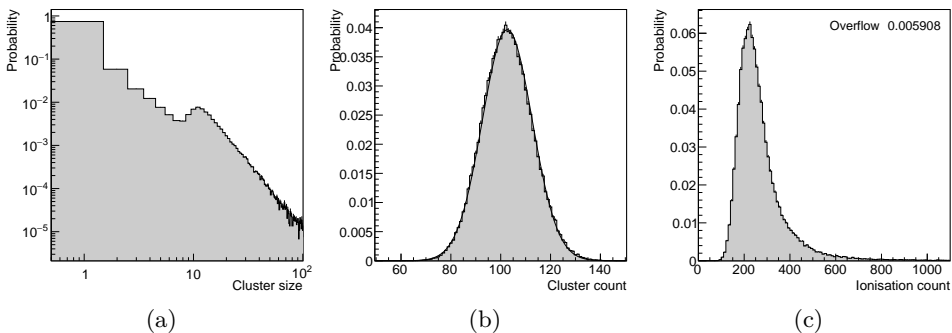


Figure 3.3: Simulated distribution of (a) the cluster size and (b) number of ionisation clusters and (c) total ionised electron ion pairs for a 2.5 GeV electron track through a 27.5 mm thick sample of a T2K gas mixture consisting of 95% Ar, 3%  $\text{CF}_4$  and 2%  $\text{iC}_4\text{H}_{10}$ . The cluster count distribution b) is fitted with a Gaussian distribution.

### 3.1.4 Multiple scattering

Successive collisions with the nuclei of the gas atoms deflect a charged particle in a process known as multiple Coulomb scattering. Multiple scattering is well described by Molière's theory [135, 136]. The total scattering angle is the result of a large number of small-angle scatters resulting in a Gaussian angular distribution. However, there is a small probability to have a large scattering angle, resulting in non-Gaussian

tails. A schematic of a high energy particle traversing some material is shown in Figure 3.4.

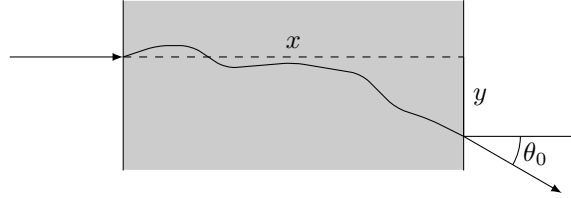


Figure 3.4: Schematic view of multiple scattering in a plane with some of the quantities discussed in the text indicated.

A useful approximation (from [137] subsequently improved by [138]) of the planar scattering angle distribution is given in terms of a Gaussian distribution with mean zero and a standard deviation  $\theta_0$  given by

$$\theta_0 = \frac{13.6 \text{ MeV}}{\beta cp} \sqrt{\frac{x}{X_0}} \left( 1 + 0.038 \ln \frac{x}{X_0} \right), \quad (3.4)$$

where  $p$  is the momentum of the particle (in MeV/c),  $x$  is the thickness and  $X_0$  is the radiation length of the traversed material. The approximation is better than 11% for  $10^{-3} < x/X_0 < 100$ . The displacement in the plane is given by  $y = \theta_0 x / \sqrt{3}$ , and it is correlated to the scattering angle with correlation coefficient  $\rho_{y\theta} = \sqrt{3}/2$ .

## 3.2 Charge transport in gas

After ionisation the electrons and ions are transported through the gas under influence of an electric field with a strength  $E$  of usually a few hundred V/cm. During the drift process they interact with the gas molecules and atoms. This section describes the transport of these charges in a gas.

### 3.2.1 Drift velocity

The average velocity of a charged particle transported in a gas is known as the drift velocity  $\mathbf{v}_{\text{drift}}$ . In the presence of an electric field  $\mathbf{E}$ , and a magnetic field  $\mathbf{B}$ , Lorentz forces determine the motion of the charge. The interactions with the gas can be modeled as a friction term proportional to the velocity (see e.g. [125]). The drift

velocity is then given by

$$\mathbf{v}_{\text{drift}} = \frac{q}{m} \frac{\tau}{1 + \omega^2 \tau^2} \left( \mathbf{E} + \frac{\omega \tau}{B} (\mathbf{E} \times \mathbf{B}) + \frac{\omega^2 \tau^2}{B^2} (\mathbf{E} \cdot \mathbf{B}) \mathbf{B} \right), \quad (3.5)$$

where  $q$  is the transported particle's charge,  $m$  is its mass,  $\omega = \frac{qB}{m}$  is the cyclotron frequency, and  $B$  is the strength of the magnetic field. The average time between collisions  $\tau$  is inversely proportional to the friction. A magnetic field  $\mathbf{B}$  in a TPC is ordinarily parallel to the electric field  $\mathbf{E}$ , in which case Equation (3.5) reduces to

$$v_{\text{drift}} = \mu E = \frac{qE}{m} \tau, \quad (3.6)$$

where  $v_{\text{drift}}$  is the drift velocity in the direction of the electric field and  $\mu$  is known as the mobility.

The average time between collisions  $\tau$  can be expressed as

$$\frac{1}{\tau} = N \sigma(\epsilon) v_{\text{instant}}(\epsilon), \quad (3.7)$$

where  $N$  is the gas density,  $\sigma$  the cross section and  $v_{\text{instant}}$  the instantaneous velocity of the particle. In general  $v_{\text{instant}}$  and  $\sigma$  depend on the particle energy  $\epsilon$ . The energy is a combination of thermal energy and energy gained from the acceleration in the electric field. The thermal contribution is  $\epsilon_{\text{thermal}} = (3/2)k_{\text{B}}T$ , where  $k_{\text{B}}$  is the Boltzmann constant and  $T$  is the temperature.

At this point we distinguish hot and cold gases for the transport of electrons in a TPC. In a cold gas the energy an electron acquires from the electric field is low and the energy of the electron is mostly thermal. This means that the drift velocity is much smaller than the instantaneous velocity, so the mobility has a weak dependence on the electric field strength. Molecular gases are usually cold gases, because the electrons constantly lose energy through interactions with the vibrational modes of the molecules.

In a TPC with a hot gas, the electrons have a higher drift velocity, which is not negligible compared to the instantaneous velocity. This makes the drift velocity depend non-trivially on the electric field. An example of these are the noble gases.

In particular, argon has a minimum in the elastic scattering cross section at an electron energy of around 0.2 eV. This is known as the Ramsauer minimum [139]. It is the result of a quantum mechanical scattering effect analogous to the scattering of a wave on a square potential well, which has a minimum when the wavelength is similar to the width of the well. As a result, in argon the drift velocity will be larger when the electrons have an energy around this minimum.

Ionisation creates electrons and ions in pairs. The ions created in the drift volume



are called primary ions<sup>1</sup>. For the typical electric fields of a few hundred V/cm the ion energy is mainly thermal energy, and their drift can be described by Equation (3.6) with a constant mobility. In comparison to the electrons, the ions drift relatively slow at a velocity of a few m/s. At a collider, ions from many subsequent bunch crossings can accumulate in the drift volume and the resulting electric field can distort the drift of the electrons.

### 3.2.2 Diffusion

The drifting particles scatter randomly on the gas molecules and atoms and spread out in space. This process, called diffusion, depends on the gas and the drift field. The diffusion brings about a Gaussian spread  $\sigma_T$  independently in both of the two transverse directions, and a Gaussian spread  $\sigma_L$  in the longitudinal direction after some time  $t$ . Since the spread is a consequence of a large number of scatters, it develops proportional to  $\sqrt{t}$ . For applications in drift chambers, the diffusion is expressed using the drift length  $\ell = v_{\text{drift}}t$  instead of time. The diffusion is characterised by the transverse and longitudinal diffusion coefficients:

$$D_T = \sigma_T / \sqrt{\ell} \quad \text{and} \quad D_L = \sigma_L / \sqrt{\ell}. \quad (3.8)$$

A magnetic field parallel to the electric field reduces the transverse diffusion by a factor  $1/\sqrt{1 + \omega^2\tau^2}$  [140].

If the particle has only thermal energy the diffusion coefficient is given by [141, 142]

$$D_{\text{thermal}} = \sqrt{\frac{2k_B T}{qE}}. \quad (3.9)$$

The thermal diffusion coefficient can be seen as a lower limit that applies both to drifting electrons and ions in transverse and longitudinal direction, and does not depend on the gas composition. For example at room temperature  $T = 294$  K and a drift field of 300 V/cm, the thermal diffusion coefficient is  $130 \mu\text{m}/\sqrt{\text{cm}}$ .

## 3.3 The amplification of charge

Before being detected, the ionisation electrons in a TPC usually require amplification in an amplification region of the gas volume. In this region, a large electric field accelerates the electron to an energy above the ionisation potential. The ionisation electrons produced by this electron will also be accelerated, causing an exponential

---

<sup>1</sup>even those from secondary ionisation

amplification of charge. This is referred to as an electron avalanche. The multiplication factor is known as the gas gain

$$G = n/n_0, \quad (3.10)$$

where  $n_0$  is the number of initial electrons from the drift region and  $n$  is the final number of electrons at the end of the avalanche.

### 3.3.1 Fluctuations on the amplification of charge

The avalanche process is governed by probabilities, therefore the total number of ionisation electrons per avalanche  $n$  is subject to large statistical fluctuations. For weak fields (up to a few tens of kV/cm), the mean distance between ionising collisions is large compared to the distance required to reach the energy corresponding to the ionisation potential of the gas. The fluctuations are therefore dominated by statistics alone and follow an exponential distribution.

For stronger fields the situation is more complicated. Slow development early in the avalanche accelerates development at a later time, and vice versa. Fluctuations are not purely statistical, so the distribution is more peaked. Phenomenologically the Polya distribution describes the gain fluctuations [143] for all detector geometries, although the physical interpretation only applies to wires. The Polya distribution is given by

$$P(n, \theta) = \frac{1}{\bar{n}} \frac{(\theta + 1)^{\theta+1}}{\Gamma(\theta + 1)} \left(\frac{n}{\bar{n}}\right)^\theta \exp\left(-(\theta + 1)\frac{n}{\bar{n}}\right) \quad (3.11)$$

where  $\bar{n}$  is the mean number of total electrons per avalanche,  $\Gamma(\theta + 1)$  is the gamma function, and  $\theta$  is a parameter related to the standard deviation  $\sigma^2 = \bar{n}^2/(\theta + 1)$ . The Polya distribution is shown in Figure 3.5 for various values of  $\theta$ . For  $\theta = 0$  the distribution corresponds to the exponential distribution seen in a weak field, and for larger  $\theta$  the distribution becomes increasingly peaked.

### 3.3.2 Ion backflow

The electron avalanches also create ions drifting at a low speed. Most of them are contained in the amplification region, but even the small fraction of ions that enter the drift region can affect the movement of electrons, and distort the reconstructed position. The Ion Backflow Fraction (IBF) is given by

$$\text{IBF} = n_{\text{IB}}/n, \quad (3.12)$$

where  $n_{\text{IB}}$  is the number of ions entering the drift region, and  $n$  is the number of avalanche ions.

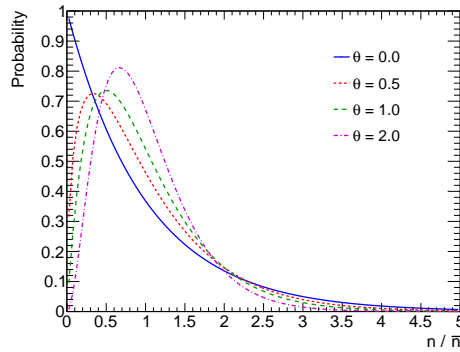


Figure 3.5: The Polya distribution for a few values of parameter  $\theta$

To limit the number of backflow ions from the amplification region a gating device can be introduced in front of the end plate in the drift volume. During the charge collection phase the gate is transparent to electrons drifting towards the end plate, but in the gated mode a potential applied to the gate causes it to block ions from the amplification region. If the time structure of the incoming events allows it, the gate can be switched such that it is transparent to the drift electrons but opaque to the back flowing ions. Originally wires were used as a gating device, but nowadays micropattern like structures can provide more effective gating.

## 3.4 Micropattern gaseous detectors

In order to create an amplification region, micropattern amplification structures are used that match or are smaller than the readout granularity. The most common in large detectors are the Gas Electron Multiplier (GEM) [21] structures and the micro-mesh gaseous structure (Micromegas) [20]. The GridPix is a more recently invented micropattern gaseous detector and is the focus of this thesis.

### 3.4.1 The gas electron multiplier (GEM)

A GEM consists of an insulating foil (usually Kapton) with a thickness of about  $50\ \mu\text{m}$  to  $100\ \mu\text{m}$  covered by a thin conducting layer (usually copper) on both sides. The foil is perforated with  $25\ \mu\text{m}$  to  $150\ \mu\text{m}$  wide holes that are  $50\ \mu\text{m}$  to  $200\ \mu\text{m}$  apart. By applying a large potential difference across the foil, an amplification region forms in the holes. A schematic view of the electric field lines is given in Figure 3.6. GEMs can be stacked to improve the amplification properties.

The amplified signal can be detected by strips, mm sized pads or even a CMOS chip. By using multiple stacked GEMs the signal spreads out across multiple pads,

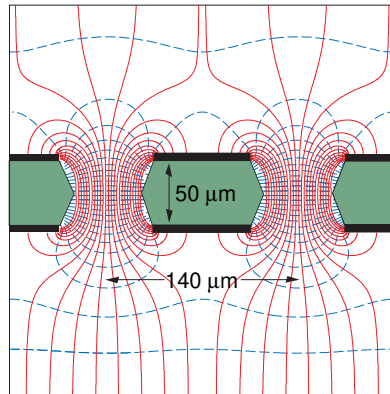


Figure 3.6: The electric field lines and equipotential lines for a cross section of a GEM. Figure taken from [45].

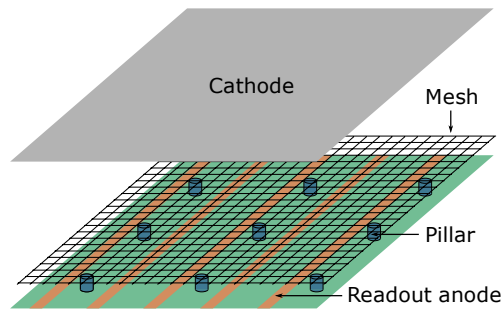


Figure 3.7: Schematic view of a Micromegas detector.

which allows for a more precise position measurement.

### 3.4.2 The micro-mesh gaseous structure (Micromegas)

Micromegas consists of a conducting mesh situated  $25\ \mu\text{m}$  to  $150\ \mu\text{m}$  above a readout plane. A schematic overview is given in Figure 3.7. A large voltage is applied between the mesh and the readout plane. The electric field lines are shown in Figure 3.8 and give rise to narrow avalanches. The amplified signal can be read out in similar ways as for the GEMs, but might require an additional charge spreading layer to distribute the signal to multiple readout channels in order to improve the spatial resolution.

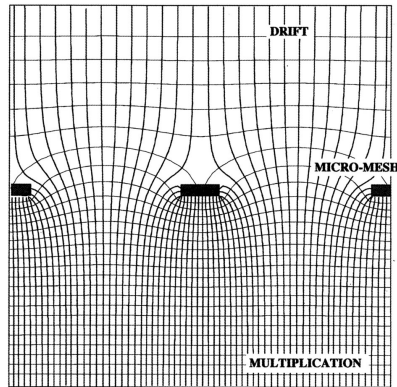


Figure 3.8: The electric field lines and equipotential lines for a cross section of a Micromegas detector. Figure taken from [144].

### 3.4.3 The GridPix

The GridPix is a CMOS pixel readout chip with a micromegas-like integrated grid [22, 23]. The grid with holes aligned to the pixels is fabricated on top of the chip by means of microelectromechanical systems (MEMS) postprocessing techniques. The main advantage of the GridPix is its capability to detect single ionisation clusters with high efficiency. This leads to excellent spatial resolutions. In the next chapter, the GridPix will be discussed in more detail.

## 3.5 The choice of a gas mixture

The choice of a gas (mixture) largely determines the properties of a gaseous detector. Here we discuss some aspects that influence the choice, and explain why the ILD TPC foresees the use of the argon based T2K gas mixture. The gas is named after the Tokai to Kamioka (T2K) long baseline neutrino oscillation experiment [145], which uses the gas in three large TPCs with a Micromegas readout.

### 3.5.1 Factors that determine the gas choice

#### The number of ionisation electron-ion pairs

The number of electron ion pairs created by a high energy charged particle determines the number of measurement points along the track. This impacts the spatial resolution, energy loss  $dE/dx$  resolution and the required gain. For example, in argon a MIP creates on average 97 electron-ion pairs per cm.

### **Drift velocity**

The drift velocity of electrons is a basic parameter that determines the charge collection time. Fast charge collection is required in high rate applications at a collider. The position along the drift direction is determined from the product of the arrival time and the drift velocity. Thus a higher drift velocity either reduces the precision of the reconstructed position, or requires a more precise time of arrival measurement.

### **Moderator**

The drift velocity in some noble gases can be increased by maintaining the energy of the drifting electrons near the Ramsauer minimum (see subsection 3.2.1). This is accomplished by adding a molecular moderator component that absorbs the excess electron energy.

### **Diffusion**

The diffusion coefficients are of crucial importance to the choice of a gas mixture, because the resolution is often limited by diffusion. The transverse diffusion coefficient reduces with increasing magnetic field strength, and has to be evaluated for the experimental conditions.

### **Effect of the electric field**

The drift velocity and diffusion both strongly depend on the electric field. Ideally the electric field is chosen at a maximum or at a minimum of the drift velocity to limit the propagation of small distortions of the electric field into the reconstructed position.

For practical purposes, it is hard to apply more than a few tens of kV anywhere in a detector before creating discharges. So for a large detector it is important that sufficiently high drift velocities are reached for an electric field of up to a few hundred V/cm.

The flow of ions is yet another factor. The drift velocity of ions is often proportional to the field and would benefit from strong drift fields, but the IBF is roughly proportional to the field ratio of the drift and amplification region and benefits from a weak drift field.

In the end, for the choice of a gas mixture it is important that a working point for the electric field exists that satisfies requirements on the drift velocity, diffusion coefficient, ion flow, and is still practical.

**Gain**

The gain is set by the choice of the electric field in the amplification region, but also depends on the gas composition. A suitable gas should have a sufficient gain at a workable strength of the electric field in the amplification region.

**Quenching**

In the avalanches photons are created that can ionise the gas, leading to additional unwanted avalanches. To quench these, a photon absorbing component such as methane is added. Many organic compounds are good quenchers, because they are efficient in absorbing photons in the relevant energy range.

**Safety and environment**

At many labs safety considerations prohibit the use of flammable gases. For this reason gases with a high concentration of hydrocarbons are excluded. For some other gases, such as sulfur hexafluoride ( $\text{SF}_6$ ), there are restrictions on emission because of their global warming potential.

**Cost**

Gases can be a considerable factor in the total cost of constructing and operating the detector. The cost of gases varies greatly, with for example neon being approximately between 10 and 100 times as expensive as argon.

**Ageing**

Certain type of gas atoms and molecules have some probability to undergo chemical reactions in the avalanches. The compounds produced in these reactions can be deposited inside the detector and impact the gain, degrade the resolution or sometimes even cause self-sustaining currents. Especially hydrocarbons are known to undergo polymerisation and form highly adhesive substances. The functionality degradation over longer time is called ageing. Functionality can sometimes be restored by (temporarily) adding small quantities of oxygen, water and solvents.

**Electron attachment**

Drift electrons can attach to electronegative molecules such as  $\text{O}_2$ ,  $\text{CO}_2$  and  $\text{H}_2\text{O}$ . These electrons are not detected in time and thus reduce the detector efficiency. For detectors with a large drift distance, it is important to keep the concentration of these molecules sufficiently low.

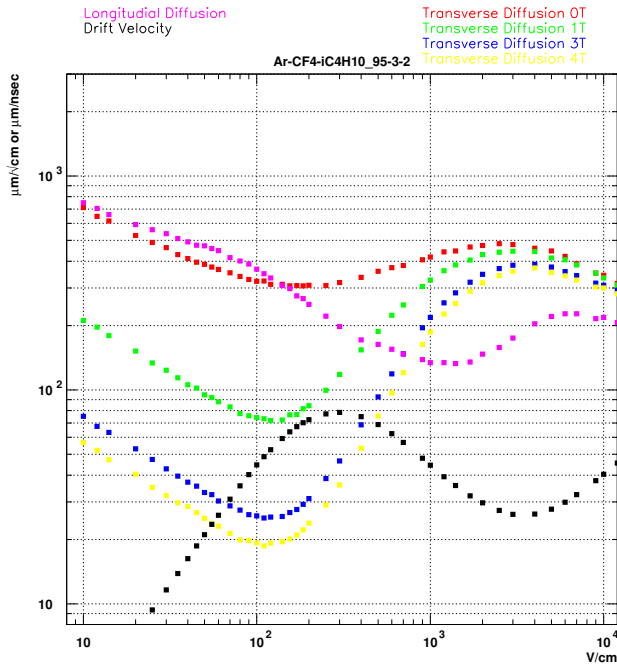


Figure 3.9: Diffusion coefficients and drift velocity for T2K gas mixture [149].

### 3.5.2 Motivation for the use of T2K gas mixture

For the ILD TPC the T2K gas mixture consisting of 95 % Ar, 3 %  $\text{CF}_4$ , and 2 %  $\text{iC}_4\text{H}_{10}$  is an excellent candidate [146]. The T2K gas mixture is an argon-based gas such that it provides enough ionisation electrons to do measurements with high statistics, and it can provide enough gain at a reasonable electric field strength. The isobutane content is sufficient to absorb photons, while at the same time it is not so large that it makes the gas flammable. The  $\text{CF}_4$  is added as a moderator to boost the electron drift velocity to up to  $75 \mu\text{m}/\text{ns}$  at a drift field of only  $280 \text{ V}/\text{cm}$ . Through a chain of reactions the most abundant ions in the gas are of the form  $\text{C}_{12}\text{H}_n^+$  and the expected ion drift velocity is about  $2.2 \text{ m}/\text{s}$  [147, 148].

However, what makes the T2K gas mixture exceptional is the low transverse diffusion coefficient of just  $20 \mu\text{m}/\sqrt{\text{cm}}$  at a magnetic field of  $4 \text{ T}$  and a drift field of  $140 \text{ V}/\text{cm}$ . The predicted drift velocity and diffusion coefficients for various magnetic field strengths are shown as a function of drift field in Figure 3.9. A downside of the T2K gas mixture is that its properties are sensitive to small contaminations of water and oxygen.



## 3.6 A TPC as a tracker in a collider experiment

In this final section some considerations for the implementation of TPCs as a tracker in detectors at colliders are discussed. Although this thesis and the described research focuses on application in the ILD detector at the ILC, considerations for applying TPC technology in detectors at other colliders are also discussed in this section.

### 3.6.1 The ILD TPC at the ILC

The ILD TPC discussed in this thesis will be located at the ILC, for which some unique properties connected to the beam conditions discussed in subsection 2.1.2 hold. As a linear collider, there are relatively large backgrounds for a lepton collider, especially at the higher energy stages. Indeed calculations show that the main source of ionisation in the TPC is from beamstrahlung backgrounds [150].

Ions produced in the drift region of the TPC accumulate over multiple bunch crossings, and lead to distortions of the drift field and thus of the reconstructed track. The amount of primary ionisation is low enough for precise measurements, but the backflow ions produced in the amplification process must be reduced to achieve the required resolution [151, 152]. Because of the special bunch structure of the ILC, gating can be employed. The 200 ms between bunch trains is ideal to stop the ions drifting into the volume. For the ILD TPC, a GEM gating grid was developed [153]. A bias potential of 3 V across the GEM gives the gate a high electron transparency of 85 %, and a reverse potential of 20 V across the GEM blocks most of the ions.

The 554 ns to 366 ns time interval between bunch crossings at the ILC is sufficiently long to associate the tracks in the TPC to individual events, and to keep the occupancy low. The time between bunch trains will also be used to save power and thus cooling capacity by powering down parts of the electronics during these phases.

### 3.6.2 A TPC for a detector at the compact linear collider

The Compact Linear Collider (CLIC) is an electron positron collider proposed to be built at the European organization for nuclear research (CERN) using novel accelerating technology with a low energy, but high intensity, proton drive beam [154]. The linear layout is exploited to construct the collider in three stages with collision energy of 380 GeV, 1.5 TeV, and 3 TeV, and with site lengths starting at 11 km ranging into 50 km for the final stage. These energies are reached with drive beams powering normal-conducting high-gradient accelerating structures.

The drive beam based accelerating technology has consequences for the bunch structure. During the first 380 GeV phase, trains with 352 bunches each are repeated at a frequency of 50 Hz. The bunch separation within these trains is only 0.5 ns.

At CLIC there are sizeable beam induced backgrounds [155]. The significant electron-positron pair production from beamstrahlung photons is mostly in the forward direction. Hadronic final states produced in two photons interactions can have a higher transverse momentum, which makes them the dominant source of (pile up) ionisation in the TPC. The CLIC bunch structure would allow for gating of the back-flow ions, but the number of primary ions from the large beam induced backgrounds is a point of attention.

The beam induced backgrounds, in combination with the short bunch spacing, pose an obstacle for the implementation of a TPC. The occupancy of the readout is a limiting factor. For an ILD style TPC, the occupancy of the inner readout pads is 100% for one bunch train at a collision energy of 3 TeV. However, the three dimensional equivalent of the pixel occupancy, the voxel occupancy is more relevant. The voxel occupancy of the inner readout pads sized  $6\text{ mm} \times 1\text{ mm}$  or  $1\text{ mm} \times 1\text{ mm}$  would be 30% and 12% respectively [156]. This is generally seen as problematic.

The pixel occupancy of the inner radius pixel TPC is expected to be 40% for one bunch train at a collision energy of 3 TeV. So depending on the capabilities to detect multiple hits per bunch train, the voxel occupancy in a pixel TPC is expected to be much lower and reach acceptable levels. The Timepix3 based readout does have multi-hit capabilities, but the minimum recovery time of 475 ns should be reduced to be less than the bunch train length of 175 ns. Alternatively moving the TPC inner radius outwards reduces occupancy at the expense of pattern recognition efficiency.

All in all because currently only one detector is foreseen at CLIC [98] a TPC tracker might not be the most straightforward choice. However, earlier proposals had a second detector in push-pull configuration [155]. Given the high occupancy, whether a TPC with pad readout at CLIC is feasible requires more study. A pixel TPC readout, featuring multi hit capability, is likely a viable option for a TPC at CLIC.

### 3.6.3 A TPC for a detector at the future circular collider

The Future Circular Collider (FCC) design study proposes to build an electron positron collider (FCC-ee) in a 100 km long underground tunnel near CERN [100, 157]. The tunnel can later be reused for a hadron collider, the FCC-hh [158]. The FCC-ee program is divided in four stages: a high luminosity  $Z$  boson production run at a centre-of-mass energy of 91.2 GeV, a run around 160 GeV near the production threshold of two  $W$  bosons, a third run as a Higgs factory at 240 GeV, and a run above the top-antitop production threshold at 350 GeV.

The most stringent requirements on TPC operation at the FCC-ee are set by the  $Z$  pole run. Backgrounds at this energy are low compared to the backgrounds at the ILC and actual  $Z$  boson events will be the main source of ionisation in the

TPC. With a luminosity of  $230 \times 10^{34} \text{ cm}^{-2}\text{s}^{-1}$  for this run, the FCC-ee will produce  $e^+e^- \rightarrow Z \rightarrow q\bar{q}$  events at a rate of approximately 100 kHz. An earlier study [159], showed that with a luminosity of  $28 \times 10^{34} \text{ cm}^{-2}\text{s}^{-1}$  the level of primary ionisation was already similar to that at the ILC. The amount of primary ionisation at the design luminosity would lead to larger distortions. In addition it will not be possible to apply gating at this event rate without seriously impacting the recorded event rate. As a result, an ILD-style TPC is probably not the most suitable tracker for detectors at the FCC-ee during  $Z$  pole running.

### 3.6.4 A TPC for a detector at the circular electron positron collider

The Circular Electron Positron Collider (CEPC), also a collider with a 100 km circumference, is proposed to be built in China [99, 160]. The project is in many ways similar to the FCC. There are three planned runs, starting with a Higgs production run at a collision energy of 240 GeV and then runs at 91.2 GeV and 160 GeV. A run above the top anti-top production threshold is under investigation.

For TPC operation the  $Z$  pole run at 91.2 GeV is, as for the FCC-ee, the most challenging, but at  $32 \times 10^{34} \text{ cm}^{-2}\text{s}^{-1}$  the expected luminosity is about one order of magnitude lower than at the FCC-ee. Some exploratory calculations indicate that the primary ionisation will be at a similar level as the ILC [161]. At an expected  $e^+e^- \rightarrow Z \rightarrow q\bar{q}$  event rate of about 10 kHz and a maximal drift time of about 30  $\mu\text{s}$ , ion backflow gating is possible but undesirable since 25% of the event data would be lost. Reference [162] concludes that operation at the CEPC during the  $Z$  pole is feasible under condition that the ion backflow can be controlled. Operating a TPC during the higher energy runs, and the corresponding lower cross sections and thus lower event rates is possible.

---

## The GridPix

---

The GridPix is a CMOS pixel readout chip with an integrated grid added by MEMS postprocessing techniques. The precise manufacturing of the supporting pillars and aluminium grid allows to realise holes aligned to the pixel input pads and to obtain a highly uniform gas gain. The silicon pixel chip digitises the charge collected on the pixel. The main advantage of a GridPix readout is its capability to precisely detect single ionisation clusters with high efficiency. For the readout of a TPC, this has several benefits.

The fine granularity allows for an improved track position measurement, especially at short drift distances where the resolution is not limited by the diffusion. The pixel readout measures tracks with a large angle with respect to the readout plane more precisely than the conventional pad readout, because the number of measurement points does not depend on the projected track length, but on the number of ionisation clusters which is proportional to the total track length. Additionally, while the rectangular pad-based readouts can achieve the best resolution only for tracks in the elongation direction, the square pixels allow for a precise track measurement irrespective of the track angle with the readout rows. The granularity and the capability to measure every ionisation electron also improves the two-track separation performance. Furthermore, the high granularity enables the identification of ionisation clusters. This improves the energy loss  $dE/dx$  resolution, because the number of ionisation clusters is Poisson distributed, unlike the total ionisation which has a much broader Landau-like distribution (see also subsection 3.1.3).

This chapter describes the GridPix, the underlying Timepix3 chip, and some properties that are important for the operation of GridPix as a readout for a TPC.

## 4.1 The GridPix

The first step towards a GridPix detector was a proof of concept of using a Micromegas grid on top of a MediPix2 CMOS chip [22, 23]. Since then, a series of developments have taken place that culminated in the GridPix detectors using Timepix chips [163]. More recently, the Timepix3 chip has been applied as the digital front end [25]. A photograph of a Timepix3 partially covered with an integrated grid is shown in Figure 4.1.

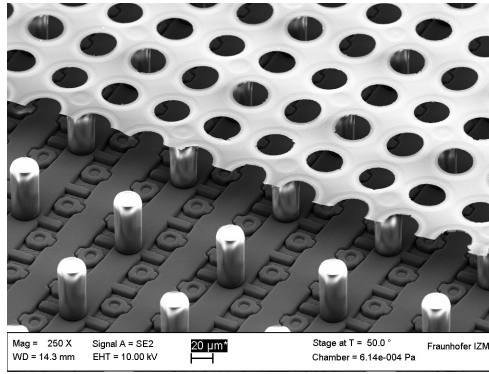


Figure 4.1: Close up of a Timepix3 based GridPix. The grid has been truncated to show the underlying structures. The picture is taken from [164].

The distinctive element of a GridPix is the integrated aluminium grid with a geometry that matches that of the underlying chip. The Timepix3's pixel pitch of  $55\ \mu\text{m} \times 55\ \mu\text{m}$  is matched by a grid with  $35\ \mu\text{m}$  diameter circular holes. The  $1\ \mu\text{m}$  thick aluminium grid is supported by  $50\ \mu\text{m}$  high SU8 pillars. The GridPix has broader covered areas called dykes along all sides to provide mechanical stability. In the re-optimized masks, these cover  $2 \times 3$  readout columns on two sides.

In a TPC, the incoming electrons from the drift volume move through the holes to the amplification region, where they are amplified and the signals are detected by the underlying electronics. Because of the large electric field ratio between the drift region and the amplification region, the electrons very rarely land on the top side of the grid. In the amplification region an approximately exponential multiplication of charge occurs and the electrons are collected by the underlying chip within about 1 ns. In addition to the fast electron component, the ions created in the amplification region induce charge on the pixel pads. The ions drift towards the grid in approximately 10 ns to 100 ns. The few ions that escape through the holes into the drift region, are called backflow ions (see subsection 3.3.2).

### 4.1.1 The protection layer

In the high field region between the anode and the grid a spark can occur leading to a discharge of the grid, possibly damaging the sensitive chip electronics. Damage can be prevented by applying a high-resistive protection layer to quench this discharge. Special care was taken to uniformly deposit a  $4\ \mu\text{m}$  thick silicon-rich silicon nitride (SiRN) protection layer. A  $4\ \mu\text{m}$  thick protection layer is expected to be sufficient to quench discharges, according to previous studies with a Timepix based GridPix [165]. Recent spark protection tests [166] using a non-functional Timepix3 based GridPix with a  $4\ \mu\text{m}$  thick SiRN protection layer in a  $200\ \text{kHz cm}^{-2}$  hadron beam confirm this and found no damage to the protection layer. However, the resistivity of this protection layer does lead to charge up effects, which are investigated in subsection 4.3.4.

### 4.1.2 Production

GridPixes are made using standard 200 mm Timepix3 wafers with 105 chips each [167]. The Post-processing steps are performed at the Fraunhofer Institute for Reliability and Microintegration (IZM) in Berlin, and are described in [166, 168]. Some of the major production steps are:



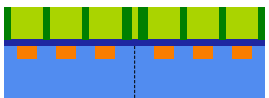
1. The wafer is prepared: the chips are probed to find electronic failures and the surface is cleaned



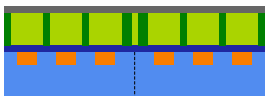
2. A high-resistive  $4\ \mu\text{m}$  thick SiRN protection layer is deposited on the chip in order to protect the chip from discharges. A protection layer on the bonding pads would hinder electrical connections, and is avoided by temporarily covering them with polyamide.



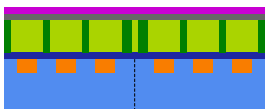
3. The wafer is covered with a  $50\ \mu\text{m}$  thick layer of SU-8 photoresist.



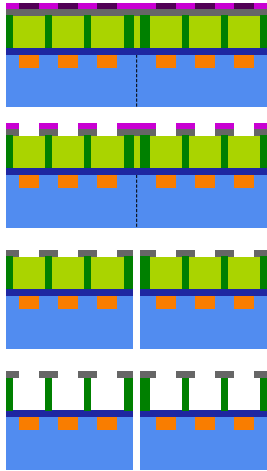
4. Using a special mask, part of the SU-8 is exposed to UV light, solidifying it to create the pillar structure.



5. A  $1\ \mu\text{m}$  thick aluminium layer is deposited.



6. Another  $1\ \mu\text{m}$  thick layer of photoresist is applied.

- 
7. With UV light and another mask, a hole pattern is created.
  8. The grid holes are chemically etched.
  9. The wafer is diced into individual chips using a saw.
  10. The unexposed SU-8 photoresist is resolved and the chips are ready.

### 4.1.3 Other applications of GridPix detectors

Besides as a TPC readout for collider experiments, the GridPix can be applied in rare event searches, and in medical applications, see [163].

A GridPix variant has been proposed as a tracking detector organised in layers, similarly to a silicon tracking detector at collider experiments. This detector is capable of measuring the direction of tracks and to detect transition radiation, which can be used for particle identification. It consists of 10 mm to 16 mm thick gas layers read out by GridPixes [169]. The thin gas layer results in the measurement of a very precise, short, track segment. By considering to what level the segments point to the IP an initial estimate of the momentum can be performed. If special transition radiation layers with different refractive indices are added, additional particle identification information can be obtained from the transition radiation emitted on the boundary of these layers. The intensity of transition radiation [170] depends on the Lorentz factor  $\gamma$  [171], and thus lighter and heavier particles can be distinguished [172]. The high energy photons can be detected using a highly absorbent xenon based gas mixture.

The GridPix detector can also be employed as an X-ray detector. Similarly to charged particles, X-rays can ionise atoms and molecules in a gas. A GridPix detector can count the number of ionisation electrons, and thus measure the X-ray's energy. A Timepix-based GridPix detector is used as an X-ray detector in the CERN Axion Solar Telescope (CAST) [173, 174], which is searching for axions and axion-like particles produced in the sun.

Application of a GridPix detector in a dual-phase pure noble gas TPC for dark matter searches has been investigated [175, 176]. However, due to the absence of a quencher component operation with sufficient gain could not be achieved. A GridPix

readout is also a possible option for directional dark matter searches using gaseous TPCs [45, 177]. The coverage fraction and cost are identified as the most pressing concerns. Some of these TPCs measure drifting negative ions instead of electrons, in order to reduce the diffusion and improve the position resolution.

Proton therapy is the irradiation of tissue with protons, often with the aim of destroying cancer cells. Compared to conventional X-ray radiotherapy, proton therapy has the potential to minimize the radiation dose delivered to healthy tissue. Currently the radiation dose is targeted using conventional X-ray based imaging techniques, but these are intrinsically inaccurate because X-rays and protons interact differently with tissue. Alternatively, detailed information can be obtained from protons by measuring their direction before and after passing through the tissue. A GridPix is well suited for these measurements, because of its low mass and high precision. A feasibility test found a good agreement between experimental results and simulated performance [178].

## 4.2 The Timepix3

The Timepix3 chip is a general purpose readout chip developed by the Medipix3 collaboration [24]. The chip can detect charge in both semiconductor detectors and gaseous detectors. Like its predecessor, the Timepix chip, it has  $256 \times 256$  pixels with a pitch of  $55 \mu\text{m} \times 55 \mu\text{m}$  and a total sensitive area of  $14.08 \text{mm} \times 14.08 \text{mm}$ . However, it offers a superior Time of Arrival (ToA) resolution of 1.56 ns, in addition to a data driven readout and simultaneous Time over Threshold (ToT) measurements with a resolution of 25 ns.

Each pixel consists of an input pad, an amplifier and a discriminator [179]. A schematic of the Timepix3's analog pixel electronics is shown in Figure 4.2. The incoming charge is collected or induced on the input pad which covers 5% of the active surface. Then the signal is amplified before being sent to the discriminator. If the charge is above the threshold, the signal is registered by the digital part.

The amplitude of the signal or the amount of incoming charge is measured in terms of the ToT. The signal amplitude is proportional to the time required to discharge the capacitor connected to the input pad. Leakage current compensation is provided by the Krummenacher feedback network [180]. Its current setting  $I_{\text{Krum}}$  controls the discharge rate of the capacitor. For the GridPix detectors in this thesis,  $I_{\text{Krum}}$  is set to the lowest operable setting of 5 counts, corresponding to 1.2 nA, as this results in the slowest discharge and thus the most precise amplitude measurement for small signals. Through a 3 nF capacitor a series of test charges can be injected on the pixel pad. With this procedure the relation between charge and the ToT can be obtained, as described in subsection 4.2.2.



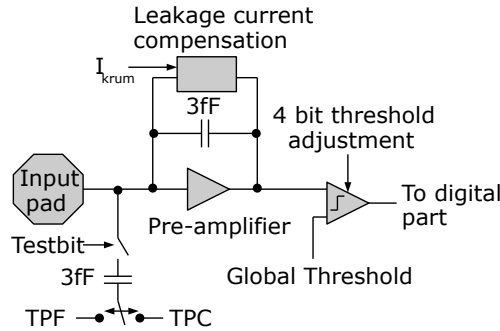


Figure 4.2: Scheme of the analogue part of a single Timepix3 pixel. The fine and coarse test pulse potentials are indicated with TPF and TPC respectively.

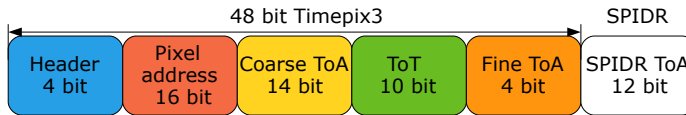


Figure 4.3: Layout of a Timepix3 data packet in the fine ToA/ToT mode after processing by the SPIDR readout.

Every detected signal or hit is registered by the digital part in its own data package, see Figure 4.3. The digital part of the Timepix3 has 3 pixel acquisition modes, but for this thesis it is only operated in the fast ToA/ToT mode. In this mode, a hit starts the 640 MHz clock, and the number of ticks until the next rising edge of the 40 MHz clock is the 4 bit fine ToA. The time of the global 40 MHz clocks is the 14 bit coarse ToA. The number of rising edges of the 40 MHz clock that occur until the signal is below threshold again defines the 10 bit ToT.

The SPIDR board reads out the Timepix3 chip [181]. A Timepix3 data packet contains 48 bits of data, but the transfer takes 60 bits after 8b/10b encoding for stabilisation and error detection. The SPIDR readout board adds another 12 bit timestamp at the end, bringing the total packet data length to 60 bit. The data is transferred through links between the Timepix3 chip and the SPIDR board. Each Timepix3 chip connects up to 8 links with a maximal speed of 640 Mbps per link. The SPIDR readout board has up to 12 links with a maximal speed of 640 Mbps and flexibility in the number of links per chip. The maximal readout rate of one link is  $10.67 \times 10^6$  hits/s.

### 4.2.1 Threshold equalisation

After fabrication, there are tiny differences in the effective thresholds of pixels. To correct for unwanted per pixel variations, the per pixel threshold can be tuned by setting a 4 bit adjustment Digital to Analog Converter (DAC). The settings that minimize the spread in thresholds are found in the threshold equalisation procedure.

In the equalisation procedure, the adjustment value per pixel is tuned with respect to the noise floor. First a noise centre scan is performed to acquire the noise floor level for the minimal (0) and maximal (15) adjustment settings. This means that for both settings, the threshold value for which the pixel reaches the maximum hit rate is determined using a fit. The scan is performed for a single pixel for every 8 by 8 pixel matrix at the same time to avoid cross talk. An example histogram of the minimal and maximal scans for all pixels is shown in red and blue in Figure 4.4. Then, the adjustment values are set such that the threshold levels of the noise floor will be as close as possible. The result of a noise scan with these adjustment values is shown in black, and has a much smaller variation than the results of the noise scan prior to the equalisation.

The detection threshold is set by adding the desired charge or potential in DAC counts (0.5 mV per DAC step) to the threshold. For the chip in the Figure 4.4, setting the detection threshold to about 515 e implies setting the threshold value 515 e, or 55 DAC counts, above the noise level of 318 DAC counts.

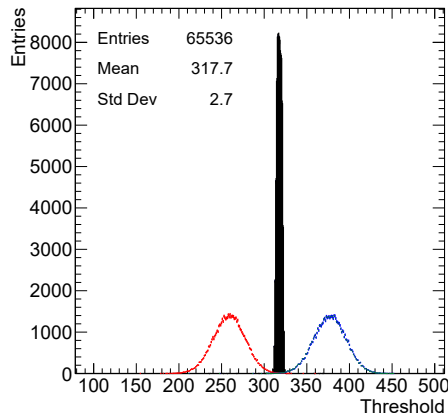


Figure 4.4: Example output of the threshold equalisation procedure for a chip in the quad detector. The distribution shows the threshold value corresponding to the noise floor for all adjustment values at 0 (blue), at 15 (red) and at the equalised value (black).

### 4.2.2 ToT–charge calibration

The Timepix3 can measure the charge indirectly using the ToT of a signal. The corresponding charge for the ToT can be found using a scan with test pulses (see e.g. [182, 183]). A test pulse is the injection of a known amount of charge into the pixel input pad. The injection is performed for only a few pixels at the time, to avoid influence from cross talk .

The charge is injected using a capacitor. As shown in Figure 4.2, the capacitor connects the pixel pad to an input that can switch between two controllable voltages: a coarse test pulse voltage that is controlled in coarse steps and is kept at a fixed level during the scan, and a fine test pulse voltage that is controlled in finer steps and over which the scan is performed.

An amount of charge proportional to the voltage difference is injected in both switching back and forth between the fine and coarse voltage. If the coarse voltage is higher than the fine voltage, negative charge is injected when switching from the coarse voltage to the fine voltage, and vice versa. This results in a curve for switching forth and a curve for switching back. The point of zero charge injection is halfway between the two curves.

An example curve is shown in Figure 4.5. The design capacitance of 3 fF and the design 2.5 mV per fine test pulse step of the Timepix3 are taken [167]. The charge is proportional to the ToT except for the values close to the threshold. The relation is fitted with the approximate function

$$\text{ToT} = aq + b - c/(q - t), \quad (4.1)$$

where  $q$  is the input charge, and  $a, b, c, t$  are parameters to be determined. This function, called a surrogate function, is utilised, because it can easily be inverted to determine the collected charge from the ToT, whilst providing a sufficient description of the data.

## 4.3 Properties of a GridPix detector

In this section we discuss some properties relevant for the operation of a GridPix detector.

### 4.3.1 Gas gain of the GridPix

The gas gain of a GridPix is the amplification factor that determines the signal strength. By approximation, the gain depends exponentially on the electric field strength which is in turn proportional to the grid potential. The gas gain is determined from the ToT of a signal, which is related to the total charge as shown in

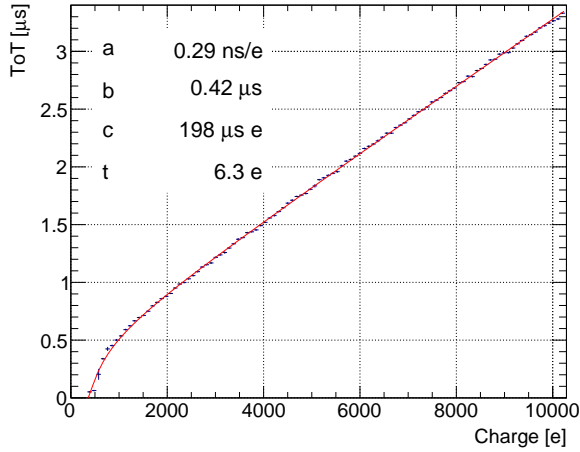


Figure 4.5: The charge–ToT curve for a pixel in the centre (at column 128 and row 128) of one of the chips on a quad. The Timepix3’s threshold was set to 515 e.

Figure 4.5. The mean ToT for four chips is shown in Figure 4.6 as a function of the grid voltage for both the T2K gas mixture and an isobutane/argon (18/82) gas mixture. The data are fitted with exponential functions, whose slopes are given in the legend. The exponential functions fit remarkably well, considering the translation from ToT to charge is not completely linear, and at the lower grid potentials the decreased detection efficiency distorts the mean. The exponential slope is around  $0.025 \text{ V}^{-1}$ , i.e. the gain doubles every 28 V.

### 4.3.2 Efficiency of a GridPix detector using source measurements

The detection efficiency of a GridPix detector is measured using a radioactive  $^{55}\text{Fe}$  source. The  $^{55}\text{Fe}$  isotope decays to  $^{55}\text{Mn}$  by K-shell electron capture, which causes the emission of X-ray photons (see e.g. [168]). The  $K_{\alpha 1}$  and  $K_{\alpha 2}$  photons have an energy of 5.90 keV and the  $K_{\beta}$  photon has an energy of 6.49 KeV. The most probable cluster size in the spectrum, which corresponds to the  $K_{\alpha}$  photon peak, is 219 electron pairs in the T2K gas mixture and 229 electron-ion pairs in the isobutane/argon (18/82) gas mixture [184, 185]. The efficiency is the ratio of the number of detected electrons to the total number of electron-ion pairs from ionisation.

An electron can be detected if the amplified signal is above the threshold. At low gain, only a fraction of the amplified signals is above threshold. Therefore, the efficiency depends on the grid potential. In Figure 4.7 the number of hits is plotted against the mean ToT for different grid potentials. The gain can be given as function of the mean ToT.

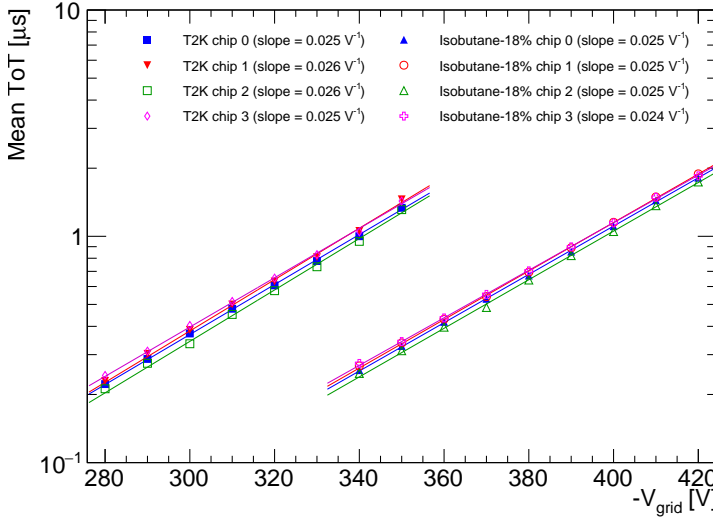


Figure 4.6: The mean ToT as a function of the negative grid potential  $-V_{\text{grid}}$  for the four chips in a quad using T2K gas mixture and using an isobutane/argon (18/82) gas mixture. The graphs are fitted with an exponential, the slope of which is given in the legend. The Timepix3's threshold was set to 515 e.

An expression for the single electron detection efficiency  $\epsilon$  is found by integrating the Polya distribution  $P(n, \theta)$  of amplified charge in Equation (3.11), starting from a threshold value  $t$  [186]. The efficiency becomes

$$\epsilon = \int_t^{\infty} P(n, \theta) dn = \frac{\Gamma(\theta + 1, (\theta + 1)\frac{t}{\bar{n}})}{\Gamma(\theta + 1)}, \quad (4.2)$$

where  $\Gamma(\theta + 1, z)$  is the upper incomplete gamma function. Assuming that  $\theta$  is independent of grid potential, and multiplying the efficiency by a constant representing the total number of hits, the expression can be fitted to the curve of the isobutane/argon (18/82) gas mixture as is shown in Figure 4.7. The fitted curve asymptotically goes to 220 electron-ion pairs, which is less than the expected 229 electron-ions per cluster. The discrepancy might be explained by saturation of the readout, acceptance of the detector, or oxygen and water contamination in the gas. For the grid potential at  $-420$  V, which corresponds to the highest gain, the efficiency is close to 100 %.

The same curve is made for the T2K gas mixture. For equal gain, measured in terms of ToT, the single electron efficiency is expected to be independent of the gas composition. At a given mean ToT, the efficiency for the T2K gas mixture is the

same as for the isobutane/argon (18/82) gas mixture. However, because of the lower share of the quenching isobutane in the T2K gas mixture, UV photons created in the avalanches can free electrons from the grid through the photo-electric effect and cause new avalanches up to a few pixels away [187]. This effect explains the data points for the T2K gas mixture at high gain in Figure 4.7. The number of hits from UV photons can be determined by comparing it to the measurements for isobutane/argon (18/82) gas mixture. For low gain with a grid voltage up to  $-300$  V the points are close to the curve for isobutane/argon (18/82) gas mixture, but at a higher grid voltage and higher gain there are more hits detected than ionisation clusters made.

For example, using the T2K gas mixture and a grid voltage of  $-330$  V, the most probable number of detected hits is 275. While for a gain corresponding to a mean ToT of  $0.78$   $\mu\text{s}$  the efficiency from the isobutane/argon (18/82) gas mixture curve is 89%, which would be 195 hits in the T2K gas mixture. Hence, there are 80 hits expected from UV photons. So for the T2K gas mixture at grid voltage of  $-330$  V, the efficiency is estimated to be 89% and there are 29% extra UV photon hits.

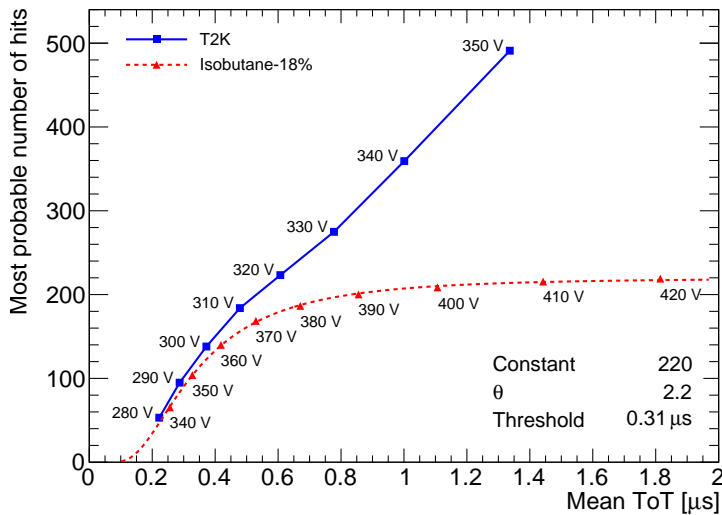


Figure 4.7: Number of hits per cluster from an  $^{55}\text{Fe}$  source for a T2K gas mixture (blue squares) and an isobutane/argon (18/82) gas mixture (red triangles). The values next to the data points indicate the negative grid potential ( $-V_{\text{grid}}$ ). The points of the isobutane-18 are fitted with Equation (4.2) shown with a red dashed line, and the points for the T2K gas mixture are connected with blue straight line segments. The Timepix3's threshold was set to 515 e.

### 4.3.3 Ion backflow

The IBF introduced in subsection 3.3.2 is an important parameter for the operation of a TPC. The IBF can be approximated using the GridPix geometry and field configuration [168]. The ions created in the amplification region of the gas have a transverse spread  $\sigma_T$  and drift approximately along the electric field lines. The electric field configuration is similar to the electric field lines of the Micromegas, as shown in Figure 3.8. Most of the electric field lines from the anode end on the grid, but a few run through the holes, and end on the cathode. The number of ions drifting through the grid is proportional to the ratio of the electric field strength in the drift region  $E_{\text{drift}}$  and in the amplification region  $E_{\text{amplification}}$ . It also depends on the spread of the ions under the grid and the hole pitch, which can be expressed as the ratio of  $\sigma_T$  and the hole pitch of the grid  $p$ . The IBF is then given by

$$\text{IBF} \propto \frac{E_{\text{drift}}}{E_{\text{amplification}}} \left( \frac{p}{\sigma_T} \right)^2. \quad (4.3)$$

From the IBF measurements of reference [168] for various grids fabricated on top of substrates, the IBF for a Timepix3 based GridPix can be estimated. For a drift field of 280 V/cm and a grid voltage of  $-340$  V, the interpolated IBF is 2.2%.

The drift of ions is investigated using a setup with 8 quad detectors [188]. A large amount of ionisation is produced using an intense nitrogen UV laser beam. By carefully monitoring the induced potential on the cathode, the ion drift is detected. From measurements with and without gas gain, the primary ion contribution can be separated from the backflowing ions. The grid current is monitored to determine the gain.

The ion drift velocity at a drift field of 280 V/cm is 2.8 m/s, which is slightly higher than the expected 2.2 m/s as given in Section 3.5.2. For a grid potential of  $-340$  V, the IBF is 1.3%. The difference with the previous measurement can possibly be explained by the difference in gas mixture, the grid sitting on a chip instead of a plain substrate, or the amount of ionisation. In the measurements with the 8 quad detectors, there were about 8 electrons per pixel.

### 4.3.4 Resistivity and charging up of the protection layer

In high rate applications, the high-resistive protection layer receives a large amount of charge. Because of the high resistivity of the layer, the protection layer can charge up. This causes a reduced electric field in the amplification region, which decreases efficiency. Therefore the resistivity of the protection layer should be high enough to quench discharges, but still low enough to drain the charge quickly. The discharge current flows through the pixel pads, and therefore also depends on the effective

pixel pad surface coverage. The Timepix3 based GridPix is equipped with the same protection layer as the Timepix based GridPix despite the smaller pixel pad size of Timepix3 chip, so the charging up effects can be more severe.

The resistivity of the protection layer depends on the specific resistance of the protection layer material. The specific resistance  $\rho$  can be expressed as

$$\rho = \frac{A\Delta V}{Id}, \quad (4.4)$$

where  $I$  is the current flowing through the surface area  $A$ ,  $d$  is the thickness of the protection layer, and  $\Delta V$  the potential drop. These quantities can either be measured with a probe, or be determined through the relation between the grid current and the rate.

### Measurement of the resistivity with a a probe

With a probe the resistivity is measured directly. A probe measures the current through a Timepix3 chip with a protection layer but without grid as a function of the potential difference across the layer. The probe consists of an 8 mm diameter stainless steel disk, and usually makes contact with the chip through a thin film of liquid mercury. However, this did not yield the expected results, probably due to the uneven chip surface and the high surface tension of the mercury. Instead, a soap solution in water was used as a conducting fluid.

The device is used to perform a series of current-voltage ( $I\Delta V$ ) measurements, which are converted to a specific resistance using Equation (4.4) where the thickness of the protection layer is  $d = 4 \mu\text{m}$  and the surface area is that of the probe taking into account the effective pixel pad surface coverage of 7%. The measurements are shown in Figure 4.8. The specific resistance of the insulator depends on the potential across the layer because of the Poole-Frenkel effect [189].

### Measurement of the resistivity through current measurements

The resistivity can also be determined indirectly through detector current measurements (see e.g. [166]). The resistivity is determined by measuring the gas gain before and after the protection layer is charged up. The grid current is measured as a proxy for the gain in two scenarios: starting from a situation without an external ionisation source the current is measured during the first few laser shots, and the current is measured again after a few minutes of irradiation with a pulsed nitrogen laser at a fixed rate of 2.5 Hz. The irradiated part of the surface is about  $1 \text{ cm}^2$ , with an effective pixel pad coverage of 7%. The grid current starts out at about 12 nA, but drops rapidly and after about 1 minute the current remains stable at a value of 3 nA. So the gain drop is a factor 4.



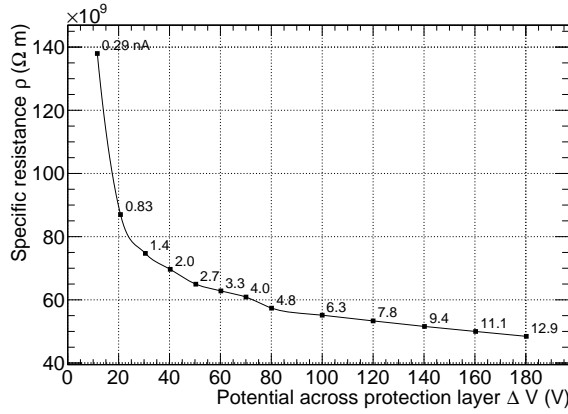


Figure 4.8: Measurement of the specific resistance of the protection layer material as a function of the potential across the protection layer. A smooth line is drawn through the data points to guide the eye. For each point the corresponding current  $I$  per chip is calculated and listed.

From these measurements the specific resistance can be calculated using Equation (4.4). The gain drop in the irradiated situation corresponds to a reduction in potential of about 56 V, see Figure 4.6. Substituting the observed values of  $I = 3$  nA,  $A = 0.07$  cm<sup>2</sup>,  $d = 4$   $\mu$ m and  $\Delta V = 56$  V, results in a specific resistance of about  $3 \times 10^{10}$   $\Omega$  m. This is of the same order of magnitude as the probe measurement of  $6 \times 10^{10}$   $\Omega$  m. Reference [166] gives a similar value of  $3.4 \times 10^{10}$   $\Omega$  m using a source, but a higher value of  $3 \times 10^{11}$   $\Omega$  m in a 200 kHz cm<sup>-2</sup> beam.

### Maximum detection rate

From the measured resistivity the maximum rate can be derived. If the maximum allowed potential drop is chosen to be 10 V, Equation (4.4) sets the maximum current at about 0.3 nA. With a gain of 2000, this equals a maximum of  $10^6$  incoming electrons per second. If a MIP frees about 100 electrons/cm in a TPC with a T2K gas mixture, the GridPix readout can handle MIPs tracks parallel to the detection surface at a rate of up to 6 kHz. The charging up of the protection layer takes seconds, so gain variations can occur if the amount of incoming charge varies on the same timescale. The 10 V voltage drop results in a reduction of the efficiency, which is a few percent for a gain of 2000.

### Tuning of the protection layer resistivity

For higher rate applications or in variable situations that require a constant gain, a lower resistivity of the protection layer is necessary to reduce the potential drop across the protection layer. In reference [166], the resistivity of the 4  $\mu\text{m}$  thick SiRN protection layer was too high for a beam with a rate of 200  $\text{kHz cm}^{-2}$ . For applications with a particle rate of up to 1  $\text{MHz cm}^{-2}$  the author of [166] roughly estimates the desired resistivity value to be  $10^7 \Omega \text{ m}$ . Here it estimated that for a beam with incoming particles parallel to the chip surface at a rate of up to 1  $\text{MHz}$  and a gain of 2000, the expected grid current is about 50 nA. To limit the voltage drop to 1 V, a desired resistivity of about  $10^8 \Omega \text{ m}$  follows from Equation (4.4) with  $A = 0.14 \text{ cm}^2$  and  $d = 4 \mu\text{m}$ . Because the resistivity depends on the electric field, this is orders of magnitude from the measured specific resistance at small potentials across the protection layer as shown in Figure 4.8.

In reference [190] it is described how the resistivity of a 1  $\mu\text{m}$  SiRN layer is tuned in the range  $2 \times 10^{10} \Omega \text{ m}$  to  $1.4 \times 10^{13} \Omega \text{ m}$ . The author also provided a 4  $\mu\text{m}$  thick SiRN protection layer with a 25 times lower resistivity. Recently, in the fabrication process of 2  $\mu\text{m}$  thick layers varying the silane ( $\text{SiH}_4$ ) flow, plasma frequency, and plasma intensity were investigated [191]. All samples yielded worse performance than the control sample except one, which requires further investigation. Alternatively a chip with a larger pixel pad size, possibly with the same pixel pitch, can help reduce charging up effects.



---

## Performance of a GridPix detector

---

This chapter describes the first beam test of a Timepix3 based Gridpix, measuring its performance using 2.5 GeV electrons. The main advantage of the Timepix3 chip over its predecessors is the higher rate capabilities and the simultaneous measurement of both ToA and ToT, allowing for a time walk correction to improve the longitudinal resolution. In the design of the detector, special attention has been given to minimise the distortions in the pixel plane and drift direction in order to meet the tracking precision needed for applications at a future collider. The detector is sensitive to single ionisation electrons in the gas, allowing for a precise energy loss  $dE/dx$  measurement for particle identification purposes.

Parts of this chapter were published in a paper [25], copyright Elsevier (2018) and proceedings [192].

### 5.1 Description of the GridPix device

In Figure 5.1 a cross section of the GridPix detector ( $14.1 \text{ mm} \times 14.1 \text{ mm}$ ) located in a small drift volume is shown. The box, shown in Figure 5.2, has a length of 69 mm, a width (not shown) of 42 mm and a height of 28 mm with a maximum drift length of about 20 mm. The beam enters the drift volume through the 5 mm thick synthetic window from the right side. The electric drift field is defined by a series of parallel conductive strips in the cage and is set to a drift field of about 280 V/cm. On the guard plane – located 1 mm above the grid – a voltage is applied that matches the local drift voltage.

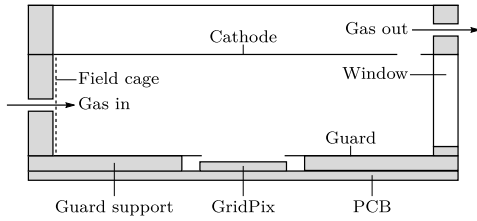


Figure 5.1: Schematic drawing of the GridPix detector.

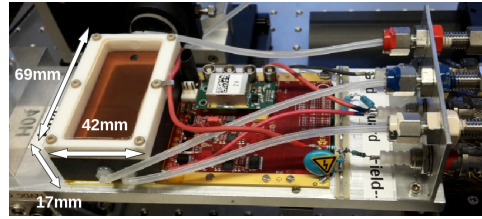


Figure 5.2: Picture of the GridPix detector with the gas volume dimensions indicated.

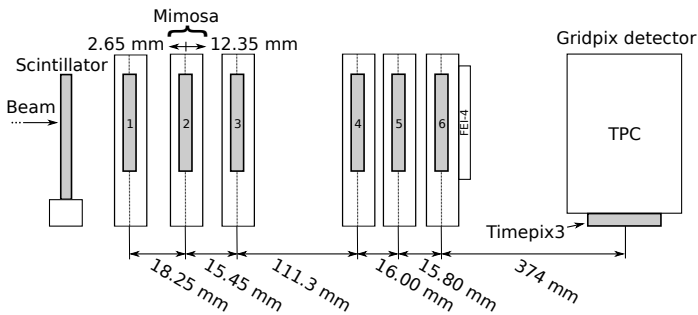


Figure 5.3: Setup with a telescope and GridPix detector.

## 5.2 Test beam measurement

In July 2017, measurements were performed at the ELSA test beam facility in Bonn. The ELSA storage ring delivered a beam of 2.5 GeV electrons at a rate set to a maximum of 10 kHz. Each beam cycle of approximately 6.5 s contained one spill of about 5 s. To acquire a precise reference track, a silicon pixel tracking telescope was introduced in the setup as shown in Figure 5.3. Electrons from the beam first passed through a scintillator that was used to provide a trigger signal. This was followed by the tracking Mimosa telescope [193], consisting of 6 silicon detection planes mounted on a slider stage with each  $1152 \times 576$  pixels sized  $18.4 \mu\text{m} \times 18.4 \mu\text{m}$ . Finally, the beam crosses the gas volume of the GridPix detector. The whole GridPix detector was mounted on a remote controllable rotation stage. The beam was perpendicular to the drift direction and at a 17 degrees angle with the chip edges. On the last telescope plane an inactive FEI4 chip [194] with a material budget of approximately  $1.5\% X_0$  was present that caused multiple scattering of the beam corresponding to a r.m.s. of 0.25 mm at the GridPix detector.

Both the Mimosa telescope and the Timepix3 chip were operated in data driven

mode. For synchronisation, triggers were numbered by a Trigger Logic Unit (TLU) [195] and saved in the two data streams. The Mimosa chips were continuously read out with a rolling shutter taking  $115.2\ \mu\text{s}$ , meaning that a single frame can contain multiple triggers. The Timepix3 hits are attributed to a single trigger by considering all hits within  $400\ \text{ns}$  of a trigger.

During data taking the gas volume of the GridPix detector was flushed with a premixed T2K gas, see subsection 3.5.2. However due to an error in the gas mixing, there might have been too little  $\text{CF}_4$  and too much  $\text{iC}_4\text{H}_{10}$ . The cathode and guard voltage of the GridPix were set such that the electric field was  $280\ \text{V/cm}$ , near the value at which the drift velocity is maximal for the T2K gas mixture, see also subsection 3.2.1. With Magboltz the drift velocity is predicted to be  $(78.86 \pm 0.01)\ \mu\text{m/ns}$  [196], but a mixture with a lower  $\text{CF}_4$  content has a smaller drift velocity. To achieve a high efficiency, the grid voltage was set at  $350\ \text{V}$ . The threshold per pixel was put at  $750\ e^-$  (80 DAC counts) to reduce the number of noise hits to a minimum. The temperature and pressure at the time of data taking were stable at  $301.6\ \text{K}$  and  $1034.20\ \text{mbar}$ . The Oxygen concentration in the gas was  $211\ \text{ppm}$ . In Table 5.1 the parameters of the analysed run are summarised.

Table 5.1: Parameters of the analysed run. The error on the grid current, the temperature, and the pressure indicates the spread during the run.

Run duration	60 minutes
Triggers	4 733 381
$V_{\text{grid}}$	350 V
$I_{\text{grid}}$	$(1.01 \pm 0.18)\ \text{nA}$
$E_{\text{drift}}$	$280\ \text{V/cm}$
Rotation (around $z$ -axis)	17 degree
Rotation (around $y$ -axis)	0 degree
Threshold	$750\ e^-$
Temperature	$(301.63 \pm 0.08)\ \text{K}$
Pressure	$(1034.20 \pm 0.05)\ \text{mbar}$
Oxygen concentration	211 ppm

For the setup, the  $x$ -axis is chosen parallel to the beam, and the drift direction is parallel to the  $z$ -axis. Apart from a rotation, the pixel column and row coordinates correspond to  $x$  and  $y$ , respectively. From the measured ToA of the Timepix3 hits, the  $z$ -position is calculated using the predicted drift velocity of  $78.86\ \mu\text{m/ns}$  for the T2K gas mixture. Because of the systematic uncertainties from electric field distortions and the scatter in the FEI-4 chip on the last telescope plane, there was no attempt to precisely measure the drift velocity.

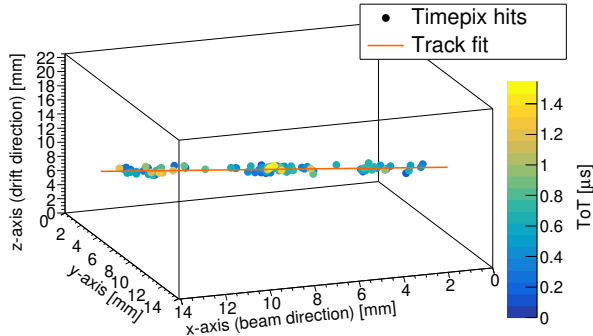


Figure 5.4: An example event with 108 GridPix detector hits including the time walk correction and the track fit (orange line).

## 5.3 Track reconstruction and event selection

The trajectory of the beam electron is reconstructed using the telescope and the GridPix detector. Triggers without a reconstructed track that satisfies the criteria given below, are rejected.

### 5.3.1 Track fitting

To reconstruct a track, the hits are fitted using a linear regression fit in  $y(x)$  and  $z(x)$ . Hits are assigned errors in the 2 directions perpendicular to the beam  $\sigma_y$  ( $= \sigma_{\text{plane}}$ ) and  $\sigma_z$  ( $= \sigma_{\text{drift}}$ ). This will be discussed in detail in Section 5.4.4 and 5.4.5.

To achieve an accurate reconstruction of the tracks, the telescope and the GridPix detector first have to be aligned. In an initial step, the positions of the 6 telescope planes are independently aligned. The planes are placed perpendicular to the beam, and their position along the beam is measured. The 5 rotations and  $4 \times 2$  shifts are iteratively determined from data by minimising the residuals. With the rotation and position of plane 2 fixed, and the position of plane 5 fixed, the other alignment parameters follow from the data. In the second step, the GridPix detector is aligned to the beam by rotating it along 3 axes and measuring the shifts in the directions perpendicular to the beam.

Since the telescope track is affected by multiple scattering, the most precise track fit is obtained by fitting the hits from the GridPix detector with the combined hits in the telescope. The hits in the telescope planes are merged in one reference point with a  $10 \mu\text{m}$  error at the centre of the last telescope plane. An example of GridPix hits with a fitted track is shown in Figure 5.4.

Table 5.2: Table with selection cuts.

Telescope
At least 4 planes hit
Reject outliers ( $> 700 \mu\text{m}$ )
Telescope track goes through TPC
GridPix detector
Hit ToT $> 0.15 \mu\text{s}$
At least 30 hits
Reject outliers ( $> 3\sigma_{\text{drift}}, > 2\sigma_{\text{plane}}$ )
At least 75% of total number of GridPix hits in fit
Track projection crosses first and last pixel column
Matching of telescope and GridPix detector
Tracks closer than 1 mm at centre of TPC
A unique track pair match

### 5.3.2 Selections

The performance of the detector is measured using events with one clean track in the GridPix detector and the telescope. Given the large amount of data collected, priority in the selection has been given to clean tracks over efficiency.

In the telescope we require the track to have hits in at least 4 out of the 6 planes. Moreover, the extrapolated telescope track should pass through the active volume of the TPC. For the GridPix detector we select hits that have at least a magnitude corresponding with a ToT of  $0.15 \mu\text{s}$  to reject the hits with the worst time walk error, see Section 5.4.3. A track is rejected if it has less than 30 GridPix hits. The GridPix track should pass through the whole TPC, that is the projection crosses both the first and last pixel column. After a first fit, the refit accepts only hits that are within  $3\sigma_{\text{drift}}$  and  $2\sigma_{\text{plane}}$ . Backgrounds and tracks with delta electrons are suppressed by requiring that at least 75% of all GridPix hits are used in the track fit and only one track is found. A telescope-GridPix track pair is defined as matched if the extrapolated telescope track is less than 1 mm away from the centre of the GridPix track. Events with an unmatched track pair or multiple matches (due to the rolling shutter) are rejected.

About 69% of the events pass all selection cuts. An overview of the selections is given in Table 5.2.



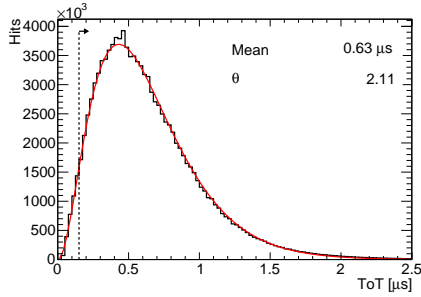


Figure 5.5: Distribution of the ToT from track hits. The arrow indicates the cut on hits with a ToT below  $0.15 \mu\text{s}$ . The curve is fitted with the Polya function (red line), defined in Equation (3.11).

## 5.4 Test beam results

From the selected data the performance of the GridPix detector is measured. The ToT distribution is used to approximate the gain. The gain determines the working point, and the number of hits. The Timepix3 chip allows for a time walk correction, which improves the resolution in the drift direction. Both the hit resolution in the drift direction, and the resolution in the pixel plane are discussed. In addition, the systematic deformations over the pixel plane are investigated. Finally, a discussion is given of energy loss measurements through both the truncated mean method and a method specifically for a GridPix readout.

### 5.4.1 Time over threshold and approximate gain

First, the ToT was found to vary as a function of the column number and therefore for each column a correction factor for the ToT is introduced. In Figure 5.5 the ToT distribution is shown. The ToT is roughly proportional to the collected charge. The fluctuation on the amplification of charge is discussed in subsection 3.3.1. Phenomenological, the Polya distribution given in Equation (3.11) multiplied by a normalisation constant provides a good fit to the data.

The mean ToT of  $0.63 \mu\text{s}$  can be translated to a collected charge by repeating the test pulse procedure discussed in subsection 4.2.2 for the applied threshold of  $750 e^-$ . The corresponding gain is found to be approximately 1700.

Comparing the mean ToT to the values from source measurements, the effective grid voltage is expected to be about  $-330 \text{ V}$ . The data was collected with a grid voltage set to  $-350 \text{ V}$ , but due to charging up effects the effective amplification voltage was lower, as discussed in subsection 4.3.4. From the measured grid current  $I_{\text{grid}}$  a

hypothetical, uniformly distributed, voltage drop of 8.5 V can be calculated. This is less than the voltage drop expected from the mean ToT, because the actual voltage drop varies over the chip due to the beam profile.

### 5.4.2 Number of hits on track

In Figure 5.6 the most probable number of hits is shown as a function of the grid voltage. One expects that the efficiency of the GridPix detector increases with the grid voltage until it reaches a plateau at an efficiency of almost 100 %, detecting all 100 electron-ion pairs/cm for the T2K gas [45]. The number of hits will continue to increase because of UV photons created in avalanches, as discussed in subsection 4.3.2. An even higher grid voltage will induce crosstalk, and far above 400 V, sparks would be produced.

The working point is determined from the mean ToT. The detection efficiency for single ionisation electrons is estimated using Figure 4.7. The measurements performed with a threshold of 515 e can be extrapolated to measurements at a higher threshold. The higher threshold reduces both the efficiency and the measured ToT by approximately 10 %. At the working point, the efficiency is approximately 80 % and there are about 25 % additional hits from UV photons produced in avalanches. So the two effects together should result in a number of hits that is slightly higher than the number of ionisation electrons.

In Figure 5.7 the number of detected GridPix hits associated to the track in the fiducial volume (216 pixels) is shown for a grid voltage of  $-350$  V. The most probable number of hits is 91 while the mean is 114 for an effective track length of 12 mm. About 8% of the hits from track ionisation is lost due to selection cuts. Still there are fewer hits than expected for the set working point, presumably because the gas contained slightly more of the quenching isobutane which reduces the amount of hits from UV photons.

Finally, previous studies using a Timepix based GridPix observed additional hits from crosstalk between pixels [165]. These hits were easily identified by their low ToT value. In this experiment, a search for double hits on neighbouring pixels did not yield any indication for crosstalk.

### 5.4.3 Time walk correction

A pixel hit is recorded when the collected charge is above the threshold. Because it takes longer to reach the threshold for a small signal than it does for a large signal, the measured ToA depends on the magnitude of the signal. This effect is called time walk. The capability to record simultaneously both ToA and ToT per pixel is one of the improvements of the Timepix3 chip over its predecessor, the Timepix chip. The

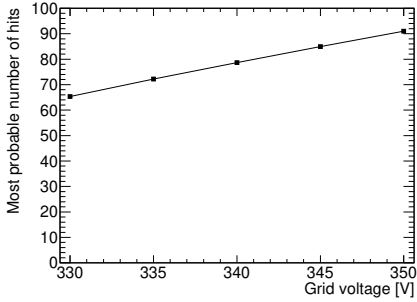


Figure 5.6: Most probable number of hits on the track as a function of grid voltage.

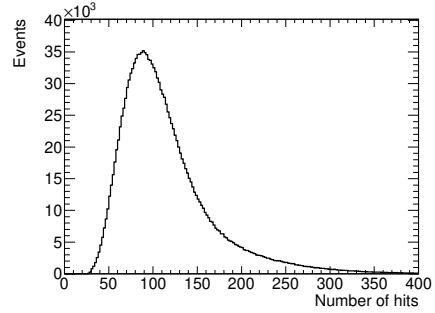


Figure 5.7: Distribution of number of hits on the track for a grid voltage of 350 V.

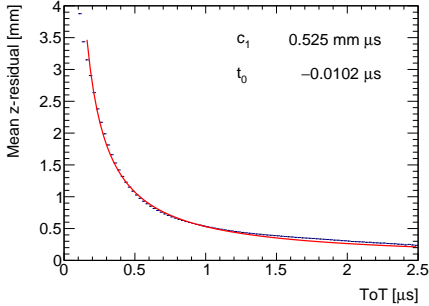


Figure 5.8: Mean  $z$ -residual without time walk correction as function of ToT, fitted with equation (5.1) (red line).

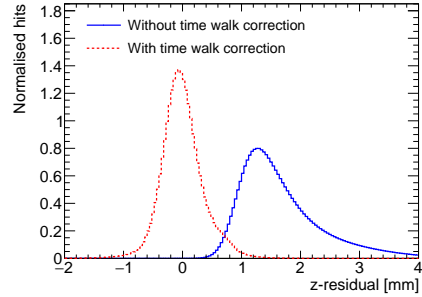


Figure 5.9: Distribution of  $z$ -residuals before (blue solid) and after (red dashed) time walk correction.

Timepix3 chip allows to correct for the time walk by using the ToT as a measure of the signal magnitude.

The uncorrected mean of  $z$ -residuals – defined as the difference of the  $z$ -position of the hit and the track fit prediction – is shown as a function of the corrected ToT in Figure 5.8. The relation can be parametrised using the time walk  $\delta z_{\text{tw}}$  as a function of the corrected ToT  $t_{\text{ToT}}$ :

$$\delta z_{\text{tw}} = \frac{c_1}{t_{\text{ToT}} + t_0}, \quad (5.1)$$

where  $c_1$  and  $t_0$  are constants to be determined from a fit. The distribution of  $z$ -residuals before and after applying the time walk correction is shown in Figure 5.9. Functions with additional degrees of freedom were also tried, but did not improve the results.

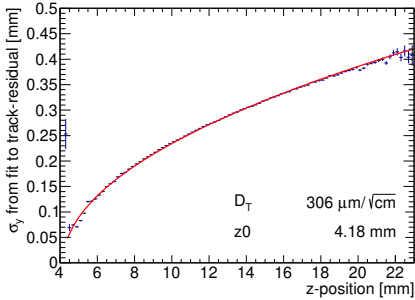


Figure 5.10: Measured hit resolution in pixel plane (blue points) fitted with the resolution according to equation (5.2) (red line), where the hit resolution at zero drift distance  $d_{\text{pixel}}/\sqrt{12}$  was fixed to  $15.9 \mu\text{m}$ .

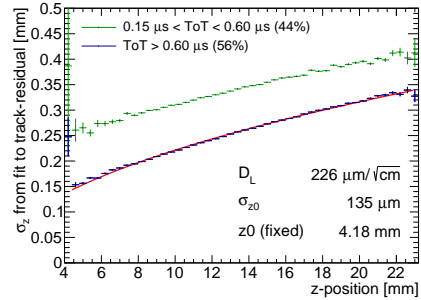


Figure 5.11: Measured hit resolution in drift direction split by ToT (green and blue points). The hits with a ToT above  $0.60 \mu\text{s}$  (blue points) are fitted with the resolution according to equation (5.3) (red line). In the legend the fraction of hits in both selections is given between round brackets.

#### 5.4.4 Hit resolution in the pixel plane

The momentum resolution of a TPC in an axial magnetic field depends on the hit resolution in the pixel plane. There are two important contributions to the hit resolution in this plane: a constant contribution caused by the pixel size  $d_{\text{pixel}}$  and a transverse drift component that scales with drift distance and the diffusion coefficient  $D_T$ , introduced in subsection 3.2.2. The resolution  $\sigma_y$  is given by:

$$\sigma_y^2 = \frac{d_{\text{pixel}}^2}{12} + D_T^2(z - z_0), \quad (5.2)$$

where  $z_0$  is the position of the grid. The measured hit resolution as a function of  $z$ -position is shown in Figure 5.10. In order to facilitate the fit, for each point an estimated systematic uncertainty of  $1 \mu\text{m}$  is added to the statistical uncertainty. The actual systematic uncertainty has not been determined, because of the multiple scattering in the telescope. With an improved telescope setup, the systematic error for a GridPix detector quad is determined in the next chapter. The diffusion gives the largest contribution to the hit resolution in most of the detector volume. The measured diffusion coefficient  $D_T = 306 \mu\text{m}/\sqrt{\text{cm}}$ , and is lower than the expected  $D_T = (318 \pm 7) \mu\text{m}/\sqrt{\text{cm}}$ . A potential cause is inaccuracies in the gas composition.

### 5.4.5 Hit resolution in the drift direction

The hit resolution in the drift direction is related to the ToA distribution. There are three contributions. A constant contribution from the Timepix3's time resolution  $\sigma_{\text{ToA}} = 1.56 \text{ ns}$  [24], a contribution from other noise sources such as jitter and time walk, and a contribution from longitudinal diffusion with coefficient  $D_L$ . The resolution  $\sigma_z$  is given by

$$\sigma_z^2 = \frac{\sigma_{\text{ToA}}^2 v_{\text{drift}}^2}{12} + \sigma_{z_0}^2 + D_L^2 (z - z_0). \quad (5.3)$$

For an assumed drift velocity of  $v_{\text{drift}} = 78.86 \mu\text{m/ns}$ , the first term is  $(35.5 \mu\text{m})^2$ . The error from time walk contained in the second term is largest for small ToT, motivating a split of the hits roughly in half at a ToT value of  $0.60 \mu\text{s}$ . The hit resolution in the drift direction is shown in Figure 5.11. To each point an estimated systematic error of  $1 \mu\text{m}$  was added. The grid position was fixed to  $z_0 = 4.18 \text{ mm}$  found in the fit to Figure 5.10. The diffusion is found to be  $D_L = 226 \mu\text{m}/\sqrt{\text{cm}}$  with negligible statistical uncertainty. This is higher than the expected value of  $D_L = (201 \pm 5) \mu\text{m}/\sqrt{\text{cm}}$ , possibly due to deviations in the gas composition. The hit resolution at zero drift distance is  $139 \mu\text{m}$  for hits with  $\text{ToT} > 0.60 \mu\text{s}$  and  $168 \mu\text{m}$  if all selected hits are included.

### 5.4.6 Deformations

For a large TPC with pixel readout it is important that systematic deviations of position measurements are small and stay well below typically  $20 \mu\text{m}$ . Here we study deformations in the pixel plane and the drift direction, caused by for example distortions in the drift field or geometric uncertainties. The chip is divided in  $64 \times 64$  bins of  $4 \times 4$  pixels each for which the mean deformation is calculated. For every hit, the expected originating position on the track is taken and the residual is filled at that bin. In Figure 5.12 and Figure 5.14 the mean residual in the  $xy$ -plane and the mean  $z$ -residual are shown, respectively. In the diagram only bins with more than 1000 entries are shown.

The red and blue areas near the edge of the detector can be identified as deformations due to electric field distortions and edge effects. The partially broken column and wrinkle in the grid outside the boxed fiducial region, each distort the position measurement perpendicular to the track, but not in the drift direction. The wrinkle in the grid is indicated in the picture of the chip shown in Figure 5.13. Additionally in the bottom-left and bottom-right some tears in the grid are visible. Part of the distortions in the drift direction can be identified as small deviations in the ToA originating from the Timepix3 chip. This is due to the power distribution over the chip,

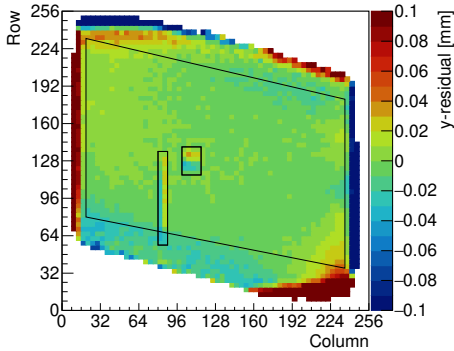


Figure 5.12: Mean residuals in the pixel plane at the expected hit position.

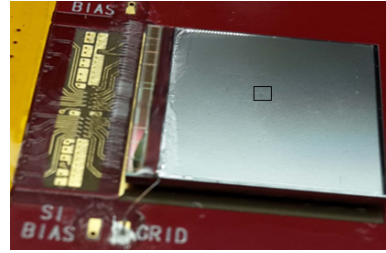


Figure 5.13: Picture of the GridPix with a visible wrinkle in the grid.

and tiny inhomogeneities introduced during the manufacturing of the chip.

Bins in the selected fiducial area were used to make the distribution of the mean residuals shown in Figure 5.15. The r.m.s. of the deviations is  $7\ \mu\text{m}$  in the pixel plane and  $21\ \mu\text{m}$  ( $0.3\ \text{ns}$ ) in the drift direction, respectively. This implies that the systematics on the position measurement in the pixel plane - the bending plane of the TPC - are less than  $10\ \mu\text{m}$ . In order to achieve the momentum resolution goal set for the ILD TPC of  $\sigma_{1/P_T} < 1 \times 10^{-4}\ \text{GeV}^{-1}$ , systematic effects should be under control to a level of better than  $30\ \mu\text{m}$  [197].

### 5.4.7 Energy loss measurement and particle identification

In a TPC particles can be identified using their characteristic energy loss. The GridPix detector measures the energy loss  $dE/dx$  by counting the number of detected electrons. Because of the large fluctuations of the energy loss as discussed in subsection 3.1.3, the mean is dominated by a few high energy deposits. In order to obtain a more reliable estimate, the truncated sum of electrons is calculated. Because of its high granularity and ability to measure individual ionisation electrons, a TPC with GridPix readout offers another method of estimating the energy loss  $dE/dx$ , which is discussed below.

#### Particle identification by a truncated sum

Along the track, the number of electrons is counted for intervals of a few pixels. A fixed fraction of intervals with the highest number of electrons is rejected. The resolution is expressed as the standard deviation divided by the mean of the truncated sum distribution. All hits in the 220 columns from 16 to 236 are used. The resolution was studied as function of the interval length and as function of the fraction used

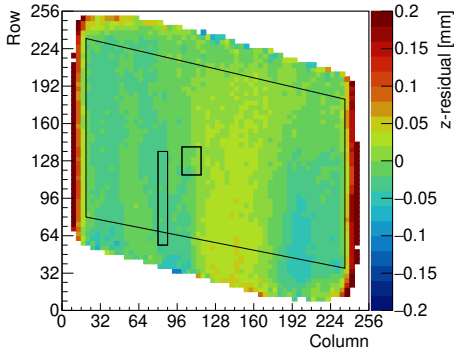


Figure 5.14: Mean residuals in the drift direction at the expected hit position.

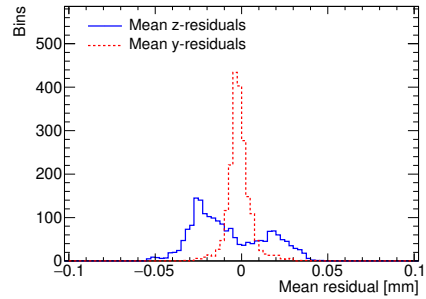


Figure 5.15: Distribution of the mean  $z$ -residuals (blue solid line) and  $y$ -residuals (red dashed line) from  $4 \times 4$  bins within the selected region.

for the truncated sum, shown in Figure 5.17 and Figure 5.16 respectively. Optimally, the top 10% of 20-pixel intervals with the highest number of detected electrons are rejected and from the other 90% of the 20-pixel intervals a truncated sum is obtained. In Figure 5.18 the distribution of the truncated sum is shown for an effective track length of 1 m or 79 events. For the optimal point, the resolution is 4.1%.

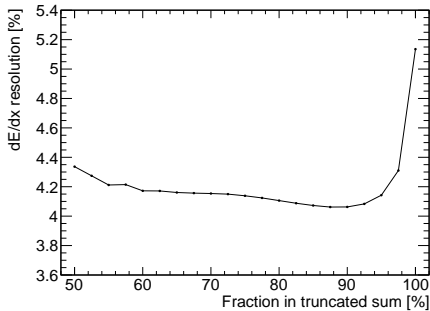


Figure 5.16:  $dE/dx$  resolution defined as the standard deviation divided by the mean as a function of the fraction of 20-pixel intervals in the truncated sum.

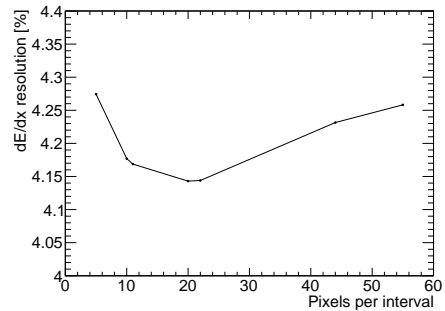


Figure 5.17:  $dE/dx$  resolution using a truncated sum of 90% of the intervals as a function of the interval length.

In order to estimate the potential for particle identification, the energy loss distribution for a MIP is estimated, see also Figure 5.18. The hit positions of the electron data are scaled track by track by a factor 0.7 to acquire the estimated ionisation for a

MIP, i.e. 0.7 m of electron data is scaled to 1 m of expected MIP data. The expected resolution for a 1 m MIP track is 5.0%.

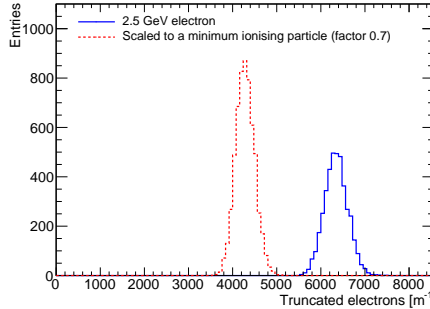


Figure 5.18: Distribution of the truncated sum of detected electrons per meter for the 2.5 GeV electron (blue solid line) and the expected distribution for a minimum ionising particle (red dashed line).

The ability of identifying particles by the detector can be expressed by the separation power  $S$  [198], defined as

$$S = \frac{\mu_e - \mu_{\text{MIP}}}{\sqrt{(\sigma_e^2 + \sigma_{\text{MIP}}^2)/2}}, \quad (5.4)$$

where  $\mu_e$  and  $\mu_{\text{MIP}}$  are the mean of the truncated sum for electrons and MIPs.  $\sigma_e$  and  $\sigma_{\text{MIP}}$  are the values of the standard deviation of the truncated sum for electrons and MIPs. Some authors use a definition that has the value of the standard deviation of either one of the two particles in the denominator, but this definition uses the average of both the standard deviations. The separation power  $S$  using a truncated sum for a 1 m long track of data is 8.6 standard deviations.

### Other methods for particle identification

The truncated sum using slices of 20 pixels, does not make full use of the fine granularity of the GridPix detector. Particle identification can be improved by employing the full resolution to resolve primary ionisation clusters [199]. In the unattainable limit where all clusters are identified perfectly, the resolution is the width of a Poisson distributed number of clusters, which is 2% for a 1 m MIP track having about 2700 clusters [45] in the T2K gas mixture.

The weighted mean distance is a method that does make use of the full granularity of the pixel detector. It is calculated by taking the weighted mean of the distance between pixel hits along the track. The distance distribution is shown in Figure 5.19



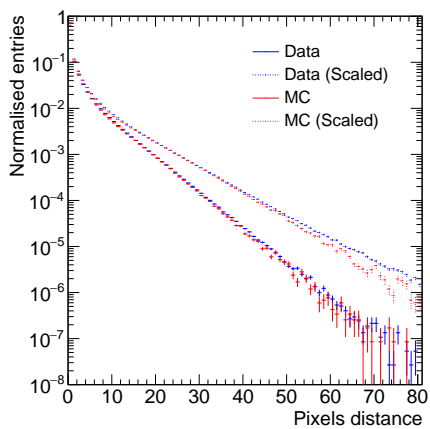


Figure 5.19: Distribution of distance between hits for a 2.5 GeV electron in pixels from test beam data (blue) and from a Monte Carlo simulation (red).

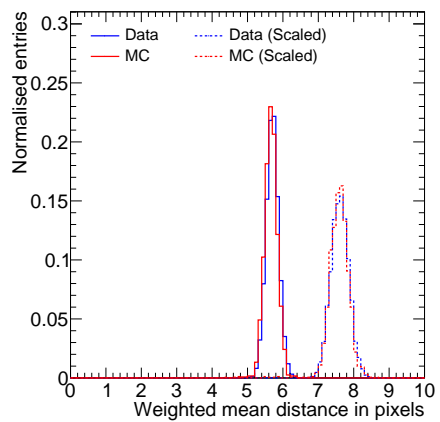


Figure 5.20: Weighted mean as described in the text for a 2.5 GeV electron from data (blue solid line) and Monte Carlo simulation (red solid line) and for a MIP from scaled data (blue dashed line) and Monte Carlo simulation (red dashed line).

in terms of pixels. The distance is also calculated with data from a simulation, which serves as a qualitative cross check.

The simulation of electrons at a  $5^\circ$  angle in GEANT4 [200] has layers of gas with a thickness equal to the pixel pitch. In order to match the simulated data to our test beam data the parameters `Tmax` and `r` of the `G4UniversalFluctuation` model and the electron conversion threshold were tuned to 3 keV, 1 and 27 eV respectively. In accordance with the expected working point, the efficiency was simulated to be 80 % and, around the initial hits, 25 % additional hits were generated to simulate hits caused by UV photons. These hits were displaced from the initial hits according to a Gaussian distribution with a standard deviation of 4 pixels.

The weighted mean distance for a track is calculated using

$$\text{weighted mean distance} = \frac{1}{N_{\text{hits}} - 1} \sum_{i=1}^{N_{\text{hits}}-1} w(d_i)d_i, \quad (5.5)$$

where  $N_{\text{hits}}$  is the total number of hits,  $d_i$  is the distance between subsequent hits in the direction along the track and  $w(d)$  is the weight as function of the distance. To the distribution in Figure 5.19 an exponential distribution is fitted in the range between 20 to 100 pixels distance. The assigned weights are the expected number of hits from the exponential distribution divided by the actual number of hits. The effect is that hits at short distances, which are more likely to come from the same cluster, get a small weight, and hits at larger distances, which are more likely to come from separate clusters, get a larger weight.

The weighted mean distance for an electron from data and simulation and a MIP from scaled data and simulation is shown in Figure 5.20. The resolution, again expressed as standard deviation divided by the mean, with this method is 3.1 % for an electron and 3.3 % for a MIP. However, because the weighted mean distance is not proportional to the energy loss this is not the most relevant measure. One can compare the method to the truncated sum using the separation power  $S$ . The separation power  $S$  for a 1 m long track of data is 8.7 standard deviations using the weighed mean distance, which is comparable to the separation of the truncated sum. A weighted combination of the truncated sum and the weighted mean distance has a combined separation power of  $S = 9.2$  standard deviations for a 1 m electron and MIP track.

## 5.5 Conclusions

A GridPix detector based on the Timepix3 chip was operated reliably in a test beam setup for the first time. In the pixel planes and in the drift direction the resolution of the detector is limited primarily by diffusion. The additional systematic uncertainties in the pixel plane are smaller than  $10 \mu\text{m}$ . Furthermore, by counting the ionisation

electrons, the energy loss  $dE/dx$  can be measured with a precision of 4.1% for an effective track length of 1 m. For particle identification the fine granularity of the pixel chip is beneficial. In the next chapter, a building block for larger size detectors is presented.

# Performance of the Gridpix detector quad

---

The single chip detector described in the previous chapter was operated reliably in a test beam experiment. For applications at a future collider, it is necessary to equip a large detector with a GridPix readout, which poses an entirely new challenge. In order to cover a large surface, it is practical to subdivide it into a number of standard building blocks or modules. Here we present the design of a quad module with four Timepix3 chips. Because the quad module has almost all services underneath its active area, it can be tiled to cover arbitrarily large areas with minimal inactive boundary regions.

The performance of a TPC consisting of a gas volume read out by a single quad module, was tested at the ELSA test beam facility in Bonn. With an improved setup of the telescope, the distortions and systematic errors in the drift direction and in the pixel plane could be determined precisely. Parts of this chapter were published in a paper [26], copyright Elsevier (2020).

## 6.1 Quad detector design and construction

A single quad module with four Timepix3 based GridPixes is designed, constructed and installed in a small drift volume with a field cage to make a TPC.

### 6.1.1 The quad module design and assembly

In order to cover large areas, the quad module shown in Figure 6.1 was developed. Because of the complexity of the GridPix technology and the fragility of the grids, a small number of four chips per module was chosen as a compromise. The chips are mounted on a common cooled base plate (COCA). They are electrically connected by wire bonds to a 6 mm wide PCB between the two pairs of chips. This allows the control and output lines to be directed to the backside of the quad to maximise the sensitive detection area. A short Kapton cable at the other side of the wire bond PCB provides a low impedance connection to the low voltage (LV) regulator. The grids are connected by 80  $\mu\text{m}$  diameter insulated copper wires to a high voltage (HV) filtering board. The connection to the common HV input uses a 100 M $\Omega$  resistor for each grid to rapidly quench a micro-discharge. To mount and cool the LV regulator board and the HV filtering board, a U-shaped support is attached by thermally conductive glue under the carrier plate. Finally, the wire bonds of the quad are covered by a 10 mm wide central guard electrode located 1.1 mm above the grids to maintain a homogeneous drift field.

The external quad dimensions are 39.6 mm  $\times$  28.38 mm of which 68.9% is active. In the present design the support components are made of aluminium contributing substantially to the material budget. If quad modules are used to read out the ILD TPC, these components are located directly in front of the end cap calorimeters. In the future the material budget can be minimised by replacing the aluminium by carbon based materials. The module consumes about 8 W of power in total of which 2 W is utilised by the LV regulator.

### 6.1.2 The quad detector

The quad detector is a TPC consisting of a single quad module, embedded in a steel box and a 40 mm high field cage to provide a homogeneous drift field. The sides of the field cage are formed by 75  $\mu\text{m}$  diameter CuBe wires with a 2 mm pitch to facilitate UV laser beam measurements. The field cage is terminated on one end by the quad module, fitted in a closely surrounding coppered frame at the grid potential, and on the other end by a solid cathode plate. The whole structure was put in a gas-tight container with 50  $\mu\text{m}$  Kapton windows on two sides to minimise the material traversed by the beam.

## 6.2 Test beam measurement

The device was tested in October 2018 at the ELSA test beam facility in Bonn. The ELSA accelerator provided 2.5 GeV electrons at a rate of approximately 10 kHz

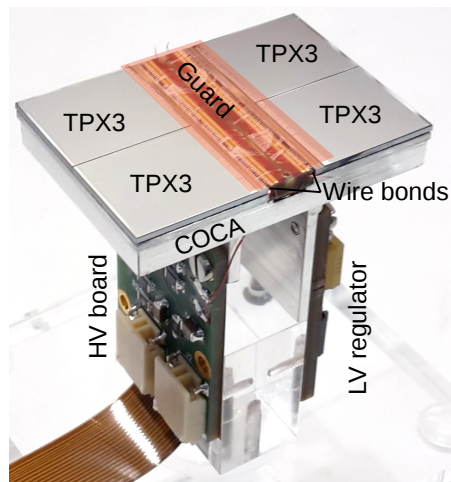


Figure 6.1: Picture of the quad detector with four Timepix3 GridPixes (TPX3) mounted on a cold carrier plate (COCA). The central guard was omitted to show the wire bond PCB, and its operating position is indicated with a transparent rectangle. On the left the high voltage (HV) board and flexible Kapton cable are visible and on the right the low voltage (LV) regulator can be seen.

during spills of 16.0 s in beam cycles of 17.1 s. The quad detector was mounted on a remotely controlled slider stage. To provide a precise reference track, the quad TPC was sandwiched between  $2 \times 3$  planes of a Mimosas26 telescope [193], see Figure 6.2 and Figure 6.3. Each plane consists of a MAPS detector with  $1152 \times 576$  pixels of size  $18.4 \mu\text{m} \times 18.4 \mu\text{m}$ .

A scintillator provided a trigger signal to the Trigger Logic Unit (TLU) [195] which numbers the triggers and subsequently directs them to both the SPIDR and telescope readout. The telescope hits were collected in time frames of  $115.2 \mu\text{s}$ . Due to the high beam intensity, the telescope frames often (22%) contain hits from more than one track.

The quad's Timepix3 was operated in data driven mode with the trigger data merged in. For the readout, one out of the eight available links per chip is connected to a speedy pixel detector readout (SPIDR) board [181] at a speed of 80 Mbps. The hardware is also capable of reading out at twice this speed.

Because of the chosen limited link speed between the Timepix3 chips and the SPIDR, a maximum of 1.3 MHits/s could be read out. This caused the majority of the hits to arrive late at the SPIDR readout, acquiring a wrong  $409.6 \mu\text{s}$  coarse timestamp. As a workaround, hits up to 200 timestamps of  $409.6 \mu\text{s}$  after the trigger were collected and analysed. The first track hit had to arrive no more than 5 timestamps late, and the average coarse timestamp should not deviate more than 150 timestamps from the trigger.

During data taking the 700 ml gas volume was flushed at a rate of 1.01/h with premixed T2K gas. This gas is a mixture consisting of 95% Ar, 3%  $\text{CF}_4$ , and 2%  $\text{iC}_4\text{H}_{10}$  suitable for large TPCs because of the relatively high drift velocity and the low diffusion in a magnetic field. However, due to an inaccuracy in the gas mixing, the  $\text{CF}_4$  content was probably slightly lower than intended. The temperature and pressure were relatively stable at 300.5 K and 1011 mbar. The gas mixture contained an 800 ppm  $\text{O}_2$  contamination and a 6000 ppm  $\text{H}_2\text{O}$  contamination, primarily due to the high gas permeability of a silicon rubber cable feed-through.

The cathode and guard voltages were set such that the electric field was 400 V/cm, which is close to the maximum drift velocity for this gas. The threshold level being a trade off between noise, sensitivity and time walk, was set to 55 DAC counts or about  $515 e^-$ . The grid voltage was set to  $-330 \text{ V}$ , at which there is limited secondary emission from the grid by UV photons produced in avalanches (see Figure 4.7). The gain depends on the beam rate, because of charging up of the protection layer, as discussed in subsection 4.3.4. The grid current  $I_{\text{grid}}$  of  $0.8 \text{ nA/chip}$  corresponds to a uniform voltage drop of about 20 V. The actual voltage drop is not uniform, but varies within a chip due to differences in the incoming charge related to the beam profile. During the high beam rate, the mean ToT is  $0.60 \mu\text{s}$ . Therefore the effective grid voltage is about  $-320 \text{ V}$  as shown in Figure 4.6, and the effective gain is about

1000 as can be read off from Figure 4.5.

Some of the relevant run parameters are summarised in Table 6.1.

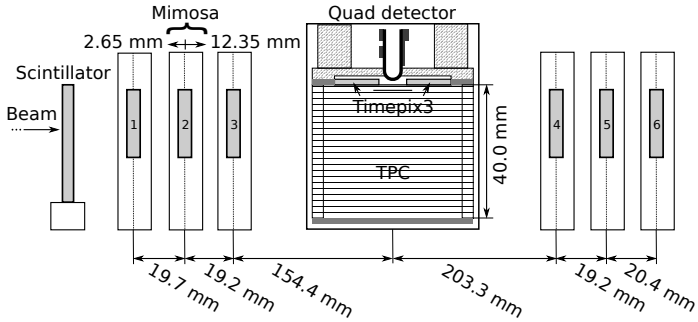


Figure 6.2: Setup of the quad with telescope at the ELSA test beam facility.

## 6.3 Track reconstruction and event selection

The track reconstruction proceeds similarly as for the single chip detector. Because of the readout problems discussed in the previous section, the selection is more stringent: the telescope track was used to select the corresponding hits in the quad detector.

### 6.3.1 Track reconstruction procedure

Tracks are reconstructed as straight lines. The  $y$ -axis is defined roughly in the direction of the beam, and the  $x$ -axis and  $z$ -axis are in the horizontal and vertical direction respectively. For the telescope, the  $y$ -coordinate is taken from the plane position, and

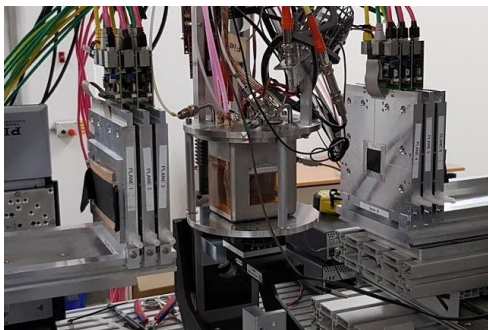


Figure 6.3: Picture of the setup at the ELSA test beam facility with quad detector, telescope and slider stages.



Table 6.1: Parameters of the three analysed runs. The error on the temperature and pressure indicates the spread during the time that the three runs were taken.

Runs duration	10 minutes
Triggers per run	$2.2 \times 10^6$ triggers
$V_{\text{grid}}$	330 V
$I_{\text{grid}}$ (per chip)	0.8 nA
$E_{\text{drift}}$	400 V/cm
Threshold	$515 e^-$
Temperature	$(300.5 \pm 0.13)$ K
Pressure	$(1011 \pm 0.16)$ mbar
Oxygen concentration	800 ppm
Water vapour concentration	6000 ppm

the  $x$ -coordinate and  $z$ -coordinate correspond to the columns and rows of the chips. Apart from a small rotation, the  $x$  and  $y$ -coordinates correspond to the columns and rows of the Timepix3 chips. The  $z$ -axis is in the direction opposite to the drift direction and the  $z$ -coordinate is calculated from the ToA and the drift velocity.

Linear track finding is performed for the telescope using a Hough transform in the  $xy$ -plane, which determines track candidates by votes in a parameter space. For every hit, a set of compatible track parameter pairs consisting of a track angle  $\theta$  and corresponding distance to the origin  $r_0$  are calculated. The most common parameters pairs in the range  $-0.01 \text{ rad} \leq \theta \leq 0.01 \text{ rad}$  and  $0 \leq r_0 \leq 20 \text{ mm}$  are taken as the track candidates. The quad GridPix hits are collected using a track detected by the telescope as a seed.

Tracks in the telescope and in the quad are fitted using a linear regression fit with hit errors in the two directions perpendicular to the beam  $\sigma_x$  and  $\sigma_z$ . The telescope hit errors are determined from the pixel size. The expressions for the GridPix error values are given in Sections 6.4.4 and 6.4.5.

The detectors are aligned using the data. First, the telescope is independently aligned. The positions in the  $y$ -direction along the beam are measured and kept fixed. Taking one plane as a reference, the other five planes can be rotated. These rotations and additionally two shifts in  $x$ -direction and  $z$ -direction for four of the planes are iteratively determined from the fitted tracks by minimising the hit residuals. Next, the quad detector is aligned. Using iterative alignment each chip has three rotations and two shifts in the  $x$  and  $z$ -directions. Additionally, because the drift direction is not necessarily perfectly perpendicular to the pixel plane, each chip has one parameter describing the angle in the  $xz$ -plane between the drift direction and the pixel plane.

An example event with a telescope track after the alignment procedure is shown in Figure 6.4.

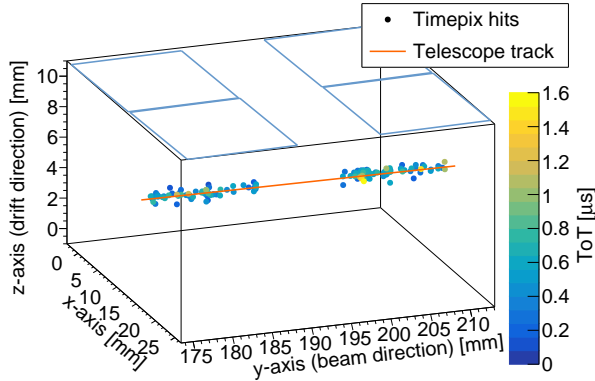


Figure 6.4: An event with 148 quad detector hits and the corresponding telescope track (orange line). The positions of the chips are outlined in blue.

### 6.3.2 Selections

In the telescope a stringent selection is made to acquire a sample of clean tracks. At least 5 planes should have a hit and the hits should be within  $50\ \mu\text{m}$  from the track. By requiring the slope difference of the track in the first three planes and in the last three planes to be smaller than  $1\ \text{mrad}$ , scattered tracks are rejected.

GridPix hits are considered if their ToA is within  $500\ \text{ns}$  of a trigger and their ToT is at least  $0.15\ \mu\text{s}$ . The hits are selected with the telescope track. Outliers are rejected by requiring the residuals  $r$  (pulls  $r/\sigma$ ) with respect to the telescope track to be smaller than  $1.5\ \text{mm}$  ( $2.0$ ) in the  $x$ -direction and  $2.0\ \text{mm}$  ( $3.0$ ) in the  $z$ -direction.

A track is rejected if it has less than 20 hits. Moreover the average position of all GridPix hits must be within  $0.3\ \text{mm}$  in the  $x$ -direction and  $z$ -direction of the telescope track. Given the high beam rate, the TPC often contains multiple tracks overlapping in time. To suppress overlapping tracks and to reject tracks with delta electrons, 80% of the hits within  $5\ \text{mm}$  of a track are required to lie within a distance of  $1.5\ \text{mm}$ .

The selections are summarised in Table 6.2 and the total event selection efficiency is about 12%. Most events are rejected because there are less than 20 GridPix hits corresponding to the telescope track.

## 6.4 Results

The performance is extracted similarly to the single chip detector in the previous chapter, but with the more precise telescope track, the hit residuals can be determined more accurately. The quad was designed to have minimal distortions and the

Table 6.2: Table with selection cuts

Telescope
Number of planes hit $\geq 5$ Reject outliers ( $r_{x,z} < 50 \mu\text{m}$ ) Slope difference between sets of planes $< 1 \text{ mrad}$
GridPix hit selection
$-500 \text{ ns} < t_{\text{hit}} - t_{\text{trigger}} < 500 \text{ ns}$ Hit ToT $> 0.15 \mu\text{s}$ Reject outliers ( $r_x < 1.5 \text{ mm}, r_z < 2 \text{ mm}$ ) Reject outliers ( $r_x < 2\sigma_x, r_z < 3\sigma_z$ )
Event Selection
$N_{\text{hits}} \geq 20$ $(N_{r_x < 1.5 \text{ mm}} / N_{r_x < 5 \text{ mm}}) > 0.8$ $ x_{\text{Timepix}} - x_{\text{telescope}}  < 0.3 \text{ mm}$ $ z_{\text{Timepix}} - z_{\text{telescope}}  < 0.3 \text{ mm}$

distortions can now be analysed with a higher accuracy. The overall quad position measurement precision is measured and some sources of measurement uncertainty are identified.

### 6.4.1 Number of hits

The expected number of hits at the working point is determined from the mean ToT of  $0.60 \mu\text{s}$  and Figure 4.7. At this operating point, the efficiency is expected to be 80% and there are about 20% of extra hits from UV photons. So the two effects cancel and the number of detected hits is expected to be about equal to the number of ionisation electrons. About 6% of these hits from track ionisation is lost due to selection cuts. The calculated most probable number of electron-ion pairs for a track length of 27.5 mm is 225, see Figure 3.3. So with a 94% selection efficiency, the expected most likely number of hits in the quad is 211.

The measured distribution of the number of track hits per chip and the total number of track hits are shown in Figure 6.5. The most probable number of hits per chip varies between 52 and 65 hits, and the mean varies between 65 and 80 hits. The most probable number of hits per quad is 131 and the mean number of track hits is 146 for an effective track length of approximately 27.5 mm. This is significantly below the expected 211 hits, potentially due to a much lower effective grid voltage or possibly due to hits lost in the readout. Because of the low single electron efficiency,

no energy loss ( $dE/dx$ ) results were extracted.

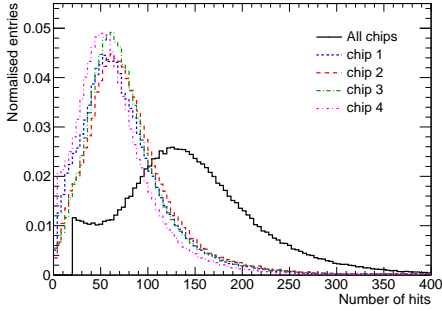


Figure 6.5: Distribution of the number of hits after track selection in total and per chip.

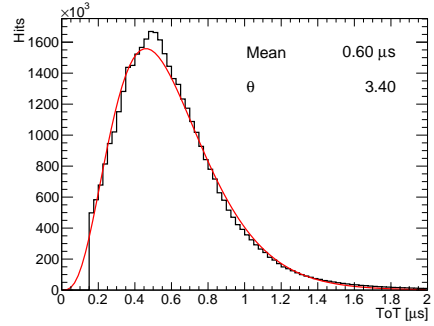


Figure 6.6: Distribution of the ToT from track hits after correction. The curve is fitted with the Polya function (red line), defined in Equation (3.11).

## 6.4.2 Hit time corrections

To increase precision in the drift direction, the hit times were calibrated. To correct for the double column structure and power distribution deformations of the Timepix3 chip, a ToT factor per column was extracted by injecting test pulses for each pixel. The distribution of the corrected ToT is shown in Figure 6.6. Furthermore, a ToA correction offset was determined from the test beam data based on the underlying substructure of  $16 \times 2$  pixels due to the clock distribution. In addition one ToA correction offset per column and one offset per row was applied. The ToT corrections are of  $\mathcal{O}(10\%)$  and the ToA corrections are of  $\mathcal{O}(1 \text{ ns})$ .

## 6.4.3 Time walk correction

A hit is registered when the collected charge exceeds the threshold. Since it takes longer for a small signal to reach the threshold than it does for a large signal, the measured ToA depends on the magnitude of the signal. This effect is called time walk and can be corrected by using the ToT as a measure of signal magnitude. In Figure 6.7 the mean of  $z$ -residuals is shown as a function of the ToT for all four chips. The relation can be parametrised using the time walk  $\delta z_{\text{tw}}$  as a function of the ToT  $t_{\text{ToT}}$ :

$$\delta z_{\text{tw}} = \frac{c_1}{t_{\text{ToT}} + t_0}, \quad (6.1)$$

where  $c_1$  and  $t_0$  are constants determined from a fit per chip.

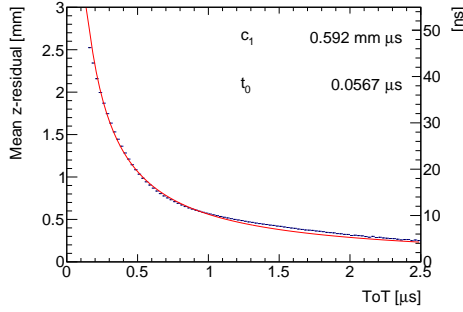


Figure 6.7: Mean  $z$ -residual without time walk correction as function of ToT, fitted with Equation (6.1) (red line). The right axis is given in units of ns using the drift velocity of  $54.6 \mu\text{m}/\text{ns}$ .

#### 6.4.4 Hit resolution in the pixel plane

The resolution of the single electrons in the transverse ( $xy$ ) plane was measured as a function of the predicted drift position ( $z$ ). Figure 6.8 displays this relation for tracks crossing a fiducial region in the centre of the chip as seen in Figures 6.11 and 6.13. The resolution for the detection of ionisation electrons  $\sigma_x$  is given by:

$$\sigma_x^2 = \frac{d_{\text{pixel}}^2}{12} + D_T^2(z - z_0), \quad (6.2)$$

where  $d_{\text{pixel}}$  is the pixel pitch size,  $z_0$  is the position of the grid, and  $D_T$  is the transverse diffusion coefficient. The resolution at zero drift distance  $d_{\text{pixel}}/\sqrt{12}$  was fixed to  $15.9 \mu\text{m}$ . Tracks with a  $z$ -position around  $0.3 \text{ mm}$  are given a larger error because they scatter on the central guard. Fitting expression (6.2) to the data gives a transverse diffusion coefficient  $D_T$  of  $398 \mu\text{m}/\sqrt{\text{cm}}$  with negligible statistical uncertainty. The measured value is larger than the value of  $270 \mu\text{m}/\sqrt{\text{cm}} \pm 3\%$  predicted by the gas simulation software Magboltz [196].

The deviation of the measured diffusion coefficient from the expected value is presumably due to an inaccuracy in the  $\text{CF}_4$  gas mixing, as discussed above. The actual gas content is not exactly known, as it is unclear to what extent the error also caused an increase in the isobutane fraction. Additionally, together with the oxygen also some nitrogen gas could have contaminated the gas mixture. The measured diffusion coefficients would roughly be in agreement with those for a mixture of 96 % argon, 2 %  $\text{CF}_4$ , and 2 % isobutane without any contaminations [149].

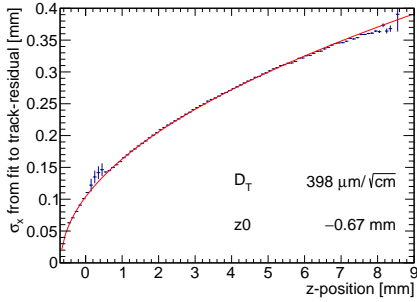


Figure 6.8: Measured hit resolution in the pixel plane (blue points) fitted with the resolution function according to Equation (6.2) (red line).

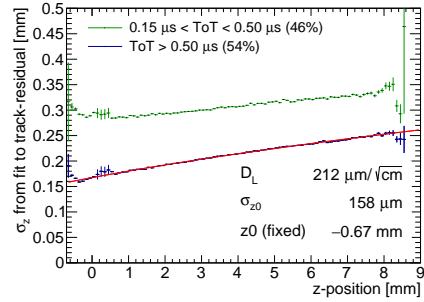


Figure 6.9: Measured hit resolution in drift direction split by ToT. The hits with a ToT above  $0.50 \mu\text{s}$  (blue points) are fitted with the resolution according to Equation (6.3) (red line). In the legend the fractions of hits in both selections are given.

### 6.4.5 Hit resolution in the drift direction

The measured  $z$ -position is directly related to the drift velocity and the time of arrival of the electrons. Using the predicted positions from the telescope, the drift velocity is measured to be  $54.6 \mu\text{m}/\text{ns}$ , which is slightly lower than the value of  $59.0 \mu\text{m}/\text{ns}$  expected by Magboltz. Both values have negligible statistical uncertainties.

The resolution for the detection of ionisation electrons  $\sigma_z$  is given by:

$$\sigma_z^2 = \sigma_{z_0}^2 + D_L^2(z - z_0), \quad (6.3)$$

where  $\sigma_{z_0}$  is the resolution at zero drift distance. The resolution as function of the drift distance is shown in Figure 6.9 for tracks crossing the fiducial region. Since tracks with a  $z$ -position around  $0.3 \text{ mm}$  scatter on the central guard, these data points are given a larger error. The longitudinal diffusion coefficient  $D_L$  was determined to be  $212 \mu\text{m}/\sqrt{\text{cm}}$  with negligible statistical uncertainty, which is equal to the expected value  $212 \mu\text{m}/\sqrt{\text{cm}} \pm 3\%$  from a Magboltz calculation.

### 6.4.6 Deformations in the pixel plane

It is important to measure possible deformations in the pixel ( $xy$ ) plane, because in a TPC these affect the momentum resolution. Because of limited statistics, the mean transverse ( $x$ ) residuals are calculated in bins of  $4 \times 4$  pixels over the quad plane using the tracks defined by the telescope, see Figure 6.10. Only bins with more than 800

entries are shown.

A distortion is present near the edges of the chips. The cause is twofold: firstly there is a geometrical bias at the edge of the detector because only part of the ionisation cloud can be detected, and secondly the grounded region at the edge of the Timepix3 die introduces a non-uniformity in the electric field.

An empirically selected function consisting of four Cauchy (Breit-Wigner) functions can be fitted to the geometrical bias and the non-uniformity of the field. Near the top and bottom edges the size of the deformations is different, as such in a second step a 4<sup>th</sup> order polynomial function in  $y$  was fitted while keeping the other parameters fixed. All in all, the fitted function is given by:

$$\delta x_{\text{deformations}} = \sum_{j=0}^4 \left( \frac{1}{\pi} \frac{\gamma_j}{(x - d_j)^2 + \gamma_j^2} \sum_{i=0}^4 (c_{ij} y^i) \right), \quad (6.4)$$

where  $d_j$  and  $\gamma_j$  are the location and scale parameters of the Cauchy distributions, and  $c_{ij}$  are the parameters of the fourth order polynomial.

The outlines of the fitted function are shown in Figure 6.10. The fitted function can be used as a correction by subtracting it from the mean residuals. The result of this procedure is shown in Figure 6.11.

The r.m.s. of the distribution of the measured mean residual over the surface - or the systematic error for a measurement before the correction in the quad plane - is 31  $\mu\text{m}$ . After subtraction of the fitted correction function (6.4), the r.m.s. of the mean values is 13  $\mu\text{m}$  over the whole plane and 9  $\mu\text{m}$  in the selected region 2 mm from the edges indicated by a black outline. The distribution of the mean  $x$ -residuals after correction are shown in Figure 6.12. The distortions could be further reduced by improving the homogeneity of the electric field near the dyke e.g. by adding a field wire above the quad detector at the boundaries between the neighbouring chips.

### 6.4.7 Deformations in the drift direction

A similar measurement is done for distortions in the drift direction. In Figure 6.13 the mean longitudinal ( $z$ ) residuals are shown in bins of  $4 \times 4$  pixels over the quad plane using the tracks defined by the telescope. Only bins with more than 800 entries are shown. As shown in Figure 6.12, the r.m.s. of the distortion is 19  $\mu\text{m}$  (0.35 ns) and 14  $\mu\text{m}$  (0.26 ns) in the black outlined central area 2 mm from the edges.

### 6.4.8 Quad detector resolution

The overall accuracy of a track position measurement using the quad detector can be tested by comparing the quad track to the telescope track. The difference will

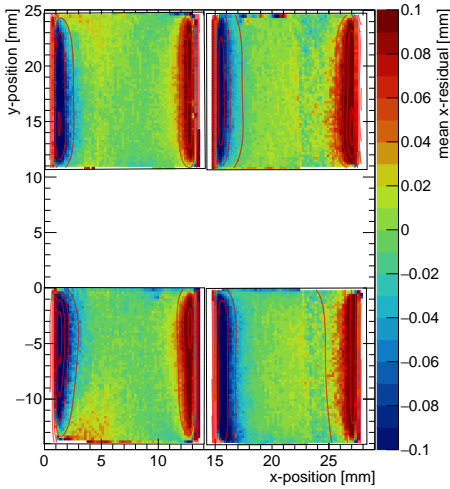


Figure 6.10: Mean residuals in the pixel plane ( $x$ -residuals) at the expected hit position, fitted with Equation(6.4) (red contours).

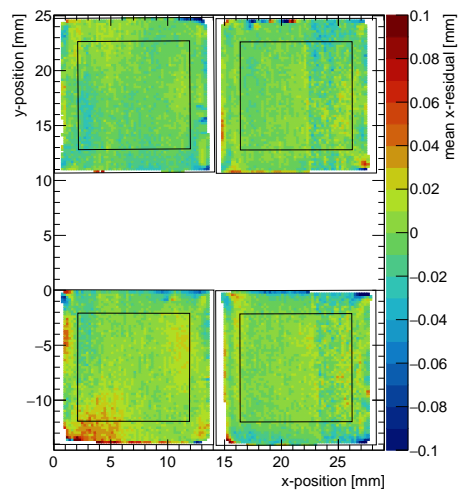


Figure 6.11: Mean residuals in the pixel plane ( $x$ -residuals) at the expected hit position after subtracting the fitted edge deformations using Equation(6.4).

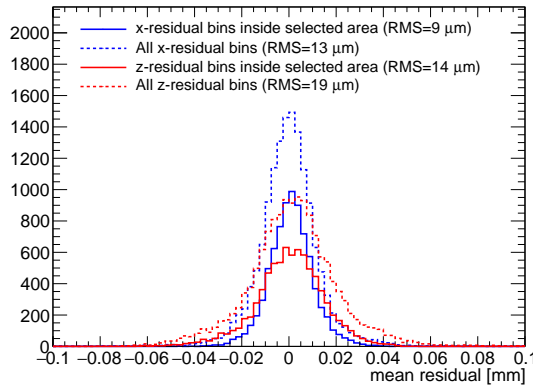


Figure 6.12: Distribution of the mean residuals from  $4 \times 4$  bins in Figure 6.11 ( $x$ -residuals in blue) and Figure 6.13 ( $z$ -residuals in red)



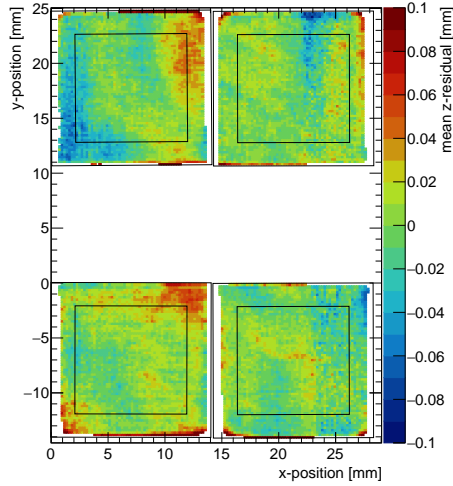


Figure 6.13: Mean residuals in the drift direction ( $z$ -residuals) at the expected hit position.

be a combination of statistical errors, systematic errors and multiple scattering contributions. Here it is important to estimate the systematic error, because multiple scattering occurs primarily outside the fiducial gas volume, and in applications with multiple quad modules the statistical errors will be further reduced.

Figure 6.14 displays the difference between the weighted mean position of all quad track hits in the fiducial region and the telescope track. The distribution has long tails, which are in part from unrelated background tracks that are erroneously matched. The number of background tracks is estimated by shifting the telescope timing by 1000 frames and is shown for comparison. In the fit, these tracks are accounted for by introducing a contribution from a uniform distribution.

A fit with a combination of a Gaussian function and a uniform distribution, yields a standard deviation  $\sigma_x^{\text{quad}}$  of  $41 \mu\text{m}$ . This value is the result of various contributions. Firstly, the statistical precision of a position measurement is acquired from a track fit of the quad hits with hit errors. This statistical precision of the position at the centre of the quad is  $25 \mu\text{m}$ . Furthermore, there is a systematic deviation of  $9 \mu\text{m}$  in the pixel plane in the fiducial region after the correction as discussed in Section 6.4.6. Additionally, there is a systematic deviation in the  $x$ -direction of  $17 \mu\text{m}$  along the drift direction most likely due to electric field inhomogeneities. This is the  $x$ -deviation as a function of  $z$ -position. which should not be confused with the  $z$ -deviation as a function of  $x$  and  $y$ -position that was mentioned before in Section 6.4.7.

In addition, the precision is limited due to multiple scattering in the setup. The

precision was calculated with a simple simulation of the setup using the equations given in subsection 3.1.4. The setup has multiple scattering contributions from the telescope planes ( $0.075\% X_0$  per plane) [193], the air ( $0.084\% X_0$ ), the TPC gas ( $0.09\% X_0$ ) and the two Kapton foils ( $0.035\% X_0$ ) [45]. The input to the simulation is shown in Figure 6.15 with an extra scattering contribution  $S$  on the quad exit window near the centre of the setup, required to match the simulation to the data. By comparing the track angle in the first three telescope planes and the second three telescope planes, the total radiation length of the setup is estimated to be  $0.82\% X_0$  ( $0.66\% X_0$  expected, so  $S = 0.16\% X_0$ ). From the simulation the multiple scattering contribution at the position of the quad centre is estimated to be  $22 \mu\text{m}$ .

An overview of the contributing errors is given in Table 6.3. In the end, there is still a small unidentified remaining systematic error of  $14 \mu\text{m}$ .

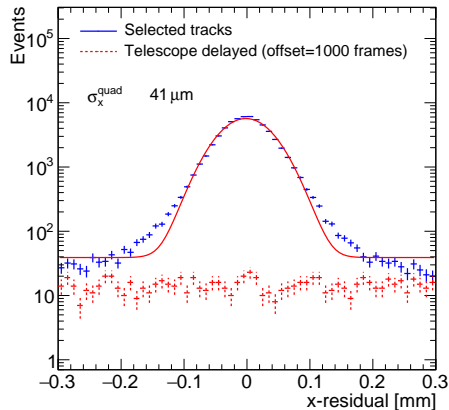


Figure 6.14: The difference between mean hit position and track prediction in the pixel plane, fitted with the sum of a Gaussian and a flat background distribution (solid red line). In comparison the background tracks are shown (dashed red), acquired by offsetting the telescope by 1000 frames.

## 6.5 Conclusions and outlook

A quad module with four Timepix3 based GridPixes has been designed and realised. The module has dimensions of  $39.6 \text{ mm} \times 28.38 \text{ mm}$  and an active surface of 68.9%. The quad module was embedded in a TPC detector and operated at the ELSA test beam facility. The single electron resolutions in the transverse and longitudinal planes are similar to the results obtained for the single-chip detector and primarily limited by diffusion. It is shown that a systematic error from the quad detector for the distortions

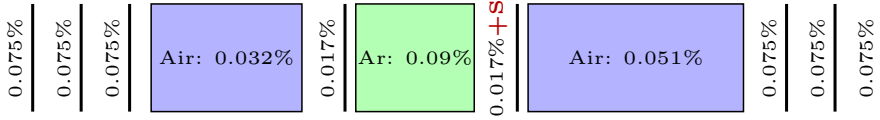


Figure 6.15: Multiple scattering contributions in  $X_0$  for the quad setup as put in the simulation representing: the three telescope planes, the volume of air, the entry window, the gas volume, the exit window, the volume of air, and another three telescope planes. An extra scatter  $S$  was added to the quad exit window.

Table 6.3: Overview of the errors on the difference between mean hit position and track prediction in the pixel plane

Observed standard deviation $\sigma_x^{\text{quad}}$	41 $\mu\text{m}$
Statistical quad detector error	25 $\mu\text{m}$
Statistical telescope error	2 $\mu\text{m}$
Systematics over the pixel plane (corrected)	9 $\mu\text{m}$
Systematics along the drift direction	17 $\mu\text{m}$
Multiple scattering contribution	22 $\mu\text{m}$
Remaining systematic error	14 $\mu\text{m}$

---

over the pixel plane of  $13\ \mu\text{m}$  ( $9\ \mu\text{m}$  in the central region) has been achieved. The demonstrated resolution of the setup is  $41\ \mu\text{m}$ , of which the statistical error is  $25\ \mu\text{m}$ , the error caused by multiple scattering in the setup is  $22\ \mu\text{m}$  and the total systematic error is  $24\ \mu\text{m}$ .

The next step is to demonstrate a large detection area with the quad module as a building block and confirm the potential of the GridPix technology for large detectors. A new detector with 8 quad modules carrying a total of 32 Timepix3 GridPix chips has already been constructed and will undergo thorough investigation.



# Simulation and reconstruction of the ILD TPC with a pixel readout

---

The ILD experiment relies on simulations for several crucial tasks. For example, the simulation of the ILD is used to assess the expected measurement performance, motivate design choices and to perform physics analysis prospect studies. In the future, a simulation can in addition be used to interpret measurements. As a result, a detailed detector simulations is essential for the design of the ILD.

For the ILD, there is one integrated simulation of the whole detector, such that the overall reconstruction can be tested and the combined performance of the different subdetectors can be studied. The initial interactions at the IP that produce high energy particles are modeled in specialised software. The produced high energy particles are fed to the detector simulation, which propagates them through the detector material and simulates their interactions with the detector components. The simulated digitisation produces the simulated detector response in terms of signals. The track reconstruction aims to translate these signals into measured physical quantities: the positions, trajectories, and momenta of the particles. At a higher level, the reconstruction identifies the particles species.

The software related to the ILC detectors is included in the ILCSoft package (v02-00-01) [201]. The package contains software for simulation, reconstruction and related tasks such as event visualisation. The ILCSoft package provides a modular framework to perform digitisation, reconstruction and analysis using processors designed for specific tasks. The special LCIO format can transfer data between processors. Parameters for the geometry, simulation and steering of the processors are given in xml parameter files.

Within this framework, a virtual geometry is built representing the detector. This virtual geometry is used both in the simulation and the reconstruction. The novel simulation and reconstruction of the TPC with pixel readout expands on the existing simulation and reconstruction of the TPC with pad readout.

## 7.1 Virtual geometry of the TPC

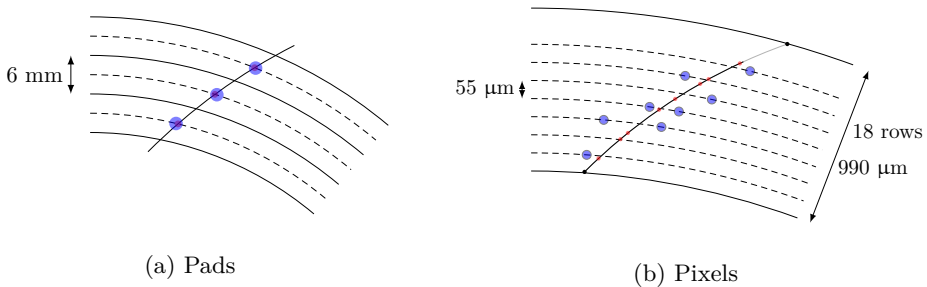


Figure 7.1: Layout of the virtual volumes of the TPC with a) a pad readout and b) a pixel readout. The (interpolated) track is shown as a curved line. The simulated crossing points are shown in red. The blue points are the hits after resolution based smearing. The black dots are the crossing points of the track and the virtual volume boundaries used to calculate the interpolated trajectory.

The sensitive part of the ILD TPC consists of one large gas volume, but the virtual geometry used for simulation and reconstruction is more complicated. The virtual geometry consists of a series of coaxial cylindrical shells. A schematic of the geometry for the pads and pixels is shown in Figure 7.1. The  $z$ -axis is defined as the cylindrical symmetry axis of the detector almost in the direction of the incoming beams, and the  $x$  and  $y$  axis are the horizontal and vertical axis respectively.

For the pad readout, there are two 3 mm thick cylindrical volumes per pad row. Their boundary in the centre of the pad row is used to record the position of the crossing of a track in the centre of the pad.

For the pixel readout, the virtual geometry consists of one 55  $\mu\text{m}$  thick cylindrical shell per pixel row. In order to optionally speed up the simulation, an alternative geometry with one 990  $\mu\text{m}$  thick volume per 18 pixel rows is also implemented.

The virtual geometry is provided through an interface with the Detector Description Toolkit for High Energy Physics (DD4hep) [202]. DD4hep provides one single generic geometry description for simulation and reconstruction. At this point, both the pad and pixel geometry are modeled as if they cover the entire readout end plate

seamlessly. The simulation of partial coverage of the readout end plate by pixel modules will be discussed in Section 8.1.1.

## 7.2 Simulation of the TPC

The detector simulation models the interactions of the provided input particles with the detectors. In the most simple case the input is a particle ‘gun’ firing specific particles with a specified momentum in a chosen direction, which is useful to study the detector performance directly. In order to perform more involved performance tests and to do physics prospect studies, the particles from a simulated collision can be used. An example of particles from a simulated collision where a Higgs boson is produced in a virtual detector is shown in Figure 7.2.

A collision is simulated in a few stages. At the most fundamental level the hard scattering is simulated using analytical matrix calculation software. For the ILC most samples are produced using simulation of the collisions using the WHIZARD event generator [203]. If strongly interacting partons are produced, (parton) showering and hadronisation occur directly after the hard scattering, which for the ILD is simulated in PYTHIA 6 [204]. During (parton) showering, soft emissions and splitting produce additional particles. In the hadronisation process strongly interacting partons cannot be treated as freely moving and start to form hadrons, which is approximated by a string fragmentation model. Some of the created particles are unstable, and subsequently decay within the detector if their lifetime is sufficiently short.

The interactions of the produced particles with the TPC gas are simulated as energy deposits in the sensitive volumes. The particle’s interactions with the detector are modeled in the GEANT4 simulation toolkit for the simulation of the passage of particles through matter [200]. The simulated hits are generated localised on the trajectories of the particles. The resolution due to the drift of electrons and due to the granularity of the readout are added in the digitisation step. The hits are displaced from their original position by drawing a random offset from a Gaussian distribution with a standard deviation equal to the expected resolution.

### 7.2.1 Simulation of the pad readout

For a pad readout in a real detector the charge is normally detected by multiple pads within every row. A hit represents all charge deposited in a single pad row and its position is the signal centroid as reconstructed using pad response functions. At short drift distances the precision is limited by the readout, i.e. the pad size and the degree of charge spreading over enough pads, but at longer drift distances the precision is limited by the diffusion of electrons in the gas, as discussed in subsection 3.2.2. In the



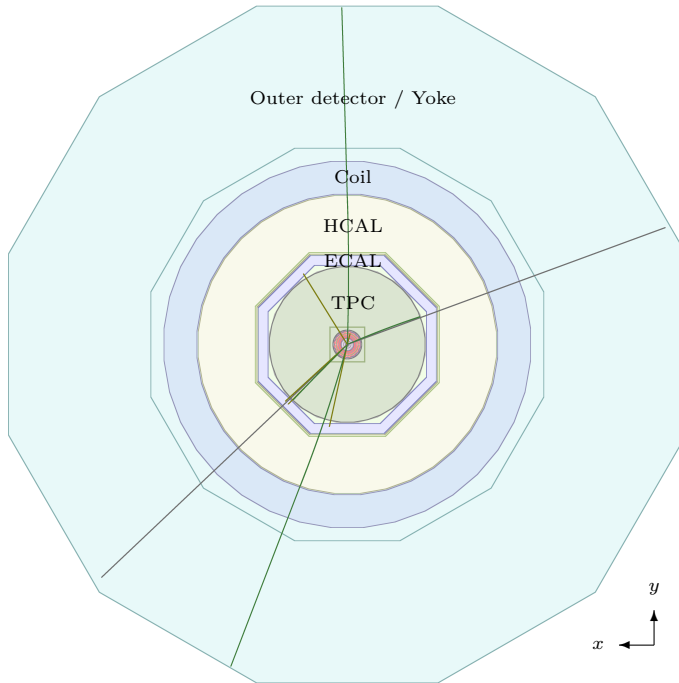


Figure 7.2: Simulated particles and the detector of a  $e^+e^- \rightarrow ZH \rightarrow \mu^+\mu^-\tau^+\tau^-$  event at a centre-of-mass energy of 250 GeV. The direction of charged particles is indicated with green lines, neutrinos with grey lines, and other neutral particles with green-yellow lines.

longitudinal direction, the resolution is limited by the time resolution of the readout and the diffusion.

In the simulation on the other hand, a hit is registered at the crossing point of the pad row centre if there is any energy deposited in that row. The simulated hit positions are displaced by an offset proportional to the hit resolution. The offset is drawn from a Gaussian distribution with a standard deviation set to the hit resolution. As far as the spatial resolution is concerned, the amount of deposited charge in the simulation is always effectively  $N_{\text{eff}} = 22$  electrons before amplification. The resolution  $\sigma_{r\phi}^{\text{pad}}$  in the  $r\phi$ -direction tangent to the surface of the cylinder in the  $xy$ -plane and the resolution

$\sigma_z^{\text{pad}}$  in the  $z$ -direction for a track at drift distance  $L$  are given by

$$\begin{aligned}\sigma_{r\phi}^{\text{pad}} &= \sqrt{(\sigma_{r\phi 0}^{\text{pad}})^2 + \sigma_{\phi 0}^2 \sin^2(\phi_{\text{track}}) + L \frac{D_{r\phi}^2}{N_{\text{eff}}} \sin(\theta_{\text{track}}) \left(\frac{6 \text{ mm}}{h_{\text{pad}}}\right) \left(\frac{4.0 \text{ T}}{B}\right)^2} \\ \sigma_z^{\text{pad}} &= \sqrt{(\sigma_{z0}^{\text{pad}})^2 + L(D_z^{\text{pad}})^2},\end{aligned}\quad (7.1)$$

where  $\sigma_{r\phi 0}^{\text{pad}} = 50 \mu\text{m}$  is the resolution in the  $r\phi$ -direction at zero drift,  $\sigma_{z0}^{\text{pad}} = 0.4 \text{ mm}$  is the resolution in the  $z$ -direction at zero drift,  $D_{r\phi} = 25 \mu\text{m}/\sqrt{\text{cm}}$  is the transverse diffusion coefficient of T2K gas at a magnetic field of  $B = 4 \text{ T}$  and a drift field of  $280 \text{ V/cm}$  corresponding to the value at which the drift speed is maximal.  $D_z^{\text{pad}} = 80 \mu\text{m}/\sqrt{\text{cm}}$  is the longitudinal diffusion coefficient and takes into account the effective number of drift electrons per pad. The expression  $\left(\frac{6 \text{ mm}}{h_{\text{pad}}}\right)$  accounts for the amount of charge collected on pads with a height  $h_{\text{pad}}$  differently from the nominal height of  $6 \text{ mm}$ .  $\left(\frac{4.0 \text{ T}}{B}\right)^2$  enables an approximate extrapolation to other magnetic field strengths  $B$ . The contribution  $\sigma_{\phi 0}^2 \sin^2(\phi_{\text{track}})$  captures the dependence on the azimuth crossing angle of the track with the pad row  $\phi_{\text{track}}$  with  $\sigma_{\phi 0} = 0.9 \text{ mm}$  being the resolution at zero drift distance for a track parallel to the pad row ( $\phi_{\text{track}} = \pi/2$ ).

## 7.2.2 Simulation of the pixel readout

For a pixel TPC readout, the situation is more straightforward. A single drift electron is detected by one pixel. For short drift distances, the resolution in the transverse direction is limited by the pixel size, in the longitudinal direction the precision of the time measurements determines the resolution. For longer drift distances the resolution in both the transverse and longitudinal direction is limited by diffusion.

For the simulation of a pixel TPC readout, the number of ionisation electrons is calculated by dividing the deposited energy by  $32 \text{ eV}$ , the average energy required to produce an ionisation electron. After this division, any remaining energy is transferred to the next layer. The simulated hits are positioned along the track and are shown in Figure 7.3. The same hits are shown in Figure 7.4 after a displacement which simulates the effect of the hit resolution. The resolutions in the transverse directions  $\sigma_r^{\text{pixel}}$  and  $\sigma_{r\phi}^{\text{pixel}}$ , and the resolution in the longitudinal  $z$ -direction for a drift distance  $L$  are given by

$$\begin{aligned}\sigma_r^{\text{pixel}} = \sigma_{r\phi}^{\text{pixel}} &= \sqrt{(\sigma_{r\phi 0}^{\text{pixel}})^2 + LD_{r\phi}^2 \left(\frac{4.0 \text{ T}}{B}\right)^2} \\ \sigma_z^{\text{pixel}} &= \sqrt{(\sigma_{z0}^{\text{pixel}})^2 + L(D_z^{\text{pixel}})^2},\end{aligned}\quad (7.2)$$

where  $\sigma_{r\phi 0}^{\text{pixel}} = 16 \mu\text{m}$  is the transverse resolution at zero drift distance calculated from the pixel size,  $\sigma_{z0}^{\text{pixel}} = 168 \mu\text{m}$  is the resolution in the longitudinal direction for all hits

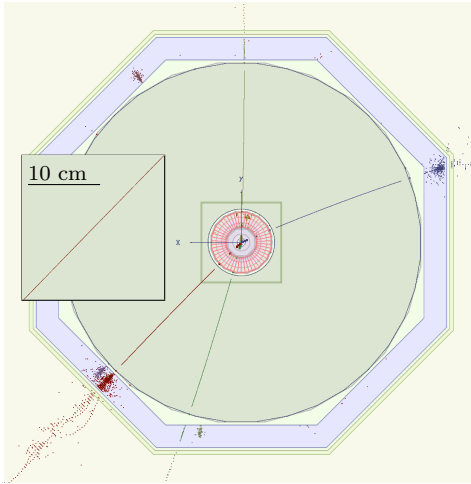


Figure 7.3: Display of simulation hits for the event shown in Figure 7.2. A closeup of an approximately 30 cm long track segment is shown in the outline. Every particle produced at the IP is assigned its own colour.

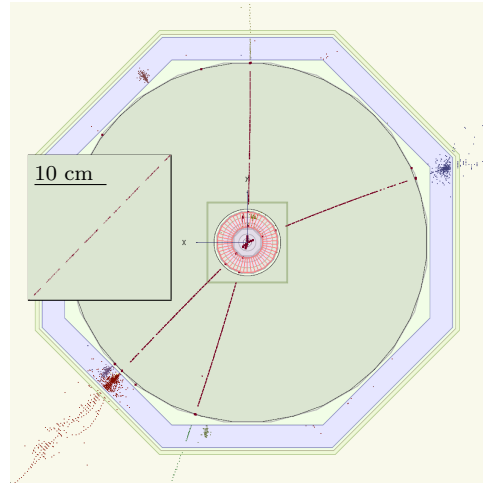


Figure 7.4: Display of digitised hits for the event shown in Figure 7.2. A closeup of an approximately 30 cm long track segment is shown in the outline. All digitised TPC hits are shown in the same red colour.

as measured with the GridPix chip detector in Section 5.4.5,  $D_z^{\text{pixel}} = 226 \mu\text{m}/\sqrt{\text{cm}}$  is the longitudinal diffusion coefficient for a single drift electron.

Two or more ionisation electrons from one simulated bunch crossing might arrive on the same pixel. The Timepix3 chip would in some cases be able to register hits from more than one ionisation electron, because the dead time per pixel of the ToT plus 475 ns is shorter than the maximum drift time of 30  $\mu\text{s}$ . In order to be conservative, it is assumed that a pixel can only register one hit per simulated bunch crossing. As a very rough approximation of the occupancy, the end plate is divided into pixel bins of  $55 \mu\text{m} \times 55 \mu\text{m}$ , and only one hit per bin is allowed. Hits are processed in the order of the simulation. Because the number of hits lost due to the occupancy is small, no attempt is made to sort the hits by drift time. A more complete treatment of the occupancy would also include backgrounds and hits from earlier and later bunch crossings.

The computational cost was found to increase rapidly with the number of virtual volumes. In order to reduce the required processing time, an optional interpolation step was introduced. The track is first simulated in 990  $\mu\text{m}$  thick volumes enclosing 18 pixel rows. Then the total number of hits per 18 pixel rows is known, and the hits have to be distributed over the pixel rows, i.e. the cluster size and number of

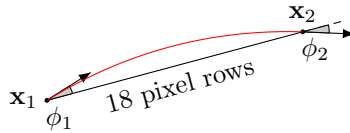


Figure 7.5: Parabolic interpolation of the track over a length of 18 pixel rows using crossing points at the boundaries  $x_1$  and  $x_2$  and the directions  $\phi_1$  and  $\phi_2$  at those points.

hits per cluster have to be generated. A good approximation was found to deposit single hits in 90% of the cases and in the remaining 10% of the cases to draw from the distribution  $P(n) = \frac{2n}{N_{\text{total}}^2 + N_{\text{total}}}$ , where  $N_{\text{total}}$  is the total number of remaining hits. The clusters are uniformly distributed along the track. A parabolic interpolation gives the location of the pixel row crossings using the position and direction of the trajectory at the boundaries of the volume, as shown in Figure 7.5.

### 7.2.3 Comparison of the hit resolution for the pad and pixel readout

In conclusion, a hit of the pad readout and a hit of the pixel readout are qualitatively different. In a TPC with pad readout a track has 220 very precise hits: one for every pad row representing effectively about 22 ionisation electrons, but for a TPC with pixel readout there are about 10 000 less precise hits: one for every ionisation electron. The situation is sketched in Figure 7.1.

The resolution for the pad and pixel readout as given in Equations (7.1) and (7.2) is compared in Figure 7.6. Per hit the pixel readout is less precise, but this is compensated by the much larger number of hits. In order to compare the two, the pixel resolution is also shown scaled by  $1/\sqrt{60}$ , as if averaged over the 60 ionisation electrons that would be detected for a track segment with the length of one pad (6 mm). For an assumed pixel readout coverage of 60%, the pixel resolution is shown scaled by  $1/\sqrt{36}$  because on average 36 ionisation electrons are detected for every pad hit.

Close to the end plate the resolution is limited by the readout. The charge spreading limits the pad readout precision and the pixel readout is more precise. For larger drift distances the resolution is limited by diffusion and the pixel resolution benefits from a larger number of effective ionisation electrons detected.

The pixel readout will be advantageous for tracks at an angle with the pad rows. The resolution of the pad readout with rectangular pads depends on the angle of the track with the pad row and the resolution of the pixel readout does not. Even a small angle of  $5^\circ$  can deteriorate the resolution, see Figure 7.6. Additionally, for

forward tracks the number of pad rows that are hit will reduce while the number of ionisation electrons and thus the number of pixel hits does not reduce as much. For more forward tracks the pad resolution does improve proportional to the number of ionisation electrons per pad, as shown in Figure 7.6. Of course, the pixel readout will also have more hits per projected track length.

The resolution of the reconstructed track parameters will be discussed in the next chapter.

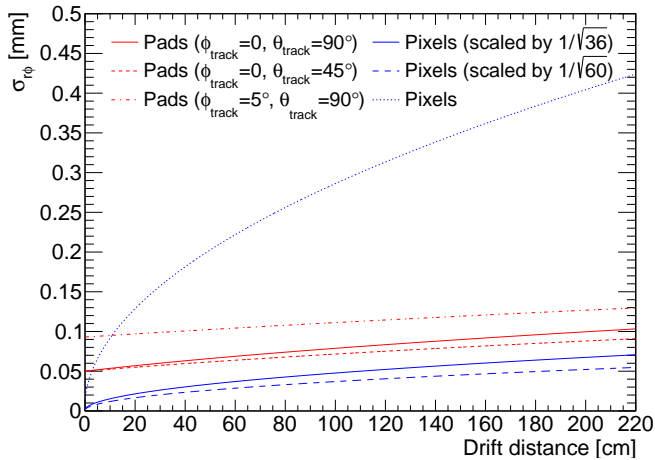


Figure 7.6: Comparison of the hit resolution for the pad (red lines) and pixel readout (blue lines).

## 7.3 Track reconstruction

The goal of track reconstruction and fitting is to estimate the set of track parameters from a series of measurements. This is achieved using a Kalman filter. The Kalman filter is a recursive fitting algorithm, which allows combined track finding and track fitting [205]. It is used because it has several advantages. The Kalman filter only uses small matrices, which enables it to run efficiently. Secondly, the model has a track state at each point, which facilitates the inclusion of ancillary effects such as multiple scattering, energy loss and noise. The drawbacks of a Kalman filter are related. Because of the track model, an additional step is required to get the optimal track state at every point. In addition, the Kalman filter requires an initial seed with error estimate. A wrong estimate might not yield the correct track.

### 7.3.1 Track parameters

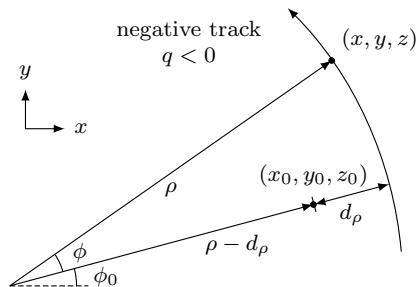


Figure 7.7: Geometric overview of some of the track parameters in the  $xy$ -plane for a track of a negatively charged particle, with the magnetic field  $B$  pointing in the positive  $z$ -direction

The trajectory of a charged particle in a detector with a magnetic field is locally well approximated by a helix [206]. In the absence of material, the helical trajectory of a charged particle in a uniform magnetic field parallel to the  $z$ -axis is described by

$$\begin{aligned} x &= x_0 + d_\rho \cos \phi_0 + \frac{1}{B\kappa} (\cos \phi_0 - \cos(\phi_0 + \phi)), \\ y &= y_0 + d_\rho \sin \phi_0 + \frac{1}{B\kappa} (\sin \phi_0 - \sin(\phi_0 + \phi)), \\ z &= z_0 + d_z - \frac{1}{B\kappa} \tan(\lambda)\phi, \end{aligned} \quad (7.3)$$

where  $(x_0, y_0, z_0)$  is a pivotal point,  $B$  is the magnetic field strength. For a given pivot and magnetic field, the helix is fully specified by the 5 parameter state vector  $\mathbf{a}$

$$\mathbf{a} = (d_\rho, \phi_0, \kappa, d_z, \tan \lambda), \quad (7.4)$$

where  $d_\rho$  and  $d_z$  are the distance of the helix to the pivotal point in the  $xy$ -plane and along the  $z$ -axis respectively,  $\phi_0$  is the azimuth angle of the pivot with respect to the helix centre and  $\lambda$  is the dip angle ( $\lambda = \pi/2 - \theta$ ). The transverse momentum  $p_T$  is given by

$$p_T = q/|\kappa| = q\rho B = 0.3 \left( \frac{\text{GeV}/c}{\text{T m}} \right) \rho B, \quad (7.5)$$

with  $q$  being the particle charge, and  $|\kappa| = 1/(\rho B)$  being a track parameter related to the radius of curvature  $\rho$ . The sign of  $\kappa$  is given by the charge of the particle. The latter part of the equation is the numerical expression for the  $p_T$  in units of  $\text{GeV}/c$  if the particle's charge is  $q = 1 e$ ,  $\rho$  is in units of  $\text{m}$  and  $B$  is in units of  $\text{T}$ . An overview of some of the parameters is given in Figure 7.7.

### 7.3.2 The extended Kalman filter

The Kalman filter is a recursive fitting algorithm. As a minimal mean square error estimator, the Kalman filter is an optimal estimator for linear systems with Gaussian distributed errors. The version described here is the non-linear extended Kalman filter described in reference [207]. The notation conventions of that review are largely adopted, and some of the equations are reproduced here.

The algorithm estimates from a series of measurements  $\mathbf{m}_i$  the state vector  $\mathbf{a}_k^j$  and covariance  $\mathbf{C}_k^j$  at site  $k$  using information from sites up to  $j$ . The extended Kalman filter minimises the  $\chi_k^2$  defined by

$$\chi_k^2 = \sum_{i=0}^k (\mathbf{m}_i - \mathbf{h}_i(\mathbf{a}_i^k))^T (\mathbf{V}_i^k)^{-1} (\mathbf{m}_i - \mathbf{h}_i(\mathbf{a}_i^k)), \quad (7.6)$$

where  $\mathbf{h}_i(\mathbf{a}_i^k)$  is the projector that gives the predicted measurement, and  $V_i$  the measurement noise. The (extended) Kalman filter arrives at an estimate using three types of actions.

**Predict** At each site  $k$  the state vector  $\mathbf{a}_k^{k-1}$  and covariance matrix  $\mathbf{C}_k^{k-1}$  is first predicted from the state vector at the previous site  $\mathbf{a}_{k-1}^{k-1}$  using the state-propagator  $\mathbf{f}_{k-1}(\mathbf{a}_{k-1}^{k-1})$ :

$$\mathbf{a}_k^{k-1} = \mathbf{f}_{k-1}(\mathbf{a}_{k-1}^{k-1}) \quad \text{and} \quad \mathbf{C}_k^{k-1} = \mathbf{F}_{k-1} \mathbf{C}_{k-1}^{k-1} \mathbf{F}_{k-1}^T + \mathbf{Q}_{k-1}, \quad (7.7)$$

where  $\mathbf{F}_{k-1} = \frac{\partial \mathbf{f}_{k-1}}{\partial \mathbf{a}_{k-1}^{k-1}}$ , and  $\mathbf{Q}_{k-1}$  is the covariance of the process noise.

**Update** The second step is to update the state vector  $\mathbf{a}_k^{k-1}$  with information from the measurement  $\mathbf{m}_k$ . The projector  $\mathbf{h}_k(\mathbf{a}_k^{k-1})$  gives the predicted measurement as a function of the state vector  $\mathbf{a}_k^{k-1}$ . These are used to calculate the updated state vector  $\mathbf{a}_k^k$ , and to calculate the updated covariance matrix  $\mathbf{C}_k^k$  as an effective weighted mean of the predicted covariance matrix  $\mathbf{C}_k^{k-1}$  and the covariance of the measurement noise  $\mathbf{V}_k$ :

$$\mathbf{a}_k^k = \mathbf{a}_k^{k-1} + \mathbf{K}_k (\mathbf{m}_k - \mathbf{h}_k(\mathbf{a}_k^{k-1})) \quad \text{and} \quad \mathbf{C}_k^k = ((\mathbf{C}_k^{k-1})^{-1} + \mathbf{H}_k^T (\mathbf{V}_k)^{-1} \mathbf{H}_k)^{-1}, \quad (7.8)$$

where  $\mathbf{K}_k = \mathbf{C}_k^{k-1} \mathbf{H}_k^T (\mathbf{V}_k + \mathbf{H}_k \mathbf{C}_k^{k-1} \mathbf{H}_k^T)^{-1}$  and  $\mathbf{H}_k = \frac{\partial \mathbf{h}_k}{\partial \mathbf{a}_k^{k-1}}$ .

**Smooth** In the end, sites can be updated with the information from all  $n$  sites by revisiting them in the reverse order. The updated state vector  $\mathbf{a}_k^n$  and covariance

matrix  $\mathbf{C}_k^n$  become

$$\mathbf{a}_k^n = \mathbf{a}_k^k + \mathbf{A}_k(\mathbf{a}_{k+1}^n - \mathbf{a}_{k+1}^k) \quad \text{and} \quad \mathbf{C}_k^n = \mathbf{C}_k^k + \mathbf{A}_k(\mathbf{a}_{k+1}^n - \mathbf{a}_{k+1}^k)\mathbf{A}_k^T, \quad (7.9)$$

where  $\mathbf{A}_k = \mathbf{C}_k^k \mathbf{F}_k^k (\mathbf{C}_{k+1}^k)^{-1}$ .

### 7.3.3 The extended Kalman filter for track fitting

The extended Kalman filter can be applied to track fitting in a magnetic field [205]. Every sub-detector is represented as a series of measurement sites, e.g. for a vertex detector each silicon plane is a measurement site. The extended Kalman filter usually starts from a hit in the more outer sites where the two-track distance is the largest to minimise confusion of hits from different tracks. Here an initial estimate is made of the track parameters, which is used as a seed for the extended Kalman filter.

Many of the physical tracking processes can naturally be accommodated in the extended Kalman filter. Multiple scattering is modeled as process noise  $\mathbf{Q}_k$  in the prediction step and depends on the amount of material between the measurement sites. Energy loss is included in the propagator. The dimension and definition of the measurement vector  $\mathbf{m}_k$  depends on the geometry of the measurement site. Measurement errors are modeled as measurement noise  $\mathbf{V}_k$ . The precise expressions can be found in reference [207].

The fit is performed inwards and ends at the IP, where the optimal track state is found. If the optimal track state is also required more outwards, for example to extrapolate the track to the calorimeters, smoothing of all track states must be performed.

### 7.3.4 Track fitting for a TPC

In order to apply the extended Kalman filter to a TPC a series of special sites and measurement vectors is defined.

#### The pad readout

For the pad readout, the measurement sites are the virtual cylindrical surfaces parallel to the  $z$ -axis that are at the centre of the volumes read out by a pad row. For each cylinder the measurement vector  $\mathbf{m}_k$  is a surface coordinate  $(u, v)$  related to hit position by

$$\mathbf{m}_k = \begin{pmatrix} u \\ v \end{pmatrix} = \begin{pmatrix} \phi_{\text{hit}} r_{\text{cylinder}} \\ z_{\text{hit}} \end{pmatrix}, \quad (7.10)$$



where  $\phi_{\text{hit}}$  is the azimuth angle of the hit with respect to the  $x$ -axis,  $r_{\text{cylinder}}$  is the radius of the cylinder, and  $z_{\text{hit}}$  is the hit  $z$  coordinate. The projector  $\mathbf{h}_k(\mathbf{a}_k)$  calculates the intersection of the helix with the layer, which is translated to the local cylinder surface coordinates  $(u, v)$  to acquire the projected measurement vector.

### The pixel readout

The reconstruction with a pixel TPC readout uses similar cylindrical surfaces, but the measurement vector is not suitable for the pixel TPC readout, because the resolution of the pixel hit in the radial direction cannot be neglected. So, the approximation of the hit being always on the cylinder surface is not valid for a pixel hit.

The chosen intricate solution is the following. An alternative measurement vector  $\mathbf{m}_k = (d_0, z)$  is defined, with  $d_0$  being the distance from the track or (predicted) measurement to the hit in the  $xy$ -plane and  $z$  being the projected coordinate on the cylinder comparable to the  $v$  coordinate above. As shown in Figure 7.8,  $d_0$  is calculated by approximating the track with a line tangent to the helix in the direction  $\phi_{\text{track}}$  and  $\tan \lambda$ . A hit simply has  $d_0 = 0$  and  $z = z_{\text{hit}}$ . For the predicted measurement, the projector becomes

$$\mathbf{h}_k(\mathbf{a}_k^{k-1}) = \begin{pmatrix} d_0 \\ z \end{pmatrix} = \begin{pmatrix} \Delta x \sin \phi_{\text{track}} - \Delta y \cos \phi_{\text{track}} \\ z_{\text{track}} + \tan \lambda (\Delta x \cos \phi_{\text{track}} + \Delta y \sin \phi_{\text{track}}) \end{pmatrix}, \quad (7.11)$$

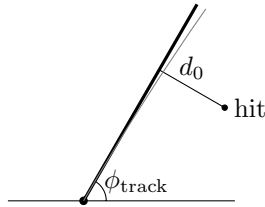
where  $\Delta x$  and  $\Delta y$  are the differences between the expected crossing point and the hit position in the  $x$  and  $y$  direction respectively, and  $z_{\text{track}}$  is the  $z$  position of the expected crossing point.

Effectively, by inserting  $d_0$  in the measurement vector, the calculation of the difference is transferred from  $\mathbf{m}_i - \mathbf{h}_i(\mathbf{a}_i)$  to within the projector  $\mathbf{h}_i(\mathbf{a}_i)$ .

Additionally the expression for multiple scattering has to be adapted for the pixel readout. The expression for multiple scattering also given in Equation (3.4) is not valid for the  $55 \mu\text{m}$  thin volumes. So instead the total scattering angle is calculated once for the whole gas volume, which is then redistributed over the pixel volumes properly taking the total track length into account.

### 7.3.5 Track finding and fitting procedure

Ultimately, track finding and fitting in the TPC come together in one procedure of several steps, described below in more detail. First, the detected signal is cleaned, removing large clusters of delta hits. From the list of all remaining hits a track seed is constructed, which is a small track segment giving an initial estimate of the direction and momentum of a track. The Kalman filter then attempts to follow the track inwards towards the IP and outwards towards the calorimeters, selecting hits that are

Figure 7.8:  $d_0$  in the  $xy$ -plane.

close enough to the predicted measurement. If enough hits can be selected, they are set apart as a track candidate. The seed building is repeated until no more suitable seeds can be found. Finally a refit of the found track candidates is performed.

### Delta hits removal

If an ionisation electron has enough energy to make an identifiable track of its own, then this is called a delta electron. Typically in the simulation there are a few tens of delta electrons per event with energies between a few tens of keV up to a few hundred keV. Their radius of curvature is up to a few hundred micrometer, which is too small to be detected. They appear as dense clusters of ionisation elongated in the direction of the magnetic field. Examples of the simulated and digitised hits of a delta electron in the  $rz$ -plane are shown in Figure 7.9 and Figure 7.10.

The hits from delta electrons are removed before the track fit, because if added to the fit this would result in incorrect parameter and error estimations. The hits are selected by their high density and the fact that clusters are elongated in the direction of the magnetic field. First, all hits are projected onto the  $xy$  plane using bins of  $0.5\text{ mm} \times 0.5\text{ mm}$ . If the density over 9 neighbouring bins is higher than 100 per  $1.5^2\text{ mm}^2$ , all hits from these bins are removed. The remaining hits after applying this selection to the hits in Figure 7.10, are shown in Figure 7.11. The efficiency of the delta hits removal procedure is discussed in the next chapter.

### Seed finding

After removal of the delta hits, seeds are selected and the track is fitted. The parameters for the seed finding are provisionally tuned using single tracks and top anti-top events at a centre-of-mass energy of 500 GeV. Seed finding starts at the radially outer 41 mm of pixel readout rows, which is equal to the outer 750 pixel readout rows if the coverage is 100%. After all seeds are checked, the cluster finding moves to the next set of pixel rows equivalent to 41 mm radial distance until reaching the inside of the

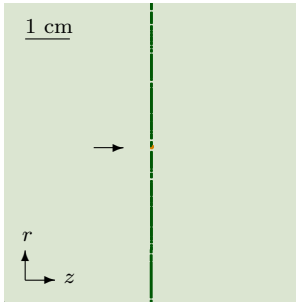


Figure 7.9: Simulated hits of a track (green) with a delta electron (orange), shown in the  $rz$ -plane.

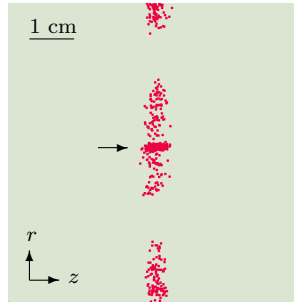


Figure 7.10: Digitised hits (red points) of a track with a delta electron, shown in the  $rz$ -plane.

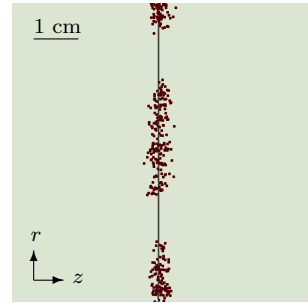


Figure 7.11: Display of the digitised hits (brown points) selected for a track fit (gray line), shown in the  $rz$ -plane.

TPC. Starting at the outer layers allows for a relatively quick selection of seeds with minimal overlapping clusters.

The seed finding proceeds through simple binned clustering. All hits in the selected layers are filled in 600 bins (equivalent to  $0.6^\circ$  per bin) by their  $\phi$  coordinate. The bin with the most hits together with two of its neighbouring bins on each side is selected. The hits from these bins are used as a seed, and shown in Figure 7.12. A straight line from the average position of these hits to the IP is used as a first track estimate. Hits further than 10 mm from this track estimate in the  $z$  or  $xy$  plane are cut from the seed. If 150 hits remain, the seed is fitted using the Kalman filter.

For every pixel row the Kalman filter makes a prediction and adds the hits that add less than 35 to the total  $\chi^2$ . After fitting the hits in the track seed, the Kalman filter proceeds to the more inner layers. If more than 150 hits are picked up in the more inner layers, the fit is considered as a track. If the seed finding did not start at the most outer layers, the track is also extended outwards using the same procedure.

## Refit

In the end, a refit is performed and the track is prepared for output. The refit allows to optionally cut hits that add more than some value to the total  $\chi^2$ , or to neglect multiple scattering or energy loss in the initial fit. The fitted tracks are shown in Figure 7.13.

The estimated parameters using only the TPC are taken from this track fit. In the final reconstruction steps, the selected TPC hits are used in combination with the other detectors. The simulated tracking performance is discussed in the next chapter.

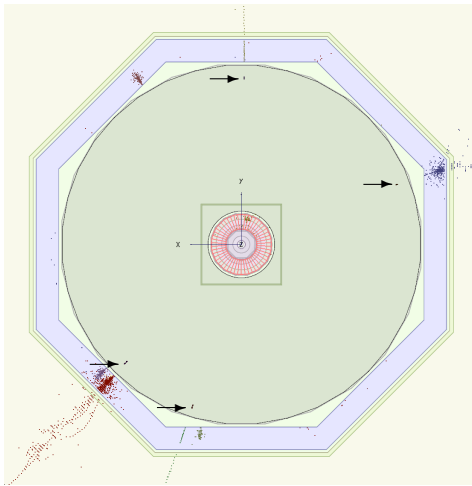


Figure 7.12: Display of track seeds indicated with arrows, for the event shown in Figure 7.2.

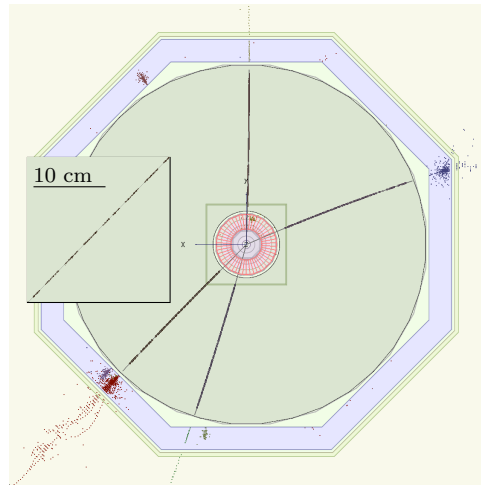


Figure 7.13: Display of the fitted tracks (gray lines) for the event shown in Figure 7.2.



---

# Performance and design of the ILD TPC with a pixel readout

---

The development of the GridPix readout, described in the previous chapters, aims at applications in a large TPC for the ILD. A GridPix readout can improve the tracking precision of the TPC, and thus improves the performance of the ILD. In the end, the most important goal is to contribute to the physics programme of the ILD.

This chapter starts by describing some properties of simulated tracks with a pixel readout, and how they can be related to the GridPix quad module in the previous chapter. Next, the tracking performance of a pixel TPC readout is calculated and compared to a pad based readout. Furthermore, the tracking performance in combination with other ILD subdetectors is described, and reconstructed Higgs strahlung events where the Higgs boson decays to tau leptons are studied. Finally, some aspects of the implementations of GridPix readout for a TPC are discussed.

## 8.1 The simulated TPC with a pixel readout

In the previous chapter, the basic ingredients of the TPC simulation with pixel readout were discussed. The interactions between the gas and high-energy, charged particles produced in the collisions are simulated using the models in the GEANT4 software [200]. For volumes with the granularity equal to the pixel size of  $55\ \mu\text{m}$ , energy deposits are calculated, which are then converted to hits. The drift of the electrons is taken into account in the expressions for the hit resolution. The hits are detected by the readout on the end plate.

The simulation discussed so far assumed an ideal detector with full coverage. A

more realistic implementation is based on the quad module, and will cover only a part of the end plate surface, due to the geometry of the quad detector. For the quad module-based end plate layout, detailed simulations are performed and the number of hits in the TPC is given.

### 8.1.1 End plate layout

In order to calculate the expected performance of a possible implementation, a realistic tiling of the TPC end plate is designed. The tiling is based on the actual dimensions of the tested quad module, as introduced in Chapter 6. The end plate module design is compatible with the pad layout, which has a total of 240 end plate modules. The layout is designed for the end plate dimensions as presented in the design report [13], but does not entirely fit for the recently updated dimensions with a slightly reduced outer radius, as given in [118]. Nevertheless, the readout end plate layout in Figure 8.1 is given for the updated dimensions, so that the most recent detector models can be simulated.

The end plate modules and the quad modules are staggered in order to prevent inactive areas lining up to form larger joint inactive zones. An inactive zone can cause a track segment to be missed, which in turn degrades tracking performance. The quad module positions are chosen by investigating the coverage of straight lines originating from the IP, which are an approximation for highly energetic particle tracks. For each line, the effective coverage is calculated. The staggering of the quad modules is optimised to give approximately the same effective coverage for every line, with as little outliers on the lower side as possible.

The overall coverage using a total of 6623 quads with 26492 chips per end plate is 60%. The number of quads per end plate module varies between 24 for the innermost end plate modules and 29 for the outermost end plate modules. Most of the effective area is lost inside the quad module itself with the guard being the principal inactive surface. Only 13.4% of the surface is lost due to tiling of the rectangular quad module on the circular end plate.

The current design is compatible with the pad readout module design. In order to improve the coverage, the end plate module layout can be optimised for a specific GridPix readout module. In the future, through-silicon via technology [208] can be developed to move the space needed for wire bonding to the back side of the chip, and thus significantly increase the fraction of sensitive surface area.

### 8.1.2 Energy loss in the TPC gas

The energy loss for simulated 50 GeV muon tracks at a polar angle of  $\theta = 85^\circ$  is shown in Figure 8.2. The distribution is Landau-like with a long tail, due to the presence of

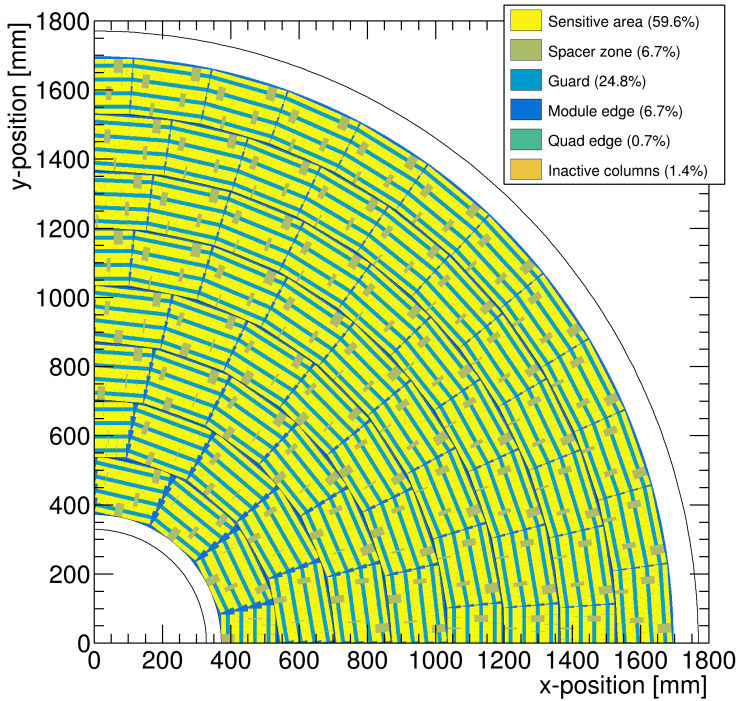


Figure 8.1: Schematic layout of the TPC end plate with pixel readout for one quadrant. The respective coverage is denoted in the legend.

delta electrons. The most probable energy loss is 380 keV. The expected energy loss is described by the Bethe-Bloch Equation (3.2), which yields 647 keV for a 50 GeV muon track in T2K gas. There is a large difference between the most probable value and the mean, because the latter is dominated by very few, very high energy deposits.

### 8.1.3 Number of pixel hits

The energy deposits are converted into pixel hits using an average energy per hit of 32 eV, see subsection 7.2.2. The total number of electron ion-pairs in the gas volume can be calculated from the total energy loss, and is almost equal to the number of hits that would be detected by an ideal, fully efficient detector with a coverage of 100%. Although in the test beam experiments, described in Chapters 5 and 6, the detection of single ionisation electrons was not fully efficient for various reasons, a GridPix can in fact be operated with a high single ionisation detection efficiency, see



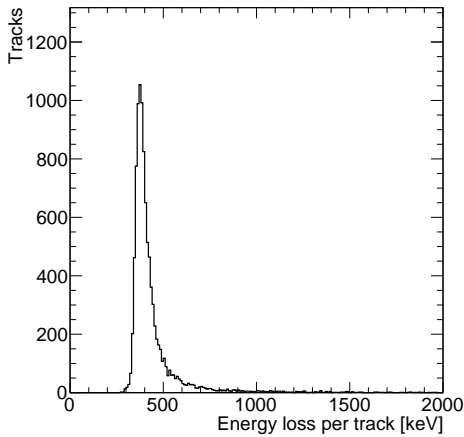


Figure 8.2: The energy loss per track for 10 000 simulated 50 GeV muon tracks at a polar angle of  $\theta = 85^\circ$ .

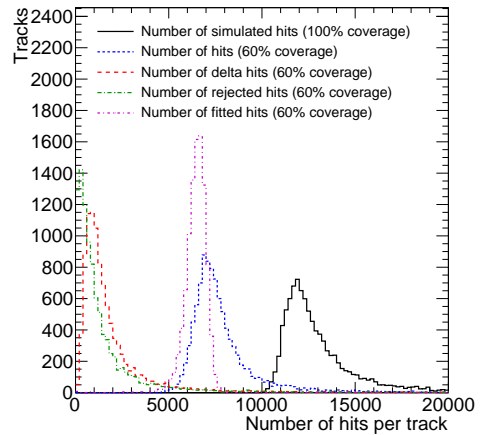


Figure 8.3: The total number of simulated hits per track (black) is shown for 10 000 simulated 50 GeV muon tracks at a polar angle of  $\theta = 85^\circ$ . Taking into account the 60% coverage of the readout end plate, the detectable number of hits (blue) and the number of these which are delta hits (red) are displayed. The delta hit removal procedure removes a number of hits (green), leaving a number of hits to be used in the track fit (purple).

subsection 4.3.2, and as a result a fully efficient detector will be assumed here. For the momentum resolution, the effect of a reduced efficiency is similar to a smaller effective coverage.

The numbers of hits in the simulation for a few categories are shown in Figure 8.3. For a single track, 0.4% of the electron-ion pairs arrive as a second ionisation electron on a pixel that has already been hit. These electron-ion pairs are expected to be undetected, because of the dead time after a pixel has been hit. For a detector with 100% coverage, the most probable number of hits is about 12 000. As expected, the number of hits for a simulated end plate readout with a coverage of 60% is reduced proportionally. In the simulation 23.0% of the electron-ion pairs are from delta electrons, but due to the hits lost on occupied pixels only 22.0% of the hits are from delta electrons. The distribution of the number of delta hits is shown separately. The delta hit removal procedure, introduced in subsection 7.3.5, removes closely clustered hits of which 85.7% are from delta electrons. The distribution of the number of hits rejected by this procedure is similar to the distribution of the delta hits. Ultimately,

the distribution of the number of hits in the track fit is much narrower than the distribution of the number of electron-ion pairs. Of the hits used in the track fit 7.5% are from delta electrons.

## 8.2 Tracking performance

The TPC is one of the tracking detectors, which together aim to determine the five track parameters at the IP. To a large extent, the vertex detector and SIT determine the measurement precision for four out of the five track parameters: the azimuth angle, polar angle, and both impact parameters. However, the measurement precision of the momentum parameter does depend significantly on the TPC performance. For the TPC, the momentum resolution is limited by the multiple scattering in the gas for low momentum tracks, and by measurement errors of the hits for high momentum tracks. Despite being more precisely measured by the vertex detector and SIT, the  $z$ -position resolution (impact parameter) of the TPC is still important, primarily because the tracks are time-stamped by comparing the  $z$ -position in TPC to the  $z$ -position in the silicon detectors. In order to benefit fully from the measurement in the TPC, even close by tracks should be separated and measured as independently as possible. This is quantified by the two-track separation. In addition to providing a measurement of the track parameters, the TPC provides input for particle identification through energy loss  $dE/dx$  measurements.

### 8.2.1 Momentum resolution

The momentum resolution is important for the determination of the energy of particles. The ILD physics programme requires a momentum resolution expressed as  $\sigma_{1/p_T}$  of better than  $10^{-4} \text{ GeV}^{-1}$  for high momentum tracks in the TPC alone. The momentum is determined from the curvature of the track in the magnetic field. So the required resolution translates into requirements on the hit resolution, which has to be met by the readout technology.

Here three separate methods to investigate the simulated momentum resolution are utilised. First, the true simulated momentum is compared to the reconstructed momentum. Any difference between the two is due to the resolution of the TPC. Secondly, the fit using the Kalman filter (see subsection 7.3.2) includes an estimate of the precision of the track parameters at each point in the form of the covariance matrix. The first and second methods are cross checked by calculating the pull distribution. The pull distribution is defined as the distribution of the difference between the simulated momentum and the reconstructed momentum divided by the expected precision, which is acquired from the covariance matrix. Lastly, the expected performance is calculated using the Gluckstern equations [209].

The Gluckstern equations are used to analytically estimate the expected momentum resolution of a tracking detector. The two most important contributions to the expected momentum error are analytically calculated by considering two extreme situations: the case when the momentum resolution is limited by the detector resolution, and the case when the momentum resolution is limited by the multiple scattering. The updated numerical expressions of the Gluckstern equations are found in [210]. The expectations from the Gluckstern equation are compared to the simulated tracking behaviour as a function of particle momentum for the pad-based readout, the pixel readout with 60% coverage, and the pixel readout with ideal 100% coverage.

### Expected performance from measurements errors

The expected momentum resolution of the tracker  $\sigma_{1/p_T} = (\delta p_T/p_T^2)$  from measurement errors can be calculated by neglecting the multiple scattering contributions. Assuming a tracker in a homogeneous magnetic field, which measures  $N$  equidistant points with a resolution  $\sigma_{r\phi}$  in the  $r\phi$ -direction, transverse to a track, the expression for the momentum resolution  $(\delta p_T/p_T)$  is

$$\left(\frac{\delta p_T}{p_T^2}\right)_{\text{meas.}} = \frac{\sigma_{r\phi}}{0.3BL_0^2} \sqrt{\frac{720}{N+4}}, \quad (8.1)$$

where  $p_T$  is the momentum of the particle in units of GeV/c,  $\sigma_{r\phi}$  is the measurement point precision in units of m,  $L_0$  is the projection of the track length in the (transverse)  $xy$ -plane in units of m, 0.3 is a factor related to the units, and  $B$  is the strength of a magnetic field parallel to the  $z$ -axis in units of T.

The error on the momentum measurement due to measurement errors expressed as  $(\delta p_T/p_T)$  turns out to be proportional to the momentum. The reduced relative tracking performance  $(\delta p_T/p_T)$  for tracks with a high transverse momentum is because the radius of curvature of these tracks is larger. For this reason, the momentum resolution is expressed as  $\sigma_{1/p_T} = (\delta p_T/p_T^2)$ .

The contribution to the resolution from measurement limitations can be calculated for muon tracks at a polar angle of  $\theta = 85^\circ$  in the ILD TPC. The velocity is  $\beta \approx 1$ , the magnetic field strength is  $B = 3.5$  T, and the track length in the radial direction without the inner and outer service areas is  $L_0 = 1.32$  m, see Table 2.2. The hit resolution is  $\sigma_{r\phi}^{\text{pixel}} = 4.1 \times 10^{-4}$  m for pixels as given in Equation (7.2), and  $\sigma_{r\phi}^{\text{pad}} = 9.9 \times 10^{-5}$  m for pads as given in Equation (7.1). For pads the number of measurement points is  $N = 220$ , and for pixels the number of measurement points is  $N = 6442$  for 60% coverage, as given in Figure 8.3, and  $N = 10880$  for 100% coverage. Using these numbers, the contribution to the momentum resolution  $\sigma_{1/p_T} = (\delta p_T/p_T^2)$  from the measurement errors is  $9.7 \times 10^{-5} \text{ GeV}^{-1}$  for pads,  $7.5 \times 10^{-5} \text{ GeV}^{-1}$  for pixels with 60% coverage, and  $5.8 \times 10^{-5} \text{ GeV}^{-1}$  for pixels with 100% coverage.

### Expected performance from multiple scattering

Multiple scattering against the nuclei of the gas atoms deflects high energy charged particles (see subsection 3.1.4), which reduces the achievable accuracy of a momentum measurement. The multiple scattering contribution to the expected performance is calculated for the gas of the TPC using the optimum weights for the measurement points. The material of the detector, i.e. the gas, is uniformly distributed. The expression for the momentum resolution  $(\delta p_T/p_T^2)$  in  $(\text{GeV}/c)^{-1}$  is

$$\left(\frac{\delta p_T}{p_T^2}\right)_{\text{m.s.}} = \frac{0.0136 \text{ GeV}/c}{0.3\beta B L_0 p_T} \sqrt{\frac{x_{\text{material}}}{X_0}} \left(1 + 0.038 \ln \frac{x_{\text{material}}}{X_0}\right) \quad (8.2)$$

With  $\beta = v/c$ , where  $v$  is the velocity,  $x_{\text{material}}$  is the total length of the traversed material,  $X_0$  is the radiation length of the material, and the other quantities have the same meaning and units as in Equation (8.1).

In the limit that multiple scattering dominates, the error on the momentum measurement expressed as  $(\delta p_T/p_T)$  is independent of the momentum, because the increased radius of curvature for higher momentum tracks is compensated by a reduced scattering angle. When added to the contribution from the measurements errors, multiple scattering limits the momentum resolution for lower momentum tracks.

The same case as for the measurement errors is considered. The multiple scattering contribution for muon tracks at a polar angle  $\theta$  of  $85^\circ$  in the ILD TPC is calculated with the same parameters as above: the velocity is  $\beta \approx 1$ , the magnetic field strength is  $B = 3.5 \text{ T}$ , and the track length in the radial direction is  $L_0 = 1.32 \text{ m}$ . For scattering in the uniform TPC gas  $x_{\text{material}} = L_0/\sin\theta$ , and the radiation length is set to  $X_0 = 115 \text{ m}$  in the simulation (a calculation using the numbers in reference [45] results in  $X_0 = 117 \text{ m}$ ). Equation (8.2) is evaluated, and the multiple scattering contribution to the momentum resolution is  $\sigma_{1/p_T} = (\delta p_T/p_T^2) = 8.7 \times 10^{-4}/p_T$ .

### The momentum resolution

The momentum resolution for muon tracks at a polar angle of  $\theta = 85^\circ$  for a pad readout, a pixel readout with a coverage of 60%, and a pixel readout with a coverage of 100% is shown in Figure 8.4. The expected momentum resolution is acquired from the covariance matrix calculated by the track fit, and results in a correctly distributed pull, i.e. it agrees with the expected momentum resolution acquired from the standard deviation of the reconstructed momentum for each data point.

The expected momentum resolution is compared to the prediction by the Gluckstern equations. The contribution from measurement errors described in Equation (8.1) and the contribution from multiple scattering described in Equation (8.2) are summed quadratically:  $(\delta p_T/p_T^2)_{\text{exp.}}^2 = (\delta p_T/p_T^2)_{\text{meas.}}^2 + (\delta p_T/p_T^2)_{\text{m.s.}}^2$ . The simulated res-

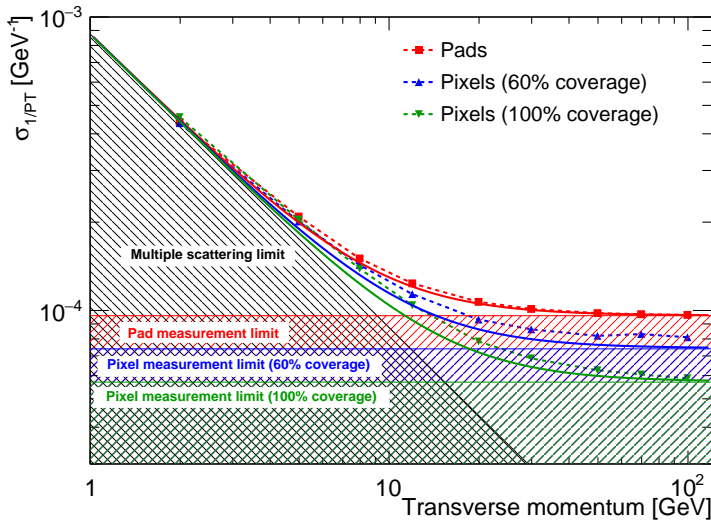


Figure 8.4: The simulated momentum resolution of the TPC expressed as  $\sigma_{1/p_T}$  for muons at a polar angle of  $\theta = 85^\circ$  as function of the transverse momentum. The different readout options discussed in the text are displayed as points connected by dashed lines. The calculated limits from multiple scattering and measurement uncertainties are filled. The thick colored curves are the sum of both contributions.

olution and the expectation agree well for the low momentum tracks in the multiple scattering dominated regime, and for high momentum tracks in the measurement error dominated regime. For the pixel readout with a coverage of 60%, the simulated resolution is not as good as the expected resolution, possibly because the assumption of equidistant measurement points is not a sufficiently good approximation, due to inactive regions on the end plate.

In the intermediate region between 8 GeV and 30 GeV, the simulated performance of the pixel TPC is not as good as the expectation from the Gluckstern equations. There are several possible explanations. The Gluckstern equations do not take into account the energy loss along the track, which gives an additional contribution to the momentum resolution. In addition, a constant number of measurement points was assumed, while for a pixel TPC the number of hits is proportional to the number of electron-ion pairs, calculated from the energy loss in the gas. The large fluctuations on the number of hits is not taken into account, and, more importantly, the number of hits depends on the momentum of traversing particle. For a muon, the energy loss for a muon with a momentum of 100 GeV is more than one and a half times as large as the energy loss for a muon with a momentum of 2 GeV, see Figure 3.2.

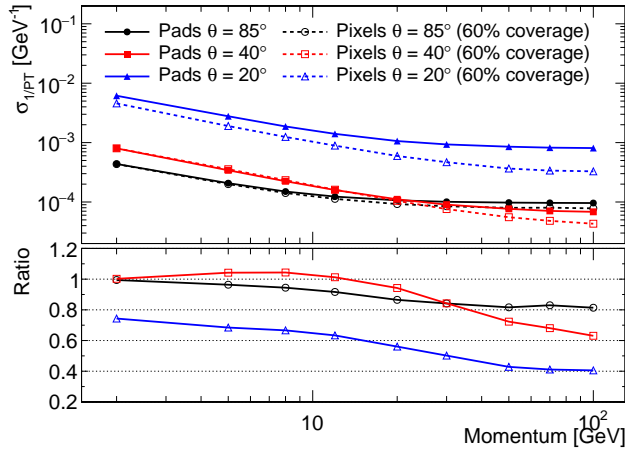


Figure 8.5: The simulated momentum resolution of the TPC expressed as  $\sigma_{1/p_T}$  for muons of a pad readout (solid lines) and a pixel readout with a 60% coverage (dashed lines) as a function of momentum at three different polar angles. The ratio of the pixel and pad momentum resolutions is given in the bottom pane (solid lines).

The momentum resolution is also investigated for tracks at different polar angles. In the top pane of Figure 8.5, the momentum resolution is shown for muon tracks with a polar angle  $\theta$  of  $85^\circ$ ,  $40^\circ$  and  $20^\circ$  as a function of muon momentum. In the bottom pane of Figure 8.5, the ratios of the pixel/pad momentum resolutions are given.

Towards lower momenta, the domination of the multiple scattering error causes the momentum resolution for the pixel and pad readouts to be roughly the same, hence their ratio is 1 for the 2 GeV tracks. For the most forward tracks at a polar angle of  $\theta = 20^\circ$  this point is not reached, because the contribution from the measurement errors is much larger.

Towards higher momentum tracks the contribution from measurement errors is dominant. The curve flattens out, because the resolution expressed as  $\sigma_{1/p_T}$  is constant as a function of momentum. The pixel readout has a higher precision than the pad readout. This especially holds for hits with a short drift distance, so the largest improvement is seen for tracks at a small polar angle. Furthermore, the very forward tracks benefit from a pixel readout, because for a pad readout the number of crossed readout rows is reduced, and therefore the number of hits is smaller. In contrast, the number of pixel hits remains proportional to the track length.

At intermediate momenta between 5 GeV and 12 GeV, the difference in momentum resolution between the pad readout and pixel readout is smaller, because of the smaller number of pixel hits for these tracks. For a track that reaches the outer TPC radius,

the number of pad hits is always 220. However, the number of pixel hits depends on the energy loss, which is smaller for lower momentum tracks in accordance with the Bethe-Bloch equation, see Figure 3.2. In a more detailed simulation, the pad resolution would also depend on the energy loss.

For the ILD TPC the contribution of the measurement errors to the momentum resolution is the most important, because the contribution from multiple scattering is only dominant for the lowest energy particles since they scatter little in a gas, and most of the particles have a momentum for which the measurement error is the dominant contribution. The higher precision of the pixel readout improves the momentum resolution over the pad readout, even for a coverage of 60%. Increasing the coverage to 100% results in a yet larger improvement.

A fully efficient pixel readout with 100% coverage gives close to the ultimate TPC readout performance in terms of momentum resolution: the hit position uncertainty from the TPC is negligible compared to the uncertainty from diffusion in the gas, and the maximal number of measurement points is reached if all ionisation electrons are detected. The momentum resolution of a TPC with a fully efficient pixel readout with 100% coverage can only be improved through other aspects of the TPC. The diffusion and multiple scattering can be reduced through an increase in the magnetic field. Alternatively, a different gas composition or different gas pressure can give a lower diffusion, a larger number of ionisation-electrons, or less scattering in the gas. Finally, a larger radius is beneficial because it reduces the contribution from multiple scattering proportional to  $\propto 1/\sqrt{L_0}$  and the contribution from measurement errors proportional to  $\propto 1/L_0^2$ .

## 8.2.2 z-resolution and time resolution

For a TPC, the time resolution is connected to the  $z$ -resolution. Here the  $z$ -resolution is the error on the  $z$ -position of the track. Tracks are time stamped by comparing their absolute  $z$ -position from the silicon trackers with the  $z$ -position determined from the drift time measurement in the TPC.

Figure 8.6 shows the  $z$ -resolution of the TPC, which is the error on the  $z$ -coordinate of the track at the inner and outer TPC radius. It can also be regarded as the resolution on the  $z$  impact parameter at the point where the track either enters the TPC at the inner radius, or exits the TPC at the outer radius.

The shape of the curves can be explained mostly by the contributions from measurement errors. Because the most precise measurement point is close to the end plate, the resolution is slightly better for tracks at a  $40^\circ$  polar angle than tracks at an  $85^\circ$  polar angle, and for these tracks the most precise measurement is close to the readout plane at the outer TPC radius. For the tracks at an  $85^\circ$  angle there is little difference in the measurement at the inner and outer radius as the drift distance is

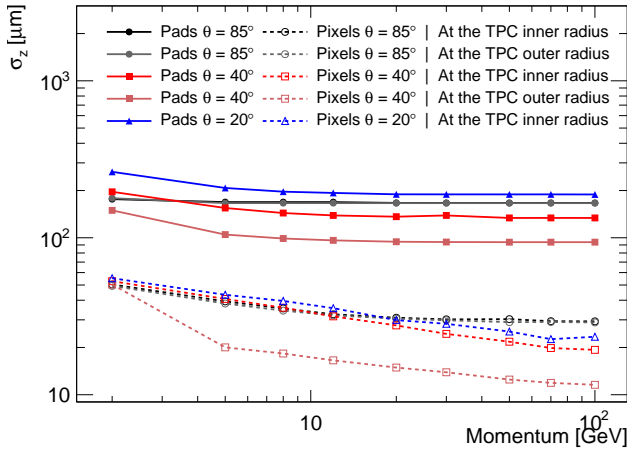


Figure 8.6: The resolution on the  $z$ -position of a muon track in a TPC with a pad readout (solid lines) and a pixel readout with a 60% coverage (dashed lines) as a function of momentum at three different polar angles. The resolution is given at the inner TPC radius. For the angles where the track reaches the TPC outer radius, the resolution is also given at the outer radius.

almost the same. The  $z$ -resolution is worse for forward tracks at a polar angle of  $\theta = 20^\circ$ , since these cross fewer pad rows and thus have fewer hits. The tracks of particles with a smaller momentum have a less precise  $z$ -resolution, because of multiple scattering. This effect is more severe for forward particles, because these traverse more material.

For the pixels the  $z$ -resolution improves with the momentum for all angles and both at the inner and outer radius. The reason is the growing number of hits with momentum, due to the increasing energy loss. At the higher momentum points, the tracks at a polar angle of  $\theta = 40^\circ$  benefit from reduced multiple scattering.

The highly precise track  $z$ -resolution of less than  $100 \mu\text{m}$  puts stringent requirements on the relative precision of the drift velocity and other systematic effects. A study for the CLIC ILD detector estimated the influence on the drift velocity of some factors: the electric field, temperature and pressure. The relative precision was estimated to be  $7 \times 10^{-6}$  corresponding to  $16 \mu\text{m}$  [211], although the maximal temperature gradient of  $1 \text{ K}$  might be too optimistic for the ILD detector at the ILC because of the different sub-detectors involved. Moreover, the hit  $z$ -resolution is assumed to be entirely uncorrelated, while in fact the alignment and a shared clock will cause some correlation, which will degrade the track  $z$ -resolution.

The  $z$ -resolution can be converted back to a time resolution. Tracks are time



stamped by comparing the absolute  $z$ -position from the silicon trackers with the  $z$ -position determined from the drift time measurement in the TPC. The time is calculated from the difference in  $z$ -position divided by the drift velocity  $v_{\text{drift}}$  of  $75 \mu\text{m}/\text{ns}$ . The silicon detectors SIT and the SET will be built from respectively 2 layers of CMOS pixels sensors and 1 double-layer of strip sensors, having a  $z$ -position resolution of approximately  $\sigma_z = 5 \mu\text{m}$  and  $\sigma_z = 50 \mu\text{m}$  respectively. For example, a total  $z$ -resolution of  $37 \mu\text{m}$  corresponds to a time resolution of about 0.5 ns. For tracks that pass through the end plate, the time resolution will depend on how well tracks that go through the readout surface can be detected.

### 8.2.3 Two-track separation performance

The ability to separate two close-by charged particle tracks is required to make an accurate measurement of all tracks in an event, especially for the tracks in dense collimated jets. An energy loss  $dE/dx$  measurement in the TPC can easily guarantee that there are two tracks, but the ILD specifications [13] require a precise measurement of the track position if the tracks are more than a few mm apart. For a pad based readout, the precision of track measurements is substantially reduced if the distance between two tracks is less than the width of a pad [212] of about 1 mm, i.e. the two-track separation is about 1 mm for a pad readout.

Because the pixel width is much smaller than the pad width, the two-track separation for a pixel readout is instead limited by diffusion. For a pixel TPC, the hit position transverse to the track is normal distributed with a maximal standard deviation of about  $400 \mu\text{m}$  for the full drift distance. For two overlapping tracks, the number of hits lost due to occupancy is maximally a few percent. A separation of 2 standard deviations is sufficiently large to have a small impact on the reconstructed track parameters. So a pixel TPC will at least be able to separate two tracks that are more than  $800 \mu\text{m}$  apart, and much less if the diffusion is smaller.

The actual two-track separation performance in the TPC will depend on the employed algorithms and techniques to use all information from the TPC and other detectors. Most high energy particles within a jet will be separated by at least a few mm when they reach the outer radius of the TPC. Information from the position along the drift direction should also be taken into account. Therefore, the choice of tracking algorithms can have a large impact on the ultimate two-track separation that can be achieved with a pixel readout.

### 8.2.4 Energy loss measurement

An important feature of a TPC is particle identification by energy loss  $dE/dx$  measurements. The measured energy loss resolutions as a function of track length for the

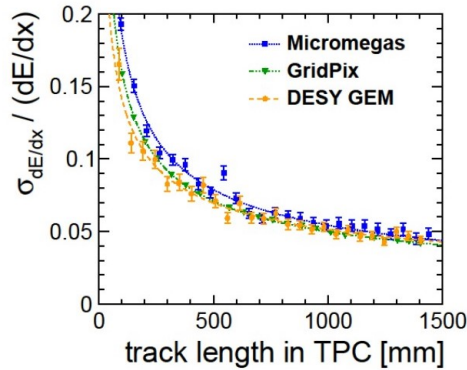


Figure 8.7:  $dE/dx$  performance comparison for the three TPC readout technologies under investigation. Figure taken from [118].

three potential readout technologies for the ILD TPC are shown in Figure 8.7. The data points for the GridPix originate from the analysis discussed in subsection 5.4.7.

The  $dE/dx$  resolution defined as the r.m.s. over the mean  $\sigma_{dE/dx} / (dE/dx)$  depends on the track length by the relation

$$\frac{\sigma_{dE/dx}}{(dE/dx)} = c_0 L^{-k}, \quad (8.3)$$

where  $L$  is the track length,  $c_0$  is a constant representing the  $dE/dx$  resolution, and  $k$  is an exponential constant. For a GridPix readout, the number of measurement points is proportional to the track length  $L$ , so an exponential constant of  $k = 0.5$  is expected.

The data points for the three technology options in Figure 8.7 are fitted with this equation. With a  $\chi^2/n.d.f.$  of 20.3/22, the relation describes the GridPix data well. The parameters are found to be  $c_0 = (1.660 \pm 0.007) \text{ mm}^{-k}$ , and  $k = 0.5073 \pm 0.0009$ .  $k$  being larger than the statistically expected 0.5 can be explained by the truncated mean method becoming more reliable as more measurements points are used.

For all three readout technologies the maximal effective track length of 132 cm can only be realised with an ideal detector with 100% coverage. The  $dE/dx$  resolutions for the ideal 100% coverage are 4.7% for the Micromegas, 4.5% for the DESY GEMs, 4.3% for the GridPix readout. The pad readouts with Micromegas or GEM amplification have an expected coverage of about 95%, but the GridPix coverage using a quad module is currently only 60%. As a result, the effective track length for a pixel readout based on the GridPix quad module is 60% of the total track length of 132 cm, which equals 79 cm. Reading of the corresponding  $dE/dx$  resolution at the expected

effective track length of 79 cm results in an expected  $dE/dx$  resolution of 5.9%, which is above the required minimal  $dE/dx$  resolution of 5%. Increasing the coverage or application of efficient cluster counting (see subsection 5.4.7) can improve the energy loss resolution.

## 8.3 Performance of the ILD

Although for the evaluation of the pixel readout the clearest measure is the performance of the TPC alone, for the optimisation of the ILD the combined performance of all subdetectors is actually more important. The TPC and silicon tracking detectors are in many ways complementary. The silicon tracking is more suitable for the inner detector layers and provides the most precise measurement of the impact parameters, while the TPC has more measurement points and can measure the energy loss  $dE/dx$ . However, for the momentum measurement the combination of both subdetectors is required to obtain the best possible precision. In this section, the contribution of the pixel readout to the overall ILD performance is discussed.

### 8.3.1 Tracking performance of the ILD

The ILD utilises the particle flow method, which requires every particle to be reconstructed. Therefore the efficiency of the charged particle pattern recognition is an important parameter. Because of the high number of hits in the TPC, it provides crucial information for track finding. Furthermore, the ILC physics programme requires a momentum resolution of at least  $\sigma_{1/p_T} = 2 \times 10^{-5} \text{ GeV}^{-1}$ , in particular for the Higgs recoil mass measurement [13]. In order to study the tracking performance of the ILD detector, and to demonstrate the integration of the pixel TPC simulation in the existing framework, a modified version of the ILDPerformance processor [201] is made and used to analyse the simulated performance. This enables an investigation of the track finding efficiency and to determine the precision of the track parameters. The simulation does not include the beam backgrounds and event overlay from neighbouring bunch crossings, which should also be studied in the future. As a result, the pad readout performance is not identical to the official numbers in [118].

#### Efficiency

The efficiency of track finding is tested using events in which a top anti-top pair is produced at a centre-of-mass energy of 500 GeV, because these events have about 40 charged particle tracks, and therefore demand a lot of the tracking performance. The difference in efficiency between a pad readout and a pixel readout is almost exclusively due to differences in the pattern recognition. Because a pixel readout is expected to

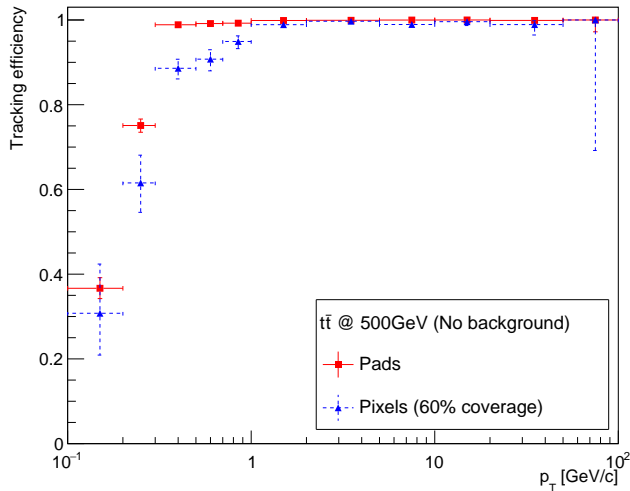


Figure 8.8: Simulated track finding efficiency for tracks from top anti-top events at a centre-of-mass energy of 500 GeV as a function of transverse momentum  $p_T$ .

be more precise and have more measurement points, the efficiency is expected to be at least as good. Nonetheless, the reduced coverage can be a reason for a loss in track finding efficiency. In addition, in the simulation of a pixel TPC, the delta electrons produce more hits because they are followed more closely due to the smaller virtual volumes.

The ILD track finding efficiency is shown in Figure 8.8 for 1000 pad events, and 90 pixel events. For 10 pixel events the reconstruction failed on one of the tracks, which possibly introduces a small bias. The efficiency is defined as the ratio of reconstructed and simulated tracks that originate from within 10 cm of the IP, have at least 4 hits, and have a hit purity of 75% or better. The hit purity is defined as the ratio of the number of hits belonging to the dominant simulated particle (excluding delta hits) and the total number of track hits. The low momentum tracks curl in the TPC and it is harder to connect the hits. The efficiency for low momentum tracks is poor for the pixel readout, because of the lack of tuning. The efficiency for low momentum tracks is expected not to depend strongly on the readout technology, but is determined by the track finding methods.

For the simulated pad readout the efficiency is very high. For the pixel readout, the efficiency is sufficiently high for simple performance studies, but should be further improved for in-depth physics analyses. In physics studies even one missing track per event can have a significant impact. The reduced track finding is most likely due to

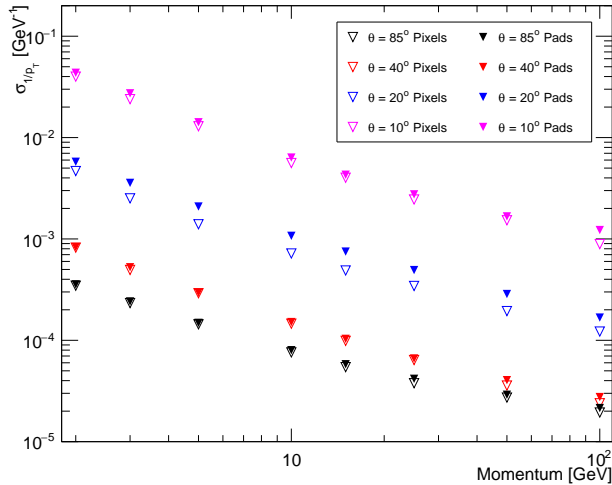


Figure 8.9: The simulated momentum resolution of the combined tracking detectors expressed as  $\sigma_{1/p_T}$  for muons of a pad readout (open triangles) and a pixel readout with a 60% coverage (solid triangles) as a function of momentum at three different polar angles.

errors in the pattern recognition. The track finding for a pad readout with almost full coverage was adapted for a pixel readout, and should be improved to better take into account the inactive regions of the TPC. In order to further improve the track finding efficiency, even for the pad readouts, a conventional method is to employ a combination of different pattern finding methods.

### Momentum resolution

The particle interactions are simulated for the entire detector, and the tracks are reconstructed in both the TPC and silicon trackers. The expected momentum resolution is shown in Figure 8.9 for the pad readout, and the pixel readout with a coverage of 60%. For both the pixel and the pad readout, the resolution is extracted from the covariance matrix of the track fit.

Compared to the resolution discussed in the previous section, and shown in Figure 8.5, additional measurements from the silicon trackers are included. For tracks at a polar angle of  $\theta = 85^\circ$ , the pixel readout has a better resolution at a momentum of 25 GeV and above. For tracks at a polar angle of  $\theta = 40^\circ$ , the transverse momentum is only a fraction of the total particle momentum, and the pixel readout is expected to perform better at a momentum of 50 GeV or higher. At low momenta,

the performance of both readouts is expected to be similar because the momentum resolution is limited by multiple scattering. For the most forward tracks the pixel readout performs better, because of the larger number of hits. The number of hits in the pad readout is limited by the number of crossed readout rows, while for the pixel TPC the number of hits is proportional to the track length. The tracks at a polar angle of  $\theta = 10^\circ$  barely have any hits in the TPC, but still a small improvement is achieved. For tracks at a polar angle of  $\theta = 20^\circ$  the performance difference between pads and pixels is the largest.

## 8.4 The Higgs boson decay to tau leptons

An example of reconstructed events is discussed to demonstrate the capabilities of the simulation, and touch upon some concepts in the context of a TPC with pixel readout. Here events with a Higgs boson produced in the process  $e^+e^- \rightarrow ZH \rightarrow \mu^+\mu^-\tau^+\tau^-$  at a centre-of-mass energy of 250 GeV are investigated. In these Higgs strahlung ( $HZ$  production) events, the  $Z$  boson decays to a pair of muons, and the Higgs decays to a pair of taus. From the pair of muons the recoil mass will be reconstructed precisely, which can be used to determine the Higgs mass and total  $\sigma(HZ)$  cross section.

The Higgs boson decay to a pair of tau leptons is specifically chosen. The tau leptons produced in the decay of the Higgs boson will decay within a few mm to a tau neutrino plus one or more charged particles and possibly neutral particles. For especially the decays to charged pions and  $\rho$  mesons, the angular distribution of the produced particles will allow to determine the spin state of the tau lepton. Using this information, the Higgs CP state can be determined [213]. Furthermore, because the Higgs boson has a much larger mass than the tau leptons, the tau leptons have a high momentum, and therefore the tau lepton decay products are collimated. For this reason tau leptons with a large momentum are known as a benchmark process for the two-track separation, especially when a tau lepton decays to three charged pions.

### 8.4.1 Cross section and number of events

This data set is used as an example and has severe limitations. The data set has about 2000 simulated events from collisions of fully left polarised electrons and fully right polarised positrons, such that their spin is aligned. The process has a cross section of 1.06 fb. At the ILC the electron and positron beams are 80% and 30% polarised respectively, and the time is shared between the four different polarisation states, see Section 2.1. For an integrated luminosity of  $500 \text{ fb}^{-1}$  acquired during the first 4.5 years of the nominal running scenario (see Figure 2.2), there are about 158 events expected for this polarisation state. The contribution from the mirror polarisation configuration with right polarised electrons and left polarised positrons is of the same order of

magnitude. Due to the chiral structure of the weak interaction, the contribution from the collisions of electrons and positrons with their spins polarised in the opposite direction is much smaller.

### 8.4.2 Object definitions

The object definitions for the simple analysis use the existing ILD particle flow framework. The particle flow algorithm builds a particle flow object for each particle that combines the measurements from the trackers, calorimeters and other subdetectors. The objects are selected using criteria inspired by a previous study [214].

Muons can be selected efficiently because they penetrate much further into the detector than other particles. Particles that deposit more energy in the hadronic calorimeter than in the electromagnetic calorimeter and deposit less than 60% of their energy in the calorimeters are selected as muons. Photons detected within 1 mrad of the muon direction are added to the muon energy. If there are multiple possible pairs of oppositely charged muon candidates, the pair whose combined invariant mass is closest to the  $Z$  boson mass is selected.

The particles originating from a single tau decay are selected by repeating the following procedure. Select the highest-energy remaining charged particle, and continue to assign particles within 1 rad of its direction while the combined invariant mass is smaller than the tau mass. In the case that exactly two photons are added to a charged particle, they are assumed to be from the decay of a single neutral pion and their momenta are scaled such that their invariant mass is equal to the neutral pion mass. The highest energy candidate of each charge is selected as the tau object. The left over objects are kept for the calculation of the momentum imbalance.

### 8.4.3 Efficiency

Each event is required to have at most 7 charged objects, a pair of oppositely charged muon candidates, and a pair of oppositely charged tau candidates. For the TPC pad readout option, 83% of the events fulfil these requirements, while for the not optimised tracking with a pixel readout only 75% events are selected. In order to compare the tracking performance alone, only the 65% of the events successfully reconstructed for both readout options are selected. In a previous study [214] additional background rejection cuts brought the signal event count down by another 25%.

### 8.4.4 Recoil mass

Because the initial state is approximately known, part of the final state products can be used to find the invariant mass of the other final state products. This is called the

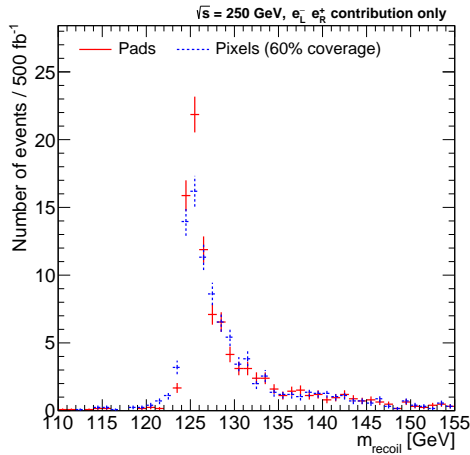


Figure 8.10: Distribution of the recoil mass  $m_{\text{recoil}}$  calculated using Equation (8.4) for simulated  $e^+e^- \rightarrow ZH \rightarrow \mu^+\mu^-\tau^+\tau^-$  events with fully left polarised electrons ( $e_L^-$ ) and fully right polarised positrons ( $e_R^+$ ). The distribution is shown for both a pad based readout (red solid line) and a pixel readout with 60% coverage (blue dashed line).

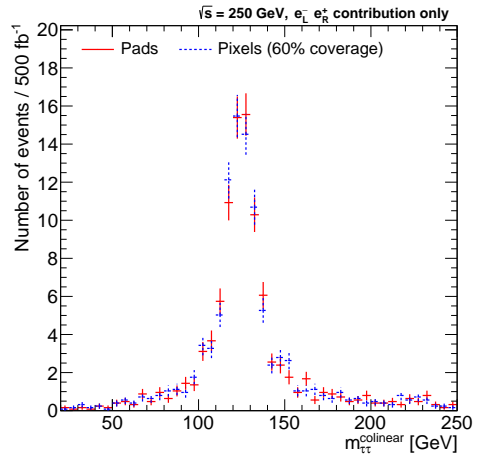


Figure 8.11: Distribution of the mass  $m_{\tau\tau}$  of a tau lepton pair calculated using the colinear approximation for simulated  $e^+e^- \rightarrow ZH \rightarrow \mu^+\mu^-\tau^+\tau^-$  events with fully left polarised electrons ( $e_L^-$ ) and fully right polarised positrons ( $e_R^+$ ). The distribution is shown for both a pad based readout (red solid line) and a pixel readout with 60% coverage (blue dashed line).

recoil mass, and can be used to find the invariant mass of the Higgs boson from the decay products of the  $Z$  boson. The recoil mass  $m_{\text{recoil}}$  is given by

$$m_{\text{recoil}}^2 = p_{\text{recoil}}^2 = (p_{\text{initial}} - p_{\mu^+} - p_{\mu^-})^2, \quad (8.4)$$

where  $p_{\text{recoil}}$  is the four-momentum of the recoiling system,  $p_{\mu^-}$  and  $p_{\mu^+}$  are the four-momenta of the muons, and  $p_{\text{initial}}$  is the four-momentum of the initial state. The initial state is defined by the centre-of-mass energy of the collision, and a small amount of horizontal momentum due to the crossing angle of the two beams. The horizontal momentum is the product of the beam energy and the crossing angle of 14 mrad.

The recoil mass from the muon pair is shown in Figure 8.10. The distribution peaks around the Higgs mass of 125 GeV. The width of the distribution is the result of measurement uncertainties and uncertainties on the energy of the incoming beams. The contribution from the energy of the beams is caused by beamstrahlung and components in the accelerator chain, such as the initial linac and damping rings.



These effects may cause downward fluctuations of the beam energy. As a result, the assumed initial state energy is higher than the actual collision energy, hence the tail towards higher recoil masses.

The distribution for the recoil mass is shown for both the pad and pixel readout. For the pad readout 83 simulated events (80% of the selected events) have a Higgs recoil mass between 115 and 135 GeV, and the Full Width at Half Maximum (FWHM) is 2.5 GeV. For the pixel readout 82 simulated events (79% of the selected events) are in this recoil mass range, and the FWHM is 3.8 GeV.

It is expected that a TPC with a pixel readout will have a higher precision on mass measurements than a TPC with a pad readout, due to a better momentum resolution. However, for the simulated pixel readout the fitted momentum of some tracks is inaccurate due to missing hits near module edges, which should be further optimised in the future. Therefore the distribution of the recoil mass in Figure 8.10 is wider for the pixel readout than it is for the pad readout.

#### 8.4.5 Tau reconstruction

The Higgs boson decays to tau leptons, which have a number of decay channels. A tau neutrino and at least one charged particle are always among the decay products. Since there is at least one neutrino, which is not detected, the momentum of the tau lepton cannot be fully reconstructed. Consequently the Higgs boson's momentum cannot be directly reconstructed from its decay products. In order to estimate the momentum of the invisible decay products, the colinear approximation [215] can be used. The invisible decay products are assumed to be colinear to the visible decay products, which approximately holds because of the tau lepton's large momentum. The magnitude of the momentum of both neutrinos is calculated from the total momentum imbalance in the event, i.e. the missing momentum.

The total invariant mass of the tau lepton pair in the colinear approximation is shown in Figure 8.11. The distribution has its peak near the Higgs mass, demonstrating the accuracy of the colinear approximation. The spread in the distribution can be explained by measurement uncertainties and uncertainties in the reconstruction of events. For both the pad and the pixel readout 58 simulated events (56% of the selected events) are within the range between 115 and 135 GeV, and the FWHM is 21 GeV for both the pad and pixel readout. Although there are small differences in momentum resolutions between pads and pixels, the distributions are similar, possibly because other aspects of the event reconstruction are more important.

#### 8.4.6 Comparison of the pixel and pad tracking performance

These simple distributions already show that a comparison between detector technologies in terms of physics performance will be difficult. Overall, the pad and pixel

reconstruction use comparable strategies, and the other detector components are the same, so the performance is similar. A good comparison between both readouts requires a well-optimised reconstruction, and an analysis tailored to the strengths of each readout. Furthermore, all polarisation states and background processes should be considered. For the pixel readout the track finding strategies should be further optimised and an improved track fit should take into account missing hits at the edge of module boundaries. Besides the performance of the detector, the integrated luminosity is important for the precision in this channel [214].

## 8.5 The TPC system with GridPix readout

In subsection 3.6.1, some aspects in the operation of a TPC at the ILC were discussed. In this section, the implementation of a GridPix readout specifically is described. Many aspects of a TPC with GridPix readout are very similar to a TPC with a pad readout, and they are especially similar to a pad readout with Micromegas amplification. However, a few things are different. The present power consumption of the GridPix readout is larger than a similar sized pad readout. This power consumption generates heat, which must be extracted using an active cooling system. For a GridPix readout, a low occupancy is required to achieve the maximal possible efficiency. The number of GridPix hits also determines the required link speeds and data volume, which is larger than for a pad readout. As for a pad readout, the number of back flows should be small.

### 8.5.1 Power consumption

The power consumption of the TPC readouts is mainly from the readout electronics. Compared to this, the power consumption of the gas amplification is negligible. The continuous operation of the pad readout requires about 25 W per module, accumulating to about 6 kW per end plate [216]. The ILC has a duty cycle of about 0.5%. By power pulsing a reduction of 50 to 100, leads to an expected power consumption of less than 120 W per end plate.

The current GridPix readout is not yet optimised for power consumption, and requires more power. The power consumption of the quad module in continuous low rate operation is 8 W of which 2 W in the LV regulator. With about 6 000 quad modules per end plate, continuous operation would need a total power of about 50 kW per end plate. Through power pulsing a power reduction of about a factor 50 can be achieved. This brings the required power for the pixel readout to 1 kW per end plate. Future optimisation of the chip design can reduce further the required power.

## 8.5.2 Cooling

The TPC is operated at around room temperature. Cooling of the readout is required because otherwise the rising temperatures cause thermal expansion of the mechanical structure, convection in the TPC gas, and in extreme cases malfunctioning of the electronics. A temperature gradient across the active TPC volume must be limited to avoid variations in the drift velocity. Furthermore, the cooling must be constructed with a minimum of material inside the detector.

The TPC can be cooled by two phase CO<sub>2</sub> cooling [217, 218]. The thermo-physical properties of CO<sub>2</sub> make it an attractive gas for cooling in particle detectors. CO<sub>2</sub> has a high volumetric cooling capacity, because of its large latent heat. This means it does not require a high flow rate or corresponding tubing. Furthermore, CO<sub>2</sub> has a low viscosity facilitating a uniform flow, it is non-toxic, and radiation hard.

The CO<sub>2</sub> flows to the detector through pipes as a liquid and gas at a high pressure. Near the heat source, the CO<sub>2</sub> absorbs heat by evaporation. The pressure controls the evaporation temperature, and at 65 bar it can take out heat at room temperature. A CO<sub>2</sub> cooling system is expected to be able to extract the generated 1 kW of heat per end plate [219].

## 8.5.3 Occupancy, necessary link speeds, and data volume

For the occupancy and necessary link speeds it is important to know how many ionisation electrons are expected. Ionisation in the drift volume is caused by charged particles from both physics events and beam backgrounds. The ionisation from the beamstrahlung backgrounds, and the resulting occupancy for a pixel readout is studied in detail in reference [186]. The ionisation from the electron-positron pair production and the  $\gamma\gamma \rightarrow$  hadronic background both amount to a few hundred thousand electron-ion pairs per bunch crossing. For comparison, the top anti-top pair production events at a centre-of-mass energy of 500 GeV have a relatively large number of a few million ionisation electrons per event. In particular low momentum curling particles cause many hits. As another example, the  $e^+e^- \rightarrow ZH \rightarrow \mu^+\mu^-\tau^+\tau^-$  events have less than a 100 000 hits per event. Because of the low rate of physics events, the amount of ionisation caused by physics events over a whole bunch train is negligible compared to ionisation from beamstrahlung backgrounds.

Reference [186] found that the pixel occupancy for the inner readout rows is 30% for a centre-of-mass energy of 500 GeV, and 60% for a centre-of-mass energy of 1 TeV. So, per chip per bunch train there are about 26 000 hits at a centre-of-mass energy of 500 GeV, and 60 000 hits at a centre-of-mass energy of 1 TeV. With the current quad readout scheme, which can handle up to 2.6 MHits/s, it will take 10 ms to read out 26 000 hits. The readout time is longer than a bunch train length of 727  $\mu$ s. This is no problem for 80% of the pixels that are only hit once, because these hits can be

read out during the time between bunch trains. However, for the 20% of the pixels hit more than once, this means that hits detected later might be lost. This readout speed is a limitation of the quad electronics, because the Timepix3 chip itself supports a readout speed of up to 80 MHits/s. At that rate, the readout time is shorter than the bunch train length, which means multiple hits per pixel can be detected. For the chips at larger radii, the occupancy is lower and thus the required readout speed is also lower.

For the necessary link speeds the total number of hits per train is important, but for long-term data storage the number of hits per physics event is more relevant, because it is not necessary to store all background hits. In order to store up to a few million hits per event, a maximal event size of  $\mathcal{O}(10\text{ MB})$  is expected. This is at most one order of magnitude more than the pad readout. Even in that case, up to 1 GB per bunch train can be managed on site, e.g. the data rate to storage will be comparable to that of some of the major LHC experiments [220, 221]. For long-term data storage an order of magnitude increase is undesirable, although not insurmountable, and compression or removal of irrelevant data becomes important.

#### 8.5.4 Influence of ions in the drift volume

Ions that accumulate in the drift volume can distort the drift of electrons, and impact the reconstructed track parameters. Ions from primary ionisation, or back flow ions produced in the avalanches drift at a velocity of about 2.2 m/s through the gas volume, see Chapter 3. The primary ions are roughly uniformly distributed over the whole drift distance along the  $z$ -direction [186], and drift to the cathode. So, due to the bunch structure of the ILC, the primary ions have a step wise distribution in the drift direction with the largest concentration near the cathode. The back flow ions of one train are created in avalanches that occur between the first bunch crossing and 30  $\mu\text{s}$  after the last bunch crossing. The back flow ions are concentrated in 3 mm thick disks that slowly drift to the cathode.

At the ILC the effect of primary ionisation is sufficiently small, but without a gate the back flow ions will distort the track position measurement and limit the achievable resolution [151, 152], see also subsection 3.6.1. Therefore, a gate is foreseen in front of the readout plane which blocks the back flow ions almost entirely. Since the gating foil will be suspended a few mm in front of the readout plane, the gate can be applied in front of all three readout technologies, including GridPix. If the gating foil is mounted accurately in front of a module, no deformations are expected. However, this has yet to be verified for the GridPix readout technology, and in the presence of a strong magnetic field of 3.5 T.

### 8.5.5 Costing

The detector cost is an important factor when considering a detector technology, but a detailed cost estimate for the pixel readout option is difficult given the lack of experience with larger detector systems with this readout. Still it is important to make an early attempt at a cost estimate, and compare it to the other options. A highly preliminary rough cost estimate of the pixel readout option indicates that the cost could be of a similar order of magnitude as the other readout options, see Appendix B

---

# Conclusions and outlook

---

## The Timepix3 based GridPix

The GridPix is a new, yet proven, gaseous detector readout technology. Two detectors with GridPixes based on the new Timepix3 chip were constructed and tested. With its fine granularity of  $55\ \mu\text{m} \times 55\ \mu\text{m}$  and sensitivity to single ionisation electrons, the GridPix readout offers close to the ultimate TPC readout performance, which is limited only by the diffusion in the gas.

The first detector with a single Timepix3 based GridPix chip was able to record single ionisation electrons with small distortions in the pixel plane ( $< 10\ \mu\text{m}$ ). The high detection efficiency of approximately 80%, allowed it to make promising energy loss  $dE/dx$  measurements of 4.1% per meter.

Compared to the earlier Timepix based GridPix, the Timepix3 chip can simultaneously record both the arrival time (ToA) and the Time over Threshold (ToT), which is a measure of the signal strength. This is used to correct time walk, thereby enhancing the resolution in the drift direction. In addition, the Timepix3 provides a faster data-driven readout, allowing it to be applied at higher beam rates.

The chip is equipped with a high-resistive protection layer, which adequately quenches discharges, and can protect the sensitive chip electronics. However, operation at beam rates higher than 10 kHz is limited, due to increased charging up of the protection layer. A protection layer with a lower resistivity will be developed for high rate applications.

## The GridPix quad module

Subsequently, a versatile quad module with four GridPix chips was built to cover arbitrarily large readout surfaces with an active surface coverage up to 68.9%. A test in a 2.5 GeV electron beam demonstrated that the distortions in the transverse plane are only  $13\ \mu\text{m}$  over the whole quad after corrections, and the total systematic error is  $24\ \mu\text{m}$ .

The quad module is utilised as a building block for a larger 8-quad detector, which is under development and shown in Figure C.1. The detector with a total of 32 chips will be tested in a 1 T magnetic field. The detector has extra guard wires suspended over the boundaries between chips. These wires shape the electric field and reduce significantly the need for electric field corrections on the hit positions near the chip edges.

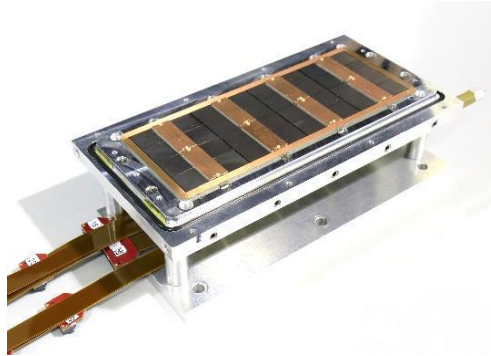


Figure C.1: Picture of the 8-quad detector without field wires and field cage.

## Future improvements

A large improvement in both position and energy loss  $dE/dx$  measurements is possible by increasing the fraction of sensitive surface. Most of the inactive surface of the quad is occupied by the wire bonds and the routing of connections to the back side. A future improvement can be accomplished by making the output connection of the chips on the backside using through-silicon via's [208]. Timepix3 chips with through-silicon via's have been produced [222]. Development of the technology is expected to be followed up for the Timepix3 chip's successor, the Timepix4 chip [223]. However, before making the through-silicon via's, the wafers have to be thinned, and therefore the GridPix post-processing afterwards will be challenging.

The next generation's Timepix chip, the Timepix4 chip [223], will improve upon the Timepix3 chip in a number of other ways. The larger Timepix4 chip will offer a better time resolution, faster readout speed, and is more energy efficient. Furthermore, the design of the wire bonds is improved, which makes connections easier. The most expensive component of the quad, the Printed Circuit Board (PCB) flex, would be greatly simplified for the Timepix4 chip, which would reduce cost and make the gas seal easier.

Another research direction is the reduction of ion back flow for the GridPix, which should be as low as possible in situations where active gating cannot be applied. A

possible reduction by approximately an order of magnitude can possibly be achieved by using two grids on top of each other to make a special electric field configuration near the chip, see [224]. An experiment using a removable Micromegas style grid (also used by [166]) should be performed to test the concept. If this proves successful, the two stacked grids (a TwinGrid) can also be manufactured by post-processing techniques [225] in a similar manner as was done for a single grid.

## Application at the ILC

The Timepix3 based GridPix can be used as a readout for the ILD TPC at the ILC. A layout of the TPC end plate using the quad module was designed, achieving an expected coverage of 60%. A pixel readout can greatly improve the momentum resolution of the TPC alone, reducing the uncertainty by up to 60% for tracks in the forward direction. The energy loss  $dE/dx$  measurements can benefit from cluster counting to improve the particle identification. The simulation and reconstruction of events in a TPC with pixel readout was accomplished, which can be used to investigate the capabilities of a pixel TPC readout. As an example, the performance of the pixel TPC was studied for the Higgs recoil mass measurement, and the reconstruction of the Higgs boson decay to tau leptons.

The GridPix readout technology recently acquired baseline status in the Linear Collider TPC Collaboration [226], which is the same formal status as the Micromegas and GEM with pads readout options. The collaboration maintains a large prototype TPC at the DESY Hamburg test beam facility [227]. A test of the Timepix3 based GridPix technology in the Large Prototype will be beneficial to directly compare performance to other readout options, study its behaviour with an ion gate, and make use of the new silicon beam telescope. Before the GridPix technology can be proposed for the ILD, all readout technologies should be tested with power pulsing and inside a large magnetic field of 3.5 T.

## Future Colliders

Preparation for the ILC in Japan has been a long and steady process. The original plans for a linear collider in Japan are more than 30 years old [228], and have been merged into the ILC project, for which the technical design report was published in 2013 [12, 13, 112, 113, 229]. After several years of discussion and evaluation of the LHC results up to then, a first stage at a centre-of-mass energy of 250 GeV was introduced to cut the cost by about 40% [230]. With this modification, the science council of Japan acknowledged the scientific merit of the ILC project in January 2020 [231]. The selected projects did not include the ILC, which is of a different scale than the other projects, and requires international collaboration. The ILC International Development Team was formed by the International Committee for Future Accelerators



to set up a framework for the preliminary organisation that will prepare for the ILC [232]. Near the candidate site in the Tohoku region, the ILC is promoted by members from academia, industries and business, and local governments [233].

Any green-light for the project will, above all, depend on whether Japan and the international partners will be able to reach an agreement on the necessary resources. The 2020 update of the European strategy report for particle physics reiterated that the realisation of the ILC has a high-priority, and expressed the wish of the European community to collaborate [10]. The United States have expressed strong support for the ILC [234], and is currently in the process of updating its long-term strategy for particle physics in the Snowmass meetings. Overall however, given the ongoing covid-19 pandemic, politically it is a difficult time to discuss large, international, scientific projects.

For the long-term, the European strategy proposes to investigate the feasibility of a hadron collider with a centre-of-mass energy of at least 100 TeV, the FCC-hh, with an electron-positron collider, the FCC-ee as a possible first stage [10]. This updated report considers CLIC less promising than the FCC-hh for a future facility at the energy frontier [235]. The strategy also calls for innovative accelerator technologies that may open up paths to pursue other future colliders, such as a muon collider. Meanwhile, there is an optimistic plan to build the CEPC in a short time span in China [236].

## Other applications

The GridPix is more widely applicable than only at the ILC. Although there are a few obstacles in the implementation of a TPC at the FCC-ee, a TPC with GridPix readout is probably a viable option for a detector at CLIC, or at the CEPC. Besides the use as a TPC readout at a collider, the GridPix can be used in an alternative configuration at a collider, as a negative ion TPC for non-collider rare event searches, or as a sensor for proton therapy. For all these applications, the Timepix3 based GridPix described in this thesis will give an improvement over the older Timepix based GridPix.

## Conclusion

An electron-positron collider has the highest priority to continue investigating the properties of the Higgs boson. The results of this collider can give indications about the energy scale of new physics. A TPC is particularly suited for the precision physics that will take place at a linear electron-positron collider, such as the ILC. It has been demonstrated that the GridPix technology is sufficiently mature, and the performance enhancement is substantial enough, to start planning applications at the next generation of colliders. In particular, the improved momentum resolution can help determine

---

the Higgs boson mass from the recoil mass measurement at the ILC. By this means, the GridPix can be an instrument to answer some of our fundamental questions.



---

# On the properties of a negative-ion TPC prototype with GridPix readout

---

C. Ligtenberg<sup>1</sup>, M. van Beuzekom<sup>1</sup>, Y. Bilevych<sup>2</sup>, K. Desch<sup>2</sup>, H. van der Graaf<sup>1</sup>, F. Hartjes<sup>1</sup>, K. Heijhoff<sup>1,2</sup>, J. Kaminski<sup>2</sup>, P.M. Kluit<sup>1</sup>, N. van der Kolk<sup>1</sup>, G. Raven<sup>1</sup>, J. Timmermans<sup>1</sup>

<sup>1</sup> *Nikhef, Science Park 105, 1098 XG Amsterdam, The Netherlands*

<sup>2</sup> *Physikalisches Institut, University of Bonn, Nussallee 12, 53115 Bonn, Germany*

Paper under review by Nuclear Instruments and Methods in Physics Research Section A: Accelerators, Spectrometers, Detectors and Associated Equipment, Elsevier

## Abstract

The performance of a GridPix detector to read out a negative ion TPC was studied using a module with four GridPix chips that are based on the Timepix3 pixelated readout ASIC. The quad module dimensions are 39.6 mm × 28.38 mm, and the maximum drift distance is 40 mm. The TPC is operated using a 93.6/5.0/1.4 gas mixture (by volume) of Ar/iC<sub>4</sub>H<sub>10</sub>/CS<sub>2</sub> with a small amount of oxygen and water vapour at a pressure of 1030 mbar and a temperature of 297 K. Tracks were produced by a pulsed N<sub>2</sub> laser. The GridPix chips are sensitive to single drift ions, and allow for the determination of the drift distance using the velocities of the different ion species. The 1.56 ns time resolution of the Timepix3 chips allows for a precise determination of the drift properties in the longitudinal direction. The measured mobility of majority ion charge carriers is  $(1.391 \pm 0.003) \text{ cm}^2/\text{V/s}$ . Using the high granularity pixel readout,

the transverse and longitudinal diffusion coefficients were measured to correspond to an effective thermal diffusion temperature of 314 K and 384 K respectively. For 429 detected ions, the precision on the absolute drift distance is expected to be 1.33 mm for a mean drift distance of 20 mm.

*Keywords:* Micromegas, gaseous pixel detector, micro-pattern gaseous detector, Timepix, GridPix, negative ion time projection chamber

## A.1 Introduction

In a negative ion Time Projection Chamber (TPC), ionisation charge is transported to the readout plane by negatively charged ions instead of electrons, thereby reducing the diffusion down to the thermal limit [237]. The TPC detects ionisation from interactions in the gas of the TPC. The primary ionisation electrons are captured by the highly electronegative  $\text{CS}_2$  gas component, and the ions formed drift to the anode by an electric field. The track position resolution depends on the electron capture length, and the transport properties in the gas. In the high field amplification region near the anode, the electrons detach and an avalanche occurs which is detected by the readout electronics.

Negative ion TPCs can be used for directional dark matter searches. For example, in the Drift IId experiment [238] a negative ion TPC was operated using a low pressure 30:10 Torr  $\text{CF}_4:\text{CS}_2$  gas mixture. It was demonstrated that when oxygen was present in the gas mixture, extra species of ions called minority carriers with a larger mobility were created [239]. From the difference in arrival time of the different ion species at the readout plane, the absolute position in the drift direction was reconstructed without the need of knowing the event time in the detector [240].

In this paper an exploratory study of GridPix technology to read out a negative ion TPC is presented. A GridPix consists of a CMOS pixel chip with integrated amplification grid added by MEMS postprocessing techniques [22, 23]. GridPix detectors based on the Timepix chip were extensively studied as TPC readouts for a future collider experiment [241] and have been used in the CERN Axion Solar Telescope [174], see also [163] for an overview of applications. However, the original Timepix chip has a limited readout rate, and cannot simultaneously record the time of arrival and the amount of detected charge. This has been overcome by the next generation GridPix [25] based on the Timepix3 [24] chip.

Recently a quad module with four Timepix3 based GridPix chips was developed for a future collider experiment [26]. The Timepix3 chip can be operated with a low threshold of  $515 e^-$ , and has a low equivalent noise charge of about  $70 e^-$ . The GridPix TPC readout is sensitive to single charge carriers, and has a fine granularity of  $55 \mu\text{m} \times 55 \mu\text{m}$ . Because of this fine granularity and the low diffusion of ions, a

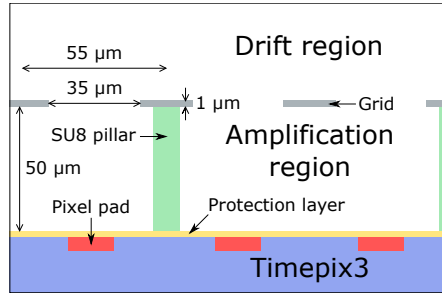


Figure A.1: Schematic drawing of the cross-section of a GridPix detector, with some of the components and dimensions indicated.

negative ion TPC with GridPix readout can provide an excellent spatial resolution without a magnetic field. This first investigation focuses on the operation of the quad module in an already existing setup at atmospheric pressure.

## A.2 Quad detector

### A.2.1 Gridpix

The GridPix is based on the Timepix3 chip [24], which has  $256 \times 256$  pixels with a pitch of  $55 \mu\text{m} \times 55 \mu\text{m}$ . On the surface of the chip a  $4 \mu\text{m}$  thick silicon-rich silicon nitride resistive protection layer is deposited in order to prevent damage to the readout electronics from discharges of the grid. Silicon-rich silicon nitride is regular silicon nitride ( $\text{Si}_3\text{N}_4$ ) doped with extra silicon to make it conductive. On top of the protection layer,  $50 \mu\text{m}$  high pillars of the epoxy-based negative photoresist SU8 support a  $1 \mu\text{m}$  thick aluminium grid with  $35 \mu\text{m}$  diameter circular holes aligned to the pixels. Some of the components and dimensions are schematically drawn in Figure A.1. The Timepix3 chip can measure a precise Time of Arrival (ToA) using a 640 MHz TDC. In addition for every hit a time over threshold (ToT) is measured, which can be converted into a detected charge by test pulse calibrations. The Timepix3 chip has a data driven readout, and is connected to a speedy pixel detector readout (SPIDR) board at a speed of 160 Mbps [242].

### A.2.2 Quad module

The quad module shown in Figure A.2, consists of four GridPix chips and is optimised for a high fraction of sensitive area of 68.9%. The external dimensions are  $39.6 \text{ mm} \times 28.38 \text{ mm}$  and it can be tiled to cover arbitrarily large areas. The four chips which are mounted on a cooled base plate (COCA), are connected with wire bonds to

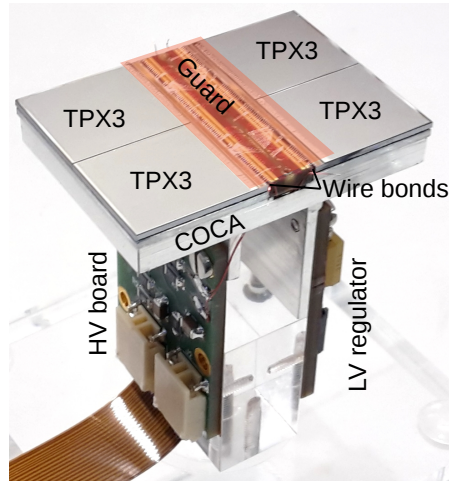


Figure A.2: Picture of the quad module with four Timepix3 GridPixes (TPX3) mounted on a cold carrier plate (COCA). The central guard was not yet installed to show the underlying wire bond PCB, and its operating position is indicated with a transparent rectangle. On the right the Low Voltage (LV) regulator is partially hidden behind the aluminium mechanical support, and on the left the High Voltage (HV) board and the flexible Kapton cable are visible. This picture was previously published in [26].

a common central 6 mm wide PCB. A 10 mm wide guard electrode is placed over the wire bonds 1.1 mm above the aluminium grids, in order to prevent field distortions of the electric drift field. The guard is the main inactive area, and its dimensions are set by the space required for the wire bonds. On the back side of the quad module, the PCB is connected to a low voltage regulator. The aluminium grids of the GridPixes are connected by 80  $\mu\text{m}$  insulated copper wires to a high voltage (HV) filtering board. The module consumes about 8 W of power of which 2 W is used in the LV regulator.

### A.2.3 Experimental setup

8 quad modules were embedded in a box, resulting in a total of 32 chips. A schematic 3-dimensional drawing of the detector is shown in Figure A.3. When the measurements were taken, one single quad module with 4 chips could be read out per SPIDR board. Hardware to simultaneously read out multiple quad modules with one SPIDR board is under development. A schematic drawing of the setup is shown in Figure A.4. The internal dimensions of the box are 79 mm along the  $x$ -axis, 192 mm along the  $y$ -

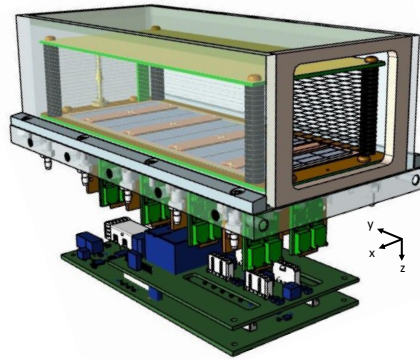


Figure A.3: Schematic 3-dimensional render of the 8-quad module detector for illustration purposes.

axis, and 53 mm along the  $z$ -axis (drift direction), and it has a maximum drift length (distance between cathode and readout anode) of 40 mm. The drift field is shaped by a series of parallel CuBe field wires of  $50\ \mu\text{m}$  diameter with a wire pitch of 2 mm and guard strips are located on all of the four sides of the active area. In addition, six guard wires are suspended over the direct boundaries of the chips, because the chip edges are at a ground potential, which would otherwise distort the electric drift field. The wires are located at a distance of 1.15 mm from the grid planes, and their potential is set to the potential at this drift distance. The box has one Kapton window and three optical glass windows (type H-K9L) to facilitate laser measurements.

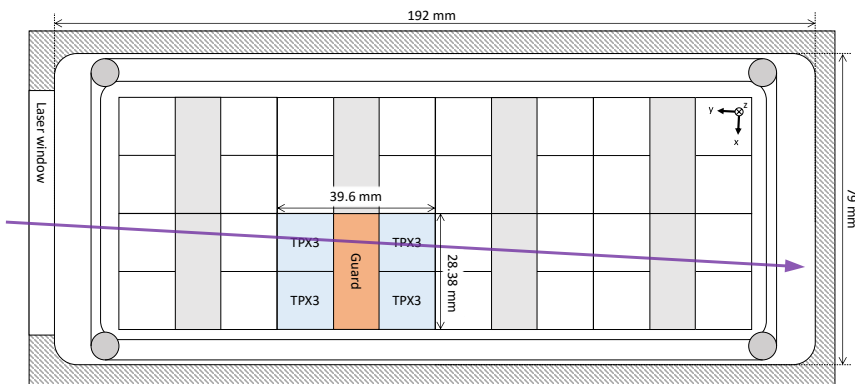


Figure A.4: Schematic drawing of the 8-quad module detector with one quad in operation. The laser track direction is shown in purple.



The gas volume of 780 ml is continuously flushed with a 93.6/5.0/1.4 gas mixture (by volume) of Ar/iC<sub>4</sub>H<sub>10</sub>/CS<sub>2</sub> at atmospheric pressure. The gas is argon based, because the setup is also used for research on TPCs with an argon based gas for future colliders. The isobutane gas was added as a quencher to absorb UV photons produced in the avalanches, and the CS<sub>2</sub> concentration is chosen high enough to capture electrons shortly after the ionisation ( $\lesssim 200 \mu\text{m}$ ). A small amount of oxygen (650 ppm to 1150 ppm) and water vapour (about 4000 ppm) are present in the drift volume because of diffusion and outgassing of some of the materials. A few ppb of tetra-methyl-phenylene-diamine (TMPD) molecules are added to enhance laser ionisation in the gas [243]. The TMPD was added through sublimation by directing the inflowing gas through a tube containing the solid TMPD grains. Once introduced, a noticeable concentration can remain in the setup for at least months under normal conditions. During data taking, the temperature was 297 K and the pressure was 1030 mbar. The experimental parameters are summarised in Table A.1.

An amplification field strength  $E_{\text{amplification}}$  of 76 kV/cm is achieved in the 50  $\mu\text{m}$  wide gap by setting the grid voltage to  $-380 \text{ V}$ . The pixel pads are normally at zero potential. A hit is registered if the charge on a pixel pad is above the threshold set to about  $515 e^-$ . The mean collected charge of the selected hits is about  $1000 e^-$ . The gain is approximately 1000, and the single ion detection efficiency is expected to be 60%. A higher gain and single ion detection efficiency can be achieved by increasing the amplification field strength.

Tracks of ionisation are created by a pulsed 337 nm N<sub>2</sub> laser at a rate of 2.5 Hz with a pulse duration of 1 ns [243]. This laser is operated using the MOPA (Master Oscillator Power Amplifier) principle to obtain a beam near the diffraction limit. The parallel beam can accurately be directed in the gas volume by means of two remotely controlled stages.

Data was taken using the data-riven mode of the Timepix3 chip in a series of nine automated experimental runs. The time of the laser pulse was added to the pixel data stream. During a run, the drift field was set to a specific strength and the beam was positioned at six different drift distances 6 mm apart and at four different  $x$ -positions. Measurements of 2400 laser pulses per run are taken in a time frame of approximately 17 minutes.

### A.3 Analysis

In the analysis the laser position is compared to the reconstructed position from the quad detector. The laser track is defined by the recorded stage position as a line parallel to the  $y$ -axis. The per pulse variations are smaller than 15  $\mu\text{m}$ . The recorded stage position is taken as the reference to which the four chips are aligned by rotation in two dimensions, and shifts in the two dimensions perpendicular to the laser beam.

Table A.1: Overview of the experimental parameters. The ranges indicate the variation over the total data taking time

Number of runs	9
Run duration	17 minutes
$E_{\text{drift}}$	100 – 500 V/cm
$E_{\text{amplification}}$	76 kV/cm
Threshold	$515 e^-$
Temperature	295.9 – 297.0 K
Pressure	1030 – 1029 mbar
Oxygen concentration	650 – 1150 ppm
Water vapour concentration	$\sim 4000$ ppm

The position of detected ionisation in the pixel plane is a direct translation from the pixels column ( $x$ -direction) and row number ( $y$ -direction). To reduce noise, only hits with a time over threshold above  $0.1 \mu\text{s}$  are considered. A time over threshold of  $0.1 \mu\text{s}$  corresponds to a charge close to the threshold of  $515 e^-$ . From the known laser pulse time, the  $z$ -position can be calculated as the product of the measured drift time  $t$  and the drift velocity  $v_{\text{drift}}$ . To remove noise from scattered laser light hitting the readout directly, hits between  $1 \mu\text{s}$  before and  $1 \mu\text{s}$  after the laser pulse are removed. All of these cuts are applied in the entire analysis below. To clean up further the data set for diffusion measurements only, in section 4.3 hits are required to be within 2 mm of a laser track in the  $x$ -direction and to be within 5 mm of the laser track in the  $z$ -direction. The alignment and the measurement of the drift velocity is an iterative process.

An example of a resulting drift time spectrum is shown in Figure A.5 for the run at a drift field strength  $E_{\text{drift}}$  of 300 V/cm. Other experiments using a 30:10:1 Torr  $\text{CF}_4:\text{CS}_2:\text{O}_2$  gas mixture could distinguish three different minority carriers as separate peaks in the drift time spectrum [239]. In contrast, in our measurements only one secondary peak can be found, which is slightly broader than the primary one. This could be due to e.g. overlapping drift time distributions, the much lower oxygen concentration, or the much higher water vapour concentration in our gas mixture affecting the minority carrier(s) production.

In order to determine the drift properties, a ‘global’ fit is made per run. Each run corresponds to a given electric field strength. A run has measurements taken at different drift distances. The drift time  $t$  is fitted with a combination of two Gaussian

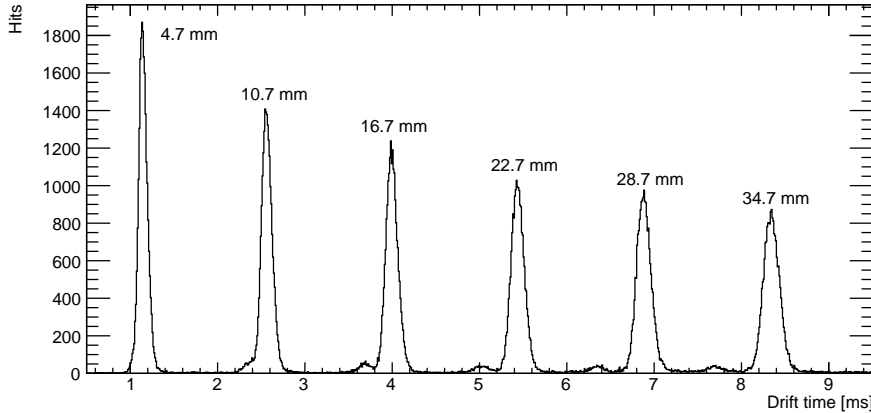


Figure A.5: Drift time distribution for 400 laser pulses per  $z$ -position, annotated with the drift distance as recorded by the laser stage.

distributions per laser  $z$ -position:

$$g(t) = n_{\text{hits}} \left[ \frac{f_1}{\sigma_1 \sqrt{2\pi}} \exp\left(-\frac{(t - \mu_1)^2}{2\sigma_1^2}\right) + \frac{f_2}{\sigma_2 \sqrt{2\pi}} \exp\left(-\frac{(t - r_2 \mu_1)^2}{2\sigma_2^2}\right) + \frac{f_{\text{noise}}}{u_{\text{width}}}\right], \quad (\text{A.1})$$

where  $n_{\text{hits}}$  is the number of hits,  $u_{\text{width}}$  is the width of a uniform distribution related to the fitted  $t$  range and  $f_1$  is the fraction of the number of detected ions from majority carrier(s) given by  $f_1 = 1 - f_2 - f_{\text{noise}}$ . Four parameters are different for each drift distance, and two parameters are the same for all drift distances. The mean time  $\mu_1$ , the standard deviation of the majority carrier distribution  $\sigma_1$ , the standard deviation of the minority carrier(s) distribution  $\sigma_2$  and the fraction of the number of ions in the flat noise distribution  $f_{\text{noise}}$ , are fitted per drift distance. In the fit, the fraction of the number of ions from minority carrier(s)  $f_2$  and the ratio of majority carrier mobility to the minority carrier(s) mobility  $r_2$  are equal for all drift distances.

## A.4 Performance

### A.4.1 Number of hits

The mean total number of detected hits per laser pulse is 43. The number of hits can be tuned by adjusting the laser intensity, and the spread on the number of hits

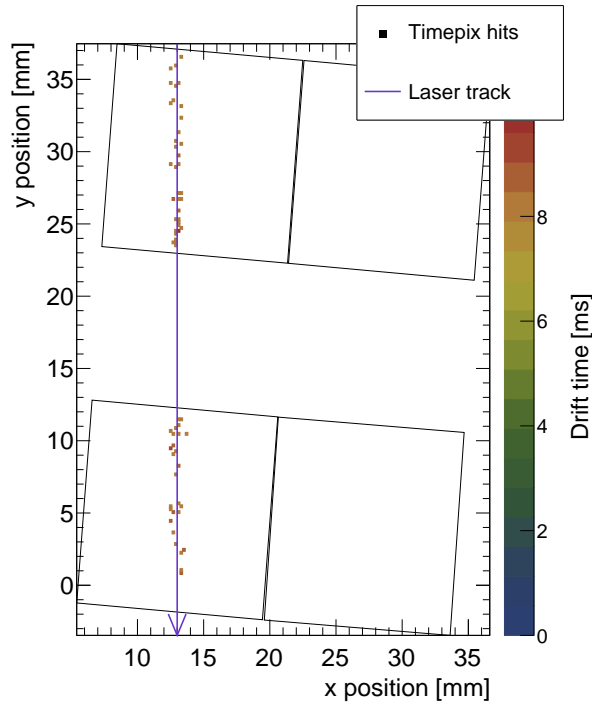


Figure A.6: Example of the detected ionisation from one laser pulse with 71 hits in total. The position of the laser track (purple line) and chip edges (black outlines) are drawn in global coordinates. The pixel hits are not to scale.

is dominated by per pulse variations of the laser intensity. In this gas, a minimum ionising particle is expected to create about 100 ionisation pairs per cm of which about 60 will be detected as hits per cm, because of the 60% single ion detection efficiency at a gain of 1000. An example event display showing the ionisation for a single laser pulse is presented in Figure A.6.

The GridPix is capable of detecting more than one hit per laser pulse per pixel. The dead time per pixel for the Timepix3 chip after being hit is the time over threshold plus 475 ns, so about 1  $\mu$ s. With a drift velocity of a few m/s, even two hits originating from the same position can both be detected, because they are sufficiently separated due to diffusion. In this case the number of hits is small, and there is only a small probability of two ions arriving on the same pixel, but for highly-ionising events the multi-hit capabilities can be advantageous.

## A.4.2 Drift velocity measurements

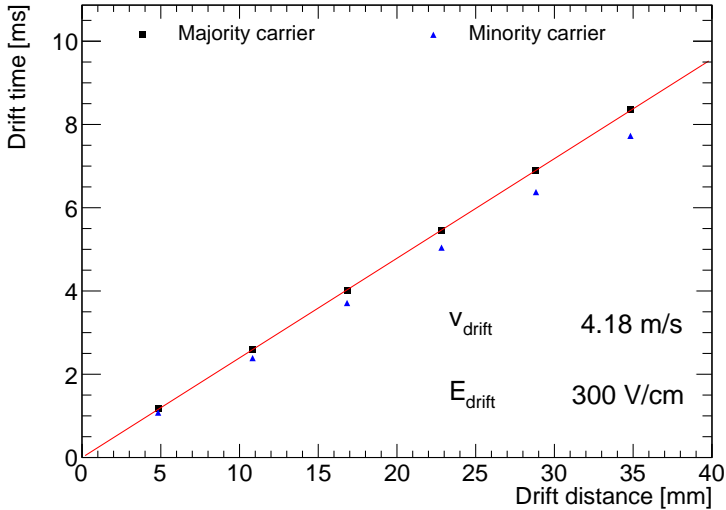


Figure A.7: Drift time as a function of the drift distance for the majority and minority carriers. The statistical error is not shown, because it is negligible compared to the systematic uncertainties.

The average drift times for the majority and minority charge carrier(s) are plotted as a function of the drift distance in Figure A.7 for a drift field strength of 300 V/cm. The drift velocity of the minority carrier is found to be 8.1% higher than that of the majority carrier.

The drift velocity measurement is repeated for 9 electric field strengths in the range 100 V/cm to 500 V/cm. The drift velocity of the majority carrier  $v_{\text{drift}}$  as function of the electric field is shown in Figure A.8. The mean measured mobility (defined as the drift velocity divided by the electric field strength) is  $(1.391 \pm 0.003) \text{ cm}^2/\text{V/s}$ . The uncertainty of the measured mobility is estimated as the r.m.s. of the given values, and is probably dominated by fluctuations in the (local) temperature and gas composition. Because of the unique gas composition the mobility cannot directly be compared to the results from other experiments. However, the mobility is the same order of magnitude as previous measurements. Reference [237] found a mobility of  $(1220 \pm 51) \text{ cm}^2/\text{V/s mbar}$  for a 9:1:14.5 Ar:CH<sub>4</sub>:CS<sub>2</sub> gas mixture at a pressure of 40 Torr (53 mbar), which corresponds to a mobility of  $(1.18 \pm 0.04) \text{ cm}^2/\text{V/s}$  at a pressure of 1030 mbar. Reference [244] found a mobility of  $0.71 \text{ cm}^2/\text{V/s}$  in a 200:500 Torr CS<sub>2</sub>:He gas mixture.

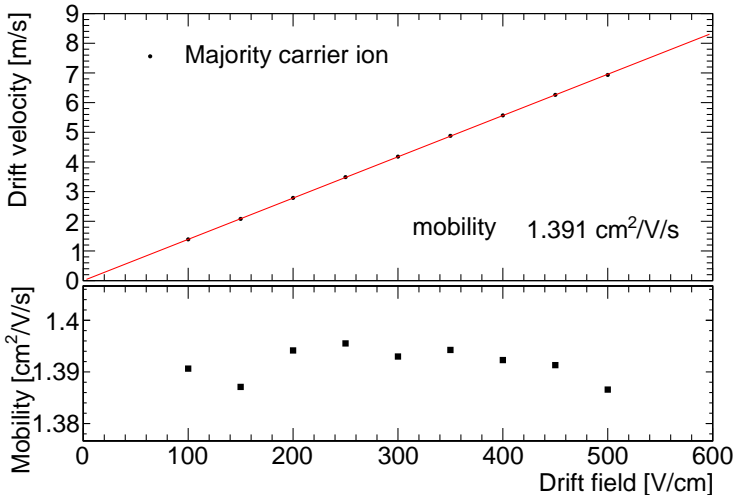


Figure A.8: Drift velocity of the majority carrier ion as a function of the drift field. The mobility is acquired from a straight line fit constrained to pass through the origin (0,0). The statistical error is not shown, because it is negligible compared to the systematic uncertainties.

### A.4.3 Diffusion measurements

As the ions drift towards the readout plane, they diffuse which gives them a Gaussian spread in the longitudinal and transverse direction. The amount of diffusion is characterised by the standard deviation of the Gaussian distribution  $\sigma_i$ , where  $i$  stands for the longitudinal direction  $z$  or the transverse direction  $x$ . This can be expressed as

$$\sigma_i^2 = \sigma_{i0}^2 + D_i^2 z_{\text{drift}}, \quad (\text{A.2})$$

where  $\sigma_{i0}$  is the standard deviation at zero drift,  $D_i$  the diffusion coefficient, and  $z_{\text{drift}}$  the drift distance.

The standard deviation in the transverse direction  $\sigma_x$  is acquired from a fit of a Gaussian function to the measured  $x$  positions of all detected ions including the minority carrier(s) ions. In the longitudinal direction the standard deviation  $\sigma_z$  is acquired from a fit of the sum of two Gaussian functions, which represent the contribution from the majority carrier ions, and the minority carrier(s) ions, see Equation (A.1). The drift time is converted to a distance using the measured drift velocity of the majority carrier  $v_{\text{drift}}$ . As an example, the standard deviation as a function of drift distance for the run at a drift field strength  $E_{\text{drift}}$  of 300 V/cm is shown in Figure A.9. In comparison to the systematic uncertainties, the statistical error is negligible.

The constant contribution in Equation A.2 is roughly independent of the electric field, and on average found to be  $\sigma_{x0} = (84 \pm 4) \mu\text{m}$  in the transverse direction which can predominantly be attributed to the laser beam width plus some small per laser pulse variation. In the longitudinal direction  $\sigma_{z0} = (141 \pm 8) \mu\text{m}$  is measured on average over all runs. This can predominantly be attributed to the laser beam width plus per laser pulse variations, the spread on the distance traveled by electrons before they are captured by the  $\text{CS}_2$  molecules and possible unrecognised minority carrier(s).

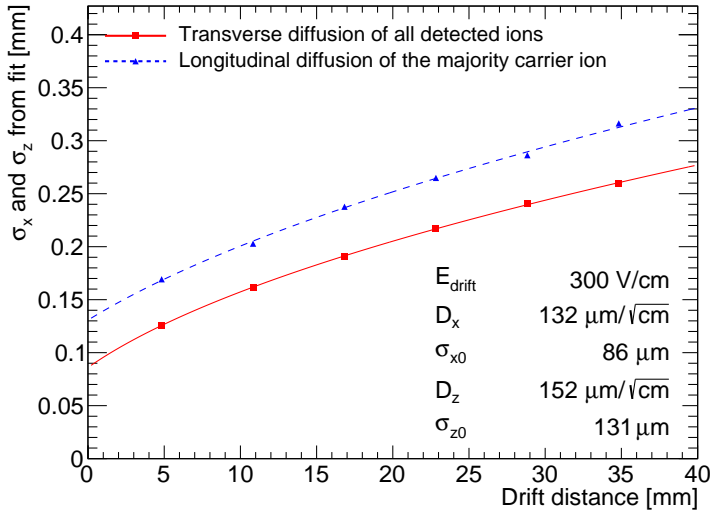


Figure A.9: Standard deviation of the hit positions of all detected ions in the transverse direction, and the standard deviation of the hit positions of the majority carrier ions in the longitudinal direction. Both are shown as a function of drift distance for the run with  $E_{\text{drift}} = 300 \text{ V/cm}$ . The data is fitted with Equation (A.2).

The diffusion coefficient depends on the electric field strength, and the measurements are shown in Figure A.10. Because of the much larger systematic uncertainties, the statistical errors are neglected. At low drift field strengths, the ions have thermal energy and the diffusion coefficient can be expressed as

$$D_{\text{thermal}} = \sqrt{\frac{2k_{\text{B}}T}{eE}}, \quad (\text{A.3})$$

where  $k_{\text{B}}$  is the Boltzmann constant,  $T$  is the temperature of the gas,  $e$  is the charge of the ion, and  $E$  is the electric field strength (see e.g. [125]). Both the transverse and longitudinal diffusion coefficients are fitted with Equation (A.3) with the tem-

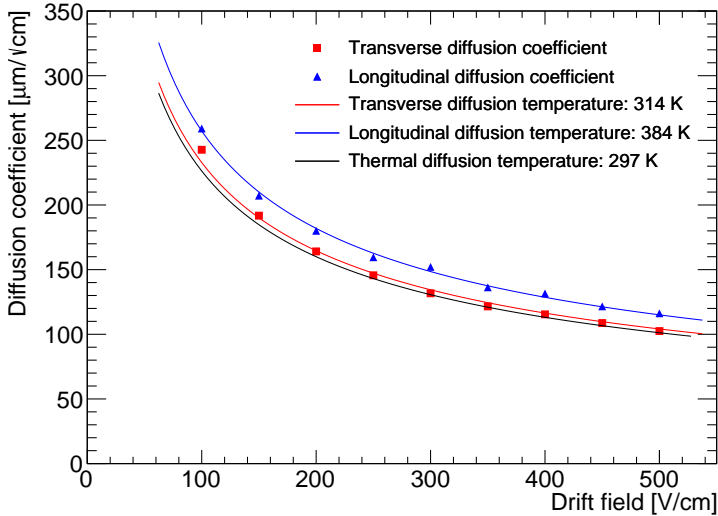


Figure A.10: The longitudinal diffusion coefficient of the majority carrier ions, and the transverse diffusion of all detected ions. Both are plotted as a function of drift field  $E$ , and fitted with Equation (A.3). For comparison the expectation for thermal diffusion is shown.

perature  $T$  as a free parameter. The transverse diffusion corresponds to an effective temperature of 314 K, which is slightly above the gas temperature. The effective temperature of the longitudinal diffusion is rather high, 384 K. This can possibly be explained by unrecognised minority carrier(s). A simple thermal model with a  $1/\sqrt{E_{\text{drift}}}$  dependence describes the data well.

In other experiments using a low pressure  $\text{CS}_2$  gas, the longitudinal diffusion is found to be in agreement with the thermal values [245]. In a 500 Torr He and 200 Torr  $\text{CS}_2$  gas mixture, longitudinal diffusion coefficients slightly below to the thermal values are found [244].

#### A.4.4 Reconstruction of drift distance

The difference in drift velocity between the majority carrier and minority carrier(s) ions can be used to reconstruct the absolute drift distance. Previously, this technique was demonstrated in a 30:10:1 Torr  $\text{CS}_2:\text{CF}_4:\text{O}_2$  gas mixture with a spread on the reconstructed drift distance of  $\pm 2$  cm for a mean drift distance of about 25 cm [240]. A precision of 16 mm was achieved using a similar technique using an  $\text{SF}_6$  gas [246]. Besides the difference in time of arrival between the majority carrier and



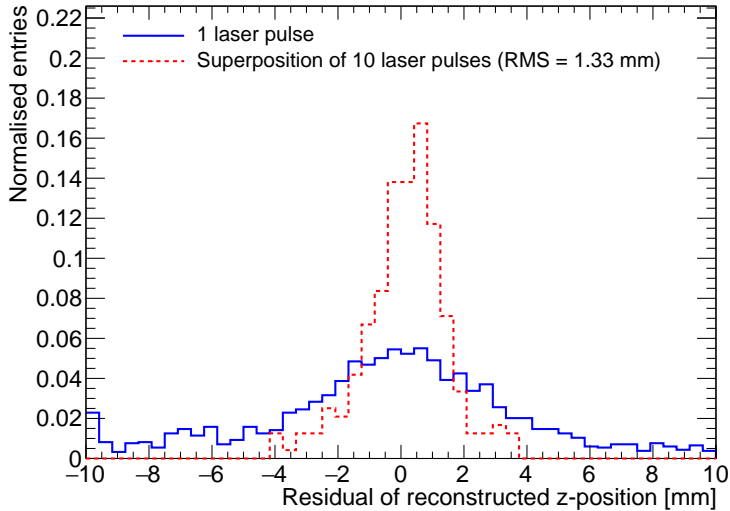


Figure A.11: Residual of reconstructed  $z$ -position for single laser pulses and a superposition of ten laser pulses for all six drift distances (4.7 mm, 10.7 mm, 16.7 mm, 22.7 mm, 28.7 mm, and 34.7 mm).

minority carrier(s), the detected spread due to diffusion can be used to determine the drift distance. A precision of 1 cm was achieved by measuring the transverse spread for 0.8 cm-long alpha track segments in a 70:30 He:CO<sub>2</sub> gas mixture at atmospheric pressure [247].

Here, fiducialisation is applied to data from the run at the largest drift field of 500 V/cm which gives the best signal peak separation, and also has the highest oxygen concentration of about 1150 ppm. About 4.4% of the hits are attributed to the minority carrier(s), whose mobility is 8.1% higher than that of the majority carrier.

The reconstruction proceeds by performing per event a binned maximum likelihood fit of Equation (A.1) to the measured relative arrival time of ions from one or more laser pulses. A new parameter  $t_0$  is introduced to absorb the now unknown laser pulse time. The parameters  $f_2$ ,  $r_2$ ,  $f_{\text{noise}}$  are fixed to their previously fitted values. For  $\sigma_1$  Equation (A.2) is used, and  $\sigma_2$  is by approximation fixed to  $\sigma_1$ . The parameter  $\mu_1$  (the mean arrival time of the primary carrier peak) are acquired from the fit. The  $z$ -position is calculated using the measured drift velocity  $v_{\text{drift}}$ . The detected spread in the transverse direction is not utilised in the determination of the  $z$ -position.

By comparing the reconstructed  $z$ -position to the  $z$ -position of the laser stage for all six drift distances (4.7 mm, 10.7 mm, 16.7 mm, 22.7 mm, 28.7 mm, and 34.7 mm), the residual shown in Figure A.11 is obtained. There are 2401 laser pulses with a mean

number of 43 detected ions and 240 superpositions of ten laser pulses with a total mean number of 429 ions. From a single laser pulse, on average 43 ions are detected and 76 % of the laser pulses fall within the  $\pm 10$  mm range. The determined  $z$ -position has a rather large spread, because very few minority carrier(s) ions are detected. In order to estimate the performance for a larger number of ions, a superposition of ten laser pulses at the same  $z$ -position is made by shifting their arrival times by the time difference between the laser pulses. From this we acquire emulated pulses with a mean total number of 429 detected ions of which about 19 ions are attributed to the minority carrier(s). The resulting r.m.s. is 1.33 mm for 239 out of the 240 combined laser pulses for a mean drift distance of 20 mm. For one entry the reconstructed  $z$ -position is off by 14 mm, and the r.m.s. is 1.62 mm if it is included as well.

## A.5 Conclusions and outlook

The performance of GridPix detector to readout a negative ion TPC was studied using a quad module with four Timepix3 based GridPix chips. The TPC is operated using a 93.6/5.0/1.4 gas mixture (by volume) of Ar/ $i$ C<sub>4</sub>H<sub>10</sub>/CS<sub>2</sub> with a small amount of oxygen and water vapour at a pressure of 1030 mbar and a temperature of 297 K. Tracks were produced by a pulsed N<sub>2</sub> laser. The 1.56 ns time resolution of the Timepix3 chips allows for a precise determination of the drift properties in the longitudinal direction. The measured ion mobility for the majority carrier ions is  $(1.391 \pm 0.003)$  cm<sup>2</sup>/V/s. Using the high granularity pixel readout, the transverse and longitudinal diffusion coefficients were measured to correspond to an effective thermal diffusion temperature of 314 K and 384 K respectively. A simple thermal model with a  $1/\sqrt{E_{\text{drift}}}$  dependence describes the data well. This confirms the expected low diffusion coefficient for ions. Furthermore, the GridPix has an efficiency of approximately 60% to detect single drift ions. This can be improved by operating the device at a higher gain. By using also the relative arrival time of about 429 detected ions with a mean drift distance of 20 mm, the absolute  $z$ -position can be measured with an expected precision of 1.33 mm.

In the future, a GridPix TPC readout might be of interest to directional dark matter experiments. The often desired operation at low pressure can be investigated in combination with a GridPix readout. For these experiments gas mixtures containing SF<sub>6</sub> have some advantages [245], and can also be studied for operation with a GridPix readout. Alternatively, for operation around atmospheric pressure replacing argon with the lighter helium could increase nuclear recoils lengths important for directional dark matter searches [237, 248].

All in all, the fine granularity and high timing precision of the GridPix TPC readout in combination with the capability to detect single ions, provide an excellent position resolution in the longitudinal and transverse direction.

## **A.6 Acknowledgements**

This research was funded by the Netherlands Organisation for Scientific Research NWO. The authors want to acknowledge the support of the mechanical and electronics departments at Nikhef.

---

## Preliminary cost estimate of the ILD TPC with a GridPix readout

---

In Chapter 8 a pixel readout option for the ILD TPC based on GridPix quad modules is discussed and compared to pad-based readout options. Because the cost is also important when comparing detector technologies, a preliminary attempt at a rough cost estimate of the pixel readout is given here.

A detailed estimation was made for the pad readout option of the ILD [118]. The cost is estimated in ILC units, which is equivalent to €1.00 (2018). According to the ILD costing rules, this estimate includes materials, labour, transport, testing, and assembly, but not research and development. The construction cost for the pad readout with Micromegas amplification is given in Table B.1. Except for the modules and electronics, the items are expected to be similar for the various readout technology options. The cost estimate for the GEM technology option is €8 800k higher. In addition to the construction cost, the expected gas consumption assuming re-circulation and filtering is 7 m<sup>3</sup>/day, which is expected to cost €22k per year.

For the ILD TPC with GridPix readout, there are two approaches to estimate the cost of the modules and electronics (see also [250]). A cost estimate can be acquired from the number of chips and the cost per chip of existing detectors. Alternatively, one can try to estimate the cost of an end plate module, similarly as was done for the pad readout module.

The total cost can be estimated from the cost of the 50 000 necessary chips for 60% coverage, or 80 000 chips for 100% coverage. Even if a custom chip design is made, the cost per chip will most likely be similar to the Timepix chips. The chip design is estimated to cost the same as the Timepix3 design, which was €500k. The cost per

Table B.1: Cost estimate in multiples of €1 000 (k€) for the ILD TPC with Micromegas amplification and pad readout [118, 249].

Item	Material cost	Labour cost
Field cages	1 930	
End plates	540	64
Modules	2 043	520
Electronics	9 470	
Ancillaries	2 307	400
Cables and pipes	50	724
Assembly on site		2 160
Management	60	1 120
Total	16 400	4 988

Table B.2: The estimated cost in multiples of €1 000 (k€) of a GridPix end plate readout module.

Item	Cost
Timepix3 chips	4
Post-processing of chips	1.5
SPIDR readout system	3
HV/LV powerboards	0.5
Dedicated PCB flex	40
Total	49

wafer with 80 useful chips is about €4k. This results in a total cost of €3 500k for the chips, although this does not account for potential losses in post processing or during detector construction. From silicon detector construction experience at the LHC, the cost for the power boards, post processing, readout systems, and mechanics is about a factor 2 of the chip cost. The total cost for the modules and electronics, excluding manpower, is €10 500k, which is similar to the pad readout cost.

Another approach is to estimate the cost per end plate module. The cost of a pad module including the electronics is about €23k. The cost of a GridPix module with current technology is €49k and detailed in Table B.2. The major cost driver is the dedicated PCB flex, which is expected to become cheaper by at least a factor 10 for future generations of chips. In that case, the cost of a GridPix TPC module is €13k, and the cost of a TPC with GridPix readout will be of the same order of magnitude as the cost of a TPC with pad readout.

---

# Acronyms

---

**$\Lambda$ CDM**  $\Lambda$  Cold Dark Matter. 9

**ASIC** application-specific integrated circuit. 30

**CAST** the CERN Axion Solar Telescope. 54

**CCD** Charge-Coupled Device. 26

**CEPC** Circular Electron Positron Collider. 50, 144

**CERN** the European organization for nuclear research. 48, 49

**CKM** Cabibbo–Kobayashi–Maskawa. 8

**CLIC** Compact Linear Collider. 48, 49, 144

**CMOS** Complementary Metal Oxide Semiconductor. 26, 27, 44, 51, 52, 128

**DAC** Digital to Analog Converter. 57, 69

**DD4hep** the Detector Description Toolkit for High Energy Physics. 102

**DEPFET** Depleted Field Effect Transistor. 26

**ECAL** Electromagnetic Calorimeter. 23, 24, 28–30

**EWSB** electroweak symmetry breaking. 8, 11

**FCC** Future Circular Collider. 49, 50, 144

**FPGA** field-programmable gate array. 30

**FTD** Forward Tracking Disks. 26, 27

**FWHM** Full Width at Half Maximum. 136

**GEM** Gas Electron Multiplier. 42, 43, 129, 143, 163

**HCAL** Hadronic Calorimeter. 23, 28–30

**IBF** Ion Backflow Fraction. 41, 45, 62

**ILC** International Linear Collider. 14, 15, 17–22, 30, 48, 50, 101, 103, 127, 130, 133, 137, 143–145, 163

**ILD** International Large Detector. 17, 21–25, 28, 30, 35, 44, 48, 50, 77, 84, 101–103, 117, 123, 126–128, 130, 134, 143, 163

- IP** beam Interaction Point. 18–20, 23, 27, 54, 101, 106, 111, 112, 114, 118, 121
- LHC** Large Hadron Collider. 14, 17, 139, 164
- MEMS** microelectromechanical systems. 44, 51
- Micromegas** micro-mesh gaseous structure. 42–44, 52, 62, 129, 137, 143, 163, 164
- MIP** Minimum Ionising Particle. 36, 44, 64, 78, 79, 81
- PAI model** Photo-Absorption Ionisation model. 36, 37
- PCB** Printed Circuit Board. 142, 164
- PMNS** Pontecorvo–Maki–Nakagawa–Sakata. 8
- QCD** quantum chromodynamics. 7, 17
- QFT** quantum field theory. 6, 10
- RTML** Ring To Main Linac. 19
- SCRF** Superconducting Radio-Frequency. 18, 19
- SET** Silicon outer layers. 26, 27, 128
- SiPM** Silicon Photo Multiplier. 29, 30
- SiRN** silicon-rich silicon nitride. 53, 65
- SIT** Silicon Inner Tracker. 26, 27, 121, 128
- SM** Standard Model of particle physics. 5, 6, 9–11
- T2K** Tokai to Kamioka. 44, 60, 61
- ToA** Time of Arrival. 55, 56, 67, 69, 73, 76, 141
- ToF** Time of Flight. 27
- ToT** Time over Threshold. 55, 56, 58–60, 67, 71–76, 90, 91, 106
- TPC** Time Projection Chamber. 25–28, 33–35, 39, 40, 44, 48–52, 54, 55, 62, 75–77, 83, 84, 86, 89, 93, 97, 102, 103, 105, 106, 111, 112, 114, 117–119, 121, 123–133, 136–138, 141, 143, 144, 163, 164
- VTX** vertex detector. 26, 27

---

# Bibliography

---

- [1] M. Thomson, *Modern particle physics*. Cambridge University Press, New York, 2013.
- [2] **ATLAS**, G. Aad *et al.*, “Observation of a new particle in the search for the Standard Model Higgs boson with the ATLAS detector at the LHC,” *Phys. Lett. B* **716** (2012) 1–29, [arXiv:1207.7214 \[hep-ex\]](#).
- [3] **CMS**, S. Chatrchyan *et al.*, “Observation of a New Boson at a Mass of 125 GeV with the CMS Experiment at the LHC,” *Phys. Lett. B* **716** (2012) 30–61, [arXiv:1207.7235 \[hep-ex\]](#).
- [4] P. W. Higgs, “Broken Symmetries and the Masses of Gauge Bosons,” *Phys. Rev. Lett.* **13** (1964) 508–509.
- [5] F. Englert and R. Brout, “Broken Symmetry and the Mass of Gauge Vector Mesons,” *Phys. Rev. Lett.* **13** (1964) 321–323.
- [6] A. Einstein, “The Foundation of the General Theory of Relativity,” *Annalen Phys.* **49** no. 7, (1916) 769–822.
- [7] **Planck**, N. Aghanim *et al.*, “Planck 2018 results. VI. Cosmological parameters,” [arXiv:1807.06209 \[astro-ph.CO\]](#).
- [8] A. Riotto, “Theories of baryogenesis,” in *ICTP Summer School in High-Energy Physics and Cosmology*, pp. 326–436. 7, 1998. [arXiv:hep-ph/9807454](#).
- [9] P. La Rocca and F. Riggi, “The upgrade programme of the major experiments at the Large Hadron Collider,” *J. Phys. Conf. Ser.* **515** (2014) 012012.
- [10] **European Strategy Group**, *2020 Update of the European Strategy for Particle Physics*. CERN Council, Geneva, 2020. <http://cds.cern.ch/record/2721370/files/CERN-ESU-015-2020%20Update%20European%20Strategy.pdf>.
- [11] J. Augustin, N. Dikansky, Y. Derbenev, J. Rees, B. Richter, A. Skrinsky, M. Tigner, and H. Wiedemann, “Limitations on Performance of e+ e- Storage Rings and Linear Colliding Beam Systems at High Energy,” *eConf C781015* (1978) 87–105.
- [12] T. Behnke, J. E. Brau, B. Foster, J. Fuster, M. Harrison, J. M. Paterson, M. Peskin, M. Stanitzki, N. Walker, and H. Yamamoto, eds., *The International Linear Collider Technical Design Report - Volume 1: Executive Summary*. 2013. [arXiv:1306.6327 \[physics.acc-ph\]](#).
- [13] T. Behnke, J. E. Brau, P. N. Burrows, J. Fuster, M. Peskin, M. Stanitzki, Y. Sugimoto, S. Yamada, and H. Yamamoto, eds., *The International Linear Collider Technical Design Report - Volume 4: Detectors*. 2013. [arXiv:1306.6329 \[physics.ins-det\]](#).



- [14] J. N. Marx and D. R. Nygren, “The Time Projection Chamber,” *Phys. Today* **31N10** (1978) 46–53.
- [15] H. Geiger and W. Müller, “Elektronenzählrohr zur Messung schwächster Aktivitäten,” *Naturwissenschaften* **16** no. 31, (Aug., 1928) 617–618.
- [16] G. Charpak, R. Bouclier, T. Bressani, J. Favier, and C. Zupancic, “The Use of Multiwire Proportional Counters to Select and Localize Charged Particles,” *Nucl. Instrum. Meth.* **62** (1968) 262–268.
- [17] A. Walenta, J. Heintze, and B. Schuerlein, “The multiwire drift chamber, a new type of proportional wire chamber,” *Nucl. Instrum. Meth.* **92** (1971) 373–380.
- [18] C. Brand *et al.*, “The DELPHI Time Projection Chamber,” *IEEE Trans. Nucl. Sci.* **36** (1989) 122–126.
- [19] W. Atwood *et al.*, “Performance of the ALEPH time projection chamber,” *Nucl. Instrum. Meth. A* **306** (1991) 446–458.
- [20] Y. Giomataris, P. Rebourgeard, J. P. Robert, and G. Charpak, “MICROMEGAS: A High granularity position sensitive gaseous detector for high particle flux environments,” *Nucl. Instrum. Meth.* **A376** (1996) 29–35.
- [21] F. Sauli, “GEM: A new concept for electron amplification in gas detectors,” *Nucl. Instrum. Meth.* **A386** (1997) 531–534.
- [22] P. Colas, A. P. Colijn, A. Fornaini, Y. Giomataris, H. van der Graaf, E. H. M. Heijne, X. Llopart, J. Schmitz, J. Timmermans, and J. L. Visschers, “The readout of a GEM- or micromegas-equipped TPC by means of the Medipix2 CMOS sensor as direct anode,” *Nucl. Instrum. Meth.* **A535** (2004) 506–510.
- [23] M. Campbell *et al.*, “Detection of single electrons by means of a micromegas-covered MediPix2 pixel CMOS readout circuit,” *Nucl. Instrum. Meth.* **A540** (2005) 295–304, [arXiv:physics/0409048](https://arxiv.org/abs/physics/0409048) [physics].
- [24] T. Poikela, J. Plosila, T. Westerlund, M. Campbell, M. De Gaspari, X. Llopart, V. Gromov, R. Kluit, M. van Beuzekom, F. Zappone, V. Zivkovic, C. Brezina, K. Desch, Y. Fu, and A. Kruth, “Timepix3: a 65K channel hybrid pixel readout chip with simultaneous ToA/ToT and sparse readout,” *JINST* **9** no. 05, (2014) C05013. <http://stacks.iop.org/1748-0221/9/i=05/a=C05013>.
- [25] C. Ligtenberg, K. Heijhoff, Y. Bilevych, K. Desch, H. van der Graaf, F. Hartjes, J. Kaminski, P. M. Kluit, G. Raven, T. Schiffer, and J. Timmermans, “Performance of a GridPix detector based on the Timepix3 chip,” *Nucl. Instrum. Meth.* **A908** (2018) 18–23.
- [26] C. Ligtenberg *et al.*, “Performance of the GridPix detector quad,” *Nucl. Instrum. Meth.* **A956** (2020) 163331, [arXiv:2001.01540](https://arxiv.org/abs/2001.01540) [physics.ins-det].
- [27] S. Glashow, “Partial Symmetries of Weak Interactions,” *Nucl. Phys.* **22** (1961) 579–588.
- [28] A. Salam, “Weak and Electromagnetic Interactions,” *Conf. Proc. C* **680519** (1968) 367–377.
- [29] S. Weinberg, “A Model of Leptons,” *Phys. Rev. Lett.* **19** (1967) 1264–1266.
- [30] G. ’t Hooft and M. Veltman, “Regularization and Renormalization of Gauge Fields,” *Nucl. Phys. B* **44** (1972) 189–213.

- [31] **Gargamelle Neutrino**, F. Hasert *et al.*, “Observation of Neutrino Like Interactions Without Muon Or Electron in the Gargamelle Neutrino Experiment,” *Phys. Lett. B* **46** (1973) 138–140.
- [32] **SLAC-SP-017**, J. Augustin *et al.*, “Discovery of a Narrow Resonance in  $e^+e^-$  Annihilation,” *Phys. Rev. Lett.* **33** (1974) 1406–1408.
- [33] **E598**, J. Aubert *et al.*, “Experimental Observation of a Heavy Particle  $J$ ,” *Phys. Rev. Lett.* **33** (1974) 1404–1406.
- [34] M. L. Perl *et al.*, “Evidence for Anomalous Lepton Production in  $e^+ - e^-$  Annihilation,” *Phys. Rev. Lett.* **35** (1975) 1489–1492.
- [35] C.-N. Yang and R. L. Mills, “Conservation of Isotopic Spin and Isotopic Gauge Invariance,” *Phys. Rev.* **96** (1954) 191–195.
- [36] M. Gell-Mann, “A Schematic Model of Baryons and Mesons,” *Phys. Lett.* **8** (1964) 214–215.
- [37] G. Zweig, “An SU(3) model for strong interaction symmetry and its breaking. Version 1,”.
- [38] J. Goldstone, A. Salam, and S. Weinberg, “Broken Symmetries,” *Phys. Rev.* **127** (1962) 965–970.
- [39] **UA1**, G. Arnison *et al.*, “Experimental Observation of Isolated Large Transverse Energy Electrons with Associated Missing Energy at  $s^{1/2} = 540$  GeV,” *Phys. Lett. B* **122** (1983) 103–116.
- [40] **UA1**, G. Arnison *et al.*, “Experimental Observation of Lepton Pairs of Invariant Mass Around 95 GeV/ $c^2$  at the CERN SPS Collider,” *Phys. Lett. B* **126** (1983) 398–410.
- [41] **CDF**, F. Abe *et al.*, “Observation of top quark production in  $\bar{p}p$  collisions,” *Phys. Rev. Lett.* **74** (1995) 2626–2631, [arXiv:hep-ex/9503002](https://arxiv.org/abs/hep-ex/9503002).
- [42] **D0**, S. Abachi *et al.*, “Observation of the top quark,” *Phys. Rev. Lett.* **74** (1995) 2632–2637, [arXiv:hep-ex/9503003](https://arxiv.org/abs/hep-ex/9503003).
- [43] **DONUT**, K. Kodama *et al.*, “Observation of tau neutrino interactions,” *Phys. Lett. B* **504** (2001) 218–224, [arXiv:hep-ex/0012035](https://arxiv.org/abs/hep-ex/0012035).
- [44] F. Halzen and A. D. Martin, *Quarks and leptons: An introductory course in modern particle physics*. John Wiley & Sons, 1, 1984.
- [45] **Particle Data Group**, M. Tanabashi *et al.*, “Review of Particle Physics,” *Phys. Rev.* **D98** no. 3, (2018) 030001.
- [46] P. A. Dirac, “The quantum theory of the electron,” *Proc. Roy. Soc. Lond. A* **117** (1928) 610–624.
- [47] D. Galbraith and C. Burgard, “A standard diagram of the current standard model of physics,” 2012.  
<http://davidgalbraith.org/portfolio/ux-standard-model-of-the-standard-model/>.
- [48] R. Feynman, “The Theory of positrons,” *Phys. Rev.* **76** (1949) 749–759.
- [49] C. Bollini and J. Giambiagi, “Dimensional Renormalization: The Number of Dimensions as a Regularizing Parameter,” *Nuovo Cim. B* **12** (1972) 20–26.
- [50] G. 't Hooft, “Dimensional regularization and the renormalization group,” *Nucl. Phys. B* **61** (1973) 455–468.

- [51] D. J. Gross and F. Wilczek, “Ultraviolet Behavior of Nonabelian Gauge Theories,” *Phys. Rev. Lett.* **30** (1973) 1343–1346.
- [52] H. Politzer, “Reliable Perturbative Results for Strong Interactions?,” *Phys. Rev. Lett.* **30** (1973) 1346–1349.
- [53] N. Cabibbo, “Unitary Symmetry and Leptonic Decays,” *Phys. Rev. Lett.* **10** (1963) 531–533.
- [54] M. Kobayashi and T. Maskawa, “CP Violation in the Renormalizable Theory of Weak Interaction,” *Prog. Theor. Phys.* **49** (1973) 652–657.
- [55] Z. Maki, M. Nakagawa, and S. Sakata, “Remarks on the unified model of elementary particles,” *Prog. Theor. Phys.* **28** (1962) 870–880.
- [56] B. Pontecorvo, “Inverse beta processes and nonconservation of lepton charge,” *Sov. Phys. JETP* **7** (1958) 172–173.
- [57] L. Wolfenstein, “Parametrization of the Kobayashi-Maskawa Matrix,” *Phys. Rev. Lett.* **51** (1983) 1945.
- [58] P. W. Higgs, “Broken symmetries, massless particles and gauge fields,” *Phys. Lett.* **12** (1964) 132–133.
- [59] G. Guralnik, C. Hagen, and T. Kibble, “Global Conservation Laws and Massless Particles,” *Phys. Rev. Lett.* **13** (1964) 585–587.
- [60] P. W. Higgs, “Spontaneous Symmetry Breakdown without Massless Bosons,” *Phys. Rev.* **145** (1966) 1156–1163.
- [61] T. Kibble, “Symmetry breaking in non-Abelian gauge theories,” *Phys. Rev.* **155** (1967) 1554–1561.
- [62] H. Yukawa, “On the Interaction of Elementary Particles I,” *Proc. Phys. Math. Soc. Jap.* **17** (1935) 48–57.
- [63] J. Wheeler, “Geons,” *Phys. Rev.* **97** (1955) 511–536.
- [64] L. Landau, A. Abrikosov, and I. Khalatnikov, “An asymptotic expression for the photon Green function in quantum electrodynamics,” *Dokl. Akad. Nauk SSSR* **95** no. 6, (1954) 1177–1180.
- [65] D. Buttazzo, G. Degrassi, P. P. Giardino, G. F. Giudice, F. Sala, A. Salvio, and A. Strumia, “Investigating the near-criticality of the Higgs boson,” *JHEP* **12** (2013) 089, [arXiv:1307.3536](https://arxiv.org/abs/1307.3536) [[hep-ph](#)].
- [66] R. K. Ellis *et al.*, “Physics Briefing Book: Input for the European Strategy for Particle Physics Update 2020,” [arXiv:1910.11775](https://arxiv.org/abs/1910.11775) [[hep-ex](#)].
- [67] Y. Nagashima, *Beyond the standard model of elementary particle physics*. Wiley-VCH, Weinheim, USA, 2014.
- [68] C. Csáki and P. Tanedo, “Beyond the Standard Model,” in *2013 European School of High-Energy Physics*, pp. 169–268. 2015. [arXiv:1602.04228](https://arxiv.org/abs/1602.04228) [[hep-ph](#)].
- [69] A. Liddle, *An introduction to modern cosmology; 2nd ed.* Wiley, Chichester, 2003. <https://cds.cern.ch/record/1010476>.
- [70] R. Adler, B. Casey, and O. Jacob, “Vacuum catastrophe: An Elementary exposition of the cosmological constant problem,” *Am. J. Phys.* **63** (1995) 620–626.

- [71] G. Gabrielse, D. Hanneke, T. Kinoshita, M. Nio, and B. C. Odom, “New Determination of the Fine Structure Constant from the Electron  $g$  Value and QED,” *Phys. Rev. Lett.* **97** (2006) 030802. [Erratum: *Phys.Rev.Lett.* 99, 039902 (2007)].
- [72] **Muon  $g-2$** , G. Bennett *et al.*, “Final Report of the Muon E821 Anomalous Magnetic Moment Measurement at BNL,” *Phys. Rev. D* **73** (2006) 072003, [arXiv:hep-ex/0602035](#).
- [73] **LHCb**, R. Aaij *et al.*, “Test of lepton universality with  $B^0 \rightarrow K^{*0} \ell^+ \ell^-$  decays,” *JHEP* **08** (2017) 055, [arXiv:1705.05802 \[hep-ex\]](#).
- [74] **LHCb**, R. Aaij *et al.*, “Search for lepton-universality violation in  $B^+ \rightarrow K^+ \ell^+ \ell^-$  decays,” *Phys. Rev. Lett.* **122** no. 19, (2019) 191801, [arXiv:1903.09252 \[hep-ex\]](#).
- [75] J. C. Pati and A. Salam, “Lepton Number as the Fourth Color,” *Phys. Rev. D* **10** (1974) 275–289. [Erratum: *Phys.Rev.D* 11, 703–703 (1975)].
- [76] H. Georgi and S. Glashow, “Unity of All Elementary Particle Forces,” *Phys. Rev. Lett.* **32** (1974) 438–441.
- [77] A. Buras, J. R. Ellis, M. Gaillard, and D. V. Nanopoulos, “Aspects of the Grand Unification of Strong, Weak and Electromagnetic Interactions,” *Nucl. Phys. B* **135** (1978) 66–92.
- [78] U. Amaldi, W. de Boer, and H. Furstenau, “Comparison of grand unified theories with electroweak and strong coupling constants measured at LEP,” *Phys. Lett. B* **260** (1991) 447–455.
- [79] M. Gell-Mann, “The Eightfold Way: A Theory of strong interaction symmetry,”.
- [80] S. Weinberg, “Implications of Dynamical Symmetry Breaking,” *Phys. Rev. D* **13** (1976) 974–996. [Addendum: *Phys.Rev.D* 19, 1277–1280 (1979)].
- [81] E. Gildener, “Gauge Symmetry Hierarchies,” *Phys. Rev. D* **14** (1976) 1667.
- [82] L. Susskind, “Dynamics of Spontaneous Symmetry Breaking in the Weinberg-Salam Theory,” *Phys. Rev. D* **20** (1979) 2619–2625.
- [83] G. 't Hooft, C. Itzykson, A. Jaffe, H. Lehmann, P. Mitter, I. Singer, and R. Stora, eds., *Recent Developments in Gauge Theories. Proceedings, Nato Advanced Study Institute, Cargese, France, August 26 - September 8, 1979*, vol. 59. 1980.
- [84] H. Miyazawa, “Baryon Number Changing Currents,” *Prog. Theor. Phys.* **36** no. 6, (1966) 1266–1276.
- [85] Y. Golfand and E. Likhtman, “Extension of the Algebra of Poincare Group Generators and Violation of  $p$  Invariance,” *JETP Lett.* **13** (1971) 323–326.
- [86] J.-L. Gervais and B. Sakita, “Field Theory Interpretation of Supergauges in Dual Models,” *Nucl. Phys. B* **34** (1971) 632–639.
- [87] D. Volkov and V. Akulov, “Is the Neutrino a Goldstone Particle?,” *Phys. Lett. B* **46** (1973) 109–110.
- [88] E. Witten, “Dynamical Breaking of Supersymmetry,” *Nucl. Phys. B* **188** (1981) 513.
- [89] R. K. Kaul, “Gauge Hierarchy in a Supersymmetric Model,” *Phys. Lett. B* **109** (1982) 19–24.
- [90] K. Agashe, R. Contino, and A. Pomarol, “The Minimal composite Higgs model,” *Nucl. Phys. B* **719** (2005) 165–187, [arXiv:hep-ph/0412089](#).

- [91] N. Arkani-Hamed, S. Dimopoulos, and G. Dvali, “The Hierarchy problem and new dimensions at a millimeter,” *Phys. Lett. B* **429** (1998) 263–272, [arXiv:hep-ph/9803315](#).
- [92] L. Randall and R. Sundrum, “A Large mass hierarchy from a small extra dimension,” *Phys. Rev. Lett.* **83** (1999) 3370–3373, [arXiv:hep-ph/9905221](#).
- [93] H. Georgi, “Effective field theory,” *Ann. Rev. Nucl. Part. Sci.* **43** (1993) 209–252.
- [94] J. R. Espinosa, “Higgs Effective Field Theory,” *PoS CORFU2015* (2016) 012.
- [95] A. Sakharov, “Violation of CP Invariance, C asymmetry, and baryon asymmetry of the universe,” *Sov. Phys. Usp.* **34** no. 5, (1991) 392–393.
- [96] C. Grojean, G. Servant, and J. D. Wells, “First-order electroweak phase transition in the standard model with a low cutoff,” *Phys. Rev. D* **71** (2005) 036001, [arXiv:hep-ph/0407019](#).
- [97] K. Kajantie, M. Laine, K. Rummukainen, and M. E. Shaposhnikov, “Is there a hot electroweak phase transition at  $m(H)$  larger or equal to  $m(W)$ ?,” *Phys. Rev. Lett.* **77** (1996) 2887–2890, [arXiv:hep-ph/9605288](#).
- [98] **CLICdp, CLIC**, T. Charles *et al.*, “The Compact Linear Collider (CLIC) - 2018 Summary Report,” [arXiv:1812.06018 \[physics.acc-ph\]](#).
- [99] **CEPC Study Group**, M. Dong *et al.*, “CEPC Conceptual Design Report: Volume 2 - Physics & Detector,” [arXiv:1811.10545 \[hep-ex\]](#).
- [100] **FCC collaboration**, A. Abada *et al.*, “FCC Physics Opportunities,” *Eur. Phys. J. C* **79** no. 6, (2019) 474.
- [101] A. Arbey *et al.*, “Physics at the  $e^+e^-$  Linear Collider,” *Eur. Phys. J. C* **75** no. 8, (2015) 371, [arXiv:1504.01726 \[hep-ph\]](#).
- [102] H. Abramowicz *et al.*, “Higgs physics at the CLIC electron–positron linear collider,” *Eur. Phys. J. C* **77** no. 7, (2017) 475, [arXiv:1608.07538 \[hep-ex\]](#).
- [103] **LHC Higgs Cross Section Working Group**, D. de Florian *et al.*, “Handbook of LHC Higgs Cross Sections: 4. Deciphering the Nature of the Higgs Sector,” [arXiv:1610.07922 \[hep-ph\]](#).
- [104] A. Denner, S. Heinemeyer, I. Puljak, D. Rebuszi, and M. Spira, “Standard Model Higgs-Boson Branching Ratios with Uncertainties,” *Eur. Phys. J. C* **71** (2011) 1753, [arXiv:1107.5909 \[hep-ph\]](#).
- [105] A. Djouadi, W. Kilian, M. Muhlleitner, and P. Zerwas, “Testing Higgs selfcouplings at  $e^+e^-$  linear colliders,” *Eur. Phys. J. C* **10** (1999) 27–43, [arXiv:hep-ph/9903229](#).
- [106] K. Fujii *et al.*, “Physics Case for the International Linear Collider,” [arXiv:1506.05992 \[hep-ex\]](#).
- [107] K. Fujii *et al.*, “Physics Case for the 250 GeV Stage of the International Linear Collider,” [arXiv:1710.07621 \[hep-ex\]](#).
- [108] **ATLAS**, “Projections for measurements of Higgs boson signal strengths and coupling parameters with the ATLAS detector at a HL-LHC,” <https://inspirehep.net/files/cc29e929281200fa41f5dcbc0bdf7f32>.  
ATL-PHYS-PUB-2014-016.

- [109] **LHC Higgs Cross Section Working Group**, A. David, A. Denner, M. Duehrssen, M. Grazzini, C. Grojean, G. Passarino, M. Schumacher, M. Spira, G. Weiglein, and M. Zanetti, “LHC HXSWG interim recommendations to explore the coupling structure of a Higgs-like particle,” [arXiv:1209.0040](https://arxiv.org/abs/1209.0040) [[hep-ph](https://arxiv.org/archive/hep)].
- [110] L. Evans and P. Bryant, “LHC Machine,” *JINST* **3** (2008) S08001.
- [111] M. Lamont, “LHC Performance in Run 2 and Beyond,” *PoS LeptonPhoton2015* (2016) 001. 8 p. <https://cds.cern.ch/record/2257503>.
- [112] C. Adolphsen, M. Barone, B. Barish, K. Buesser, P. Burrows, J. Carwardine, J. Clark, H. Mainaud Durand, G. Dugan, E. Elsen, *et al.*, “The International Linear Collider Technical Design Report - Volume 3.II: Accelerator Baseline Design,” [arXiv:1306.6328](https://arxiv.org/abs/1306.6328) [[physics.acc-ph](https://arxiv.org/archive/physics)].
- [113] C. Adolphsen, M. Barone, B. Barish, K. Buesser, P. Burrows, J. Carwardine, J. Clark, H. Mainaud Durand, G. Dugan, E. Elsen, *et al.*, “The International Linear Collider Technical Design Report - Volume 3.I: Accelerator R&D in the Technical Design Phase,” [arXiv:1306.6353](https://arxiv.org/abs/1306.6353) [[physics.acc-ph](https://arxiv.org/archive/physics)].
- [114] P. Bambade *et al.*, “The International Linear Collider: A Global Project,” [arXiv:1903.01629](https://arxiv.org/abs/1903.01629) [[hep-ex](https://arxiv.org/archive/hep)].
- [115] D. Reschke, V. Gubarev, J. Schaffran, L. Steder, N. Walker, M. Wenskat, and L. Monaco, “Performance in the vertical test of the 832 nine-cell 1.3 GHz cavities for the European X-ray Free Electron Laser,” *Phys. Rev. Accel. Beams* **20** (2017) 042004.
- [116] M. Harrison, M. Ross, and N. Walker, “Luminosity Upgrades for ILC,” in *Proceedings, 2013 Community Summer Study on the Future of U.S. Particle Physics: Snowmass on the Mississippi (CSS2013): Minneapolis, MN, USA, July 29-August 6, 2013*. 2013. [arXiv:1308.3726](https://arxiv.org/abs/1308.3726) [[physics.acc-ph](https://arxiv.org/archive/physics)].
- [117] **Linear Collider ILD Concept Group**, T. Abe *et al.*, “The International Large Detector: Letter of Intent,” [arXiv:1006.3396](https://arxiv.org/abs/1006.3396) [[hep-ex](https://arxiv.org/archive/hep)].
- [118] **ILD collaboration**, T. Behnke, K. Buesser, K. Fujii, F. Gaede, K. Kawagoe, J. List, A. Miyamoto, C. Vallée, and H. Videau, eds., *International Large Detector: Interim Design Report*. 2020. [arXiv:2003.01116](https://arxiv.org/abs/2003.01116) [[physics.ins-det](https://arxiv.org/archive/physics)].
- [119] **ALEPH collaboration**, D. Buskulic *et al.*, “Performance of the ALEPH detector at LEP,” *Nucl. Instrum. Meth.* **A360** (1995) 481–506.
- [120] J.-C. Brient and H. Videau, “The Calorimetry at the future  $e^+e^-$  linear collider,” *eConf C010630* (2001) E3047, [arXiv:hep-ex/0202004](https://arxiv.org/abs/hep-ex/0202004) [[hep-ex](https://arxiv.org/archive/hep)].
- [121] M. A. Thomson, “Particle Flow Calorimetry and the PandoraPFA Algorithm,” *Nucl. Instrum. Meth.* **A611** (2009) 25–40, [arXiv:0907.3577](https://arxiv.org/abs/0907.3577) [[physics.ins-det](https://arxiv.org/archive/physics)].
- [122] D. R. Nygren, “Proposal to investigate the feasibility of a novel concept in particle detection,” 1974.
- [123] D. Nygren, “The Time Projection Chamber: A New 4 pi Detector for Charged Particles,” *eConf C740805* (1974) 58.
- [124] O. Schäfer, “Working principle of a TPC,” 2020. <https://www.lctpc.org/e8/e57671/>. Retrieved january 2020.

- [125] W. Blum, L. Rolandi, and W. Riegler, *Particle detection with drift chambers*. Particle Acceleration and Detection. Springer, 2008.  
<https://www.springer.com/gp/book/9783540766834>.
- [126] F. M. Penning, “Über Ionisation durch metastabile Atome,” *Naturwissenschaften* **15** no. 40, (Oct, 1927) 818–818.
- [127] H. Bethe, “Zur Theorie des Durchgangs schneller Korpuskularstrahlen durch Materie,” *Annalen der Physik* **397** no. 3, (Jan, 1930) 325–400.
- [128] F. Bloch, “Zur Bremsung Rasch Bewegter Teilchen beim Durchgang durch Materie,” *Annalen Phys.* **408** (1933) 285–320.
- [129] E. Fermi, “The Ionization Loss of Energy in Gases and in Condensed Materials,” *Phys. Rev.* **57** (1940) 485–493.
- [130] L. Landau, “On the energy loss of fast particles by ionization,” *J. Phys.(USSR)* **8** (1944) 201–205.
- [131] H. Bichsel, “Straggling in Thin Silicon Detectors,” *Rev. Mod. Phys.* **60** (1988) 663–699.
- [132] W. W. M. Allison and J. H. Cobb, “Relativistic Charged Particle Identification by Energy Loss,” *Ann. Rev. Nucl. Part. Sci.* **30** (1980) 253–298.
- [133] H. Fischle, J. Heintze, and B. Schmidt, “Experimental determination of ionization cluster size distributions in counting gases,” *Nucl. Instrum. Meth. A* **301** (1991) 202–214.
- [134] I. B. Smirnov, “Modeling of ionization produced by fast charged particles in gases,” *Nucl. Instrum. Meth.* **A554** (2005) 474–493.
- [135] G. Molière, “Theorie der Streuung schneller geladener Teilchen II. Mehrfach- und Vielfachstreuung,” *Zeitschrift Naturforschung Teil A* **3** (Feb., 1948) 78–97.
- [136] H. A. Bethe, “Molière’s theory of multiple scattering,” *Phys. Rev.* **89** (Mar, 1953) 1256–1266.  
<https://link.aps.org/doi/10.1103/PhysRev.89.1256>.
- [137] V. L. Highland, “Some practical remarks on multiple scattering,” *Nucl. Instrum. Meth.* **129** no. 2, (1975) 497–499.
- [138] G. R. Lynch and O. I. Dahl, “Approximations to multiple coulomb scattering,” *Nucl. Instrum. Meth. B* **58** no. 1, (1991) 6–10.
- [139] C. Ramsauer, “Über den wirkungsquerschnitt der gasmoleküle gegenüber langsamen elektronen. i. fortsetzung,” *Annalen der Physik* **371** no. 24, (1922) 546–558.  
<https://doi.org/10.1002/andp.19223712403>.
- [140] W. P. Allis, *Motions of Ions and Electrons*, pp. 383–444. Springer Berlin Heidelberg, Berlin, Heidelberg, 1956. [https://doi.org/10.1007/978-3-642-45844-6\\_5](https://doi.org/10.1007/978-3-642-45844-6_5).
- [141] J. S. Townsend and H. T. Tizard, “The Motion of Electrons in Gases,” *Proceedings of the Royal Society of London Series A* **88** no. 604, (June, 1913) 336–347.
- [142] J. Townsend and V. Bailey, “XCVII. The motion of electrons in gases,” *The London, Edinburgh, and Dublin Philosophical Magazine and Journal of Science* **42** no. 252, (1921) 873–891. <https://doi.org/10.1080/14786442108633831>.
- [143] J. Byrne, “III.—Statistics of the Electron-Multiplication Process in Proportional Counters,” *Proceedings of the Royal Society of Edinburgh. Section A. Mathematical and Physical Sciences* **66** no. 1, (1962) 33–41.

- [144] F. Sauli, “Gaseous Radiation Detectors,” *Camb. Monogr. Part. Phys. Nucl. Phys. Cosmol.* **36** (2014) pp.1–497.
- [145] **T2K collaboration**, K. Abe *et al.*, “The T2K Experiment,” *Nucl. Instrum. Meth. A* **659** (2011) 106–135, [arXiv:1106.1238](https://arxiv.org/abs/1106.1238) [physics.ins-det].
- [146] M. Kobayashi *et al.*, “Cosmic ray tests of a GEM-based TPC prototype operated in Ar-CF<sub>4</sub>-isobutane gas mixtures,” *Nucl. Instrum. Meth.* **A641** (2011) 37–47, [arXiv:1008.5068](https://arxiv.org/abs/1008.5068) [physics.ins-det]. [Erratum: *Nucl. Instrum. Meth.*A697,122(2013)].
- [147] A. F. V. Cortez, M. A. G. Santos, R. Veenhof, P. N. B. Neves, F. I. G. M. Borges, and C. A. N. Conde, “Experimental ion mobility measurements for the LCTPC Collaboration,” *Nucl. Instrum. Meth.* **A936** (2019) 451–452.
- [148] A. F. V. Cortez, M. A. G. Santos, R. Veenhof, J. Escada, P. N. B. Neves, F. P. Santos, C. A. N. Conde, and F. I. G. M. Borges, “Experimental ion mobility measurements in pure iC<sub>4</sub>H<sub>10</sub> and Ar-iC<sub>4</sub>H<sub>10</sub> mixtures,” *JINST* **14** no. 04, (2019) P04010.
- [149] A. Ishikawa, “Gas properties.” <http://skipper.physics.sunysb.edu/~kdehmelt/gas/>. retrieved January 2020.
- [150] A. Vogel, *Beam-induced backgrounds in detectors at the ILC*. PhD thesis, Hamburg U., 2008. DESY-THESIS-2008-036.
- [151] D. Arai, “Ion problem report,” 2012. [https://agenda.linearcollider.org/event/5522/contributions/24724/subcontributions/824/attachments/20286/32007/ion\\_report\\_wp.pdf](https://agenda.linearcollider.org/event/5522/contributions/24724/subcontributions/824/attachments/20286/32007/ion_report_wp.pdf).
- [152] K. Fujii, “Positive ion effects,” 2012. <https://agenda.linearcollider.org/event/5504/contributions/24543/attachments/20144/31818/PositiveIonEffects-kf.pdf>.
- [153] M. Kobayashi *et al.*, “Measurement of the electron transmission rate of the gating foil for the TPC of the ILC experiment,” *Nucl. Instrum. Meth.* **A918** (2019) 41–53, [arXiv:1903.01717](https://arxiv.org/abs/1903.01717) [physics.ins-det].
- [154] M. Aicheler, P. Burrows, M. Draper, T. Garvey, P. Lebrun, K. Peach, N. Phinney, H. Schmickler, D. Schulte, and N. Toge, eds., *A Multi-TeV Linear Collider Based on CLIC Technology*. 2012. CERN-2012-007.
- [155] L. Linssen, A. Miyamoto, M. Stanitzki, and H. Weerts, eds., *Physics and Detectors at CLIC: CLIC Conceptual Design Report*. 2012. [arXiv:1202.5940](https://arxiv.org/abs/1202.5940) [physics.ins-det]. CERN-2012-003.
- [156] **CERN Linear Collider Detector collaboration**, M. Killenberg, “Occupancy in the CLIC ILD Time Projection Chamber using Pixelised Readout,” <https://cds.cern.ch/record/1543486>. LCD-Note-2013-005.
- [157] **FCC collaboration**, A. Abada *et al.*, “FCC-ee: The Lepton Collider,” *Eur. Phys. J. ST* **228** no. 2, (2019) 261–623.
- [158] **FCC collaboration**, A. Abada *et al.*, “FCC-hh: The Hadron Collider,” *Eur. Phys. J. ST* **228** no. 4, (2019) 755–1107.
- [159] P. Schwemling, “TPC studies for FCC-ee.” Talk presented at Joint CEA-IHEP/Tsinghua meeting, 14-15 december, Saclay, Paris, 2015. [https://indico.cern.ch/event/467955/contributions/1146290/attachments/1204735/1755443/TLEP\\_141215.pdf](https://indico.cern.ch/event/467955/contributions/1146290/attachments/1204735/1755443/TLEP_141215.pdf).
- [160] **CEPC Study Group**, “CEPC Conceptual Design Report: Volume 1 - Accelerator,” [arXiv:1809.00285](https://arxiv.org/abs/1809.00285) [physics.acc-ph].



- [161] P. Kluit, “Pixel TPC for CEPC,” 2020. [https://agenda.linearcollider.org/event/8362/contributions/45037/attachments/35258/54650/PixelTPC\\_CEPC.pdf](https://agenda.linearcollider.org/event/8362/contributions/45037/attachments/35258/54650/PixelTPC_CEPC.pdf). Talk at the LCTPC collaboration meeting, DESY.
- [162] M. Zhao, M. Ruan, H. Qi, and Y. Gao, “Feasibility study of TPC at electron positron colliders at  $Z$  pole operation,” *JINST* **12** no. 07, (2017) P07005, arXiv:1704.04401 [physics.ins-det].
- [163] J. Kaminski, Y. Bilevych, K. Desch, C. Krieger, and M. Lupberger, “GridPix detectors - introduction and applications,” *Nucl. Instrum. Meth.* **A845** (2017) 233–235.
- [164] J. Kaminski, “GridPix detector with Timepix3 ASIC,” 2017. [https://indico.cern.ch/event/581417/contributions/2522462/attachments/1465797/2265982/GridPix\\_TP3.pdf](https://indico.cern.ch/event/581417/contributions/2522462/attachments/1465797/2265982/GridPix_TP3.pdf). Talk at MPGD 2017, May 22 - 26 Philadelphia.
- [165] M. Fransen, *Gridpix: TPC development on the right track. The development and characterisation of a TPC with a CMOS pixel chip read out*. PhD thesis, Amsterdam U., 2012. [http://www.nikhef.nl/pub/services/biblio/theses\\_pdf/thesis\\_M\\_Fransen.pdf](http://www.nikhef.nl/pub/services/biblio/theses_pdf/thesis_M_Fransen.pdf).
- [166] S. Tsigaridas, *New Generation GridPix: Development and characterization of pixelated gaseous detectors based on the Timepix3 chip*. PhD thesis, Amsterdam U., 2017. [http://www.nikhef.nl/pub/services/biblio/theses\\_pdf/thesis\\_S\\_Tsigaridas.pdf](http://www.nikhef.nl/pub/services/biblio/theses_pdf/thesis_S_Tsigaridas.pdf).
- [167] X. Llopert and T. Poikela, *Timepix3 Manual v2.0*. CERN, 2016.
- [168] M. A. Chefdeville, *Development of Micromegas-like Gaseous Detectors Using a Pixel Readout Chip as Collecting Anode*. PhD thesis, Amsterdam U., 2009. [http://www.nikhef.nl/pub/services/biblio/theses\\_pdf/thesis\\_MA\\_Chefdeville.pdf](http://www.nikhef.nl/pub/services/biblio/theses_pdf/thesis_MA_Chefdeville.pdf).
- [169] F. Hartjes, N. Hessey, M. Fransen, S. Konovalov, W. Koppert, S. Morozov, A. Romaniouk, V. Tikhomirov, and H. Van Der Graaf, “Test beam studies of the GasPixel transition radiation detector prototype,” *Nucl. Instrum. Meth.* **A706** (2013) 59–64.
- [170] V. Ginzburg and I. Frank, “Radiation of a uniformly moving electron due to its transition from one medium into another,” *J. Phys. (USSR)* **9** (1945) 353–362. <http://inspirehep.net/record/45474/>.
- [171] V. Ginzburg, “Transition Radiation Effects in Particle Energy Losses,” *J. Phys. (USSR)* **37** (1959) 527–533. [http://www.jetp.ac.ru/cgi-bin/dn/e\\_010\\_02\\_0372.pdf](http://www.jetp.ac.ru/cgi-bin/dn/e_010_02_0372.pdf).
- [172] B. Dolgoshein, “Transition radiation detectors,” *Nucl. Instrum. Meth. A* **326** no. 3, (Mar., 1993) 434–469. <http://ivanik3.narod.ru/Vacuum/DolgosheinNIMdet.pdf>.
- [173] K. Zioutas *et al.*, “A Decommissioned LHC model magnet as an axion telescope,” *Nucl. Instrum. Meth.* **A425** (1999) 480–487, arXiv:astro-ph/9801176 [astro-ph].
- [174] C. Krieger, J. Kaminski, M. Lupberger, and K. Desch, “A GridPix-based X-ray detector for the CAST experiment,” *Nucl. Instrum. Meth.* **A867** (2017) 101–107.
- [175] R. Schön, M. Alfonsi, G. Hemink, M. P. Decowski, N. van Bakel, and H. van der Graaf, “Operating the GridPix detector in dark matter search experiments,” *Nucl. Instrum. Meth.* **A718** (2013) 446–449.
- [176] R. Schön, *XAMS - development of liquid xenon detector technology for dark matter searches*. PhD thesis, Amsterdam U., 2015. [http://www.nikhef.nl/pub/services/biblio/theses\\_pdf/thesis\\_R\\_Schon.pdf](http://www.nikhef.nl/pub/services/biblio/theses_pdf/thesis_R_Schon.pdf).
- [177] J. B. R. Battat *et al.*, “Readout technologies for directional WIMP Dark Matter detection,” *Phys. Rept.* **662** (2016) 1–46, arXiv:1610.02396 [physics.ins-det].

- [178] A. Biegun, J. Visser, T. Klaver, N. Ghazanfari, M.-J. van Goethem, E. Koffeman, M. van Beuzekom, and S. Brandenburg, "Proton radiography with timepix based time projection chambers," *Ieee transactions on medical imaging* **35** no. 4, (4, 2016) 1099–1105.
- [179] M. De Gaspari, J. Alozy, R. Ballabriga, M. Campbell, E. Fröjdh, J. Idarraga, S. Kulis, X. Llopart, T. Poikela, P. Valerio, and W. Wong, "Design of the analog front-end for the Timepix3 and Smallpix hybrid pixel detectors in 130 nm CMOS technology," *JINST* **9** no. 01, (2014) C01037. <https://cds.cern.ch/record/2025861>.
- [180] F. Krummenacher, "Pixel detectors with local intelligence: an IC designer point of view," *Nucl. Instrum. Meth. A* **305** no. 3, (Aug., 1991) 527–532.
- [181] J. Visser, M. van Beuzekom, H. Boterenbrood, B. van der Heijden, J. I. Muñoz, S. Kulis, B. Munneke, and F. Schreuder, "SPIDR: a read-out system for Medipix3 & Timepix3," *JINST* **10** no. 12, (2015) C12028.
- [182] F. M. Pitters, N. Alipour Tehrani, D. Dannheim, A. Fiergolski, D. Hynds, W. Klempt, X. Llopart Cudie, M. Munker, A. M. Nurnberg, S. Spannagel, and M. J. Williams, "Time and Energy Calibration of Timepix3 Assemblies with Thin Silicon Sensors," <https://cds.cern.ch/record/2649493>. CLICdp-Note-2018-008.
- [183] M. Schut, "Characterisation of the Timepix3 chip using a gaseous detector," Master's thesis, Nikhef, Science Park 105, Amsterdam, 2, 2015. [https://wiki.nikhef.nl/detector/pub/Main/ArticlesAndTalks/thesis\\_mijke\\_schut.pdf](https://wiki.nikhef.nl/detector/pub/Main/ArticlesAndTalks/thesis_mijke_schut.pdf).
- [184] "Garfield++," 2019. <https://garfieldpp.web.cern.ch/garfieldpp/>.
- [185] L. Scharenberg, "Studies on the thermal behaviour of GridPix-based detectors," Master's thesis, University of Bonn, 2019. <https://www.lhc-ilc.physik.uni-bonn.de/ergebnisse/dateien/t00000113.pdf?c=t&id=113>. Master thesis.
- [186] T. Krautscheid, *Design Studies for the Pixelized Readout of a TPC for the ILLD*. PhD thesis, Bonn U., 2015. <http://hdl.handle.net/20.500.11811/6877>.
- [187] M. Gruber, "Study of ionisation and amplification processes in gridpix detectors," Master's thesis, University of Bonn, 2018. <https://web.physik.uni-bonn.de/group/view.php?&group=1&lang=de&c=t&id=99>. Master presentation.
- [188] F. Hartjes, "Positive ionic drift in T2K gas," 2020. <https://indico.nikhef.nl/event/2202/contribution/0/1/material/slides/1.pdf>.
- [189] J. Frenkel, "On pre-breakdown phenomena in insulators and electronic semi-conductors," *Phys. Rev.* **54** (Oct, 1938) 647–648. <https://link.aps.org/doi/10.1103/PhysRev.54.647>.
- [190] V. Prodanovic, *Ultra-thin mems fabricated tynodes for electron multiplication*. PhD thesis, Delft University of Technology, 2019. <https://doi.org/10.4233/uuid:1f889837-0d94-415c-8137-6065c0a44245>.
- [191] F. Hartjes, "Investigating protection layers," Oct., 2020. <https://indico.nikhef.nl/event/2714/contribution/0/4/material/slides/0.pdf>.
- [192] C. Ligtenberg *et al.*, "Performance of a GridPix TPC readout based on the Timepix3 chip," in *Proceedings of the International Workshop on Future Linear Colliders (LCWS2018) Arlington, Texas, USA, October 22-26, 2018*. 2018. arXiv:1902.01987 [physics.ins-det].

- [193] H. Jansen, S. Spannagel, J. Behr, A. Bulgheroni, G. Claus, E. Corrin, D. Cussans, J. Dreyling-Eschweiler, D. Eckstein, T. Eichhorn, M. Goffe, I. M. Gregor, D. Haas, C. Muhl, H. Perrey, R. Peschke, P. Roloff, I. Rubinskiy, and M. Winter, “Performance of the eudet-type beam telescopes,” *EPJ Techniques and Instrumentation* **3** no. 1, (Oct, 2016) 7. <https://doi.org/10.1140/epjti/s40485-016-0033-2>.
- [194] M. Garcia-Sciveres *et al.*, “The FE-I4 pixel readout integrated circuit,” *Nucl. Instrum. Meth.* **A636** (2011) S155–S159.
- [195] D. Cussans, *Description of the JRA1 Trigger Logic Unit (TLU), v0.2c*. EUDET Collaboration, 2009. <https://www.eudet.org/e26/e28/e42441/e57298/EUDET-MEM0-2009-04.pdf>.
- [196] S. F. Biagi, “Monte Carlo simulation of electron drift and diffusion in counting gases under the influence of electric and magnetic fields,” *Nucl. Instrum. Meth.* **A421** no. 1-2, (1999) 234–240.
- [197] P. Schade, “Correction Methods for TPC Operation in Inhomogeneous Magnetic Fields.” DESY, Aug., 2010. [https://flc.desy.de/lcnotes/notes/localfsExplorer\\_read?currentPath=/afs/desy.de/group/flc/lcnotes/LC-DET-2010-001.pdf](https://flc.desy.de/lcnotes/notes/localfsExplorer_read?currentPath=/afs/desy.de/group/flc/lcnotes/LC-DET-2010-001.pdf).
- [198] M. Hauschild, “Progress in dE/dx techniques used for particle identification,” *Nucl. Instrum. Meth. A* **379** (1996) 436–441.
- [199] M. Hauschild, “2D and 3D cluster counting with GEMs and small pads: The digital TPC?,” in *Linear colliders. Proceedings, International Workshop on physics and experiments with future electron-positron linear colliders, LCWS 2002, Seogwipo, Jeju Island, Korea, August 26-30*, pp. 464–469. 2002.
- [200] **GEANT4 collaboration**, S. Agostinelli *et al.*, “GEANT4: A Simulation toolkit,” *Nucl. Instrum. Meth.* **A506** (2003) 250–303.
- [201] “ILCSOft,” 2020. <https://github.com/iLCSOft>.
- [202] M. Frank, F. Gaede, M. Petric, and A. Sailer, “Aidasoft/dd4hep,” Oct., 2018. <https://doi.org/10.5281/zenodo.592244>. webpage: <http://dd4hep.cern.ch/>.
- [203] W. Kilian, T. Ohl, and J. Reuter, “WHIZARD: Simulating Multi-Particle Processes at LHC and ILC,” *Eur. Phys. J.* **C71** (2011) 1742, [arXiv:0708.4233](https://arxiv.org/abs/0708.4233) [[hep-ph](#)].
- [204] T. Sjostrand, S. Mrenna, and P. Z. Skands, “PYTHIA 6.4 Physics and Manual,” *JHEP* **05** (2006) 026, [arXiv:hep-ph/0603175](https://arxiv.org/abs/hep-ph/0603175) [[hep-ph](#)].
- [205] R. Fruhwirth, “Application of Kalman filtering to track and vertex fitting,” *Nucl. Instrum. Meth.* **A262** (1987) 444–450.
- [206] K. Fujii, “Introduction to helical track manipulations.” Internal communications, JLC Physics Group, KEK, Tsukuba 305, Japan, 12, 1998. [https://www-jlc.kek.jp/subg/off1/lib/docs/helix\\_manip/main.html](https://www-jlc.kek.jp/subg/off1/lib/docs/helix_manip/main.html).
- [207] K. Fujii, “Extended Kalman filter,” <https://www-jlc.kek.jp/2004sep/subg/off1/kaltest/doc/ReferenceManual.pdf>.
- [208] W. Shockley, “Semiconductive wafer and method of making the same,” July, 1962. <https://patents.google.com/patent/US3044909>. US Patent 3,044,909, filed October 1958.
- [209] R. Gluckstern, “Uncertainties in track momentum and direction, due to multiple scattering and measurement errors,” *Nucl. Instrum. Meth.* **24** (1963) 381–389.

- [210] Z. Drasal and W. Riegler, “An extension of the Gluckstern formulae for multiple scattering: Analytic expressions for track parameter resolution using optimum weights,” *Nucl. Instrum. Meth. A* **910** (2018) 127–132, [arXiv:1805.12014](https://arxiv.org/abs/1805.12014) [physics.ins-det].
- [211] M. Killenberg, “Time Stamping of TPC Tracks in the CLIC\_ILD Detector,” <https://edms.cern.ch/document/1158960/1>. LCD-Note-2011-030.
- [212] D. Karlen, P. Poffenberger, and G. Rosenbaum, “Study of GEM-TPC Performance in Magnetic Fields,” *eConf* **C050318** (2005) 0825.
- [213] D. Jeans and G. Wilson, “Measuring the CP state of tau lepton pairs from Higgs decay at the ILC,” *Phys. Rev. D* **98** no. 1, (2018) 013007, [arXiv:1804.01241](https://arxiv.org/abs/1804.01241) [hep-ex].
- [214] S.-i. Kawada, K. Fujii, T. Suehara, T. Takahashi, and T. Tanabe, “A study of the measurement precision of the Higgs boson decaying into tau pairs at the ILC,” *Eur. Phys. J. C* **75** no. 12, (2015) 617, [arXiv:1509.01885](https://arxiv.org/abs/1509.01885) [hep-ex].
- [215] R. Ellis, I. Hinchliffe, M. Soldate, and J. van der Bij, “Higgs Decay to tau+ tau-: A Possible Signature of Intermediate Mass Higgs Bosons at the SSC,” *Nucl. Phys. B* **297** (1988) 221–243.
- [216] P. Colas, R. Diener, K. Fujii, L. Jönsson, J. Kaminski, P. Kluit, H. Qi, R. Settles, O. Schaefer, A. Sugiyama, J. Timmermans, and H. Videau, “TPC Interface Control Document,” [https://edmsdirect.desy.de/item/D00000001162555\\_A, 1, 1](https://edmsdirect.desy.de/item/D00000001162555_A_1_1).
- [217] B. Verlaat *et al.*, “TRACI, a multipurpose CO<sub>2</sub> cooling system for R&D,” in *proceedings of 10th IIR Gustav Lorentzen Conference on Natural Refrigerants*. Delft, Netherlands, 2012. [https://www.nikhef.nl/pub/services/biblio/bib\\_PN/GL2012\\_Verlaat\\_208.pdf](https://www.nikhef.nl/pub/services/biblio/bib_PN/GL2012_Verlaat_208.pdf).
- [218] D. S. Bhattacharya, D. Attié, P. Colas, S. Mukhopadhyay, N. Majumdar, S. Bhattacharya, S. Sarkar, A. Bhattacharya, and S. Ganjour, “Measurement and simulation of two-phase CO<sub>2</sub> cooling in Micromegas modules for a Large Prototype of Time Projection Chamber,” *JINST* **10** no. 08, (2015) P08001, [arXiv:1801.00304](https://arxiv.org/abs/1801.00304) [physics.ins-det].
- [219] B. Verlaat, “CO<sub>2</sub> cooling of an endplate with Timepix readout,” 9, 2009. <https://agenda.linearcollider.org/event/3742/contributions/14411/attachments/11611/19189/C02coolingForLCTPCsep09.pdf>. Talk at the LCTPC collaboration meeting, DESY.
- [220] T. Bawej *et al.*, “The New CMS DAQ System for Run-2 of the LHC,” *IEEE Trans. Nucl. Sci.* **62** no. 3, (2015) 1099–1103.
- [221] **ATLAS**, G. Aad *et al.*, “Technical Design Report for the Phase-I Upgrade of the ATLAS TDAQ System,”. CERN-LHCC-2013-018, ATLAS-TDR-023.
- [222] M. Campbell, J. Alozy, R. Ballabriga, E. Frojdh, E. Heijne, X. Llopart, T. Poikela, L. Tlustos, P. Valerio, and W. Wong, “Towards a new generation of pixel detector readout chips,” *JINST* **11** no. 01, (2016) C01007. <https://cds.cern.ch/record/2244412>.
- [223] X. Llopart, “The Timepix chip family.” Talk presented at the Medipix Symposium, CERN, Sep, 2019. [https://indico.cern.ch/event/782801/contributions/3470092/attachments/1909919/3155657/xavi\\_timepix.pdf](https://indico.cern.ch/event/782801/contributions/3470092/attachments/1909919/3155657/xavi_timepix.pdf).
- [224] P. Kluit, “Pixel tpc gating and double grid studies,” 2020. [https://agenda.linearcollider.org/event/8508/contributions/45461/subcontributions/1488/attachments/35476/54999/LCTPC\\_Gating.pdf](https://agenda.linearcollider.org/event/8508/contributions/45461/subcontributions/1488/attachments/35476/54999/LCTPC_Gating.pdf). Talk presented at the LCTPC WP meeting.

- [225] Y. Bilevych, V. Blanco Carballo, M. Chefdeville, M. Fransen, H. van der Graaf, C. Salm, J. Schmitz, and J. Timmermans, “TwinGrid: A wafer post-processed multistage micro patterned gaseous detector,” *Nucl. Instrum. Meth. A* **610** (2009) 644–648.
- [226] **Linear Collider TPC Collaboration**, “Collaboration board meeting,” DESY, Hamburg, Jan, 2020. [https://agenda.linearcollider.org/event/8362/sessions/4990/attachments/35280/54683/CB\\_agenda2020.pdf](https://agenda.linearcollider.org/event/8362/sessions/4990/attachments/35280/54683/CB_agenda2020.pdf).
- [227] **Linear Collider TPC Collaboration**, P. Schade and J. Kaminski, “A large TPC prototype for a linear collider detector,” *Nucl. Instrum. Meth. A* **628** (2011) 128–132.
- [228] S. Takeda, “Japan Linear Collider (JLC),” *Part. Accel.* **30** (1990) 143–152.
- [229] H. Baer, T. Barklow, K. Fujii, Y. Gao, A. Hoang, S. Kanemura, J. List, H. E. Logan, A. Nomerotski, M. Perelstein, *et al.*, “The International Linear Collider Technical Design Report - Volume 2: Physics,” [arXiv:1306.6352](https://arxiv.org/abs/1306.6352) [[hep-ph](#)].
- [230] **Linear Collider Collaboration**, L. Evans and S. Michizono, “The International Linear Collider Machine Staging Report 2017,” [arXiv:1711.00568](https://arxiv.org/abs/1711.00568) [[physics.acc-ph](#)].
- [231] **Science Council of Japan**, “SCJ Master Plan 2020,” Jan, 2020. <http://www.scj.go.jp/ja/info/kohyo/pdf/kohyo-24-t286-1.pdf>. As referenced by T. Tanabe, ILD General Meeting, Feb, 2020. [https://agenda.linearcollider.org/event/8404/contributions/45175/attachments/35306/54723/20200204\\_ILD\\_tanabe\\_V4.pdf](https://agenda.linearcollider.org/event/8404/contributions/45175/attachments/35306/54723/20200204_ILD_tanabe_V4.pdf).
- [232] **ICFA**, “ILC International Development Team,” Aug, 2020. [https://icfa.fnal.gov/wp-content/uploads/ICFA\\_IDT\\_Structure.pdf](https://icfa.fnal.gov/wp-content/uploads/ICFA_IDT_Structure.pdf).
- [233] T. Mori, “Recent Progress Towards the Realization of the ILC in Japan: Cooperative Efforts by Academia, Industry, and Local Region,” Dec, 2019. [http://www.jahep.org/files/input\\_JapanHEPC\\_20191213.pdf](http://www.jahep.org/files/input_JapanHEPC_20191213.pdf).
- [234] M. Pavsek, “US-Japan Cooperation in Science and Technology,” Nov, 2019. [https://agenda.linearcollider.org/event/8217/contributions/44502/attachments/35114/54363/Sendai\\_ILC\\_draft\\_remarks-\\_final\\_for\\_Jim.pdf](https://agenda.linearcollider.org/event/8217/contributions/44502/attachments/35114/54363/Sendai_ILC_draft_remarks-_final_for_Jim.pdf). Remarks at the Linear Collider Board Meeting, Sendai, Miyagi, Japan.
- [235] T. E. S. Group, “Deliberation document on the 2020 Update of the European Strategy for Particle Physics,” Tech. Rep. CERN-ESU-014, Geneva, 2020. <https://cds.cern.ch/record/2720131>.
- [236] “Supporting note for briefing book 2020: Towards an update of the European Strategy for Particle Physics,” Tech. Rep. CERN-ESU-005, Geneva, Sep, 2019. <http://cds.cern.ch/record/2705370>.
- [237] C. Martoff, D. Snowden-Ifft, T. Ohnuki, N. Spooner, and M. Lehner, “Suppressing drift chamber diffusion without magnetic field,” *Nucl. Instrum. Meth. A* **440** (2000) 355–359.
- [238] **DRIFT**, J. Battat *et al.*, “Low Threshold Results and Limits from the DRIFT Directional Dark Matter Detector,” *Astropart. Phys.* **91** (2017) 65–74, [arXiv:1701.00171](https://arxiv.org/abs/1701.00171) [[astro-ph.IM](#)].
- [239] D. P. Snowden-Ifft, “Discovery of Multiple, Ionization-Created Anions in Gas Mixtures Containing CS<sub>2</sub> and O<sub>2</sub>,” [arXiv:1308.0354](https://arxiv.org/abs/1308.0354) [[physics.ins-det](#)].
- [240] **DRIFT**, J. Battat *et al.*, “First background-free limit from a directional dark matter experiment: results from a fully fiducialised DRIFT detector,” *Phys. Dark Univ.* **9-10** (2015) 1–7, [arXiv:1410.7821](https://arxiv.org/abs/1410.7821) [[hep-ex](#)].

- [241] M. Lupberger, Y. Bilevych, H. Blank, D. Danilov, K. Desch, A. Hamann, J. Kaminski, W. Ockenfels, J. Tomtschak, and S. Zigann-Wack, "Toward the Pixel-TPC: Construction and Operation of a Large Area GridPix Detector," *IEEE Trans. Nucl. Sci.* **64** no. 5, (2017) 1159–1167.
- [242] B. van der Heijden, J. Visser, M. van Beuzekom, H. Boterenbrood, S. Kulis, B. Munneke, and F. Schreuder, "SPIDR, a general-purpose readout system for pixel ASICs," *JINST* **12** no. 02, (2017) C02040.
- [243] F. Hartjes, *A diffraction limited nitrogen laser for detector calibration in high energy physics*. PhD thesis, University of Amsterdam, 1990.  
[https://www.nikhef.nl/pub/services/biblio/theses\\_pdf/thesis\\_F\\_Hartjes.pdf](https://www.nikhef.nl/pub/services/biblio/theses_pdf/thesis_F_Hartjes.pdf).
- [244] C. Martoff, R. Ayad, M. Katz-Hyman, G. Bonvicini, and A. Schreiner, "Negative ion drift and diffusion in a TPC near 1 bar," *Nucl. Instrum. Meth. A* **555** (2005) 55–58, [arXiv:physics/0406114](https://arxiv.org/abs/physics/0406114).
- [245] N. Phan, R. Lafler, R. Lauer, E. Lee, D. Loomba, J. Matthews, and E. Miller, "The novel properties of SF<sub>6</sub> for directional dark matter experiments," *JINST* **12** no. 02, (2017) P02012, [arXiv:1609.05249](https://arxiv.org/abs/1609.05249) [physics.ins-det].
- [246] T. Ikeda, T. Shimada, H. Ishiura, K. Nakamura, T. Nakamura, and K. Miuchi, "Development of a Negative Ion Micro TPC Detector with SF<sub>6</sub> Gas for the Directional Dark Matter Search," [arXiv:2004.09706](https://arxiv.org/abs/2004.09706) [physics.ins-det].
- [247] P. Lewis, S. Vahsen, I. Seong, M. Hedges, I. Jaegle, and T. Thorpe, "Absolute Position Measurement in a Gas Time Projection Chamber via Transverse Diffusion of Drift Charge," *Nucl. Instrum. Meth. A* **789** (2015) 81–85, [arXiv:1410.1131](https://arxiv.org/abs/1410.1131) [physics.ins-det].
- [248] E. Baracchini, G. Cavoto, G. Mazzitelli, F. Murtas, F. Renga, and S. Tomassini, "Negative Ion Time Projection Chamber operation with SF<sub>6</sub> at nearly atmospheric pressure," *JINST* **13** no. 04, (2018) P04022, [arXiv:1710.01994](https://arxiv.org/abs/1710.01994) [physics.ins-det].
- [249] P. Colas, "TPC Costing," 1, 2020. <https://agenda.linearcollider.org/event/8362/contributions/45040/attachments/35277/54674/TPC-Costing20200114.pdf>. Talk at the LCTPC collaboration meeting, DESY.
- [250] P. Kluit, "Pixel TPC Modules costing estimate," 2020. [https://agenda.linearcollider.org/event/8362/contributions/45043/attachments/35270/54682/PixelTPC\\_costing.pdf](https://agenda.linearcollider.org/event/8362/contributions/45043/attachments/35270/54682/PixelTPC_costing.pdf). Talk at the LCTPC collaboration meeting, DESY.



---

# Summary

---

The Standard Model of particle physics provides a highly precise description of physics at the most fundamental scale. The most recent particle that was discovered in 2012 is the Higgs boson, which can induce electroweak symmetry breaking, and give masses to the gauge bosons. Additionally, it provides a mechanism to generate masses for the fermions. Although all known particles have now been observed, the Standard Model is not a complete description of nature: it does not explain why there is more matter than anti-matter, nor does it describe the properties of dark matter. Furthermore, many properties and parameters in the theory are arbitrary. For instance, it is a mystery what the origin of electroweak symmetry breaking is, and why the masses are what they are.

These problems can be solved by introducing new physics, but this will also modify the couplings between the Higgs boson and the Standard Model particles. Consequently, the existence of new physics, can be inferred from precision measurements of these couplings.

The study of the Higgs boson and its properties with very high precision will be an important goal of a future high-energy electron positron collider. At a future electron positron collider (at  $\sqrt{s} = 250$  GeV), the Higgs boson will primarily be produced in association with a  $Z$  boson. Both the well-known initial state, and relatively clean collision environment at an electron positron collider, will allow to reconstruct the production of the Higgs boson from the decay products of the recoiling  $Z$  boson alone. This enables accurate measurements of the absolute cross section and the Higgs boson mass, even if the Higgs boson decays to states invisible to the detector.

These measurements can be performed at the future International Linear Collider (ILC), which is one of the proposed electron positron colliders. Around the collision point a series of subdetectors will be placed to record the particles produced in the collision. One of the subdetectors is a gaseous Time Projection Chamber (TPC), which will measure the trajectory of the charged particles. A high precision position measurement is required to accurately determine the momentum of a particle from the curvature of its trajectory in a magnetic field.



In a gaseous TPC charged particles are detected through ionisation of the gas atoms and molecules in a drift volume. An electric field causes the ionisation electrons to drift toward the readout end plate. Near the end plate, the ionisation electrons enter the amplification region of the gas volume that has a strong electric field. Here, each ionisation electron causes an avalanche of ionisation, which induces charge on the readout plane. Electronics record the position and time of arrival of the signals, such that the 3-dimensional origin of the ionisation electrons can be reconstructed. Conventionally the charge is collected on mm-sized pads, but a silicon pixel readout chip has much finer granularity and can make an even more precise measurement.

The GridPix is a gaseous detector readout concept consisting of a pixel readout chip with an integrated amplification grid. The grid holes are precisely manufactured to be aligned to the pixels, which allows for the detection of single ionisation electrons. The GridPix as a TPC readout is shown in Figure S.1. The GridPix is based on a Timepix3 chip, which has  $256 \times 256$  pixels with a pitch of  $55 \mu\text{m} \times 55 \mu\text{m}$ , and can simultaneously per pixel record both the time of arrival of a signal and the time over threshold as a measure of the signal strength.

A single Timepix3 based GridPix was embedded in a small TPC to test its performance using a beam of 2.5 GeV electrons. A recorded track is shown in Figure S.2. The Timepix3 chip's capability to record the time over threshold allows for time walk corrections, which improve the hit resolution in the longitudinal (drift) direction. The resolution in the pixel plane is important for the momentum measurement in a large-scale TPC, and is shown in Figure S.3. Diffusion is found to be the dominating error on the track position measurement in both the pixel plane and in the drift direction.

Besides an accurate measurement of the trajectory, a TPC also measures the

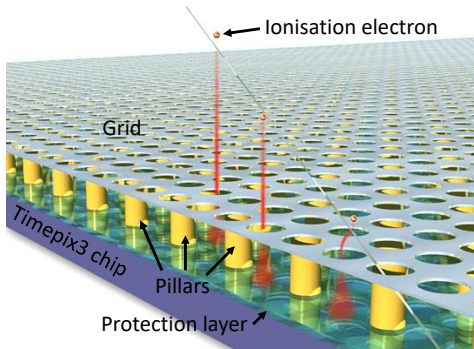


Figure S.1: Schematic of the GridPix as a TPC readout <sup>1</sup>.

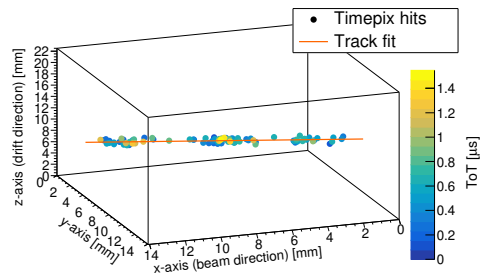


Figure S.2: A track recorded in a GridPix detector.

<sup>1</sup>Figure adapted from V. Blanco Carballo et al., "Applications of GridPix detectors," JINST 5 (2010) P02002

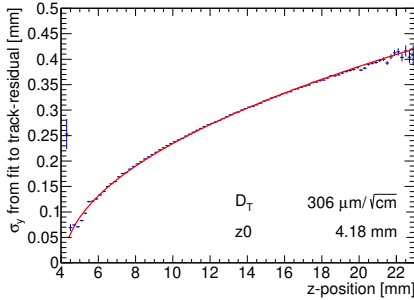


Figure S.3: Measured hit resolution in the pixel plane (blue points) as a function of the drift distance ( $z$ -position).

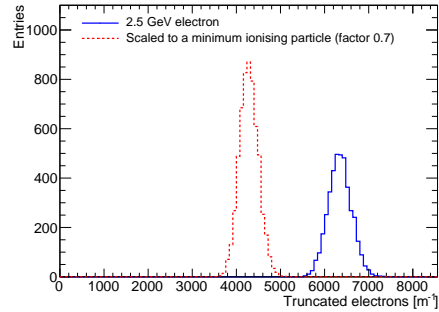


Figure S.4: Distribution of the truncated sum of detected electrons per meter for the 2.5 GeV electron (blue solid line) and the expected distribution for a minimum ionising particle (red dashed line).

energy loss  $dE/dx$  of charged particles in order to help identifying them. In Figure S.4, a truncated sum of 90% of the 20-pixel long intervals with the least number of detected ionisation electrons is shown for a measured 1 m electron track, together with the expected distribution for a 1 m track of a minimum ionising particle. The energy loss  $dE/dx$  resolution of 4.1% is found for an effective track length of 1 m. Using the fine granularity and sensitivity to single ionisation electrons, the energy loss  $dE/dx$  measurement can be further improved by employing cluster counting methods.

In order to cover the larger readout areas required for a full-size TPC readout at a collider experiment, the quad module with four GridPixes is developed. The module, shown in Figure S.5, has dimensions of  $39.6 \text{ mm} \times 28.38 \text{ mm}$  and is optimised for a large fraction of active surface of 68.9%. The quad module can be tiled to cover arbitrarily large areas.

The quad module was used to readout a small TPC, that was also tested using 2.5 GeV electrons. It is important to measure systematic errors, such as possible deformations in the pixel ( $xy$ ) plane of the TPC, because in a collider experiment these affect the momentum resolution. A silicon detector telescope provided a precise reference track, against which the detected hit positions of the quad can be compared. Near the edges of the chips there are small deformations due to inhomogeneities in the electric field. The mean residuals after correction for the electric field distortions are shown in Figure S.6. The systematic error from the quad detector for the distortions over the pixel plane is as small as  $13 \mu\text{m}$  ( $9 \mu\text{m}$  in the central region). The demonstrated resolution of the entire setup is  $41 \mu\text{m}$ .

The quad module can be applied in the International Large Detector at the ILC.

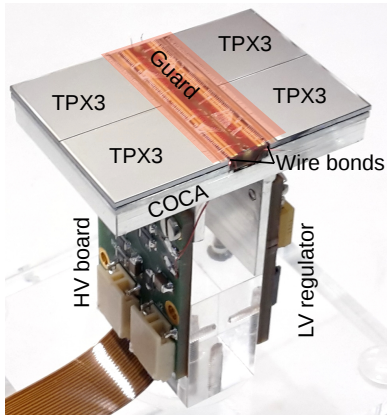


Figure S.5: Picture of the quad detector with four Timepix3 GridPixes (TPX3).

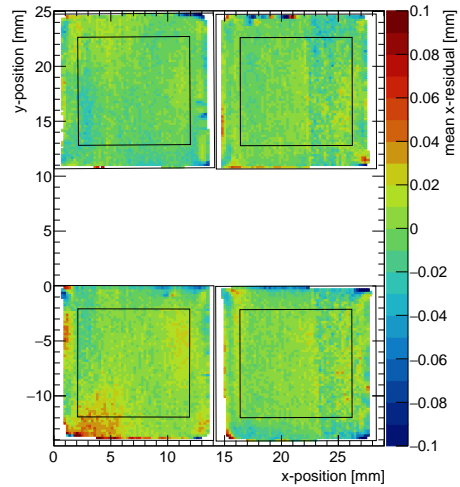


Figure S.6: Mean residuals in the pixel plane ( $x$ -residuals) at the expected hit position after corrections.

The layout of the end plate with a possible implementation based on the GridPix quad module has a fraction of sensitive area of 60%. The design is integrated in the simulation of the detector, and the Kalman filter reconstruction is adapted to the pixel readout.

The simulation of the TPC with pixel readout is used to estimate the momentum resolution. In Figure S.7 the momentum resolution for muon tracks of pixel readouts with an effective area of 60% and 100% are compared to the conventional pad readout. The momentum resolution knows two important limitations. The resolution is limited by the precision of the readout, and multiple scattering on the gas atoms and molecules. The latter is equal for all readouts, and dominant for low momentum tracks ( $< 10$  GeV), resulting in a similar momentum resolution of the pixel and pad readout for low momentum tracks. The measurement error of the readout is dominant for high momentum tracks ( $> 50$  GeV), and for these tracks the more precise pixel readout performs better. For a high momentum muon track at a polar angle of  $\theta = 85^\circ$ , a pixel readout with 60% coverage achieves an improvement of 20% over the conventional pad based readout. For more forward tracks, the improvement is even larger.

The simulation of the detector with a pixel TPC readout can be utilised to study its impact on the experimental study of the Higgs boson. Events with the production of a Higgs boson in association with a  $Z$  boson are simulated in a detector with pixel

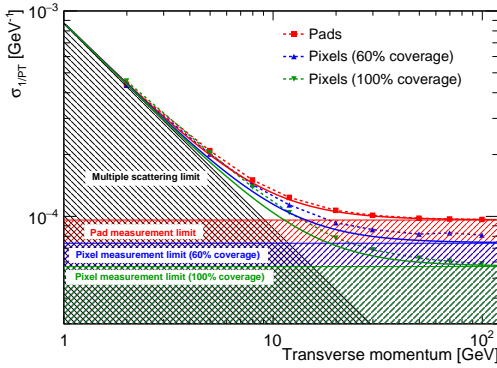


Figure S.7: The simulated momentum resolution of the TPC expressed as  $\sigma_{1/P_T}$  for muons at a polar angle of  $\theta = 85^\circ$  as function of the transverse momentum.

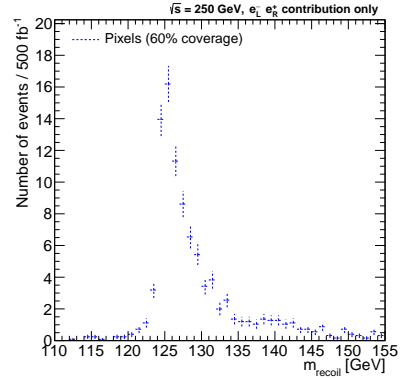


Figure S.8: Distribution of the recoil mass  $m_{\text{recoil}}$  for simulated  $e^+e^- \rightarrow ZH \rightarrow \mu^+\mu^-\tau^+\tau^-$  events.

TPC readout. The mass of the Higgs boson can be reconstructed from the decay products of the recoiling  $Z$  boson, which is shown in Figure S.8. Thus demonstrating how a pixel TPC readout might contribute to precision measurements of the Higgs boson.

In the quest for a more complete theory of nature, the precise investigation of the Higgs boson at a future electron positron collider has the highest priority. The best tracking performance for a TPC at the proposed International Linear Collider is offered by a TPC with a GridPix readout. The viability of a GridPix TPC readout has been demonstrated in the two detector tests described in this thesis, and the expected performance is established in a comprehensive simulation. In conclusion, the GridPix has a lot of potential for experiments at the next generation of high-energy electron positron colliders.



---

# Samenvatting

---

Het standaardmodel van de deeltjesfysica is een precieze beschrijving van de fundamentele natuurwetten. Het meest recente fundamentele deeltje waarvan het ontstaan in 2012 werd aangetoond, is het higgsboson. Dit deeltje kan zowel via elektro-zwakke symmetriebreking massa geven aan de ijkbosonen, als voorzien in een mechanisme dat massa geeft aan de fermionen. Hoewel met die ontdekking alle bekende deeltjes nu zijn waargenomen, is het standaardmodel niet een volledige beschrijving van de natuur: een verklaring voor waarom er meer materie dan antimaterie is ontbreekt, evenals een goede beschrijving van donkere materie. Bovendien heeft de theorie een aantal ogenschijnlijk arbitraire eigenschappen zoals de onduidelijke oorsprong van de elektro-zwakke symmetriebreking en de vele onverklaarde massaparameters.

Deze problemen zouden kunnen worden opgelost door de theorie uit te breiden, maar dit zou ook gevolgen hebben voor de koppelingsconstanten van de interacties tussen het higgsboson en de andere ongedekte deeltjes. Het bestaan van nieuwe elementen in de theorie kan dus afgeleid worden door het zoeken van kleine afwijkingen in deze interacties door middel van precisieingen.

Het onderzoek naar het higgsboson en het bepalen van zijn eigenschappen met een zeer hoge precisie is een belangrijk doel van een toekomstige hoogenergetische elektron-positronversneller. In een toekomstige elektron-positronversneller (bij  $\sqrt{s} = 250$  GeV), zal het higgsboson voornamelijk samen met een terugspringend  $Z$ -boson geproduceerd worden. De combinatie van een bekende begintoestand en een botsingsomgeving met weinig ruis maakt het mogelijk om de productie van een higgsboson af te leiden uit enkel de vervalproducten van dit gelijktijdig geproduceerde  $Z$ -boson. Dit maakt nauwkeurige metingen van de absolute dwarsdoorsnede en de massa van het higgsboson mogelijk, zelfs in het geval dat de vervalproducten van het higgsboson onzichtbaar zijn voor de detector.

Deze metingen kunnen uitgevoerd worden bij de toekomstige International Linear Collider (ILC), een van de voorgestelde elektron-positronversnellers. Om de deeltjes die bij een botsing worden geproduceerd te registreren, wordt een reeks detectieapparaten rondom het botsingspunt geplaatst. Een van de detectieapparaten is een gas-

gevulde tijdprojectiekamer (TPC), die het spoor van de geladen deeltjes zal meten. Een precieze positiemeting is vereist om het momentum van een deeltje nauwkeurig te bepalen aan de hand van de kromming van zijn baan in een magnetisch veld.

In een gasgevulde TPC worden geladen deeltjes waargenomen door ionisatie van gasatomen en moleculen in het drijfvolume. Een elektrisch veld zorgt ervoor dat de ionisatie-elektronen naar de uitleeseindplaat drijven. Nabij de eindplaat gaan de ionisatie-elektronen het versterkingsgebied van het gasvolume binnen. Hier is een sterk elektrisch veld waardoor elk ionisatie-elektron een lawine van ionisatie veroorzaakt, die lading induceert op het uitleesvlak. Elektronica registreert de positie en het tijdstip van aankomst van de signalen, zodat de 3-dimensionale oorsprong van de ionisatie-elektronen kan worden gereconstrueerd. Gewoonlijk wordt de lading verzameld op plaatjes van mm-formaat, maar een microchip met pixels heeft een veel fijnere granulariteit en kan een nog nauwkeurigere meting uitvoeren.

De GridPix is een uitleesconcept voor gasgevulde detectieapparaten dat bestaat uit een pixelchip met een geïntegreerd versterkingsrooster. Door precieze vervaardiging zijn de rastergaten uitgelijnd met de pixels, wat de detectie van individuele ionisatie-elektronen mogelijk maakt. Figuur S.1 toont de GridPix TPC uitlezing. De Timepix3 chip met  $256 \times 256$  pixels van  $55 \mu\text{m} \times 55 \mu\text{m}$  vormt de basis van de GridPix, en meet gelijktijdig per pixel de aankomsttijd van een signaal en de duur van het signaal boven de drempelwaarde als een maat voor de signaalsterkte.

Een enkele, op de Timepix3 gebaseerde GridPix werd ingebed in een kleine TPC om de prestaties te testen met behulp van een bundel met 2.5 GeV elektronen. Een geregistreerd spoor is getoond in Figuur S.2. Het vermogen van de Timepix3-chip om de duur van een signaal boven de drempelwaarde vast te leggen, maakt aankom-

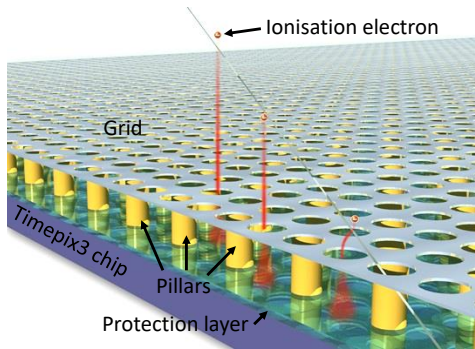


Figure S.1: Schematische weergave van de GridPix als een TPC uitlezing <sup>1</sup>.

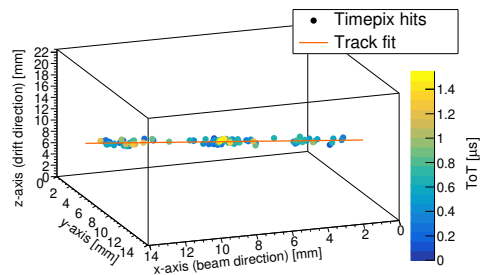


Figure S.2: Een spoor geregistreerd in een GridPix detectieapparaat.

<sup>1</sup>Figuur aangepast van V. Blanco Carballo et al., "Applications of GridPix detectors," JINST 5 (2010) P02002

stijdcorrecties mogelijk, die de plaatsbepaling in de longitudinale (drijf)richting verbeteren. De resolutie in het pixelvlak is belangrijk voor de impulsbepaling in een grootschalige TPC, en is weergegeven in Figuur S.3. Diffusie blijkt de voornaamste meetfout te zijn van de spoorpositiebepaling in zowel het pixelvlak als in de driftrichting.

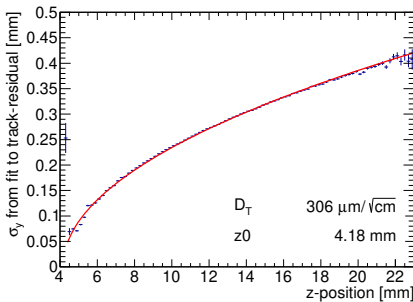


Figure S.3: De precisie van de positiemeting in het pixelvlak (blauwe punten) als functie van de drijfafstand ( $z$ -positie).

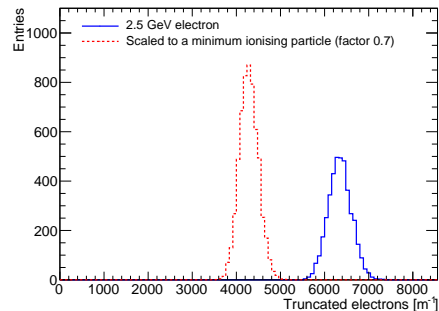


Figure S.4: Verdeling van de afgekapte som van gedetecteerde elektronen per meter voor een 2.5 GeV elektron (blauwe ononderbroken lijn) and dezelfde verwachte verdeling voor een minimaal ioniserend deeltje (rode onderbroken lijn).

Naast een nauwkeurige meting van de baan, meet een TPC ook het energieverlies  $dE/dx$  van een geladen deeltje om bij te dragen aan het vaststellen van het soort deeltje. In Figuur S.4 wordt een afgekapte som van 90% van de 20-pixel-lange intervallen met het minste aantal geregistreerde ionisatie-elektronen getoond voor een gemeten 1 m elektronenspoor, samen met de verwachte verdeling voor een 1 m-lang spoor van een minimaal ioniserend deeltje. De gevonden energieverliesresolutie  $dE/dx$  is 4.1% voor een effectieve baanlengte van 1 m. Door gebruik te maken van de fijne granulariteit en de gevoeligheid voor enkele ionisatie-elektronen, kunnen groeptelmethoden ingezet worden om de energieverlies  $dE/dx$ -meting verder te verbeteren.

Om te voorzien in de grotere uitleesvlakken die nodig zijn voor een TPC-uitlezings in een versnellerexperiment, is de quad-module met vier GridPixes ontwikkeld. De module, weergegeven in Figuur S.5, heeft afmetingen van  $39.6 \text{ mm} \times 28.38 \text{ mm}$  en is geoptimaliseerd voor een maximale fractie gevoelig oppervlak van 68,9 %. Door middel van betegeling met de quad-module, kunnen oppervlakten van elke grote worden bedekt.

De quad-module is gebruikt om een kleine TPC uit te lezen, die ook is getest met 2.5 GeV-elektronen. Het is belangrijk om systematische fouten te meten, zoals mo-



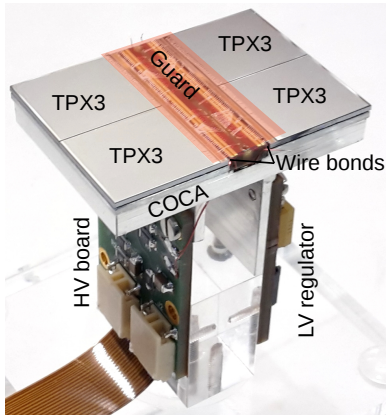


Figure S.5: Afbeelding van de quad-detector met de vier Timepix3 GridPixes (TPX3).

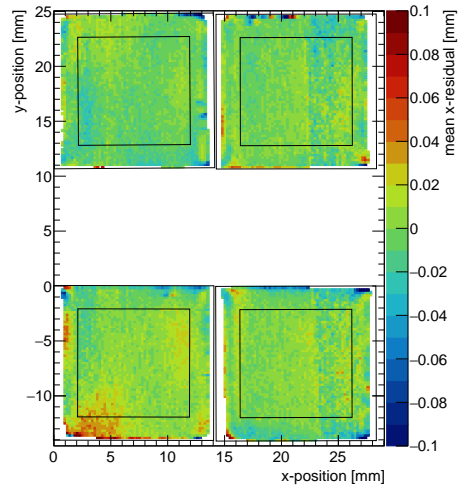


Figure S.6: Gemiddelde afwijkingen in het pixelvlak ( $x$ -afwijking) op het verwachte meetpunt na correctie.

gelijke verstoringen in het pixelvlak ( $xy$ ) van de TPC, omdat deze bij een botsingsexperiment de precisie van impulsbepaling beïnvloeden. Een telescoop met silicium detectieapparaten verzorgde een nauwkeurig referentiespoor, waarmee de gedetecteerde hitposities van de quad vergeleken konden worden. Nabij de randen van de chips zijn er kleine verstoringen als gevolg van vervormingen van het elektrische veld. De gemiddelde overgebleven afwijkingen na correctie voor deze elektrische veldvervormingen zijn weergegeven in Figuur S.6. De systematische fout van de quad-detectieapparaat door de vervormingen over het pixelvlak is slechts  $13\ \mu\text{m}$  (en  $9\ \mu\text{m}$  in het centrale deel). De aangetoonde nauwkeurigheid van de hele opstelling is  $41\ \mu\text{m}$ .

De quad-module kan toegepast worden in de International Large Detector bij de ILC. Een indeling van de eindplaat met een mogelijke, op de GridPix quad-module gebaseerde implementatie bereikt een gevoelig-oppervlaktefractie van 60%. Het ontwerp is geïntegreerd in de simulatie van de detector en de Kalmanfilterreconstructie is aangepast aan de pixeluitlezing.

Een simulatie van de TPC met pixeluitlezing wordt gebruikt om de impulsresolutie te bepalen. In Figuur S.7 wordt de impulsresolutie voor muonsporen van pixeluitlezingen met gevoelig-oppervlaktefracties van 60% en 100% vergeleken met de conventionele paduitlezing. De impulsresolutie kent in het algemeen twee belangrijke beperkingen: de precisie van de uitlezing en meervoudige verstrooiing door de gasatomen en moleculen. Dit laatste is gelijk voor alle uitlezingstechnologieën en

is dominant voor deeltjes met een klein impuls ( $< 10$  GeV), wat resulteert in een vergelijkbare impulsresolutie van de pixel- en paduitlezing voor tracks met een klein impuls. De meetfout van de uitlezing is dominant voor tracks met een groot impuls ( $> 50$  GeV), en voor deze tracks presteert de nauwkeurigere pixeluitlezing beter. Voor een muonspoor met een klein impuls onder een grote poolhoek van  $\theta = 85^\circ$ , bereikt een pixeluitlezing met 60% dekking een verbetering van 20% ten opzichte van de conventionele paduitlezing, en de verbetering is zelfs nog groter voor tracks onder een kleinere hoek.

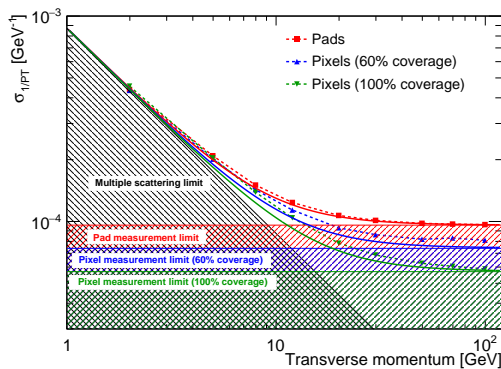


Figure S.7: De gesimuleerde impulsresolutie van de TPC uitgedrukt als  $\sigma_{1/P_T}$  voor muonen bij een poolhoek van  $\theta = 85^\circ$  als functie van het transversale impuls.

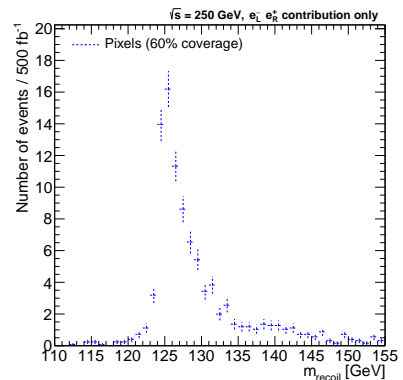


Figure S.8: Verdeling van de terugspringmassa  $m_{\text{recoil}}$  voor gesimuleerde  $e^+e^- \rightarrow ZH \rightarrow \mu^+\mu^-\tau^+\tau^-$  botsingsgevallen.

De simulatie van het detectieapparaat kan worden gebruikt om de impact van een pixel-TPC-uitlezing op de experimentele studie van het higgsboson te bestuderen. Botsingen met de productie van een higgsboson in combinatie met een  $Z$ -boson worden gesimuleerd in een detector met pixel-TPC-uitlezing. De massa van het higgsboson kan worden gereconstrueerd uit de vervalproducten van het terugspringende  $Z$  boson, zoals weergegeven in Figuur S.8. Hiermee wordt aangetoond hoe een pixel-TPC-uitlezing kan bijdragen aan precisieingen van het higgsboson.

In de zoektocht naar een completere beschrijving van het universum heeft het onderzoek naar het higgsboson bij een toekomstige elektron-positronversneller de hoogste prioriteit. Een TPC met een GridPix-uitlezing biedt de beste prestaties bij de voorgestelde International Linear Collider. De haalbaarheid van een GridPix TPC-uitlezing is aangetoond in de twee detectortests die in dit proefschrift worden beschreven, en de verwachte prestaties zijn vastgesteld met een uitgebreide simulatie. Kortom, de GridPix heeft veel potentie voor experimenten bij de volgende generatie hoogenergetische elektronen-positronversnellers.



---

# Acknowledgements

---

I owe many people a lot of gratitude for giving me the opportunity to do my PhD. I received a lot of help in performing research and in writing this thesis. Furthermore I want to thank everyone for making the past few years such a great time.

Ten eerste gaat mijn dank uit naar Peter, mijn supervisor. Jij had steeds tijd om mij met veel geduld te helpen. Met jouw enthousiasme en ideeën wist je mij zeer te motiveren. Ik heb bewondering voor hoe je mij altijd van waardevolle feedback voorzag, als iets minder goed ging, maar ook als het wel goed ging. Met veel sympathie heb je mij door mijn promotie geleid, waardoor ik terugkijk op een zeer fijne tijd.

Mijn dank gaat uit naar Fred, wiens ervaring en vaardigheden onontbeerlijk waren voor het onderzoek. Ik vind het knap wat je in het lab gedaan kreeg, en hoe je altijd intuïtief leek te weten wat er moest gebeuren aan de opstelling om een experiment tot een succes te maken.

Jan heeft me altijd geduldig uitleg en context geleverd bij alle experimenten. Veel dank voor het altijd nauwgezet controleren van al mijn werk, inclusief deze thesis met jouw ‘Timmermansoog’. Ik heb ook zeer genoten van de mooie verhalen van eerdere experimenten uit de tijd nog voordat ik mijn PhD begon.

Gerhard wil ik bedanken voor zijn bijdrage als promotor, en het werk dat hij heeft geleverd om het onderzoek in goede banen te leiden. Hij heeft mij van waardevol advies voorzien.

Het was een genoegen om op het Nikhef samen te werken aan de experimenten met Kevin, Naomi, Harry, Stergios, Martin, en anderen. Ook mijn dank aan Bas, Sander, en alle anderen in de mechanische en elektronica-afdelingen die meegewerkt hebben aan de opstellingen.

I would like to thank Jochen, Yevgen, Klaus and others from Bonn for their contributions to this research. The many calls and discussions were valuable. It was nice to work with you on the test-beam experiments, and thank you for hosting us in Bonn.

Mijn dank gaat ook uit naar Stan, mijn tweede promotor. Door de C3 gesprekken met Nicolo heb ik steeds een oog op de planning en ontwikkeling gehouden. Ook wil

ik mijn de promotiecommissie bedanken voor het beoordelen van dit werk.

A big thanks to the KEK student programme organisers and everyone who made my one-month stay at KEK a great experience. Daniel Jeans was my host and had setup a very interesting project and provided me with all the necessary help. Keisuke Fuji and everyone in the research group was very welcoming, especially Tomohisa Ogawa, who kindly showed me around in Tokyo.

I had a lot of useful discussions with the members of the LCTPC collaboration. The meetings, both online and offline, were always a great pleasure. In addition, I owe the members of the ILD collaboration my gratitude.

At Nikhef I want to thank everyone who kept me company in the past years. We had a nice time in the summer schools, at conferences and during the friday afternoon drinks. A thanks to Marc for being so cheerful, Brian for always talking passionately about physics, Marko for his cool stories, Matteo for being pleasant company during the many breaks, Pepijn for always being available for an abstract discussion. I am grateful for the many interactions with the members of the Nikhef ATLAS group (who let me reside in their office), and the great times I had with all the wonderful and kind people at Nikhef in general. I want to thank everyone with whom I had a lively daily lunch, enjoyed lectures, shared the office or played table football together with: Alice, Allesio, Ann-Kathrin, Ashley, Birgit, Bryan, Broos, Daan, Denys, Edwin, Federica, Jordy, Milo, Michiel, Peter, Rahul, Remco, Terry, Tim, Wouter, and so many others.

Mijn dank gaat ook uit naar vrienden en familie die mij ondersteund hebben. Tot slot, wil ik mijn vrouw, Laura, bedanken voor haar onophoudelijke steun gedurende mijn promotietraject.